SUBMILLIMETER VIDEO IMAGING WITH A SUPERCONDUCTING BOLOMETER ARRAY

by

DANIEL THOMAS BECKER

B.S., Rice University, 1994

M.S., University of Colorado, 2009

A dissertation submitted to the

Faculty of the Graduate School of the

University of Colorado in partial fulfillment

of the requirements for the degree of

Doctor of Philosophy

Department of Physics

2014

This dissertation entitled:
Submillimeter Video Imaging with a Superconducting Bolometer Array
written by Daniel Thomas Becker
has been approved for the Department of Physics

Nils Halverson

Kent Irwin

Date

The final copy of this dissertation has been examined by the signatories, and we find that both the content and the form meet acceptable presentation standards of scholarly work in the above mentioned discipline.

Becker, Daniel Thomas (Ph.D., Physics)
Submillimeter Video Imaging with a Superconducting Bolometer Array
Dissertation directed by Associate Professor Nils Halverson

Millimeter wavelength radiation holds promise for detection of security threats at a distance, including suicide bombers and maritime threats in poor weather. The high sensitivity of superconducting Transition Edge Sensor (TES) bolometers makes them ideal for passive imaging of thermal signals at millimeter and submillimeter wavelengths.

I have built a 350 GHz video-rate imaging system using an array of feedhorn-coupled TES bolometers. The system operates at standoff distances of 16 m to 28 m with a measured spatial resolution of 1.4 cm (at 17 m). It currently contains one 251-detector sub-array, and can be expanded to contain four sub-arrays for a total of 1004 detectors. The system has been used to take video images that reveal the presence of weapons concealed beneath a shirt in an indoor setting.

This dissertation describes the design, implementation and characterization of this system. It presents an overview of the challenges associated with standoff passive imaging and how these problems can be overcome through the use of large-format TES bolometer arrays. I describe the design of the system and cover the results of detector and optical characterization. I explain the procedure used to generate video images using the system, and present a noise analysis of those images. This analysis indicates that the Noise Equivalent Temperature Difference (NETD) of the video images is currently limited by artifacts of the scanning process. More sophisticated image processing algorithms can eliminate these artifacts and reduce the NETD to 100 mK, which is the target value for the most demanding passive imaging scenarios. I finish with an overview of future directions for this system.

Acknowledgements

It is a truth universally acknowledged that a graduate student in possession of a draft dissertation must be in want of an editor. I thank Nils Halverson, Bill Becker, and Linda Becker for carefully reading this dissertation and providing much useful feedback and advice. Any remaining grammatical, spelling, or other errors are entirely my own.

I had help from many different people while performing the work described in this dissertation. At some point in time, everyone associated with NIST's Quantum Sensors Project provided either useful advice as I worked through the design process, or gave concrete help in the lab. The sections at the ends of Chapters 4 and 5 give the names of people who were particularly helpful with specific areas. I would also like to thank Mike Niemack, who explained to me how to use the MCE as well as giving useful advice regarding the design and testing of the detectors. Conversations with Doug Bennett have been helpful in understanding TES detectors in general. Hannes Hubmayr was a useful resource for TES detectors and submillimeter detection. Randy Doriese helped me to understand SQUID readout. Carl Reintsema designed circuit boards for reading out the prototype detectors, and came up with the idea of reading out the mirror position using the SQUID readout system. Colin Fitzgerald, Jon Gard, Cale Gentry, and Bob Schwall all helped mount and unmount the cryostat from the primary mirror, a time-consuming and vexing task.

Of course none of this work would be possible without good advisors, and I thank Nils Halverson for giving me an initial opportunity to work in the field of submillimeter detection, and Kent Irwin for the opportunity to continue working in the field. Both Nils and Kent have been very supportive of me, particularly in light of the challenges I have faced as a graduate student attempting to support a family with young children, and I deeply appreciate their support and help.

I am blessed with a supportive family and extended family. I particularly thank my parents for, well, everything, and my sister Kate for serving as an inspiration in many different ways. During the months of writing this dissertation my children have had to put up with a father spending too much time writing in the basement, and I thank them for their patience with me. Finally, and most importantly, I thank my wife, Terzah, who helped in many small as well as large ways, and without whose love and support none of this would be possible.

Contents

List of Tables

List of Figures

Chapter 1

Introduction

This dissertation demonstrates that practical passive video imaging at millimeter and submillimeter wavelengths can be achieved through the use of large-format arrays of cryogenic detectors. This wavelength regime has been the subject of intense interest for military and security imaging applications for over 30 years. The reason for this interest is that the spectral region from 100 GHz – 1000 GHz offers a good compromise between transmission through obscuring materials (favoring lower frequencies) and spatial resolution (favoring higher frequencies) [1]. "Obscuring" here could refer to dust or fog for, e.g., helicopter landing assist systems, or clothing for concealed weapons detection. This region also contains spectral lines associated with the vibrational modes of molecules such as explosives that are of security interest [2, 3]. This interest has helped to drive technological advances in sources, detectors, and other technologies at these wavelengths [4–6]. This advancement has taken place in both spectroscopy and imaging applications, including "active" imaging, in which an observation target is illuminated by light and the reflections from that target are detected, and "passive" imaging, in which the target's thermal emissions are detected.

The millimeter and submillimeter astronomical community has also been interested in these wavelengths. In particular, the desire to make more and more detailed maps of the Cosmic Microwave Background (CMB) radiation has motivated this community to build instruments capable of higher and higher sensitivities. During the 1980s and early 1990s individual cooled bolometric detectors capable of achieving photon-noise-limited performance were developed. By 1994 it was clear that for astronomical applications the only way to increase map sensitivity was to develop arrays of detectors, but at that time no technology for the production of monolithic arrays was yet available [7].

The development of voltage-biased superconducting Transition Edge Sensor (TES) detectors enabled the development of large-scale cryogenic detector arrays [8]. These detectors use superconducting films as the bolometer's thermometer element, and can be fabricated in large arrays using standard lithographic techniques. The basics of TES operation and their advantages for passive imaging are described in Section 2.2 and Section 2.3. Chapter 3 provides more details on their behavior and operation. To read out these detector arrays, multiplexed readout systems based on Superconducting Quantum Interference Devices (SQUIDs) have been developed [9, 10]. The last few decades have also seen advances in the development of mechanical cryocoolers capable of reaching liquid-helium temperatures, removing the need to transport liquid cryogens to the often remote locations that are used for ground-based millimeter and submillimeter astronomy. This entire suite of technology — TES detectors, multiplexed SQUID readout, and cryogenics — is now mature and is routinely deployed on both ground and balloon-borne experiments in arrays containing up to 10,000 detectors [11].

The development of this technology offers new opportunities for passive imaging for security and other applications. Specifically, it is now possible to develop focal planes capable of video-rate imaging with temperature resolution of 100 mK or less. This dissertation describes the design and development of the National Institute of Standards and Technology (NIST) 350 GHz Video Imager, a system developed to detect concealed weapons at distances of 16 m – 28 m by producing video-rate images at 350 GHz. It will be used as a "gold standard" system for investigating the phenomenology of passive video imaging in order to determine the specifications for specific operational scenarios. It will also serve as a test-bed for evaluating new capabilities such as using polarization and spectroscopy to improve image contrast.

An outline of this dissertation is as follows. This chapter provides an overview of passive millimeter and submillimeter wavelength imaging for security applications, and describes the reasons for using detectors operating at cryogenic temperatures. Chapter 2 describes the specifications of the 350 GHz Video Imager and gives an overview of the approach used to meet those specifications, as well as a brief summary of other passive imaging systems that use cryogenic detectors. Chapter 3 presents the TES theory required to understand this dissertation. The overall design of the system is described in Chapter 4 and the design of the detectors and focal plane is covered in Chapter 5. Chapter 6 describes measurements taken to characterize the first of four planned 251-detector sub-arrays. The goal of this project is to generate video images at 350 GHz, and Chapter 7 describes how the 350 GHz Video Imager is used to do this, including quantitative evaluation of image quality. Chapter 8 provides a brief summary of the achievements of this project and gives directions for future work.

The system described in this dissertation is the result of work done by a number of different people both at NIST and at other institutions. The project was started by William Duncan, who also designed, procured, and assembled the optics. Bob Schwall designed the cryogenic system. The author of this dissertation was responsible for commissioning the cryogenic system, designing the feedhorns used to guide light onto the detectors, the design of both the prototype and production detectors (including optical coupling components), layout of the detectors and the focal plane wiring, design and assembly of the focal plane, characterization of both the prototype detectors and first production detector sub-array, and optical testing of the system including the generation of video images. Hsiao-Mei (Sherry) Cho fabricated the detectors. The acknowledgments at the end of Chapter 4 and Chapter 5 highlight important contributions from additional people both at NIST and elsewhere.

1.1 Security Imaging

The frequency range 100 GHz – 1000 GHz is attractive for detection of concealed weapons or contraband because common clothing materials have high transmission in this range [12]. As shown in Figure 1.1, transmission through clothing steadily decreases as frequency increases. This trend tends to push systems toward lower frequencies. A familiar example is the L3 ProVision systems operating at airport screening areas within the USA. These are "holographic radar" systems operating at 30 GHz, intended for close-range portal screening, and are based on technology developed at the Pacific Northwest National Lab (PNNL) [13, 14]. For applications in which it is acceptable to require individuals to pass through and pause at a particular location, these systems have excellent image quality for concealed items that are thick enough to provide radar contrast. Although the ProVision system takes still images with ~ 2 s image acquisition time, similar portal screening systems with video-rate capabilities are also under development [15].

But there are other applications and operational scenarios in which portal screening systems are not feasible. These include detection of suicide bomb belts and packs, crowd surveillance or imaging through fog or dust, all scenarios in which is it either desirable or required to make a detection while the object being observed is some distance away. In these scenarios it is not always reasonable to expect observation targets to be stationary,

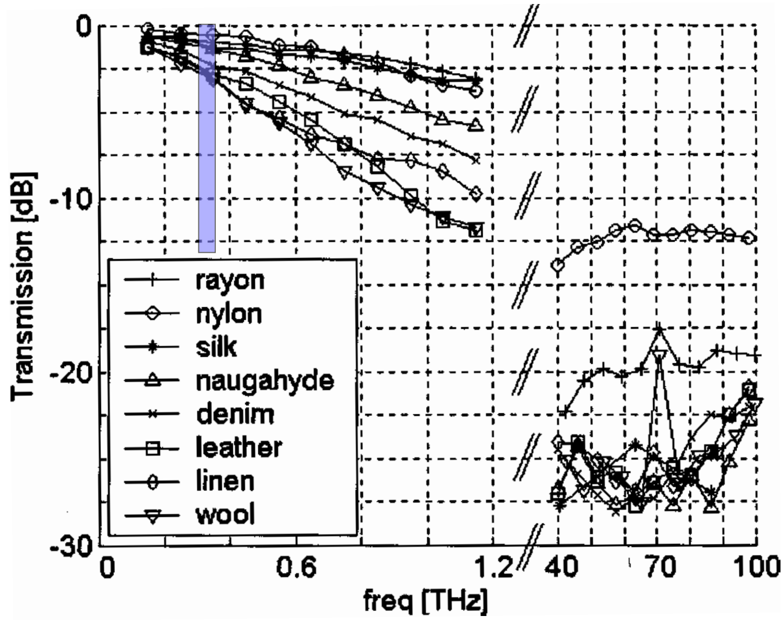

Figure 1.1: Plot of clothing transmission vs frequency. As frequency increases, transmission through different kinds of clothing decreases. The -10 dB observation band of the 350 GHz Video Imager is highlighted (318 GHz – 376 GHz). Taken from [12].

so video-rate imaging is also required. These applications are generally referred to as "standoff" detection because the imaging system "stands off" some distance from the target being imaged.

For these applications the choice of optical frequency is less clear than for portal imaging, because the lower frequencies favored by clothing transmission also imply worse spatial resolution for a fixed optical aperture size. The angular full-width-half-maximum (FWHM) θ of the beam produced by a circular aperture of diameter D observing at wavelength λ is [17],

$$\theta \sim 1.0\lambda/D. \tag{1.1}$$

For portal screening this is not prohibitive; the L3 Provision system has an effective aperture of 1.7 m [14]. But for standoff distances of 10 m or more, a system operating at 30 GHz would need an aperture of size ~10 m in order to achieve 1 cm resolution. This strongly drives the choice of frequency for standoff detection to frequencies above 100 GHz.

A final factor to consider in the choice of operating frequency is atmospheric transmission. As shown in Figure 1.2, not only does transmission through clothing fall with increasing frequency, but transmission through the atmosphere does as well, although

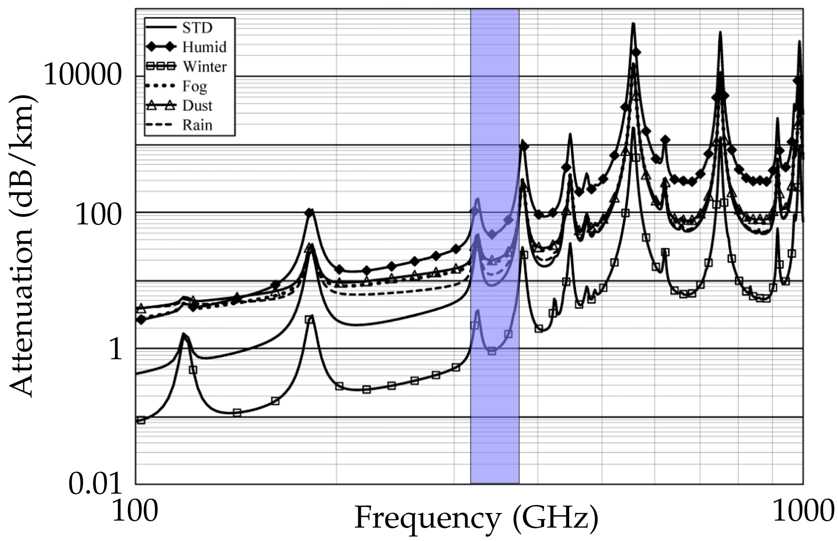

Figure 1.2: Plot showing attenuation through the atmosphere at sea level pressure for different weather and particulate conditions. Under the worst conditions in the 350 GHz Video Imager's band (curve labeled "Humid"), attenuation would be ~ 1.2 dB over 16 m, and a 0.15 dB under standard conditions (curve labeled "STD"). In the 640 GHz band, which would allow better spatial resolution, attenuation under standard conditions is already 1.2 dB and under the worst conditions is almost 10 dB at 16 m. The −10 dB observation band of the 350 GHz Video Imager is highlighted (318 GHz – 376 GHz). Taken from [16].

the trend is not monotonic. For the 350 GHz band used by the 350 GHz Video Imager, under the worst atmospheric conditions (hot and humid weather) transmission over 16 m is ~ 75 %. Indoors, in the dry winter climate of Boulder, CO, transmission over 16 m will be close to 100 %.

Security imaging systems for standoff applications broadly fall into two categories: "active" and "passive" [16, 18]. Active systems illuminate the target to be imaged with light and use the reflected light to obtain an image. Passive systems detect thermal blackbody emissions that are naturally emitted by all objects. Passive systems have the advantages that they are inherently covert, and do not suffer from public resistance due to worries about the health effects of illumination by millimeter-wavelength "radiation". Active systems would seem to have an inherent signal-to-noise advantage over passive systems, due to the low temperatures of the objects being observed (~ 300 K). But active imaging suffers from two problems that to-date have allowed passive imaging systems to generally exceed the image quality achieved with active systems.

Active Standoff Imaging

Both problems stem from the fact that active imaging systems generally use single-moded coherent sources of light; see [19] for a good overview of the issues. The first problem is generally referred to as “specular reflections”. This refers to the fact that the intensity of light that is reflected from the target and subsequently detected by the active imaging system is strongly dependent on the angle of incidence of the illuminating beam to the target. This leads to strong highlight areas in active images which can be 40 dB or more higher than neighboring areas, making images difficult to interpret.

The second problem is known as “speckle”. When a coherent light source is diffusely reflected from a surface which varies on distance scales comparable to or larger than a wavelength, some areas of the surface will randomly be oriented more favorably than others for reflecting light back to the system. The resulting random distribution of bright spots in the image is called speckle [20]. This phenomenon acts as a kind of noise in active images, and the signal-to-noise ratio of active imaging systems is often limited by speckle rather than noise inherent in the detection system itself.

The active imaging community has long been aware of these issues and is working to address them. One recent approach uses modulated multi-moded illumination to avoid these issues [21, 22]. Another approach is to use active illumination to build a radar system. Because radar systems detect time-of-flight or phase differences rather than intensity differences, they should be less susceptible to specular reflections and speckle. The active imaging system that at this time is closest to producing video-rate imaging largely free of specular-reflection and speckle artifacts is the 675 GHz radar system developed at the Jet Propulsion Laboratory [23]. This system operates at standoff distances of 16 m achieving a spatial resolution of 1 cm at 4 frames per second.

1.2 Required Image Noise for Passive Imaging

Passive imaging does not suffer from the problems of specular reflection and speckle. Instead, the primary challenge for passive imaging is implementing sufficiently sensitive detectors to achieve low-noise images at video frame rates. One commonly used figure-of-merit for noise in a passive imaging system is the Noise Equivalent Temperature Difference (NETD) of the image, defined as the smallest difference in the temperature distribution on the observation target that can not be distinguished from noise in the image. Few detailed studies of the NETD required for detection of concealed weapons or other contraband have been published, but the "lore" in the field is that for non-metallic concealed threats in an indoor environment, image signals are 0.5 K – 1.0 K, with 200 mK or lower NETD required for detection. One published estimate gives 100 mK as the required noise level [24] under some scenarios. The remainder of this section justifies this lore quantitatively.

To estimate the required NETD for a passive imaging system we must investigate both the required signal-to-noise for detection and the expected contrast (signal) in passive imaging scenarios. The required signal-to-noise ratio for object detection depends on the size of the object [25]. This is explored in a simple way in Figure 1.3. This figure shows a sequence of simulated images with a 22.5 cm (9 in) knife in the middle left of the image, and a 2×2 bright pixel block in the upper right. At a signal to noise ratio of 1, the knife is barely visible if you know where to look for it. At a signal-to-noise ratio of 2, the knife becomes visible but the much smaller block is not. The block can barely be made out at S/N 4, and at S/N 6 both block and knife are clearly visible. Based on this, I assume a required S/N of 4 for detection; this means that to reliably detect an object with a thermal contrast of 1 K in an image, the required NETD is 0.25 K.

The contrast in a passive image is set by the temperatures, emissivities and transmittivities of the objects being imaged, along with the temperature of the surrounding environment. Although passive imaging systems detect optical power, not the temperature of objects directly, these systems operate in the Rayleigh-Jeans limit where the optical power per mode is directly proportional to temperature; see Section 1.3. Figure 1.4 depicts the situation schematically. We consider an object at temperature T_1 with emissivity ϵ_1, covered by an object at temperature T_{cov} and transmittivity τ_{cov}. The entire scene is illuminated by blackbody radiation at temperature T_{amb}. We assume that the covering object has no reflection, so that $\epsilon_{cov} = 1 - \tau_{cov}$. The total temperature seen by an observer looking at the object through the covering will be

$$T_{tot,1} = (1-\epsilon_1)\tau_{cov}^2 T_{amb} + (1 + \tau_{cov}(1-\epsilon_1))(1-\tau_{cov})T_{cov} + \tau_{cov}\epsilon_1 T_1 \tag{1.2}$$

A second object behind the cover with temperature T_2 and emissivity ϵ_2 will appear to have a temperature given by Equation 1.2 with the subscript 1 replaced by 2 everywhere. The contrast seen between these two objects will then be

$$\Delta T_{1,2} = \tau_{cov}\left[(\epsilon_2 - \epsilon_1)\tau_{cov} T_{amb} + (\epsilon_2 - \epsilon_1)(1-\tau_{cov})T_{cov} + (T_1\epsilon_1 - T_2\epsilon_2)\right] \tag{1.3}$$

This equation shows that in order for contrast to appear in the image, we require a difference in temperature or emissivity or both between the two objects.

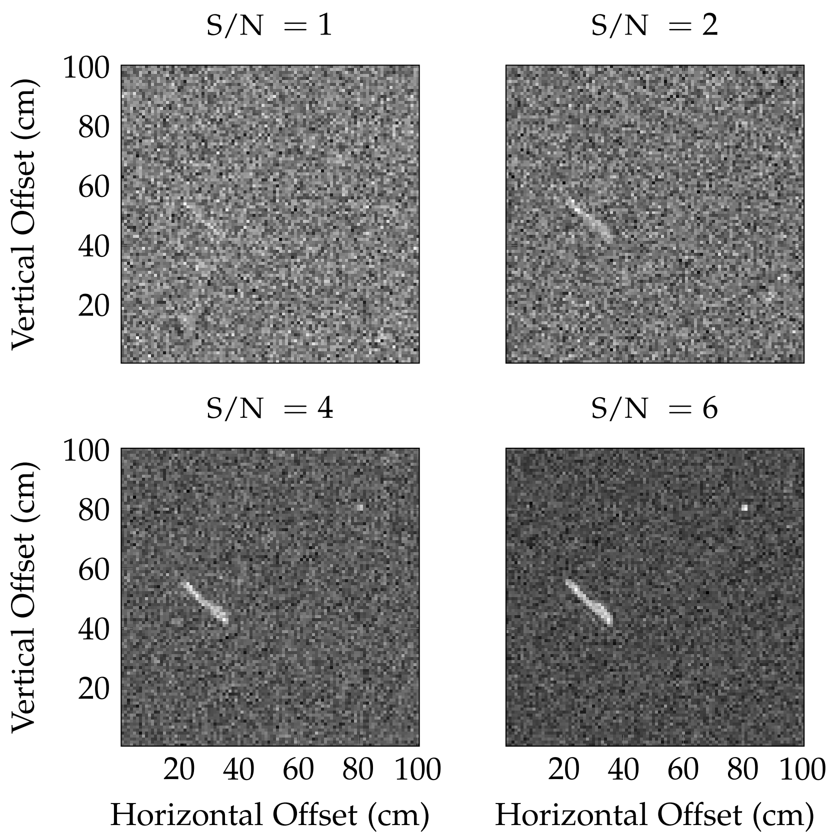

Figure 1.3: Exploration of signal-to-noise ratio (S/N) required for object detection. Each simulated image contains 100×100 pixels. In the middle left of each image is a simple 22.5 cm model of a knife. In the upper right a 2×2 block of pixels has been set to be bright. Gaussian noise was added to each image with a level appropriate for the S/N listed in the title. At S/N $= 1$ the knife is perhaps visible if you know where to look but the block is not. At S/N $= 2$ the knife become visible but the much smaller block is not. The block begins to become visible at S/N $= 4$, and is clearly visible at S/N $= 6$.

We consider the case where the objects have the same temperature but different emissivities. This would be the case for objects strapped next to skin, underneath clothing for a period of time so that objects come into thermal equilibrium with the body. In this case Equation 1.3 reduces to

$$\Delta T_{1,2} = \tau_{cov}(\epsilon_1 - \epsilon_2) \left[(1 - \tau_{cov})(T - T_{cov}) + \tau_{cov}(T - T_{amb})\right]. \tag{1.4}$$

In security screening scenarios we would typically expect $T > T_{cov} > T_{amb}$, so the rightmost factor will be positive. If we further assume that T_{cov} is midway between T and

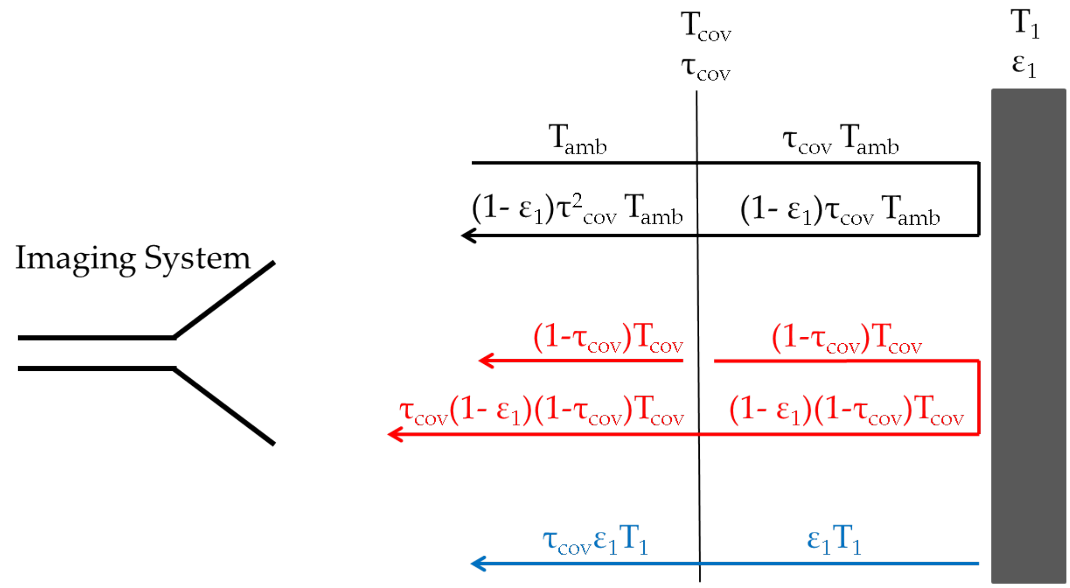

$$T_{tot} = (1-\varepsilon_1)\tau^2_{cov}\, T_{amb} + (1+\tau_{cov}(1-\varepsilon_1))(1-\tau_{cov})T_{cov} + \tau_{cov}\varepsilon_1 T_1$$

Figure 1.4: Schematic showing total temperature seen looking at an object at temperature T_1 with emissivity ϵ_1 through a cover at temperature T_{cov} with transmittivity τ_{cov}, all illuminated by ambient temperature T_{amb}. The Rayleigh-Jeans limit is assumed to hold, so that emitted optical power is directly proportional to the temperatures of the emitting sources. The object is assumed to have no transmission and the cover to have no reflection. The black arrows indicate transmission of ambient light through the cover, reflecting off the object, and passing back through the cover to the detecting system. The red arrows show the emission of the cover, which reaches the detector both directly and after reflecting off the object. The blue arrows show the emission of the object itself.

T_{amb}, then this further simplifies to

$$\Delta T_{1,2} = \frac{1}{2}\tau_{cov}(1+\tau_{cov})(\epsilon_1 - \epsilon_2)(T - T_{amb}). \tag{1.5}$$

The factor of $\frac{1}{2}$ represents the fact that at low τ, under these assumptions, the contrast is dominated by the difference in temperature between the cover and the object, which is half of the difference between the object and the ambient light.

In outdoor applications, T_{amb} will have contributions both from the ground (or structures/vegetation at ground level) and from the sky. The sky temperature depends strongly on the weather, and at 350 GHz could be as low as 100 K on a clear winter day, or approach 310 K on a hot day with high humidity [16]. Depending on the temperature and emission properties of local ground cover, under the worst-case scenario T_{amb} outdoors could be very close to human body temperature. This means that requirements on NETD for outdoor imaging in the worst-case scenarios could easily be 200 mK or lower, which motivates the search for imaging systems with NETD at or below 100 mK for outdoor applications.

Indoors, T_{amb} will be determined by the temperature of the room, typically 295 K = 72 °F. We can take as a challenging scenario the detection of plastic explosives hidden beneath a woolen sweater. From [12] we use $\tau_{cov} = 0.5$ and from [16] we can take $\epsilon_{explosive} - \epsilon_{skin} = 0.08$, a case where the emissivity of the explosive is higher than that of skin. Equation 1.5 gives $\Delta T_{1,2} = 0.45\,\mathrm{K}$, or a required NETD of 112.5 mK assuming a required S/N of 4. If the explosive material is cooler than body temperature then the requirements on NETD will be eased, but it is the worst-case scenarios that should drive system requirements.

From this we conclude that NETD values of 100 mK or lower are required for the most challenging passive imaging scenarios. The above analysis represents a simplification of any real-world scenario. It does not address requirements for object detection on more complicated backgrounds which may confuse an observer. The 350 GHz Video Imager will be used to investigate these requirements. But in the absence of any published studies of measured contrast in a variety of scenarios, we are justified in using these estimates as guidelines for the development of a system intended to perform those studies. The question remains as to what technology is capable of reaching this level of sensitivity.

1.3 Passive Imaging Technology

One option for the detection of light at 100 GHz – 1000 GHz is the use of incoherent direct detectors, including photo-diodes and other photon detectors as well as bolometers. These devices are square-law detectors, sensitive to the square of the incident electromagnetic field, i.e. to incident optical power. They can be characterized by a Noise Equivalent Power (NEP), defined as the detected signal power equal to the standard deviation of the detector noise in a 1 Hz post-detection bandwidth. To convert the NEP of the detectors to an NETD for an image, we must first have a conversion between detected optical power and source temperature. For a detector sensitive to M polarization-dependent spatial modes of the electromagnetic field and with total optical efficiency η_{tot}, the optical power detected per unit optical frequency is given by the Planck law in the form [7]

$$P_\nu(\nu,T)d\nu = \eta_{tot} M h\nu \frac{1}{e^{\frac{h\nu}{k_B T}} - 1} d\nu, \tag{1.6}$$

where h is Planck's constant, k_B is Boltzmann's constant, and T is the temperature of the source. If the detector is sensitive to all light incident from all directions, then $M = 2\pi\nu^2/c^2$, where c is the speed of light, and the result is Planck's law. The 350 GHz Video Imager's detectors are at the back of single-moded waveguide, and sensitive to both polarizations, so $M = 2$.

For detection of light around 350 GHz, and source temperatures in the range 50 K – 300 K, the Rayleigh-Jeans approximation

$$\frac{1}{e^{\frac{h\nu}{k_B T}} - 1} \approx \frac{k_B T}{h\nu} \tag{1.7}$$

holds to within 20 %, so that the total optical power in an optical bandwidth reduces to

$$P_\nu = \eta_{tot} M k_B T \Delta\nu. \tag{1.8}$$

This allows us to convert a detector NEP to a Noise Equivalent Temperature (NET) via

$$NET = \frac{NEP}{\eta_{tot} M k_B \Delta\nu}. \tag{1.9}$$

To convert this detector NET to an NETD for an image, we make the assumptions that noise for each detector can be modeled as an uncorrelated Gaussian noise source, so that the noise for a given pixel in the image will be given by the NET divided by the square root of twice the integration time for that pixel across all detectors[1]. We consider an image covering an area A with square pixels of side length s, produced by an imaging system with N detectors and video frame rate of FPS. The integration time per pixel τ_{int} will then be given by

$$\tau_{int} = \frac{N/FPS}{A/s^2}, \tag{1.10}$$

[1]The factor of 2 accounts for the fact that NEP is defined to give the total variance of a signal when integrated to only the Nyquist frequency, whereas the full bandwidth up to the sampling frequency is available for reducing noise.

and so the NETD of each image will be

$$NETD = \frac{NET}{\sqrt{2\tau_{int}}} \tag{1.11}$$

$$= \frac{NET}{\sqrt{2\frac{N/FPS}{A/s^2}}} \tag{1.12}$$

$$= \frac{NEP}{\eta_{tot} M k_B \Delta\nu} \frac{1}{s} \sqrt{\frac{A\,FPS}{2N}}. \tag{1.13}$$

Micro-bolometers have an advantage in that they can be fabricated in arrays with relative ease. Typical NEP values for uncooled micro-bolometers in the millimeter-wave region are $10\,\mathrm{pW}/\sqrt{\mathrm{Hz}}$–$100\,\mathrm{pW}/\sqrt{\mathrm{Hz}}$ [5, 26]. To convert this NEP into an NETD we must make some assumptions. In order to achieve sufficient spatial resolution, detectors at these wavelengths are typically sensitive to two modes, one per polarization, so we set $M = 2$. We can generously assume a non-scanning array with one detector per image pixel, so that $\sqrt{A/N}/s = 1$. A very good optical efficiency would be $\eta_{tot} = 0.5$, and a typical bandwidth at 350 GHz is 35 GHz. The minimum frame rate for video imaging is approximately 6 frames per second. Plugging these numbers into Equation 1.13 leads to an NETD of 50 K for the best-case scenario of $10\,\mathrm{pW}/\sqrt{\mathrm{Hz}}$ NEP. This is more than two orders of magnitude higher than the requirements discussed in Section 1.2.

Perhaps the most promising approach for room-temperature direct detection of millimeter and submillimeter light is an approach using backward tunnel diodes for operation at 90 GHz, which has achieved $0.1\,\mathrm{pW}/\sqrt{\mathrm{Hz}}$ NEP with a 32-channel linear array [27, 28]. Under the same assumptions as in the previous paragraph, a non-scanning array would achieve 5 K NETD, still insufficient to achieve the NETD requirements of Section 1.2.

A second option for room-temperature passive imaging is the use of coherent heterodyne detectors [5, 6]. This technology has advanced sufficiently that commercial systems are available today. The most promising option to-date is the ThruVision[2] family of imagers operating at 250 GHz [29, 30]. Video frame rates are 6 frames per second and claimed NETD is 1 K. The system also has the ability the average consecutive video frames when the target being observed is stationary, in order to reduce noise. The system has standoff distances up to 15 m, but with poor spatial resolution due to apertures that are only ~20 cm in diameter.

The Microsemi GEN 2 system[3] is another commercial system operating at 90 GHz.

[2] Digital Barriers plc, London, UK. `http://www.digitalbarriers.com/products/thruvision`

[3] Microsemi Corporation, Aliso Viejo, CA. This technology was acquired from Brijot systems in 2011.

This system achieves 5 cm resolution at 4–12 frames per second at standoff distances of a few meters. NETD is not quoted, but is presumably not better than 1 K. The performance of these two room-temperature imaging systems is listed in Table 2.1, along with other cryogenic passive imaging systems and the 350 GHz Video Imager described in this dissertation.

The conclusion is that to achieve sufficient NETD and spatial resolution for passive standoff imaging at distances of 10 m and greater, room temperature detectors to-date do not have sufficient noise performance. For this reason the 350 GHz Video Imager uses TES bolometers operating at cryogenic temperatures. The next chapter gives the specifications for our system and explains how TES bolometer arrays meet those specifications.

Chapter 2

System Specifications and Solutions

The 350 GHz Video Imager's specifications were chosen to allow the system to serve as a "gold standard" for investigating the phenomenology of passive video imaging. The system will eventually be used to take video images of a variety of concealed weapons and other objects, hidden beneath different types of clothing, in realistic operational scenarios. The goal of these studies will be to gain a thorough understanding of trade-offs between video frame rate, image resolution, and noise. This understanding will then aid the design of future systems for use in specific operational scenarios.

To that end, the system has been designed to achieve high resolution images with NETD that is limited by photon noise. This chapter describes the specifications for the 350 GHz Video Imager, and summarizes the technical approach taken to meet those specifications.

2.1 Specifications

The first goal of the 350 GHz Video Imager is to achieve uncompromised noise performance through the use of a large number of photon-noise-limited detectors. As discussed below, this requires the use of detectors at cryogenic temperatures. We have chosen to use 1004 Transition Edge Sensor (TES) bolometers as the detectors. The detectors will be installed as four individual 251-detector sub-arrays. This dissertation discusses results using one of these four sub-arrays.

The atmospheric window at $\sim$350 GHz ($\sim$860 µm) was chosen for the optical band. As can be seen from Figure 1.1 and Figure 1.2, this band is a good trade-off between transmission through the atmosphere and clothing (which favors lower frequencies) and spatial resolution (which favors higher frequencies). A 35 GHz full-width-half-maximum (FWHM) band was chosen to fit within this atmospheric window.

The design standoff distances from the observed target are 16 m – 28 m, configurable by changing the distance between the cryostat containing the detectors and the rest of the optical system. This range of standoff distances was chosen to provide separation from observation targets such as a suicide bomber, without requiring an unreasonably large optical aperture. A desirable spatial resolution at 16 m standoff would be 1 cm. However, at the center wavelength of the observation band of $\lambda_0 = 863\,\mu\text{m}$ (see Section 4.3), using the criterion of Equation 1.1 leads to a required aperture size of

$$D = 1.0 \times 863\,\mu\text{m} \times \frac{16\,\text{m}}{1\,\text{cm}} = 1.4\,\text{m}. \tag{2.1}$$

The chosen diameter for the mirror was somewhat smaller than this at 1.3 m. After accounting for the fact that the outer edge of the primary mirror is not illuminated (Section 4.2), the predicted resolution of the system is 1.2 cm (Section 4.4).

Security applications can require observing a moving target, so video frame-rates are needed. Exactly how fast the frame-rate needs to be in order to support accurate tracking can vary based on the scenario. The components of the 350 GHz Video Imager have all been designed to allow frame rates of up to 20 frames per second. The design field of view at 16 m is 1 m × 1 m.

In order to achieve all of these requirements, other aspects of the system design were compromised. In particular, the desire for high spatial resolution at longer standoff distances requires a large optical aperture, which increases the size of the system, reducing portability. Although the system is mounted on rollers so that it can be moved within the lab or into other labs, the location at which it points can not be steered in real-time. Additionally, the focus distance can only be changed by reconfiguring the mounting structure that connects the cryostat to the optics. In a deployable system the aperture could be made lighter through the use of different materials, and the focus and steering could be changed in real-time by an automatic mount, either at a fixed point or mounted on a vehicle.

2.2 Transition Edge Sensor Bolometer Basics

A bolometer detects optical power by measuring the temperature of an isolated object which absorbs the optical power. Figure 2.1 shows a schematic illustration of a bolometer.

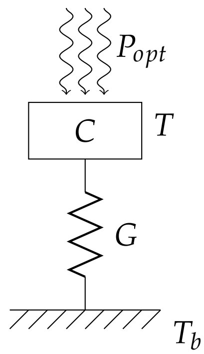

Figure 2.1: Schematic illustration of a bolometer. The bolometer detects optical power P_{opt} by absorbing it in an absorber with heat capacity C. The absorbed optical power causes the absorber temperature to rise to a temperature T above a thermal bath held at T_b. The rise in temperature is determined by the thermal conductance G.

Optical power P_{opt} falls onto an absorber with heat capacity C. The optical power is thermalized in the absorber, causing its temperature T to rise. The temperature T to which it rises is determined by the thermal conductance G which connects the absorber to a thermal bath at temperature T_b. See [7] for an excellent overview of bolometric detectors.

In a Transition Edge Sensor (TES) bolometer a thin superconducting film is used as a thermometer to measure the temperature T. A superconductor is a material which loses all electrical resistance when its temperature falls below a critical temperature T_c [31]. This phase transition from the "normal" to "superconducting" state can be very narrow. The steepness of the transition is characterized by the logarithmic temperature sensitivity α given by

$$\alpha = \frac{T_0}{R_0}\frac{\partial R}{\partial T}. \tag{2.2}$$

Typical values of α for TES detectors are 100 – 1000.

The first demonstration of a TES bolometer was in 1941 [32], and the first demonstration using Al (the material used for the detectors in this dissertation) was in 1977 [33]. But operation of a TES detector requires maintaining the temperature of the TES within the narrow transition, which proved challenging. An increase in the temperature of the TES — caused by an increase in absorbed optical power — causes a rise in the temperature of the TES. When current-biased, this rise in temperature causes an increase in I^2R Joule heating, causing the temperature of the detector to rise further, leading to instability.

Thus, TES bolometers did not come into widespread use until the development of the voltage-biased TES sensors [8] coupled with Superconducting Quantum Interference Device (SQUID) readout systems. When voltage-biased, a rise in TES temperature leads to a decrease in Joule heating, which lowers the temperature of the device. With a sufficiently steep transition, this electrothermal feedback process allows any change in incident power to be exactly matched by an opposite change in Joule heating, so that the device self-stabilizes at a new current level in the normal-to-superconducting transition while leaving the device temperature unchanged.

Because the device is voltage-biased, absorbed optical power causes a current change, so that a current amplifier is required for readout. This is accomplished through the use of SQUIDs, which are very sensitive magnetometers and so can be used to detect small changes in current. The use of SQUIDs for some applications is inconvenient because of the requirement to operate them at cryogenic temperatures. But they are ideal for the readout of cryogenic bolometers, because they operate at the same temperature and dissipate much less power than semiconductor amplifiers.

Chapter 3 covers the theory of TES operation required for understanding of this dissertation. The most detailed and authoritative reference for TES detectors is by Irwin and Hilton [34].

2.3 Transition Edge Sensors for Passive Imaging

TES detectors have two important advantages for building passive imaging systems: they can be photon-noise-limited, and it is straightforward to manufacture, operate, and read out arrays containing large numbers of them.

The fundamental noise limit in bolometers is set by random thermal fluctuations of the temperature of the absorbing element, termed “thermal fluctuation noise”. As described in Section 5.2, the noise equivalent power (NEP) of this noise source, expressed in units of $\mathrm{W}/\sqrt{\mathrm{Hz}}$ referred to power absorbed in the bolometer, is proportional to $\sqrt{k_B T_b P_{opt}}$. In a properly designed TES, this source of noise will dominate other sources of noise in the system (Johnson noise in the TES, SQUID noise). A sufficiently low bath temperature T_b can reduce thermal fluctuation noise to below the noise level caused by fluctuations in the arrival rate of photons. As described in Section 5.8, the expected NETD for the 350 GHz Video Imager populated with 1004 detectors is 38 mK, well below the performance benchmark established in Section 1.2.

The ability to put large numbers of TES detectors onto focal planes is due to two factors.

First, they can be fabricated using standard lithographic clean-room techniques, which allows development of array-scale focal planes. Second, the self-stabilizing behavior of voltage-biased TES detectors enables array-scale operation because it greatly relaxes requirements on uniformity of detector characteristics across a wafer in the fabrication process.

Reading out a large number of detectors individually requires an even larger number of wires, which complicates cryogenic designs. An important part of the success of TES detector arrays for millimeter and submillimeter astronomy has been the development of multiplexed SQUID readout systems. The 350 GHz Video Imager uses a time-division multiplexed readout system, the basics of which are described in Section 4.7, and the details of which can be found in the references cited there.

2.4 Other Cooled Detector Imaging Systems

Aside from the work described in this dissertation, three other groups are also working on cooled detector passive imaging systems. See Table 2.1 for a summary of some characteristics of these and other security imaging systems.

One system has been developed by a group working at the Institute of Photonic Technology (IPHT) in Jena, Germany. The first generation of this system [35] operates at 350 GHz with a 23 % optical bandwidth. NETD is measured at 0.4 K at 10 frames per second over a 1 m diameter field of view. This system operates at much colder temperature than the 350 GHz Video Imager using He3-sorption refrigerator, which would make it more complex and expensive to deploy, without a corresponding improvement in NETD performance. A second-generation system is currently under development [36, 37]. This system increases the number of detectors from 20 to 64 and the frame rate from 10 to 25 frames per second. NETD is predicted to be 160 mK.

A second system is under development by a group at MilliLab in Finland, working in collaboration with researchers at NIST. The first generation of this system operated over a wide optical band, 200 GHz – 1000 GHz, achieving 0.6 K NETD [38]. A second generation system is currently underway, with most changes intended to reduce the size and power requirements of the system, while also doubling the number of detectors from 64 to 128 [39]. The system uses superconducting TES bolometers with $T_c \approx 9\,\mathrm{K}$. The readout system is entirely different than that used by the Jena system and the system described in this dissertation. In order to eliminate the use of SQUIDs, an approach based on room-temperature amplification was developed that relies on negative feedback to keep the detectors voltage-biased [40]. While this system may be simpler and less expensive to deploy, it will be much less sensitive.

Finally, a group based at Cardiff University in Wales is in the early stages of developing a passive imaging system [41] based on Microwave Kinetic Inductance Detectors [42]. No images or NETD estimates have yet been presented publicly for this system.

Table 2.1: Table summarizing capabilities of different security video imaging systems. The values for the MilliLab II and IPHT Jena II systems are predicted, not measured, as measurements of the performance of these systems have not yet been published. As discussed in Section 7.9, the NETD for the 350 GHz Video Imager is based on a "flat field" video. Values labeled "N/A" are unavailable.

System	Optical Band (GHz)	Detector Count	Frame Rate	Standoff Distance (m)	Field of View ($m \times m$)	Resolution (cm)	NETD (mK)
ThruVision	250 ± 20	8	6	5.0 – 15.0	1×1 (at 10 m)	N/A	1000
Microsemi GEN 2	90± N/A	N/A	4 – 12	~ 3	N/A	5	N/A
MilliLab I	200 – 1000	64	6	5.0	4×2	4.0	600
MilliLab II	200 – 1000	128	6	5.0	2×1	2.5	400
IPHT Jena I	350 ± 40	20	10	8.5	1 m diam.	1.7	400
IPHT Jena II	350 ± 40	64	25	8.5	2×1	1.0	160
NIST 350 GHz Video Imager	347 ± 17	251	6	16	0.78×0.55	1.7	100

Chapter 3

TES Bolometer Theory

This chapter summarizes the TES theory used in this dissertation. I start by describing the TES electrical and thermal circuits, defining relevant parameters, and stating the linearized TES equations. For reference, I then summarize the important consequences of these equations, including expressions for detector responsivity, detector response to step functions in applied power and bias current, and detector noise. I do not derive most of these results, because excellent references are available [8, 34, 43].

I discuss the derivation of two results in more detail. First, I give an expression for the time-domain response to a step function in applied detector bias current. Second, I describe a new approach for measuring the natural detector time constant τ by extrapolating several measurements of the effective detector time constant τ_{eff} high in the transition.

3.1 TES Electrical And Thermal Circuits

Figure 3.1 shows the electrical and thermal circuits for a TES bolometer. The bolometer is voltage-biased by passing a bias current I_{bias} through a shunt resistor R_{sh} which has a much lower resistance than the normal-state resistance R_n of the TES. The current through the TES is inductively coupled into a SQUID for readout. The inductance L in the diagram represents the sum of the input inductance of the SQUID, a Nyquist inductor used to limit the noise bandwidth of the detector circuit, and any parasitic inductance present in the circuit.

The TES itself is represented by a variable resistance R, which depends on both the current through the TES and the temperature of the TES. The TES is thermally sunk to a heat capacity C which is weakly linked to a temperature bath T_b through a thermal conductance G. Optical power is absorbed by the heat capacity, causing the temperature T of the heat capacity and the TES to rise above T_b. Power dissipated in any heater resistor[1] present on the TES also contributes to this temperature rise.

Because the resistance of the TES depends on the temperature of the TES, and the temperature of the TES depends on the resistance of the TES through Joule heating, the electrical and thermal behavior of the TES are coupled. This coupling acts as feedback, termed "negative electrothermal feedback", first described in the context of TES detectors by Irwin[8]. As the optical power absorbed by the TES increases, the temperature of the TES increases, which causes the resistance of the TES to increase as well. Because the TES is voltage-biased, the Joule heating is inversely proportional to the resistance, so the Joule heating decreases, which causes the temperature of the TES to decrease, opposing the effect of the increased optical power. The negative electrothermal feedback speeds up the response time of the detector and allows the detector to self-bias into the superconducting transition.

[1] As described in Section 6.3, 31 detectors have heater resistors

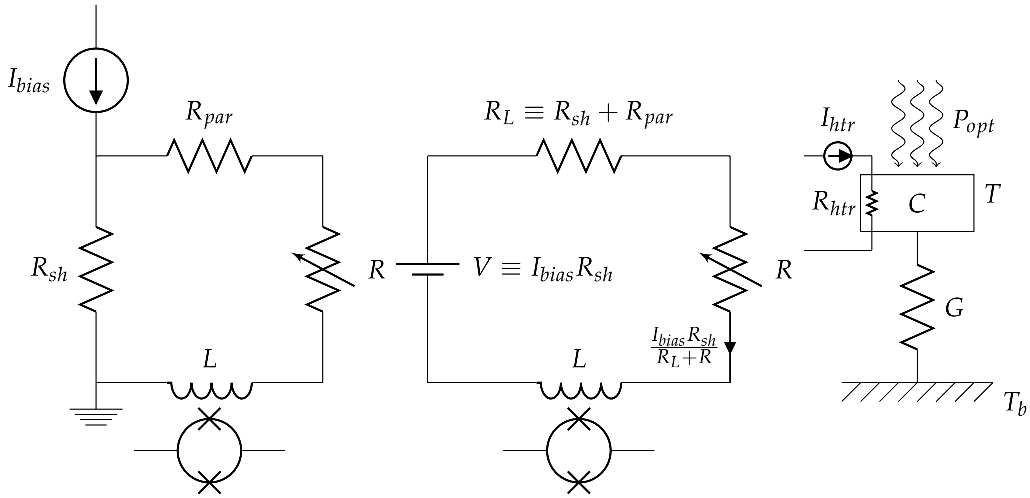

Figure 3.1: Electrical and thermal TES circuits. **Left** Schematic of real electrical TES circuit. The TES is biased by a stiff current I_{bias} shunted across a resistor R_{sh} that is much smaller than the normal-state resistance of the TES. The TES is represented by a variable resistance R, and R_{par} represents any parasitic resistance in the circuit. The current through the TES is inductively coupled into a SQUID for readout. The inductance L represents the sum of the input inductance of the SQUID, a Nyquist inductor, and any parasitic inductance present in the circuit. **Middle** Thevenin-equivalent TES circuit used in derivation of the linearized electrical and thermal equations for the TES. **Right** Thermal TES circuit. The TES is thermally sunk to a heat capacity C which absorbs optical power. The heat capacity C is connected to a heat bath T_b by a weak thermal link G, so that its temperature is elevated to a temperature T above T_b by applied optical power P_{opt}, power dissipated in a heater via I_{htr} (if present), and Joule heating of the TES itself.

3.2 Linearized Electrical and Thermal Circuits

In the limit of small changes in TES current and temperature, the resistance of the TES can be expressed as

$$R(T_0 + \delta T, I_0 + \delta I) = R_0 + \alpha \frac{R_0}{T_0} \delta T + \beta_I \frac{R_0}{I_0} \delta I, \tag{3.1}$$

where R_0, I_0 and T_0 are the resistance of the TES, the current flowing through the TES, and the temperature of the TES at the operating bias point, α is the TES temperature sensitivity, β_I is the TES current sensitivity, and $\tau \equiv C/G$ is the “natural” detector time constant. Note that all terms used in these equations and the rest of this chapter are defined in Table 3.1.

The power P_b flowing through the thermal link G is assumed to follow a power law of the form

$$P_b = K(T^n - T_b^n), \tag{3.2}$$

which can also be written in the form

$$P_b = \frac{GT}{n}\left(1 - \left(\frac{T_b}{T}\right)^n\right), \tag{3.3}$$

where

$$G \equiv \frac{dP_b}{dT} = KnT^{n-1}. \tag{3.4}$$

With these definitions it can be shown [34] that the behavior of the TES is described by a pair of coupled first-order differential equations:

$$\frac{d}{dt}\begin{pmatrix}\delta I\\ \delta T\end{pmatrix} = -\mathcal{M}\begin{pmatrix}\delta I\\ \delta T\end{pmatrix} + \begin{pmatrix}\delta V/L\\ \delta P/C\end{pmatrix}, \tag{3.5}$$

where the matrix $\mathcal{M}$ is

$$\mathcal{M} = \begin{pmatrix}\dfrac{1}{\tau_{el}} & \dfrac{\mathcal{L}_I G}{I_0 L}\\ -\dfrac{I_0 R_0 (2+\beta_I)}{C} & \dfrac{1}{\tau_I}\end{pmatrix}. \tag{3.6}$$

Here $\tau_{el} \equiv L/(R_0(1+\beta_I)+R_L)$ is the electrical time constant of the detector, $\mathcal{L}_I \equiv I_0^2 R_0 \alpha / G T_0$ is the detector loop gain, and $\tau_I \equiv \tau/(1-\mathcal{L}_I)$.

These coupled equations can be solved under different initial conditions and applied forces δV and δP. Discussion of three cases follows.

TES Power-to-Current Responsivity Driving the TES with a sinusoidal δP term and holding detector bias constant leads to the following expression for the detector power-to-current responsivity:

$$s_I(\omega) = -\frac{\dfrac{1}{V_0}\dfrac{1}{\gamma}\dfrac{\mathcal{L}_I}{\mathcal{L}_I+1}}{1 + j\omega\left(\tau_{eff} - \dfrac{1}{\gamma}\dfrac{\mathcal{L}_I}{\mathcal{L}_I+1}\dfrac{L}{R_0}\right) - \omega^2 \dfrac{L}{R_0}\dfrac{\tau_{eff}}{1+\beta_I+R_L/R_0}}, \tag{3.7}$$

$$\gamma \equiv 1 + \frac{\beta_I}{1+\mathcal{L}_I} - \frac{\mathcal{L}_I - 1}{\mathcal{L}_I+1}\frac{R_L}{R_0}. \tag{3.8}$$

Here τ_{eff} is the "effective" detector time constant and is given by

$$\tau_{eff} \equiv \frac{\tau}{1 + \dfrac{1-R_L/R_0}{1+\beta_I+R_L/R_0}\mathcal{L}_I}. \tag{3.9}$$

While imposing, these expressions are much simpler in the limit which generally hold for operating TES detectors: strong voltage bias ($R_L \ll R_0$), and $\tau \ll L/R$. In this limit the power-to-current responsivity becomes

$$s_I(\omega) = -\frac{1}{V_0}\frac{\mathcal{L}_I}{1+\beta_I+\mathcal{L}_I}\frac{1}{1+j\omega\frac{\tau}{1+\mathcal{L}_I/(1+\beta_I)}} \tag{3.10}$$

The detector response time is given by the natural detector time constant τ, sped up by a factor of $1+\mathcal{L}_I(1+\beta_I)$; for $\beta_I \ll 1$, this factor is typical of negative feedback, and justifies calling $\mathcal{L}_I$ the "loop gain" of the detector. In the further limit of strong electrothermal feedback ($\mathcal{L}_I \gg 1$, $\mathcal{L}_I \gg \beta_I$), the DC responsivity $s_I(0)$ is simply the inverse of the voltage bias. This means that because of the strong electrothermal coupling, any increase in applied optical (or heater) power is exactly canceled by a decrease in detector Joule heating, so that the TES temperature remains unchanged.

TES Response to Step Function in Power As demonstrated in Section 6.7, our detectors are always operated in a regime where $\tau_{eff} \gg \tau_{el}$. Under these conditions, Equation 3.7 simplifies to

$$s_I(\omega) = -\frac{1}{V_0\gamma}\frac{\mathcal{L}_I}{\mathcal{L}_I+1}\left(1+j\omega\tau_{eff}\right)^{-1}. \tag{3.11}$$

This implies that the time-domain response to step in applied power, for example from a heater, is

$$\delta I(t) = -\delta P s_I(0)(1-e^{-t/\tau_{eff}}) \tag{3.12}$$

$$= -\frac{\delta P}{V_0\gamma}\frac{\mathcal{L}_I}{\mathcal{L}_I+1}(1-e^{-t/\tau_{eff}}). \tag{3.13}$$

This can be used to measure τ_{eff} directly as well as the DC responsivity once the heater power has been calibrated (Section 6.6). As described in Section 3.3, it can also be used to measure the detector natural time constant τ. These measurements are described further in Section 6.4.

TES Response to Step Function in Bias Current To derive the behavior of the TES after a step function in applied bias, we solve the equations under the conditions

$$\begin{pmatrix}\delta I(0)\\ \delta T(0)\end{pmatrix} = \begin{pmatrix}0\\0\end{pmatrix} \tag{3.14}$$

with constant driving force starting at time zero of

$$\begin{pmatrix}\delta I_{bias}R_{sh}/L\\ 0\end{pmatrix} \tag{3.15}$$

Solving this system leads to the following expression for the TES current as a function of time:[2]

$$\delta I(t) = -\frac{\delta I_{bias} R_{sh}}{R_0} \frac{(\mathcal{L}_I - 1)\left(1 - \frac{\tau_{eff} - \tau_I}{\tau_{eff} - \tau_{el}} e^{-t/\tau_{eff}} + \frac{\tau_{el} - \tau_I}{\tau_{eff} - \tau_{el}} e^{-t/\tau_{el}}\right)}{1 + \beta_I + R_L/R_0 + \mathcal{L}_I(1 - R_L/R_0)}. \tag{3.16}$$

This expression is complex, but the behavior can be understood as follows. Immediately after an increase in bias current the voltage across the TES begins to increase, with a time constant of τ_{el}. As the voltage increases, the Joule power in the TES increases, which warms the TES. This warming increases the resistance of the TES. Because the TES is voltage-biased, this reduces Joule power in the TES, which tends to cool the detector as well as reduce current through the detector. This negative electrothermal feedback effect occurs with a time constant of τ_{eff}. Whether the final current through the TES is higher or lower than the original current depends on the loop gain. For $\mathcal{L}_I < 1$ the current increases, for $\mathcal{L}_I > 1$ it decreases and for $\mathcal{L}_I = 1$ the current through the TES remains unchanged.

Equation 3.16 depends on $\mathcal{L}_I$ and β_I in a complex way through τ_{eff}, τ_I, τ_{el}, and the prefactor. Nevertheless, if the response of a TES to a bias step can be measured with sufficient bandwidth to track the initial fast electrical response, bias steps can be used to measure $\mathcal{L}_I$ and β_I by performing non-linear parameter fitting to Equation 3.16. Measurements of $\mathcal{L}_I$ and β_I using this technique are described in Section 6.7.

When the TES is superconducting, Equation 3.16 takes on a much simpler form. Setting $R_0 = \mathcal{L}_I = \beta_I = 0$, the result is

$$\delta I(t) = -\frac{\delta I_{bias} R_{sh}}{R_L} \left(1 - e^{-t/(L/R_L)}\right). \tag{3.17}$$

Similarly, when the detector is fully normal, so that $\mathcal{L}_I = \beta_I = 0$, Equation 3.16 becomes

$$\delta I(t) = -\frac{\delta I_{bias} R_{sh}}{R_n + R_L} \left(1 - e^{-t/(L/(R_n + R_L))}\right). \tag{3.18}$$

The TES response to bias steps in the superconducting and normal states can thus be used as measurements of L and R_n.

[2]A Mathematica notebook which verifies this solution, as well as other solutions to the linearized TES equations, can be found at https://gist.github.com/danbek/8591076

Table 3.1: Symbols and parameters used in describing behavior of TES detectors.

Symbol	Explanation
I_{bias}	Current applied across shunt to bias TES.
R	TES resistance (depends on temperature and current)
R_n	TES normal-state resistance
R_{sh}	Shunt resistance
R_{par}	Represents any parasitic resistance in TES circuit
$R_L \equiv R_{sh} + R_{par}$	Load resistance used in analysis of TES circuit
T	TES temperature
T_b	Thermal bath temperature
I_0, R_0, V_0, T_0	TES current, resistance, voltage, and temperature at bias point
$P_{bath} = K(T^n - T_b^n)$	Total heat flow from TES island to heat bath
n	Power-flow index
P_{opt}	Optical power falling onto TES heat capacity
P_{htr}	Power applied to TES by heater resistor
P_J	Joule power dissipated by TES
C	Heat capacity of TES island
$G \equiv \frac{dP_{bath}}{dT} = KnT^{n-1}$	Weak-link differential thermal conductance
$\tau \equiv \frac{C}{G}$	TES natural time constant
$\tau_{el} \equiv \dfrac{L}{R_L + R_0(1+\beta_I)}$	TES electrical time constant
$\tau_I \equiv \dfrac{\tau}{1-\mathcal{L}_I}$	TES constant-current time constant
$\tau_{eff} \equiv \dfrac{\tau}{1 + \frac{1-R_L/R_0}{1+\beta_I+R_L/R_0}\mathcal{L}_I}$	TES effective time constant
$\alpha \equiv \frac{T_0}{R_0}\frac{\partial R}{\partial T}$	Logarithmic TES temperature sensitivity
$\beta_I \equiv \frac{I_0}{R_0}\frac{\partial R}{\partial I}$	Logarithmic TES current sensitivity
$\mathcal{L}_I \equiv \frac{I_0^2 R_0 \alpha}{G T_0}$	Loop gain
$\delta V = \delta I_{bias} R_{sh}$	Change in bias voltage applied to TES
δP	Change in power (optical or heater) falling on TES

3.3 Measurement of Natural Time Constant

Near the top of the superconducting transition, $\mathcal{L}_I < 1$, so that $\tau_{eff} > 0.5\tau$. The TES detectors used for the 350 GHz Video Imager have been designed so that $\tau \gg L/R_n$ (see Section 5.2), so that the response to a step in applied heater power is given by Equation 3.12. As the fully normal state is approached, τ_{eff} approaches τ, so that measuring the τ_{eff} very high in the transition will give a measurement of τ. However, the power-to-current responsivity decreases high in the transition, reducing the signal-to-noise of the measurement.

To avoid this problem, an expression can be obtained linking τ and τ_{eff} that holds independent of location in the transition, as long as the assumption $\tau_{eff} \gg L/R_0$ holds. The DC response to a step in applied power δP is given by

$$\delta I = \frac{\delta P}{I_0 R_0} \frac{\mathcal{L}_I}{1 + \beta_I + R_L/R_0 + (1 - R_L/R_0)\mathcal{L}_I}. \tag{3.19}$$

This equation can be solved for $\mathcal{L}_I$, and then substituted into the expression for τ_{eff}. This leads to

$$\tau_{eff} = \tau - \tau \mathcal{K} I_{bias} \delta I, \tag{3.20}$$

$$\mathcal{K} \equiv \frac{R_{sh}}{\delta P} \frac{R_0 - R_L}{R_0 + R_L}. \tag{3.21}$$

Here the relation

$$I = I_{bias} \frac{R_{sh}}{R + R_L} \tag{3.22}$$

has also been used.

Equation 3.20 holds independent of $\mathcal{L}_I$ and β_I. The factor $\mathcal{K}$ depends on the bias point, but high in the transition this dependence is weak, so that $\mathcal{K}$ can be treated as a constant.

To use Equation 3.20 to measure τ, steps in heater power are applied to the TES at a set of bias points close to the normal state. At each bias point the DC change in TES current δI and τ_{eff} are measured by fitting the TES response to Equation 3.12, and the bias current I_{bias} is recorded. A non-linear curve fit can then be applied to Equation 3.20 to solve for τ and $\mathcal{K}$. Alternately, $\mathcal{K}$ can be calculated if all factors feeding into it are known, and then Equation 3.20 can be solved directly for τ.

Section 6.4 presents measurements of τ for four detectors using this technique.

3.4 IV Curve Analysis

TES detector current-vs-voltage (IV) curves contain important information about the behavior of TES detectors. They directly yield the resistance of the TES in both the normal state and throughout the superconducting transition. But they also allow other properties of the TES to be measured by comparing IV curves taken under different operating conditions, such as different bath temperatures and applied heater and/or optical power loads.

The total amount of power flowing through the TES thermal conductance G is given by

$$P_{tot} = K(T^n - T_b^n) = P_{opt} + P_{htr} + I^2R(T, I). \tag{3.23}$$

We can make the assumption that at the start of the superconducting transition, where $R \approx R_n$, $\beta_I = 0$, i.e. the resistance of the TES depends only on the TES temperature, and not on the current through the TES. This assumption has been observed to hold empirically for many different types of TES detectors, and there are also theoretical reasons to expect it to be true [44]. Under this assumption, near the top of the transition the total power P_{tot} is current-independent, so the following relationship must hold:

$$P_J \equiv I^2R = P_{tot} - P_{opt} - P_{htr} = P_{tot} - P_{opt} - I_{htr}^2 R_{htr}. \tag{3.24}$$

In practice, I treat $R = 0.99R_n$ as sufficiently high in the transition for this relationship to hold.

Equation 3.24 is used in two different ways in this dissertation to extract information about the TES detectors, as described in the following subsections.

Calibration of Heater Resistors

If a set of IV curves are taken at the same bath temperature but different heater biases, Equation 3.24 allows measurement of the resistance of the TES heater by fitting for R_{htr} and $(P_{tot} - P_{opt})$. Figure 6.2 (reproduced in this chapter for convenience as Figure 3.2) shows how this is done using a series of IV curves, all of which were taken for a particular detector labeled R28C0. The upper left plot shows a set of TES IV curves taken at $T_b = 1100$ mK, with only the applied heater bias varying. The upper right plot shows the same data, but in terms of TES Joule power and TES resistance. As applied heater current decreases, the Joule power at the top of the transition decreases. In the lower left, the Joule power at $0.99R_n$ is plotted vs applied heater current. A fit to Equation 3.24

is also plotted. Finally, the lower right plot shows R vs P_J after the heater power has been added to each curve. This plot shows that the powers are equal very high in the transition, where the assumption that Joule power only depends on TES resistance holds. It also shows that this assumption breaks down deeper in the transition.

Note that in order to determine the value of R_{htr} one must know the heater current. Any error in the assumed heater current will lead to a corresponding error in the derived R_{htr} value. But because R_{htr} is derived from the power dissipated in the resistor, the product $I_{htr}^2 R_{htr}$ will remain unchanged. This means that whenever the value R_{htr} is used to calculated a power, the power value will be correct even with an incorrect value for the heater current.

Section 6.3 uses this approach to calculate R_{htr} for the seven working heaters on columns 0 and 1.

Measurement of TES Differential Thermal Conductance G

With knowledge of the heater resistances, IV curves can be taken over a wide range of bath temperatures, which enables a measurement of the TES thermal conductance G and transition temperature T_c. In this case P_{tot} will be different for each IV curve, so that Equation 3.23 can be used in the form

$$P_{htr} + P_J + P_{opt} = \frac{GT_c}{n}\left(1 - \left(\frac{T_b}{T_c}\right)^n\right). \tag{3.25}$$

A non-linear curve fit can then be used to find G, T_c, and n. The upper plots in Figure 6.4 (reproduced in this chapter for convenience as Figure 3.3) show an example of this fit for the detector labeled R30C1. The fit procedure leads to correlation between the fit values of G and n which indicated degeneracy in the fit between G and n.

Section 6.5 uses this approach to calculate G, T_c and n for the seven detectors with working heaters on columns 0 and 1.

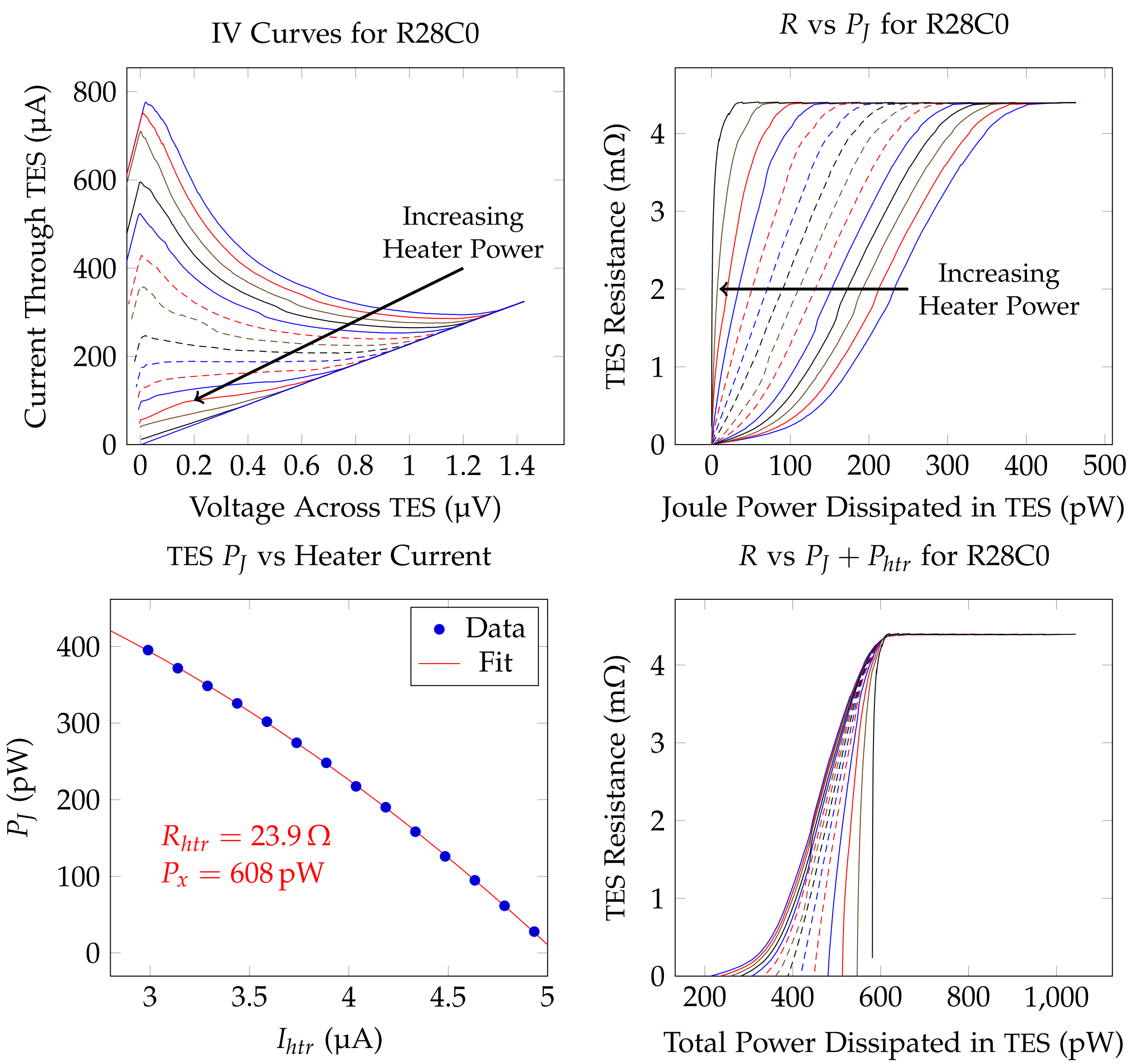

Figure 3.2: Plots describing heater measurements, for the case of the detector labeled R28C0. **Upper Left** IV curves. The IV curves should become vertical when the detector becomes fully superconducting at zero voltage, but these curves shows a non-infinite slope. The reason for this is that the readout system as configured for these IV curves was unable keep up with the rapid change of current in the superconducting branch. **Upper Right** Same data as in upper left plot, but represented in terms of TES Joule power and resistance. As the bias current for the heaters is increased, the curves shift to the left. **Lower Left** Measured P_J vs heater current at $0.99R_n$, as well as fit to Equation 3.24. **Lower Right** Same plot as upper right, but the heater power based on $R_{htr} = 23.6\,\Omega$ has been added to each curve. This demonstrates that $\beta_I = 0$ does not hold below the very top of the transition.

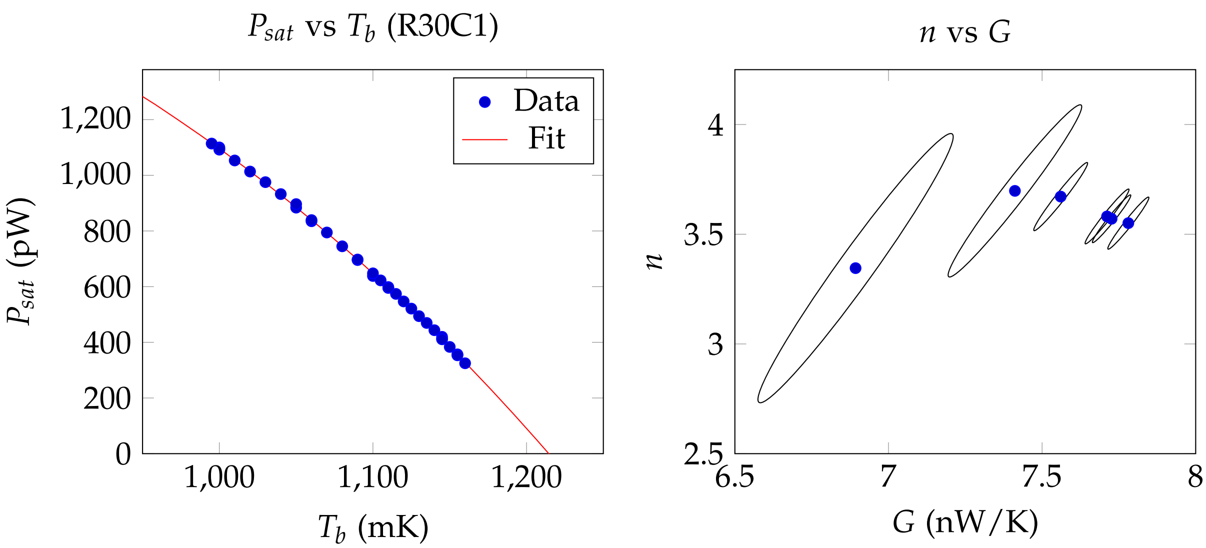

Figure 3.3: Plots showing fit to Equation 3.25 for the detector labeled R30C1. **Left** Plot showing P_{sat} vs T_b assuming $P_{opt} = 150$ pW (see Section 6.5). The red line shows the best fit to Equation 3.25. The data cover 36 data points including 25 temperatures from 995 mK – 1160 mK and 11 different heater biases. **Right** Scatter plot showing covariance between the fitted values of G and n, in terms of 95 % confidence ellipses.

3.5 TES Saturation Power

Consider Equation 3.23:

$$P_{tot} = K(T^n - T_b^n) = P_{opt} + P_{htr} + I^2 R(T, I). \tag{3.26}$$

The value of P_{tot} when $T = T_c$, is called the "saturation power" (P_{sat}) of the detector:

$$P_{sat} \equiv K(T_c^n - T_b^n) \tag{3.27}$$

$$= \frac{GT_c}{n}\left(1 - \left(\frac{T_b}{T_c}\right)^n\right). \tag{3.28}$$

If the power flowing across G is larger than this value the detector temperature is forced to be higher than T_c so that the detector goes normal and no longer works. This is an important parameter of a TES, and G must be chosen so that $P_{opt} < P_{sat}$. The ratio P_{sat}/P_{opt} is called the "safety factor".

3.6 Stability of TES Bolometers

In any physical system in which negative feedback is applied, the system response can become unstable if the feedback is applied with a phase change that approaches 180°.

This situation can occur in TES detectors if the inductance in the TES bias circuit is so large that the TES electrical time constant $\tau_{el} = L/(R_0(1+\beta_I)+R_L)$ becomes too close to the TES effective time constant τ_{eff}. For a voltage-biased TES with $R_L \ll R_0$, the criteria for stable operation is [34]

$$L > \left[\mathcal{L}_I(3+\beta_I)+(1+\beta_I)-2\sqrt{\mathcal{L}_I(2+\beta_I)(1+\beta+\mathcal{L}_I)}\right]\frac{R_0\tau}{(\mathcal{L}_I-1)^2} \tag{3.29}$$

3.7 TES Bolometer Noise

There are three sources of detector noise in TES bolometers: Johnson noise in the TES resistance, Johnson noise in the load resistor R_L, and thermal fluctuation noise across the weak thermal link G. Additionally, intrinsic fluctuations in the number of arriving photons leads to photon noise, which can be a significant source of noise for low-temperature TES bolometers. Expressions for these sources of noise are shown in Table 3.2.

The function F that enters into the thermal fluctuation noise accounts for the temperature gradient between the TES and the bath. The form of F depends on whether the mean free path of phonons crossing the thermal link is long or short compared with the length of the link. In the case of a short mean free path, F depends on n and is given by [43]

$$F(T_0,T_b) = \frac{n}{2n+1}\frac{1-(T_b/T_0)^{2n+1}}{1-(T_b/T_0)^n}. \tag{3.30}$$

In the case of a long mean free path, F is independent of n and is given by [45]

$$F(T_0,T_b) = \frac{1}{2}(1+(T_b/T_0)^5) \tag{3.31}$$

For the detectors described in this dissertation, $n \approx 3.5$, $T_0 \approx 1.2$ K, and $T_b \approx 1.1$ K. Under these conditions, both expressions for F have approximately the same value, 0.83.

For typical operating conditions of TES bolometers, thermal fluctuation noise dominates Johnson noise at low frequencies. This can be see by taking the ratio of S^2_{TES} to S^2_{TFN}. After some simplifying algebra the result is (ignoring factors of order unity):

$$\frac{S^2_{TES}}{S^2_{TFN}} \approx \frac{1}{\alpha\mathcal{L}_I}(1+(\omega\tau)^2) \tag{3.32}$$

At low frequencies the TES resistor current noise is suppressed below thermal fluctuation noise by a factor of $1/\alpha\mathcal{L}_I$. TES detectors are always biased so that $\mathcal{L}_I > 1$, and values for α in the transition for our detectors are 20–400 (see Figure 6.8 in Section 6.7). Examination

Table 3.2: Noise in TES bolometers, referred to power absorbed in bolometer. To obtain current noise passing through the bolometer, multiply each power spectral density by $|s_I(\omega)|^2$.

Noise Source	Noise Power Spectral Density
TES Resistor	$S^2_{TES} = 4k_B T_0 I_0^2 R_0 \xi(I_0) \frac{(1+(\omega\tau)^2)}{\mathcal{L}_I^2}$
Load Resistor	$S^2_L = 4k_B T_L I_0^2 R_L \frac{(1+(\omega\tau_I)^2)(\mathcal{L}_I-1)^2}{\mathcal{L}_I^2}$
Thermal Fluctuation Noise	$S^2_{TFN} = 4k_B T_0^2 G F(T_0, T_b)$

of Table 3.2 shows that current noise from the load resistor is lower than that from the TES resistor by a factor of $(\mathcal{L}_I - 1)^2(R_0/R_L)(T_0/T_L)$. Therefore, intrinsic detector noise in our TES bolometers is dominated by thermal fluctuation noise.

Another source of noise in any bolometer is Photon noise, arising due to quantum fluctuations in the number of photons arriving during a given time interval. This noise is expressed as [46]

$$S^2_{ph} = 2h\nu P_{opt}(1 + \eta\bar{n}), \tag{3.33}$$

where $\bar{n}$ is the photon occupation number, given by

$$\bar{n} = \frac{1}{e^{\frac{h\nu}{k_B T}} + 1} \tag{3.34}$$

Section 5.8 discusses predicted noise levels for our detectors. Section 6.11 discusses measurements of detector noise.

Chapter 4

System Design Overview

4.1 Cryostat Design

The cryostat for the 350 GHz Video Imager was designed with the goals of simplicity, reliability and turn-key automated operation. It was built by Precision Cryogenics[1] to designs provided by the 350 GHz Video Imager team. The first two temperature intercept stages are provided by a Cryomech PT407 Pulse Tube Cryorefrigerator[2] (PTC). The PT407 has two cooling stages. The first stage has 25 W of cooling power at 55 K while the second stage has 0.7 W at 4.2 K. Our PT407 uses a remote motor, so that the cold head attached to the cryostat has no moving parts, minimizing vibration of the cryostat. Vibration of the cryostat can lead to temperature fluctuations of the 1 K cold stage, or to microphonic pickup either directly in the detectors themselves or in the readout circuitry, leading to much higher detector noise (see Section 6.9).

Figure 4.1 shows a cutaway view of the cryostat, and Table 4.1 lists the temperatures typically reached by different parts of the cryostat during operation when the cryostat is open optically. The cryostat has two main parts: a cylinder containing both the PTC and the He4-sorption refrigerator, and a box located at the bottom of the cylinder which contains temperature intercept plates and the focal plane. There are three temperature stages: the "80 K" Cold Plate, the "6 K" Cold Plate, and the Focal Plane. The PTC 1st stage is connected to the 80 K Cold Plate by a tube of Al 1100 and a set of CDA-101 Cu braids. The combination of this long thermal path with the high heat load on the optical filters sunk to the 80 K stage explains the 36 K temperature differential between the 80 K

[1]Precision Cryogenics Systems, Inc. Indianapolis, IN. `http://www.precisioncryo.com`
[2]Cryomech, Inc. Syracuse, NY. `http://www.cryomech.com`

Table 4.1: Temperatures reached under optical load

Temperature Stage	Temperature (K)
PTC 1st Stage Cold Head	48
PTC 2st Stage Cold Head	3.5
Cryostat 80 K Cold Plate	84
Cryostat 6 K Cold Plate	6.4
Sorption Fridge Condensation Plate	3.7
Focal Plane	0.970

cold plate and the PTC 1st stage. The PTC 2nd stage is connected to the 6 K Cold Plate by a large (3.0 in diameter by 2.78 in long) cylinder of CDA-110 Cu[3], followed by a tube of alloy CDA-101 Cu, followed by a set of CDA-101 copper braids. The Cu tube is broken into two halves, and the condensation plate (see below) of the sorption fridge is clamped between these two halves. The 80 K Cold Plate stands off from the cryostat vacuum jacket by four "roll wrapped" carbon fiber tube standoffs. The 6 K Cold Plate stands off from the 80 K Cold Plate by eight supports made of G-10.

Options for reaching temperatures below the ~1.2 K transition temperature of our TES detectors include: dilution refrigerators, adiabatic magnetization refrigerators, pumped He4 baths, and He3- and/or He4-sorption refrigerators. We chose a He4-sorption fridge because the typical base temperature under no load of ~700 mK is well-matched to our application. He-sorption fridges are also inexpensive and easy to operate compared to these other solutions. A He4-sorption fridge works by using a charcoal adsorber to pump on a bath of liquid He4, reducing the He4 boiling point and thus the temperature of the bath. The He4 is contained within a sealed reservoir so that the refrigerator acts as a closed system requiring no He4 replenishment. While He4-sorption fridges are commercially available, our team choose to design and build a custom fridge based on a design that has been proven in astronomical applications [47].

Figure 4.2 shows a schematic depiction of the 350 GHz Video Imager's He4-sorption refrigerator. The entire refrigerator is filled with 2.07 mol of He4 gas, giving a pressure of 900 psi at room temperature. In normal operation the heat switch between the charcoal pumping chamber ("pump") and the He4 condensation plate is closed, keeping the charcoal close to the condensation plate temperature of 3.7 K, in order to adsorb as much gaseous He4 as possible, which in turn cools the 1 K cold head and focal plane.

[3]This cryostat was originally designed to work with a different cryocooler. The PTC currently installed has a shorter distance between the 1st and 2nd stages; the Cu cylinder takes up this extra space.

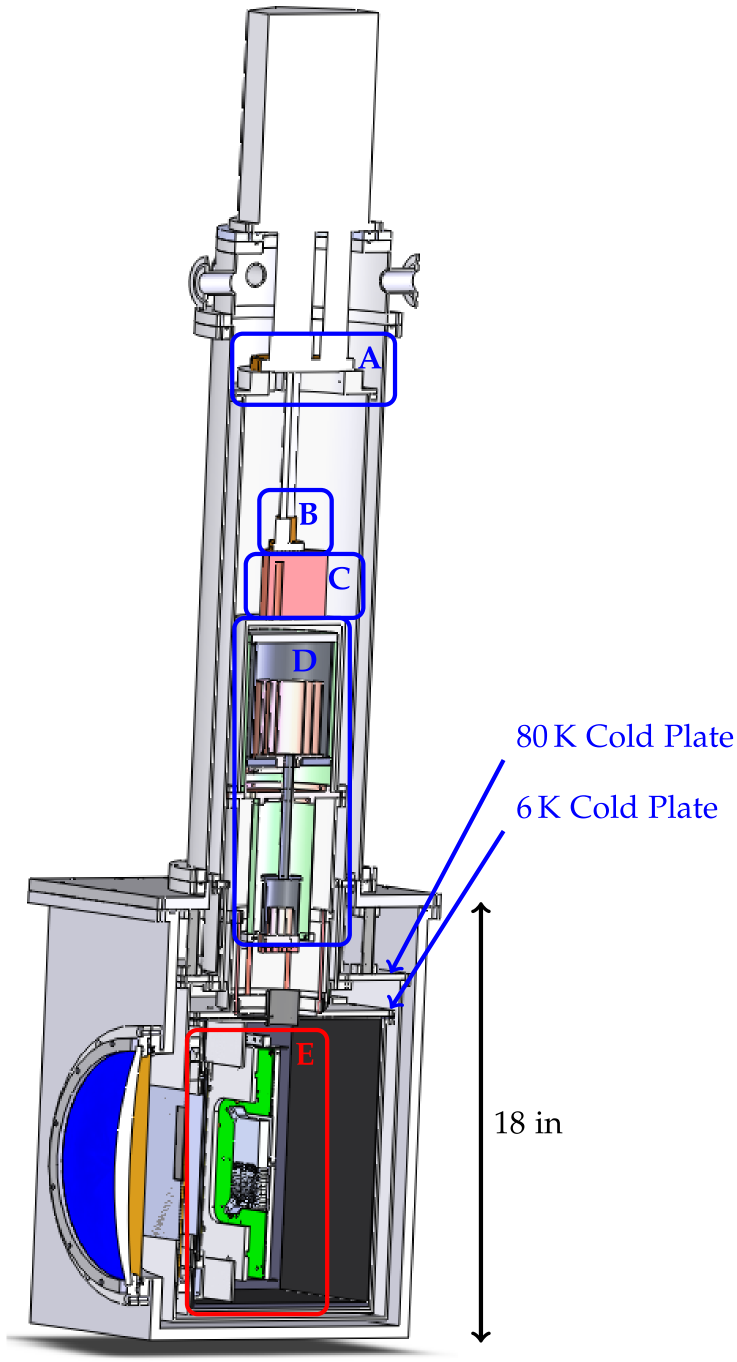

Figure 4.1: Cutaway view of the 350 GHz Video Imager. **A:** PT407 1st stage cold head **B:** PT407 2nd stage cold head **C:** Cu cylinder connecting the PT407 2nd stage cold head to a Cu tube, which then connects to the He4-sorption refrigerator condensation plate. **D:** He4-sorption refrigerator **E:** Focal Plane. The Cu ropes that connect the focal plane to the 1 K cold plate are not visible in this view.

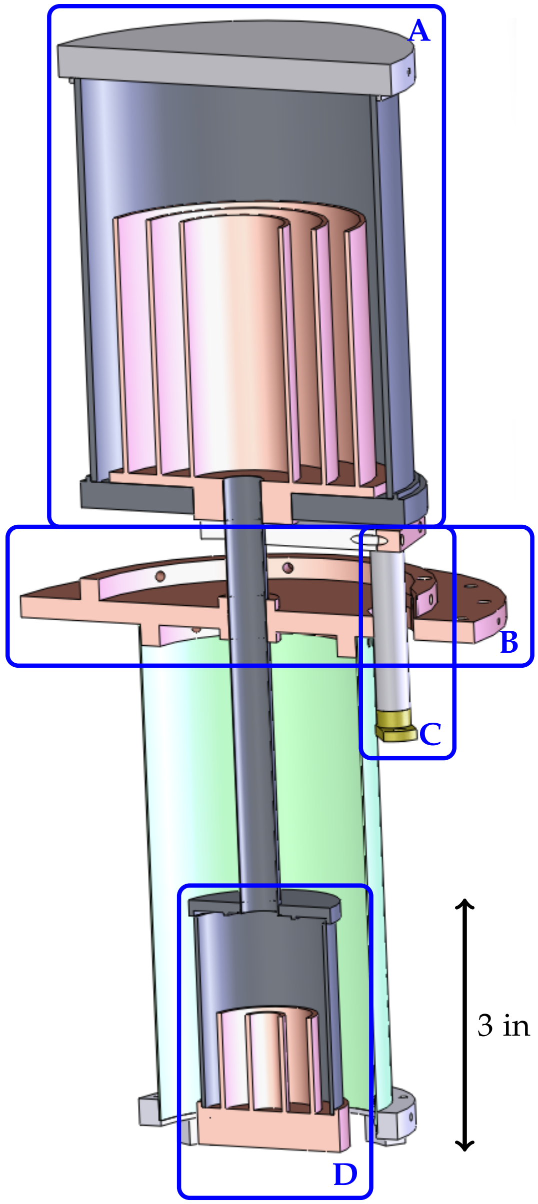

Figure 4.2: Cutaway view of the He4-sorption refrigerator. **A:** Charcoal pumping chamber ("pump"). The charcoal is attached to the concentric copper cylinders, used to maximize the surface area covered by the charcoal. **B:** Condensation plate. This copper plate is kept below the boiling point of He4 in order to provide a point in the refrigerator for He4 to condense and drip into the condensation pot. **C:** He4 gas gap heat switch. This heat switch is used to cool the charcoal in order to pump on the He4 bath in the condensation pot. **D:** He4 condensation pot ("pot"). The condensed He4 accumulates here. The concentric cylinders provide additional surface area for thermal contact to the liquid He4. Not shown is a sapphire 1 mm constriction in the stainless steel tube connecting the pump and pot, intended to restrict the flow of super-fluid He4 away from the pot (Swiss Jewel Company, part A34.00).

Cycling the refrigerator requires four steps. First the heat switch is opened. The He4-sorption refrigerator uses a He4 gas-gap heat switch manufactured by Chase Cryogenics[4], which requires 5 minutes of waiting time in order for the switch to fully open. Second, the pump is heated by applying 5 W via a 500 Ω power resistor. This power is applied until the temperature of the pump reaches 40 K, which is high enough to drive nearly all of the adsorbed He4 off of the charcoal. Third, the power to the pump is turned off. Once the temperature of the condensation plate falls below the boiling point of He4, He4 will begin to condense on its walls, dripping into the He4 condensation pot ("pot"). Fourth, once the temperature of the pot has fallen to 4.0 K, the heat switch is turned back on. This cools the pump, allowing He4 to again adsorb onto the charcoal, which has the effect of pumping strongly on the pot, and cooling the He4 contained there to the base temperature of 970 mK under optical load. This process is easy to automate, and a LabVIEW program cycles the fridge automatically every night while the system is operating.

A Cryo-con Model 44[5] temperature controller is used to control the temperature of the stage, using a 6.4 kΩ resistor attached to the focal plane. As discussed in Section 6.8, the temperature variations over several-minute timescales are a few parts in 10^4 when the Cryo-con unit is used to hold the temperature steady.

Under optical load, a full cycle of the He4-sorption refrigerator takes approximately 4 hours, reaching a base temperature of 970 mK. When no additional load is applied the hold time is 9 hours. When the temperature of the stage is held at the typical operating temperature of 1100 mK the hold time is only 3:45 hours. This will need to be lengthened in a future design iteration for practical device operation.

Table 4.2 lists contributions to the heat load on the He4-sorption refrigerator. It excludes parasitic load inherent to the sorption refrigerator itself; we have estimated this parasitic load as ~ 0.5 mW.

[4]Chase Research Cryogenics, Ltd. Sheffield, UK
[5]Cryogenic Control Systems, Inc., Rancho Santa Fe, CA

Table 4.2: Predicted thermal load on 1 K stage. The "Ti-6Al-4V spiders" provide the structural link between the 1 K cold stage and the 6 K cold plate; see Section 5.6 and Figure 5.6. These calculations assume that the readout wiring and Ti-6Al-4V spiders are running from 6.4 K to 1.0 K. All wires are AWG36 Phosphor Bronze with thermal conductivity taken from the Lake Shore Cryogenics reference tables [48]. The load from the readout wiring is lower when running only 251 detectors because this only requires two of the five connectors carrying these wires to be connected to the focal plane. Assumed thermal conductivity k of the Ti-6Al-4V alloy used for the spiders is $k(T) = (150\,\mu\mathrm{W\,cm^{-1}\,K^{-1}})T$ (William Duncan, personal communication). "LM-1 readout wires" refers to the wires running from room temperature used to readout the position of the secondary mirror; see Section 7.2. The heat load from these wires is high because they are not currently intercepted anywhere between room temperature and the 1 K stage. Intercepting them at the 6 K Cold Plate would reduce their load to 1.1 µW. "Other optical power" refers to in-band power that reaches the 1 K stage but is not absorbed by the detectors. The number quoted assumes that all of this power is absorbed on the 1 K stage; this results in an overestimate because it is likely that most of this power is reflected by the feedhorn array, rather than being absorbed. "Out-of-band optical power" is assumed to be zero because the only warm object directly illuminating the 1K stage — the W1275 bandpass filter — is only 16 K, and is not emissive at the wavelengths at which it would be radiating (see Section 4.3 and [49]).

	Predicted Thermal Load	
Heat Load Source	1004 Detectors (µW)	251 Detectors (µW)
Readout wiring	52	130
Series array SQUID modules	0.2	0.6
SQUID multiplexing chips	0.4	1.6
Shunt resistors	5	18
Ti-6Al-4V spiders	130	130
Detectors (Optical + Electrical)	0.25	1
Other in-band optical power	5.6	5.6
Out-of-band optical power	0	0
LM-1 readout wires	507	507
Total	700	794

4.2 Optical Design

The optical system is a Cassegrain design, chosen because circular symmetry makes these systems easy to design for on-axis performance at finite distances. Figure 4.3 shows a schematic of the optical system including the focal plane. Light enters the system from the left in this schematic, and reflects off the primary mirror onto the secondary mirror.

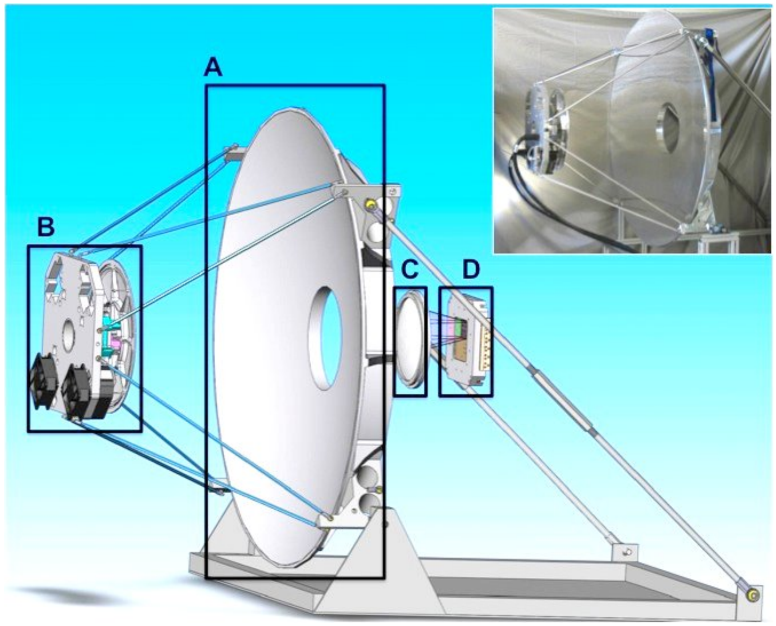

Figure 4.3: Schematic showing elements of optical system. **A:** 1.3 m elliptical primary mirror. **B:** Platform on which secondary mirror is mounted. **C:** High-density-polyethylene (HDPE) cryostat window. This window acts as a lens to make the system telecentric. **D:** Detector focal plane package. The lid covering the focal plane holds an optical filter which defines the band of observation; see Section 4.3.

From the secondary mirror the light passes through a hole in the center of the primary mirror and through a window into the cryostat. The cryostat window is a high-density polyethylene (HDPE) lens that makes the system telecentric; this means that the focal surface of the system inside the cryostat is planar, not curved, and simplifies the design of the detector focal plane. Smooth-walled conical feedhorns couple the incident light onto the detectors.

The secondary mirror's mount allows it to pivot and change where the system is pointing. Two LM-1 linear motors[6] mounted 90° apart can move the mirror in arbitrary scanning patterns. Figure 4.4 shows the secondary mirror mounted on its supporting platform, as well as the LM-1 motors.

Scanning the secondary mirror is necessary to generate Nyquist-sampled images. A point source in the far-field will generate an Airy intensity pattern on the focal plane with FWHM $\sim 1.03F\lambda$. Here F is the F-number of the optical system, defined as the ratio of the focal length to the aperture size. As shown in Table 4.4, $F = 2.0$ for the 350 GHz Video

[6]Bose ElectroForce, Framingham MA

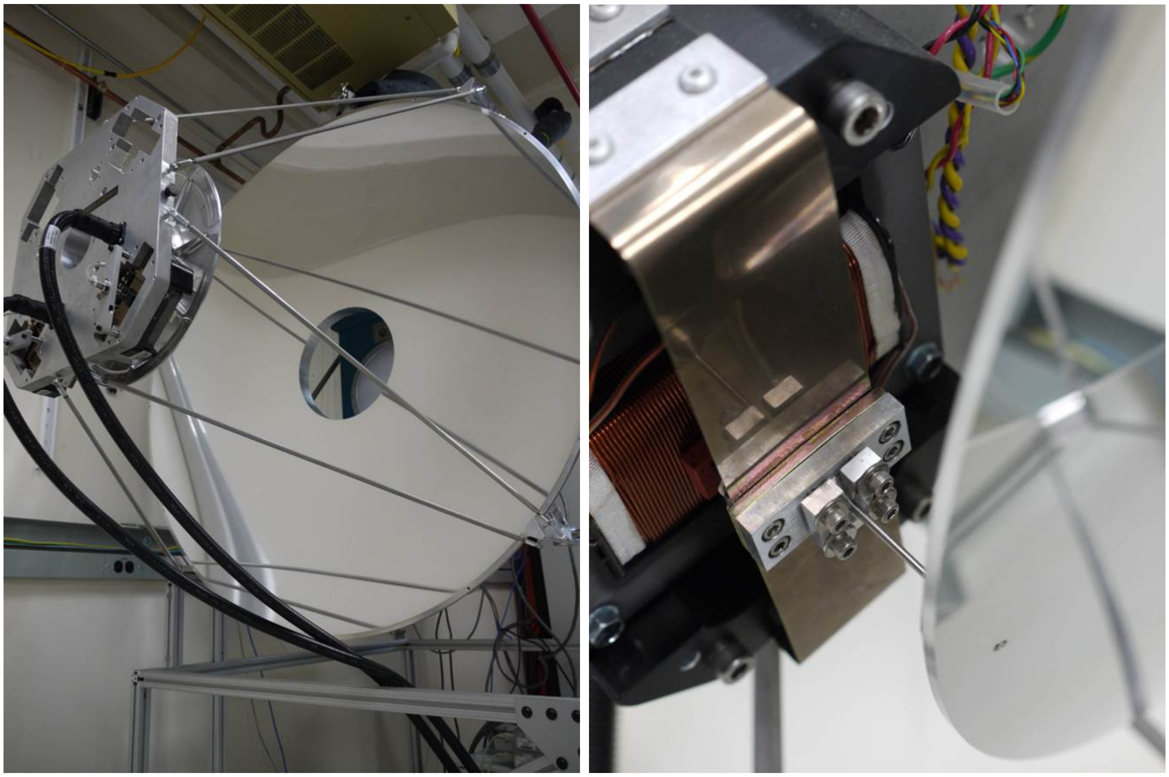

Figure 4.4: Photographs of the optical system. **Left** The primary and secondary mirrors. The secondary is mounted on the Al platform in the upper left of the photograph. The black cables leading away from the platform go to the control system for the LM-1 linear motors. **Right** Close-up view of one of the LM-1 linear motors. The secondary mirror itself is located on the right of the photograph, while the right side of the photograph shows the LM-1. A titanium strut connects the LM-1 to the mirror.

Imager, so that the spot size on the focal plane is ~ 1.7 mm. By the Nyquist theorem, detectors would need to be spaced every $1.7\,\text{mm}/2 \approx 0.9$ mm on the focal plane to record all details of the optical image. But the detector spacing is 2.71 mm (Section 4.4), so that the focal plane is under-sampled by a factor of $(2.71/0.90)^2 \approx 9$. This problem can be overcome by scanning the system so that the "in-between" locations in the images are sampled.

Table 4.3 lists important properties and parameters for the optical elements of the system. Figure 4.6 shows spot diagrams for the optical system generated by a ZEMAX model for the system focused at 16 m. They demonstrate that the system's optical performance is diffraction-limited over the entire focal plane for mirror rotations in both directions of up to 1°, the maximum angle the mirror is displaced in operation.

Figure 4.5 contains a system ray-trace diagram for the system focused at 16 m. It shows

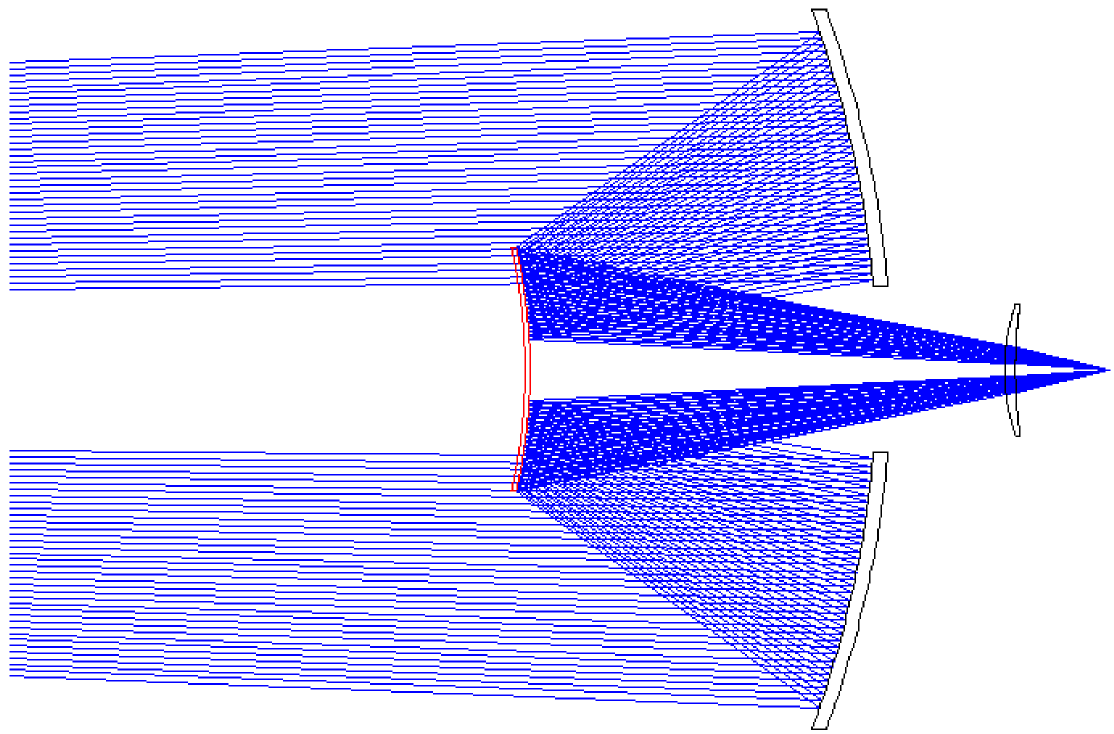

Figure 4.5: Ray-trace diagram produced by ZEMAX for the system focused at 16 m. The outermost ray is determined not by the primary mirror but by the secondary mirror, so that the outer edge of the primary mirror is unused, which reduces the resolution of the system. The innermost ray is also determined by the secondary mirror. Note that in this diagram several inner rays that are actually blocked by the secondary are displayed.

that the outermost ray is determined not by the primary mirror but by the secondary mirror; this means that the outer edge of the primary mirror is unused, slightly reducing the resolution of the system. The innermost ray is also determined by the secondary mirror. Table 4.4 lists important optical properties of the system obtained from the ZEMAX model.

The HDPE window does not have an anti-reflection coating. The index of refraction of HDPE is $n = 1.525$ with an absorption coefficient at 350 GHz of $\alpha = 0.044\,\mathrm{cm}^{-1}$ [50]. Using the standard formulas for Fabry-Perot fringing when light passes through a lossy 2 cm thick dielectric slab [51, Chapter 5], the band-averaged transmission through the window is calculated to be 84 %, with 7.6 % reflection due to the change in dielectric constant, and 9.1 % due to absorptive loss in the dielectric.

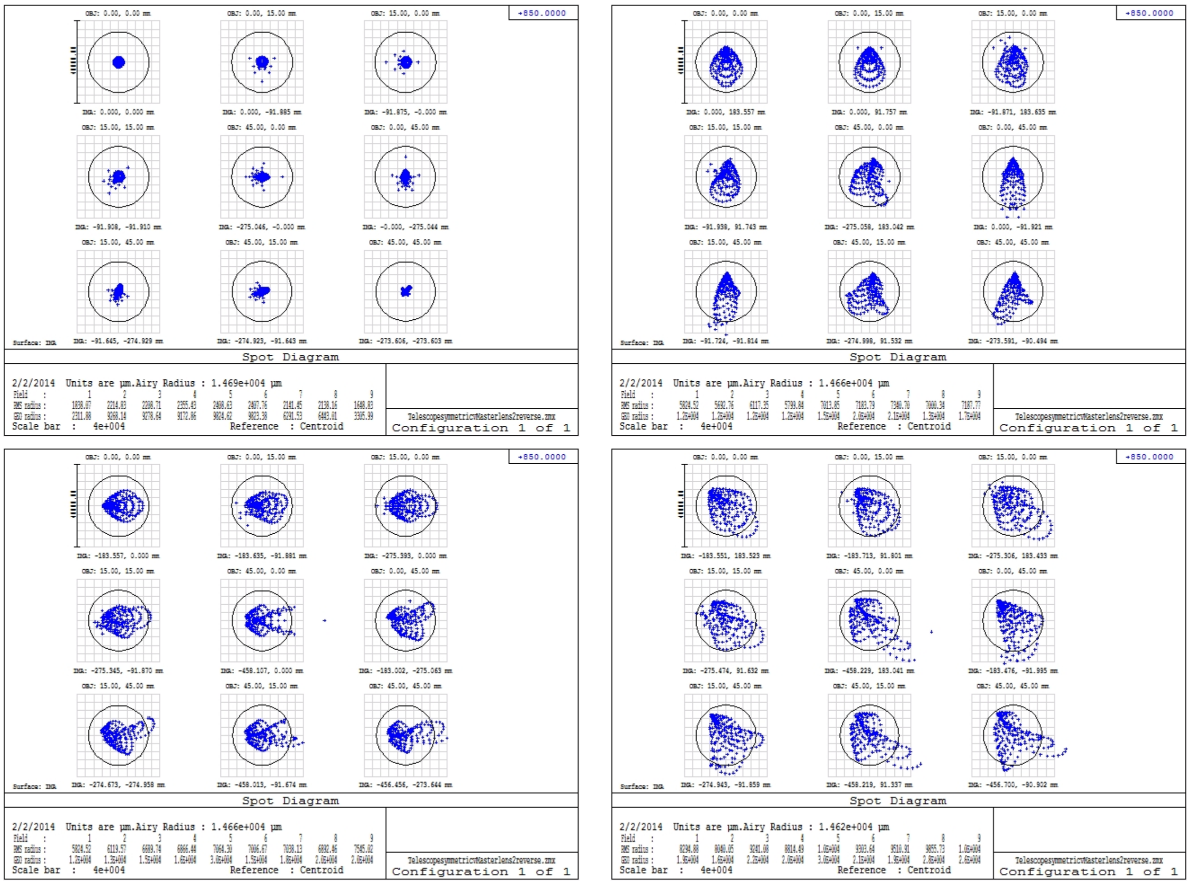

Figure 4.6: ZEMAX spot diagrams for the 350 GHz Video Imager's optical system when focused to 16 m. This represents the distribution of points on the focal plane to which rays from a point on the object trace to. Each plot shows spot diagrams for nine points in the focal plane covering the area over which detectors in the sub-array are located. The four plots (moving left to right and top to bottom) are for the secondary mirror with no tilt, 1° tilt about one axis, 1° title about other axis, and 1° tilt about both axes. The black circle gives ZEMAX's estimate of the size of the Airy disk for the optical system, which is defined as the location of the first null in the system's diffraction pattern. In all cases, nearly all rays map to within the Airy disk, indicating that the performance of the optical system is diffraction-limited.

Table 4.3: Optical system specifications. Some of the dimensions and parameters are listed to precisions higher than achievable manufacturing tolerances; these dimensions and parameters were chosen by optimization routines in ZEMAX and are kept to full precision here for archival purposes. The shape of the elliptical and hyperbolic mirrors follows the equation $z(r) = cr^2/(1+\sqrt{1-(1+k)c^2r^2})$, where c is the inverse of the mirror radius, k is the conic parameter, and r is the radial distance from the center of the mirrors. The lens surfaces follow the equation given in the table.

Optical Element	Type	Outer Diameter	Details
Primary Mirror	Elliptical Mirror	1.3 m	Vertex 16 m from far-field focal plane ZEMAX radius $c^{-1} = 1801.453{,}127$ mm ZEMAX conic $k = -0.878{,}728$ Semi-major axis: 14.85 m Semi-minor axis: 5.17 m Distances from mirror vertex to foci: 0.93 m and 28.8 m
Secondary Mirror	Hyperbolic Mirror	0.44 m	Vertex 626.82 mm from primary mirror vertex ZEMAX radius $c^{-1} = 937.371{,}87$ mm ZEMAX conic $k = -4.466{,}172$ Eccentricity 2.11
Cryostat Window	HDPE Aspheric Lens	0.24 m	Outer vertex location depends on focus distance; see Table 4.4 2 cm thick at center Index of refraction $n = 1.525$ (7.6 % band-averaged reflection) $\tan\delta = 4.0 \times 10^{-4}$ (9.1 % band-averaged absorption) Outer Surface: $z(k) = cr^2/(1+\sqrt{1-c^2r^2}) + \sum_{k=1}^{k=8}\beta_k r^k$, where $c^{-1} = -1052.933$ mm, $\beta_1 = -4724.966$ mm, $\beta_2 = (0\,\text{mm})^{-2}$, $\beta_3 = (88.649\,\text{mm})^{-3}$, $\beta_4 = -(67.854\,\text{mm})^{-4}$, $\beta_5 = (90.995\,\text{mm})^{-5}$, $\beta_6 = (89.966\,\text{mm})^{-6}$, $\beta_7 = -(97.618\,\text{mm})^{-7}$, $\beta_8 = -(191.31\,\text{mm})^{-8}$ Inner Surface: $z(k) = cr^2/(1+\sqrt{1-c^2r^2}) + \sum_{k=1}^{k=8}\beta_k r^k$, where $c^{-1} = -699.782$ mm, $\beta_1 = -62.359$ mm, $\beta_2 = (0\,\text{mm})^{-2}$, $\beta_3 = -(45.520\,\text{mm})^{-3}$, $\beta_4 = (59.477\,\text{mm})^{-4}$, $\beta_5 = -(74.141\,\text{mm})^{-5}$, $\beta_6 = (86.306\,\text{mm})^{-6}$, $\beta_7 = -(107.763\,\text{mm})^{-7}$, $\beta_8 = -(124.984\,\text{mm})^{-8}$
Detector Focal Plane		N/A	171.541 mm from vertex of inner surface of cryostat window

Table 4.4: Parameters of the optical system extracted from ZEMAX simulations. "Focus Distance" is the distance from the vertex of the primary mirror to the far-field plane at which the system is focused. "Lens Distance" is the distance from the outer vertex of the lens to the vertex of the primary. "Plate Scale" gives the ratio of distances on the far-field focal plane to the detector focal plane. "Mirror Rotation" gives the distance that the on-axis point moves when the mirror is rotated by 1°. "F-Number" gives the ratio of the focal distance to the aperture size as viewed from the detector focal plane; this the "Working F/#" from ZEMAX. "Marginal Rays" gives the angle away from the optical axis of the inner/outer marginal rays; these are the most extreme rays emerging from the detector focal plane that reach the far-field focal plane. "Primary Range" gives the innermost and outermost radius of the primary that is actually used, e.g., when focused at 16 m, the outer 4 cm of the primary is not used. See Figure 4.5.

Focus Distance (m)	Lens Distance (mm)	Plate Scale (cm/cm)	Mirror Rotation (cm/°)	F-Number	Marginal Rays (°)	Primary Range (mm)
16	230.475	6.111	18.354	2.01	5.14° / 13.61°	229.1 / 610.4
17	197.18	6.638	19.330	1.96	5.24° / 14.03°	228.6 / 614.5
28	8.0	12.589	30.037	1.71	5.99° / 16.91°	225.1 / 642.2

4.3 Optical Filtering

A series of optical filters located inside the cryostat serves to reduce the thermal load on the 1 K focal plane and to define the observing band. These filters are shown schematically in Figure 4.7. These filters include thin thermal blocking filters located at 300 K, 80 K, and 6 K; multi-layer lowpass filters at 80 K and 6 K; and a band-defining filter located at 1 K. The transmission properties of these filter listed in this section are from measurements made at Cardiff University, where the filters were made.

The transmission of the bandpass filter is plotted in blue in Figure 4.8. The integrated bandwidth of the bandpass filter is 31.1 GHz, with a full-width-half-maximum (FWHM) band of 35.0 GHz. There is some ambiguity in defining the bandwidth and efficiency of a bandpass filter that does not have a top-hat shape. In this dissertation I have chosen to described the filter as having a bandwidth of 35.0 GHz with efficiency $31.1/35.0 = 88.5\,\%$. I chose this definition because the concept of a “full-width-half-maximum” bandwidth is familiar and easy to physically interpret, and because the non-unity efficiency emphasizes the fact that the filter does not have perfect transmission at any frequency.

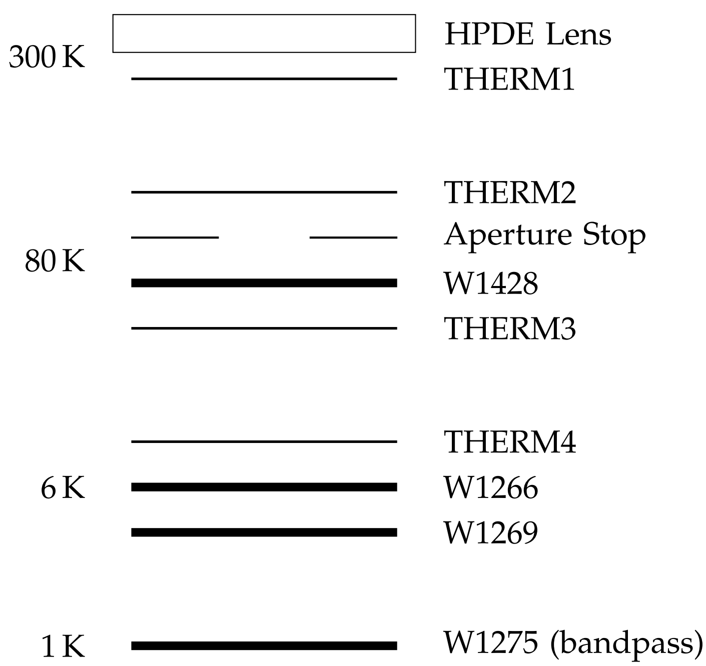

Figure 4.7: Schematic showing locations of all filters in the 350 GHz Video Imager. Everything shown here is internal to the cryostat. On the left the nominal temperatures for each stage are listed, and on the right the names and cutoff wavelengths are listed.

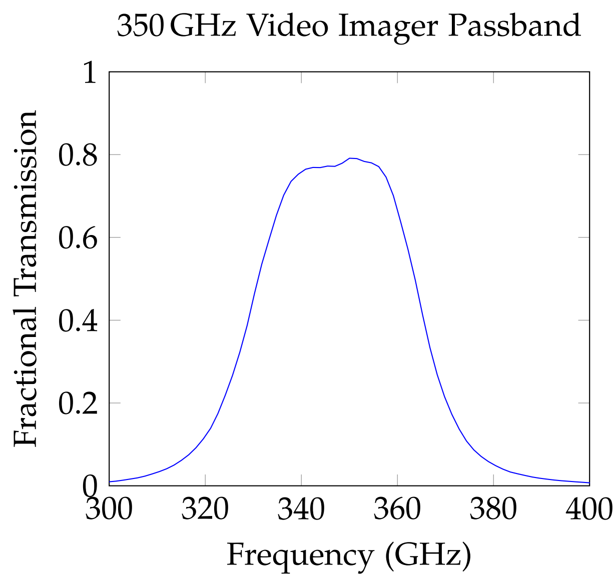

Figure 4.8: Plot showing transmission of the bandpass filter.

The thermal blocking filters are sheets of 3.3 μm polypropylene with capacitive metal grids printed on each side. Because they are so thin, these filters have little emission even at the infrared wavelengths at which polypropylene is highly absorptive [49]. The cutoff wavelengths of these filters are listed in Table 4.5.

The 350 GHz Video Imager also contains thicker multi-layer filters that act as lowpass filters at wavelengths closer to the observing band. These filters are also made of metal meshes and polypropylene, but many meshes and polypropylene layers are sandwiched together to form filters that are ~1 mm thick. These filters have excellent transmission in-band as well as good out-of-band rejection [52], but the thick polypropylene substrates mean that they are also highly absorptive — and thus also emissive – in the near-infrared. Additionally, polypropylene has poor thermal conductivity. This means that unless they are heat-sunk very well, the centers of the filters will be much warmer than the stage at which they are anchored, and so they will re-radiate infrared power into the cryostat. The filters in the 350 GHz Video Imager are clamped in place using spiral springs, using a design that is similar to that used by the Atacama Cosmology Telescope receiver [53].

Table 4.5 lists all filters in the system and gives temperatures for the centers of some of the filters, taken while the cryostat was open optically. The outermost multi-layer filter is very warm (190 K), and this is a significant source of loading on the 6 K stage, which also warms the 6 K multi-layer filters, leading to a level of loading on the 1 K stage that prevents it from being cooled below 1.2 K unless the aperture is stopped down to reduce

Table 4.5: Details of filters installed in the 350 GHz Video Imager. The filters are listed in order from the outside of the cryostat to the inside. "Stage" refers to the cryostat temperature stage at which the filter is located. "Cutoff" refers to the point at which the filter transmission falls to ~ -10 dB. "Transmission" gives the band-averaged transmission of the filter. "Temperature" gives the temperature at the center of a filter as measured by embedding a diode in a blob of Apiezon-N thermal grease placed on top of a layer of Kapton tape (which prevents applying grease to the filter itself). The temperature of W1428 was measured without the aperture stop in place and while it was located after THERM3 rather than before. The current placement of this filter between two thermal blocking filters prevents measuring its temperature in the current configuration. The temperatures for W1269 and W1275 were measured both with and without a $(2.25\,\mathrm{in})^2$ aperture stop, which covers 40 % less area than the stop used in all other measurements in this dissertation. Temperature measurements are not available for the other filters.

Stage	Filter Label	Cutoff (μm)	Cutoff (THz)	Transmission	Temperature (K)
300 K	THERM1 1.9 μm	1.9	158	1.00	
80 K	THERM2 4 μm	4	75	1.00	
	W1428 18 cm^{-1}	556	0.54	0.96	193
	THERM3 6 μm	6	50	1.00	
6 K	THERM4			1.00	
	W1266 14 cm^{-1}	714	0.42	0.94	
	W1269 32 cm^{-1}	313	0.96	0.98	14–37
1 K	W1275	N/A	N/A	0.885	3.7–7.8

IR loading. This has been accomplished by installing an aperture between the thermal blocking and multi-layer filters on the 80 K stage. With a 2.25 in × 2.25 in aperture, the bandpass filter center reaches a temperature of 3.7 K. The aperture stop used for all optical measurements in this dissertation was 2.875 in × 2.875 in. Table 4.5 also lists the in-band transmission of each filter. The total transmission of the filter stack excluding the bandpass filter is 88.4 %.

4.4 Feedhorn Design

Millimeter and submillimeter astronomical instruments using TES detectors use many different strategies for coupling light onto detectors, including filled arrays of absorbers [11, 53], antennas with lenslets [54], phased antenna arrays [55], corrugated feedhorns [56, 57], and smooth-walled conical feedhorns [58, 59]. The 350 GHz Video Imager uses smooth-walled conical feedhorns because they are easy to design and easy to machine. Smooth-walled feedhorns do not have the low cross-polarization properties of corrugated feedhorns [60], but this is not a concern here because the 350 GHz Video Imager's detectors are polarization-insensitive.

Although the 350 GHz Video Imager is always receiving radiation, never transmitting, this dissertation often refers to the transmitting beam pattern, because in some cases this is easier to conceptualize. Beams in transmission and reception are the same, a consequences of the reciprocity relationships obeyed by the Maxwell equations (see, e.g. [61]).

Figure 4.9 depicts a smooth-walled conical feedhorn and its interaction with the optical system. Although the optical system has a secondary mirror as well, for the purposes of feedhorn design an equivalent optical system with only one mirror can be used, with the same focal length [62].

If a feedhorn is observing a temperature distribution $T_{target}(\theta, \phi)$, and is pointed in a direction (θ_0, ϕ_0), then the temperature observed by the feedhorn will be

$$T_{eff}(\theta_0, \phi_0) = \int d\Omega \, T_{target}(\theta - \theta_0, \phi - \phi_0) P(\theta, \phi). \tag{4.1}$$

The function P is called the "beam" or "beam pattern" of the feedhorn, and describes the angular pattern of radiation to which the feedhorn is sensitive. When using this expression one must keep in mind that the fraction of the beam that spills off the primary mirror (e.g. the unshaded region in Figure 4.9) will see not the temperature distribution of the target, but a temperature distribution determined by what is beyond the primary mirror[7]. The fraction of the beam that strikes the primary mirror and proceeds to the target is called the spillover efficiency η_s.

The important design parameters for a smooth-walled conical feedhorn are the opening diameter D and the opening half-angle α_0. The feedhorn opening diameter D is chosen to minimize the total NETD of the system. The total NETD was given in Section 1.2 as

$$NETD = \frac{NEP_{tot}}{2k_B \Delta\nu \eta_{tot} \sqrt{2\tau}}. \tag{4.2}$$

To make the factors depending on the size of the feedhorns more clear we can break the optical efficiency η_{tot} into a product of two factors, η_s and $\eta_{other} = \eta_{tot}/\eta_s$. We then note that the integration time per pixel τ is proportional to the number of detectors N. This

[7]Because of the presence of the secondary mirror, some of this temperature distribution will be in front of the system, and some will be behind.

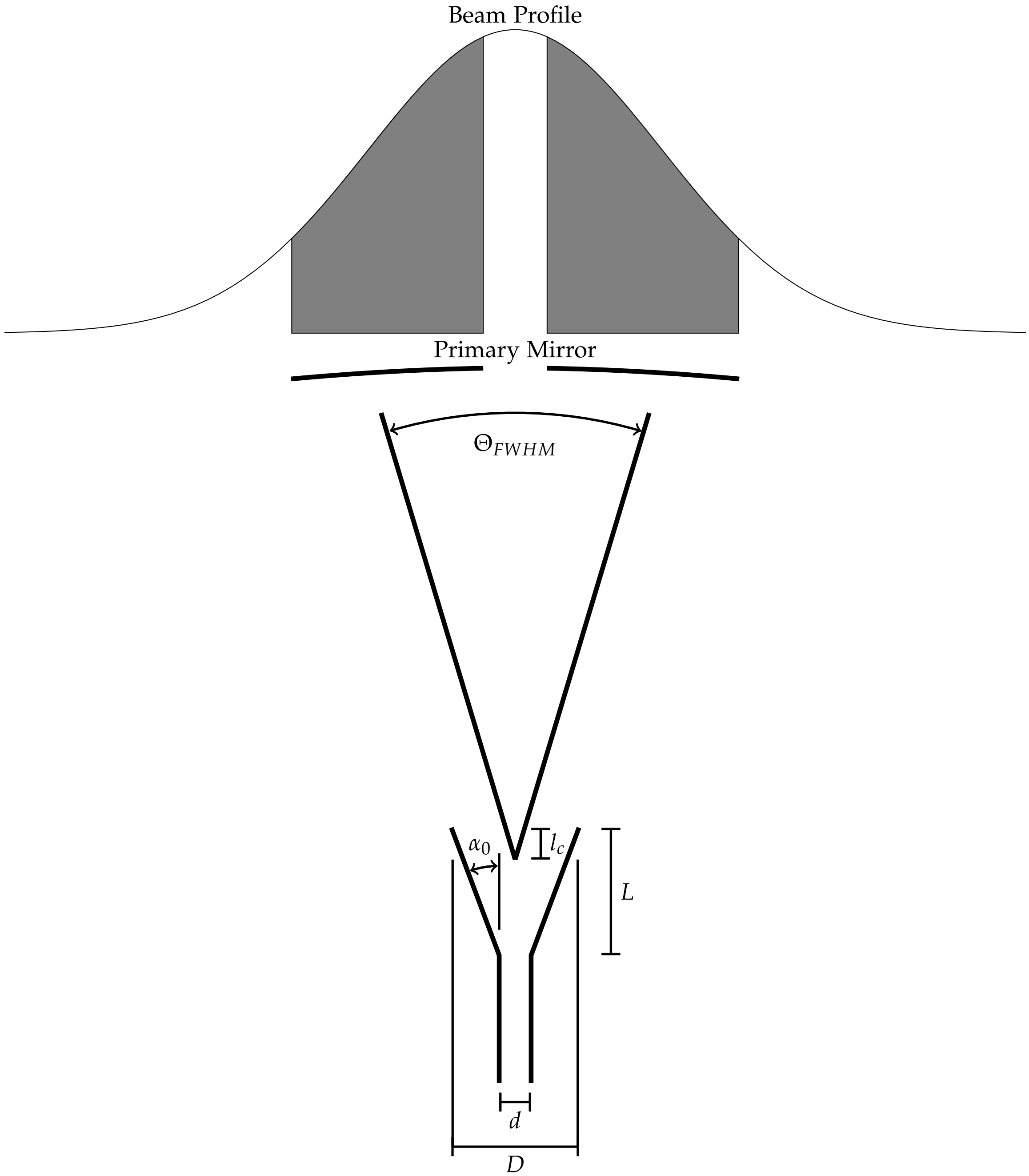

Figure 4.9: Schematic showing important parameters of a feedhorn and its beam. The beam appears to emerge from the phase center, a distance l_c behind the mouth of the feedhorn in this diagram. The main lobe of the beam is approximated well by a Gaussian, here characterized by a full-width-half-maximum (FWHM) beam width. The shaded fraction of the Gaussian represents the part of the beam that falls onto the primary mirror and reaches the target. As discussed in the text, for the purposes of feedhorn design the secondary mirror can be ignored and the system treated as a system of feedhorns illuminating only a primary mirror with a hole in its center.

leads to

$$NETD \propto \frac{NEP_{tot}}{\sqrt{N}\eta_s}. \tag{4.3}$$

The critical relationship is that as a feedhorn's opening diameter increases, the width of the beam becomes smaller. Small beam angles increase η_s, which improves NETD. However, the diffraction-limited area on the focal plane that can be covered by feedhorns is fixed, so that increases in the horn opening diameter reduce the number of detectors N, which worsens NETD. Choosing an optimal feedhorn size requires trading these two effects off against each other to minimize NETD.

There are four additional factors to consider. First, NEP_{tot} is not independent of η_s. In a system that is photon-noise-limited, NEP_{tot} may worsen, stay the same, or improve, depending on the temperature seen by the spilled over portion of the beam. Indoors, all of the beam will see roughly the same temperature as the target, so that total photon noise will stay the same. Outdoors the situation is more complicated because the temperature seen by the spilled over beam will depend on the local scenery and weather conditions. For simplicity, the analysis of optimum feedhorn size in this chapter makes the assumption that the noise seen by a detector is independent of the beam size.

Second, for a Cassegrain optical system, η_s is not a monotonic function of D, because the secondary mirror obstructs the central part of the beam, preventing it from reaching the target. This means that narrow beams can have poor η_s because a large fraction of the main lobe of the beam will be blocked.

Third, the dependence of the number of detectors N on the feedhorn diameter D is not a smooth function, because it is not possible to have, e.g., 1/3 of a feedhorn. As explained in Section 5.5, the 350 GHz Video Imager's detectors are laid out on a square grid. So it is more helpful to think of the feedhorn diameter as taking on a discrete set of values that depends on the number of feedhorns per each side of the grid.

Finally, the choice of readout system and wiring places a firm upper limit of 1024 on the number of detectors in the system.

A MATLAB program was used to find the optimum feedhorn size. The program uses an analytic expression for the beam pattern developed in [63, 64]. The far-field electric field pattern takes the form

$$\vec{E}(\theta,\phi) = E_\theta(\theta)\sin\phi\hat{\theta} + E_\phi(\theta)\cos\phi\hat{\phi}. \tag{4.4}$$

Here E_θ and E_ϕ are functions depending the horn diameter D and opening half-angle α_0, and involving definite integrals of Bessel functions, given in [63, 64]. This expression is for the waveguide mode polarized along the $\pi/2$ direction. The 350 GHz Video Imager's detectors are unpolarized, so they detect both waveguide polarizations equally; see Section 4.5 for confirmation of this via simulations. The total power beam map is thus given by the incoherent sum

$$P(\theta,\phi) = |\vec{E}(\theta,\phi)|^2 + |\vec{E}(\theta,\phi+\pi/2)|^2, \tag{4.5}$$

which simplifies to

$$P(\theta) = |E_\theta(\theta)|^2 + |E_\phi(\theta)|^2, \tag{4.6}$$

which is independent of ϕ, as expected for an unpolarized detector.

To calculate the spillover efficiency of an individual feedhorn, the MATLAB program integrates P over the angles θ that illuminate the primary mirror and reach the target: 5.2° – 14.0° at 17 m[8]. Figure 4.10 shows a contour plot of spillover efficiency for an individual conical feedhorn as a function of D and α_0. The black dot shows the parameters for the feedhorns chosen for the 350 GHz Video Imager. This plot shows that η_s depends much more strongly on D than on α_0. $\alpha_0 = 9.4°$ was chosen as a value that is easy to machine, keeps the thermal mass of the feedhorn array low (small values of α_0 lead to long feedhorns and higher thermal mass), and is not too far from the maximum achievable η_s for any fixed feedhorn diameter D.

To find the number of horns per array size that minimizes NETD the program assumes that the feedhorns must cover a square 43.9 mm per side. It allows for 1 mil spacing between the edges of the feedhorns, and also accounts for a thermal contraction factor of 4.14 parts per thousand [65, Appendix A6.4]. Four horns from each sub-array are assumed to be missing in order to accommodate other features on the detector wafer. The resulting NETD estimates — normalized to the NETD for the actual feedhorns chosen — is shown in Figure 4.11. The optimal number of feedhorns per array side is 19, for a total (across all four sub-arrays) of 1428 feedhorns of diameter 2.25 mm cold. Because of readout limitations, the actual number of detectors per side is 16, for 1004 feedhorns with diameter 2.68 mm (108 mils at room temperature)[9]. The loss in NETD from this sub-optimal choice is only 1.7 %.

Figure 4.12 contains plots of both the beam pattern for the conical feedhorn and the far-field beam pattern of the entire optical system (also called the "point spread function"). The feedhorn beam pattern follows the model described above, and is well-approximated

[8] see Section 4.2

[9] Five locations in the 16×16 grid are missing detectors; see Section 5.5.

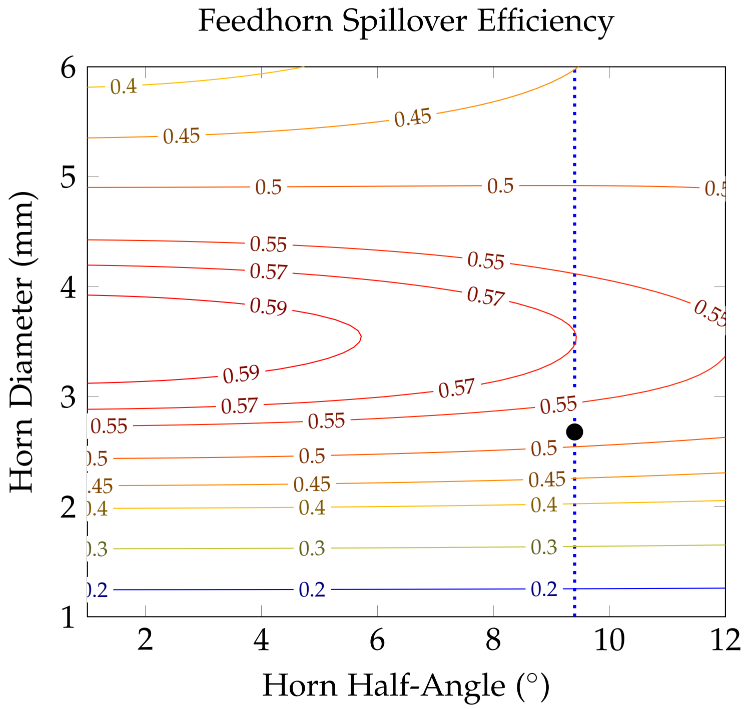

Figure 4.10: Plot showing feedhorn spillover efficiency η_s as a function of horn diameter D and horn flare half-angle α_0. The blue dotted line is for $\alpha_0 = 9.4°$, the value assumed during optimization. The black dot shows the feedhorn parameters used in the 350 GHz Video Imager: $D = 2.68$ mm (cold) and $\alpha_0 = 9.4°$

over the primary mirror by a Gaussian with FWHM of 21.2°, or 929 mm in terms of radial distance on the primary. To calculate a theoretical far-field beam, we can make the simplifying assumption that the primary mirror is illuminated by an electric field with a circularly symmetric Gaussian profile, with a FWHM of $\sqrt{2} \times 929\,\text{mm} = 1313\,\text{mm}$, where the $\sqrt{2}$ converts from power to electric field. This assumption ignores the ellipticity of the feedhorn beam for a single polarization, but since the detectors are sensitive to both polarizations equally, the approximation should be accurate.

The far-field angular power pattern is then given by [17]

$$P(\theta) = \left[\int_{\rho_{in}}^{\rho_{out}} e^{-\frac{1}{2}\frac{\rho^2}{(560\,\text{mm})^2}} J_0\left(\frac{2\pi}{\lambda}\rho \sin(\theta)\right)\rho d\rho \right]^2, \tag{4.7}$$

where J_0 is a Bessel function of the first kind, λ is the central wavelength of the optical band, and ρ_{in} and ρ_{out} are taken from Table 4.4. This formula accounts for the edge taper of the feedhorn pattern, the obstruction caused by the secondary mirror, and the

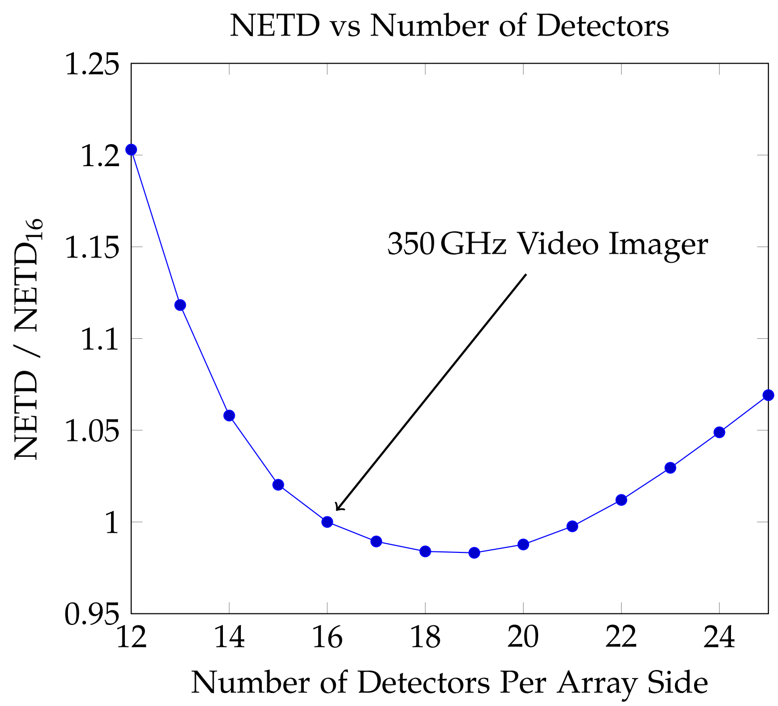

Figure 4.11: Plot showing how NETD depends on the number of feedhorns in each sub-array. As discussed in the text, due to the square array the important parameter determining the total number of feedhorns is the number per side of the grid. The NETD is plotted relative to the NETD for an array with 16 feedhorns per side, which is the value chosen for this system. NETD is minimized with 19 feedhorns per side, giving a total of 1428 feedhorns of diameter 2.25 mm (cold), but the 350 GHz Video Imager uses 1004 feedhorns of diameter 2.68 mm (cold) because of readout limitations. The cost in NETD is only 1.7 %.

under-illumination of the primary mirror. The result is a FWHM of 1.2 cm for a point source when focused at 17 m.

Chapter 7 presents maps of both a 0.2 in and 1.791 cm sources. After convolution with a 0.2 in circle the predicted FWHM is still 1.2 cm, and after convolving with a 1.791 cm circle the predicted FWHM is 1.7 cm.

A final important parameter of the feedhorn is its phase center, defined as the point along the axis of the horn from which the far-field spherical wavefront appears to emerge. In order to achieve optimum performance from a system, the focal plane of the optical system should coincide with the phase centers of the horns. For the 350 GHz Video Imager I used published tables to estimate the location of the phase center for our feedhorns, which give a distance of 0.9 mm behind the opening of the feedhorn as the

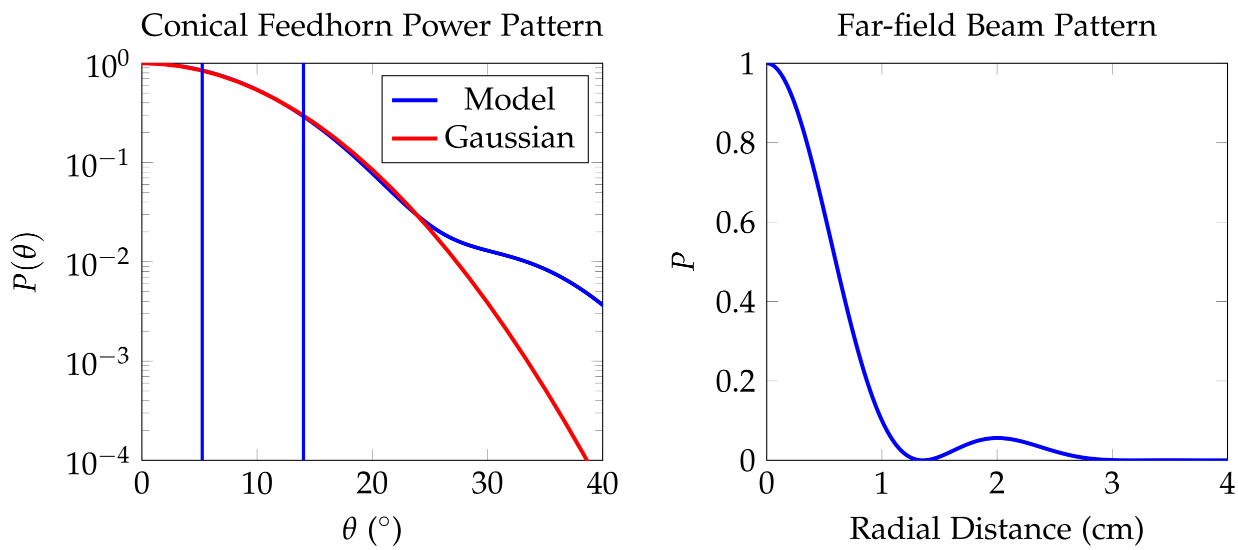

Figure 4.12: Plots showing theoretical beam pattern for the design feedhorns. **Left** The unpolarized power pattern for a conical feedhorn with diameter 2.68 mm and opening half-angle $\alpha_0 = 9.4°$, at the center frequency for our band. The region between the vertical blue lines indicates the part of the beam that strikes the primary mirror and reaches the far-field focal plane. Also plotted is the best-fit Gaussian within the blue lines, which has a FWHM beam width of 21.2°. **Right** 17 m theoretical far-field unpolarized power pattern. The plot includes the effect of blockage by the secondary mirror as well as the edge taper of the beam on the primary. The FWHM beam width is 1.2 cm. The side-lobe is caused by the secondary mirror, and is ~5 % high.

phase center averaged over both polarizations [66, Page 353].

The feedhorns were machined out of Al 6061 and then Au-plated. An estimate of the insertion loss of the feedhorns requires the conductivity of this plated Au at 1 K, but this quantity is not known. I assumed that the Au has the standard value for conductivity at room temperature of 41×10^6 S/m, with a residual resistivity ratio of 3. Using this value, and assuming a surface roughness of 5 μm, HFSS simulations predict an insertion loss of −10.5 dB, including both the feedhorn and the waveguide. This corresponds to a feedhorn efficiency of 91 %. HFSS simulations indicate that the return loss for the feedhorns is −28 dB, so I ignore return loss.

4.5 Optical Coupling to Detectors

The feedhorns described in Section 4.4 couple incoming light into circular waveguide. The waveguide carries the light to the bolometer, where it is absorbed by a Palladium

Gold (PdAu) mesh. This section describes the waveguide and absorbing structures.

The diameter of the circular waveguide was chosen to place the cutoff frequency of the first propagating mode (TE11) below the optical band of the 350 GHz Video Imager. The cutoff frequency of this mode is given by [67, Chapter 5]:

$$f_c = \frac{1.841c}{2\pi a}, \tag{4.8}$$

where c is the speed of light in free space and a is the radius of the waveguide. For our waveguide I chose a diameter of 0.6 mm, which gives a cutoff frequency of 292 GHz, well below the lowest frequency in the band. This choice was made so that the waveguide impedance was more uniform across the waveguide, which makes designing an efficient absorbing structure easier.

The ideal absorbing structure for unpolarized light would be to cover the entire area of the waveguide with a sheet having a surface impedance equal to the waveguide impedance. The characteristic impedance at frequency f for a TE mode in waveguide is [67, Chapter 2]

$$Z(f) = \frac{\eta_f}{\sqrt{1-(f_c/f)^2}}, \tag{4.9}$$

where $\eta_f \approx 377\,\Omega$ is the impedance of free space and f_c the cutoff frequency for the mode. For our waveguide, the impedance at the band-center frequency of 347 GHz is 700 Ω. The highest-resistance material available in the fabrication process for the 350 GHz Video Imager's detectors is a 20 nm thick layer of PdAu, which for our fabrication process has a surface impedance of 12 Ω/sq, far too low to serve as an effective full-width waveguide absorber.

However, the 12 Ω/sq PdAu can still be used to create an absorbing structure with an effective sheet impedance of ~700 Ω by reducing the filling factor of the material, by, for example, making an absorber that consists of a grid of narrow strips. A design rule-of-thumb for grid absorbing structures is that the effective sheet impedance of the absorber is given by

$$Z_{eff} = R_s \frac{A_{tot}}{A_{abs}}, \tag{4.10}$$

where R_s is the impedance of the absorbing material, A_{abs} is the area covered by the absorbing material, and A_{tot} is the total area of the waveguide. This rule-of-thumb has been justified via semi-empirical means [68, 69] for free-space absorbing grids. Theoretical and empirical support for its accuracy for a single strip in waveguide has also been given, provided that an additional factor of 2 is inserted in front of A_{tot} [70].

For the 350 GHz Video Imager, I used this rule-of-thumb as a starting point, but to design the final absorbing structure I ran simulations using HFSS[10]. The HFSS model has the following features:

- 0.6 mm diameter circular waveguide leading to the detector. The waveguide walls are treated as lossless; insertion loss of the feedhorn is calculated separately in Section 4.4.

- 135 µm "air gap" between the bottom of the feedhorn array and the back of the detector wafer; see Figure 5.3.

- Proper backshort diameter of 844 µm and backshort height of 275 µm.

- To keep the design simple, the backshort walls are not metalized. Rather, the detectors were fabricated on degenerate (Boron P-type) Si wafers with resistivity 4 mΩ cm. The fields inside the Si are not solved for in this model. Instead, the Si is treated as a conductor with a surface impedance appropriate for its conductivity. The skin depth in this Si is 350 GHz is 5.5 µm, justifying this approximation. At low temperatures the electrical resistivity of this type of Si is expected to fall slightly [71], but I have assumed the room-temperature value of 4 mΩ cm in the simulations.

- The exact PdAu mesh used in the fabrication was included, using 12 Ω/sq as the surface impedance of the PdAu itself.

- The Au heat-capacity ring (see Section 5.3) and the Al TES are included as well, treated as perfectly conducting surfaces.

- The bottom surface of the backshort is assigned a surface impedance appropriate for Au with RRR = 20, which is typical for thick Au layers fabricated in the NIST cleanroom.

Figure 4.13 shows a schematic of the HFSS model, including the fields propagating through the waveguide. It also shows a close-up view of the current distribution on a portion of the PdAu mesh.

The results of these simulations are shown in Figure 4.14. The band-averaged coupling efficiency of the mesh for unpolarized light is 87 %. Although the two polarizations have

[10] ANSYS, Inc., Canonsburg, PA

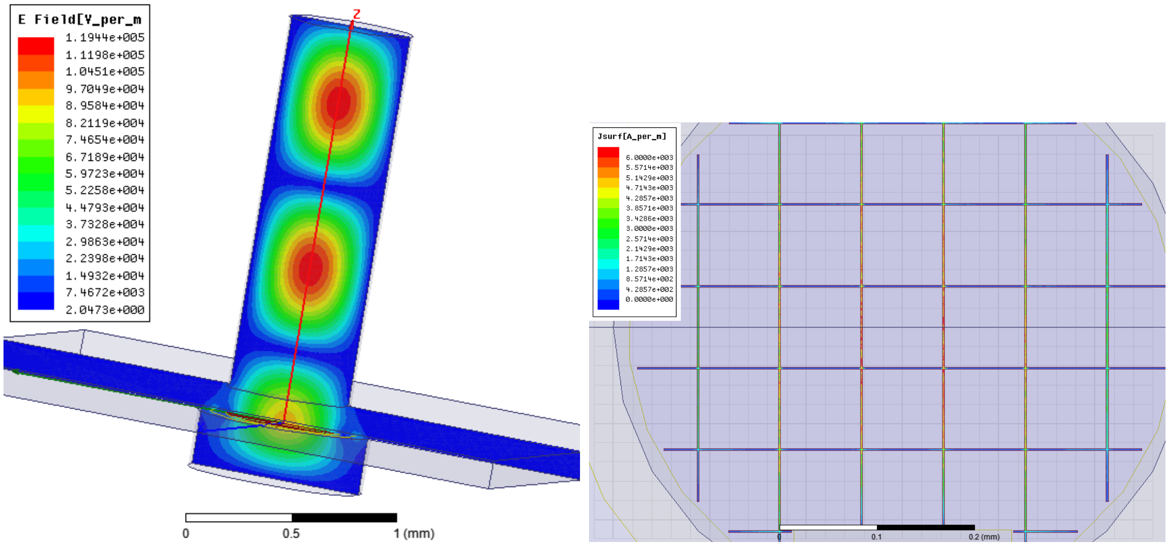

Figure 4.13: Screen-shots taken from the HFSS model used to simulate the absorbing grid. **Left** View of the full model, with the magnitude of the electric field plotted on a plane bisecting the model. **Right** Close-up view of the absorbing grid, with the surface current density plotted. The waveguide mode being excited is polarized in the up/down direction. Because the wires are thin compared to the width of the waveguide (2 µm vs 600 µm), the current distribution is difficult to see in this plot. But close examination shows that the wires perpendicular to the excited polarization have very low current, while those parallel have higher current. The current decays towards the edges of the waveguide as expected.

different absorption curves, with peak absorption at different frequencies, after averaging over the band their difference in efficiency is only $\sim 1\,\%$.

Also shown in Figure 4.14 is the frequency at which the TM01 waveguide mode turns on: 383 GHz. Only 0.9 % of the optical bandwidth is located above this frequency, so I have ignored any coupling to TM01 and all higher order modes.

Figure 4.15 shows the effect of misalignment between the feedhorns and the detectors. For small misalignment (less than 100 µm $\approx$ 4 mils) the loss in coupling efficiency is small. But for large misalignment the loss is efficiency will be large, and one mode will couple much worse than the other. Because the beam for each individual mode is elliptical, this differential mode-coupling will lead to elliptical beams. This could be part of the explanation for the combination of poor optical efficiency and elliptical beams described in Chapter 7.

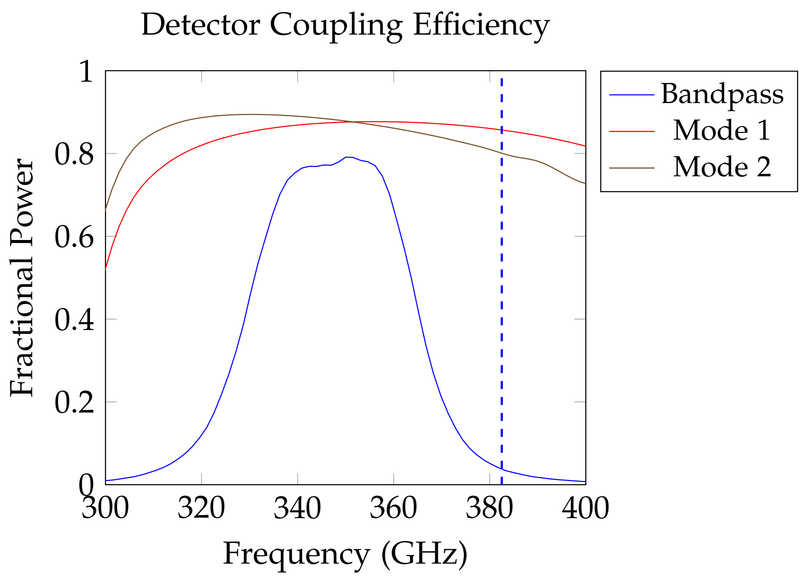

Figure 4.14: Plot showing coupling efficiency of the detectors. The blue line is the transmission of the bandpass filter. The red and brown lines show the fractional power absorbed in the grid absorber. Although theses curves have different shapes, their integrated absorption over the band is within 1 % of each other. The band-averaged absorption for unpolarized light is 87 %. The blue dashed vertical line at 383 GHz indicates the cutoff frequency of the next-highest-order mode, TM01; 0.9 % of the bandwidth is above this frequency.

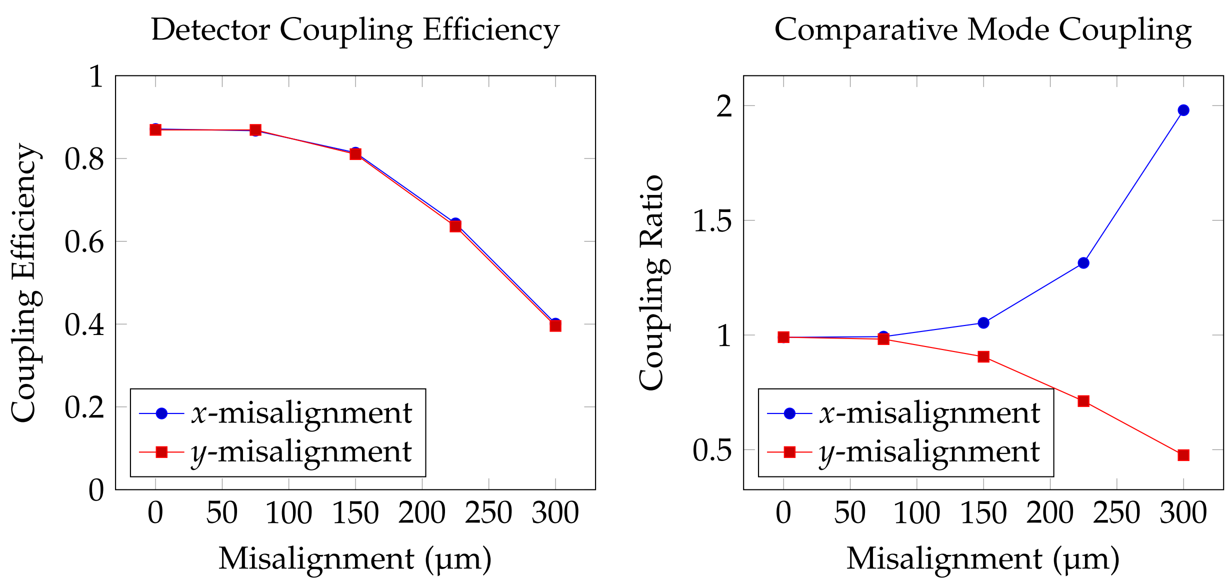

Figure 4.15: Plots showing impact of misalignment between feedhorns and detectors. The left plot shows band-averaged coupling efficiency vs misalignment, for misalignment in both x and y directions. The right plot shows the ratio of band-averaged coupling efficiency of the x-polarized mode to the y-polarized mode, again for misalignment in both x and y directions. For misalignment up to 100 µm loss in coupling efficiency is small. But for large misalignment the efficiency drops substantially, and the modes couple with different strengths, which will lead to an elliptical beam.

4.6 Predicted Optical Efficiency and Optical Loading on Detectors

The waveguide behind the feedhorns in the 350 GHz Video Imager causes the detectors to be sensitive to only the two degenerate TE11 waveguide modes over 99 % of their bandwidth. Because some of the light detected by the 350 GHz Video Imager is reflected, we expect the light to be polarized to some extent. But to simplify the analysis, I assume here that the light is unpolarized, so that the detectors are sensitive to two uncorrelated waveguide modes.

The optical power from a source of temperature T in a single mode detected by a detector with efficiency $\eta(\nu)$ is given by [46]

$$P_{opt}(T) = \int \eta(\nu) h\nu n(\nu, T) d\nu, \tag{4.11}$$

where n is the photon occupation number given by the Bose-Einstein factor

$$n(\nu, T) = \frac{1}{e^{\frac{h\nu}{k_B T}} - 1}. \tag{4.12}$$

For 350 GHz light emitted by a 300 K source, $n \approx 17$, so the Rayleigh-Jeans limit $h\nu \ll k_B T$ holds, and Equation 4.11 simplifies to

$$2k_B T \int \eta(\nu) d\nu = 2k_B T \eta_{tot} \Delta\nu, \tag{4.13}$$

where η_{tot} is the total optical efficiency of the system and $\Delta\nu$ is the optical bandwidth. My calculations below assume the exact from of Equation 4.11, but Equation 4.13 is useful for quick calculations and checks.

Photon NEP is given by [46, Equation 51]

$$NEP_{ph}^2 = 4 \int (h\nu)^2 \eta(\nu) n(\nu, T)(1 + \eta(\nu) n(\nu, T)) d\nu. \tag{4.14}$$

Here the second term represents "photon bunching", which only becomes important when many photons are occupying a spatial mode. For millimeter and submillimeter astronomy observing cold sources such as the Cosmic Microwave Background Radiation, this second term is often negligible, but it is important for the 350 GHz Video Imager because we are observing ~300 K targets.

The 350 GHz Video Imager is not viewing a single temperature T that reaches the detectors with efficiency η. Rather, the 350 GHz Video Imager is viewing a ~300 K source that is attenuated by a series of lossy elements, each of which is at non-zero temperature and so emits power itself. Because of the photon bunching term, it is not correct to calculate NEP_{ph} for each optical component separately and then sum all values; doing so will underestimate the noise due to photon bunching.

The correct generalizations of Equation 4.11 and Equation 4.14 are to treat the term $\eta(\nu)n(\nu, T)$ as a total photon occupation number that includes contributions from all sources. I make the simplifying approximation that the frequency-dependence of the efficiency $\eta\nu$ is the same for all source of optical power; i.e., it is set by the bandpass filter alone. The total occupation number absorbed in the detectors is then given by

$$\eta(\nu)n(\nu, T) \equiv \tau_{bp}(\nu) \sum_k \eta_k \epsilon_k n_k(\nu, T_k). \tag{4.15}$$

Here $\tau_{bp}(\nu)$ is the transmission of the bandpass, $\eta_k = \prod_{k' \leq k} \epsilon_{k'}$ is the cumulative efficiency for light from source k to be absorbed in the detector, ϵ_k is the emissivity of source k and $n(\nu, T_k)$ is the Bose-Einstein factor Equation 4.12 for source k, which is at temperature T_k.

Under these assumptions the expression for optical power becomes

$$2 \int h\nu \tau_{bp}(\nu) \left(\sum_k \eta_k \epsilon_k n(\nu, T_k) \right) d\nu. \tag{4.16}$$

Note that in this case the optical powers from each source can be calculated separately and then summed. NEP_{ph} is given by

$$NEP_{ph}^2 = 4 \int (h\nu)^2 \tau_{bp}(\nu) \left(\sum_k \eta_k \epsilon_k n(\nu, T_k) \right) \left(1 + \tau_{bp}(\nu) \left(\sum_k \eta_k \epsilon_k n(\nu, T_k) \right) \right) d\nu. \tag{4.17}$$

Table 4.6 lists all components of the 350 GHz Video Imager that contribute to optical loading. For each component Equation 4.16 is integrated over the 350 GHz Video Imager's optical band. The temperatures listed for the filters inside the cryostat are estimates based on measurements described in Table 4.5. Also listed are the photon occupation quantities $\epsilon_k \eta_k n(\nu_0, T_k)$ at the band-center frequency of $\nu_0 = 347$ GHz. The predicted total optical loading on each detector is 180 pW, and the predicted optical $NEP_{ph} = 0.85\,\mathrm{fW}/\sqrt{\mathrm{Hz}}$.

Table 4.6: Optical load and photon noise from all components in the 350 GHz Video Imager. P_{opt} for each component is calculated according to Equation 4.16. $\epsilon\eta n$ is calculated at the center frequency of the band (347 GHz) and also includes the transmission of the bandpass filter at that frequency. All powers are the power absorbed in the bolometer, and the NEP_{ph} value is referred to power absorbed in the bolometer. The efficiency of the lens accounts for losses due to both reflection from the lens and absorption in the lens. "Beam" refers to power from the far-field that reaches detectors, while "Spillover" refers to power that reaches the detectors due to the portion of the beam that misses the primary mirror.

Component	Temperature (K)	Efficiency	Emissivity	P_{opt} (pW)	$\epsilon\eta n$	Cumulative Efficiency
Bolometer	1	0.87				0.87
Feedhorn	1	0.91				0.79
W1275	5	0.89				0.70
W1266	16	0.98	0.02	0.1	0.0	0.69
W1269	85	0.94	0.06	2.9	0.2	0.65
W1428	200	0.96	0.04	4.7	0.3	0.62
Lens	295	0.84	0.16	27.7	1.5	0.52
Beam	295	0.52	0.48	69.5	3.8	0.27
Spillover	295	0.00	1.00	75.3	4.1	0.00
Total				180.2	9.8	0.27
Total NEP_{ph}	$0.85 \times 10^{-15}\,\mathrm{W}/\sqrt{\mathrm{Hz}}$					

4.7 Detector Readout

As described in Chapter 3, the 350 GHz Video Imager's detectors are voltage-biased, so that the detector output signal is a changing current. To read out the detectors a low-noise current amplifier is required. The 350 GHz Video Imager uses a multiplexed SQUID readout system to accomplish this.

A SQUID is a Superconducting Quantum Interference Device [72]. For the purposes of understanding the operation of the 350 GHz Video Imager, it suffices to know that a SQUID is a very sensitive magnetometer, and by coupling the magnetic field produced by a current into the SQUID, the SQUID can also be used to read out a current signal.

An important aspect of the response of a SQUID to an input current is that the response is not linear; it is periodic. Figure 7.1 and Figure 7.2 show examples of this behavior for the SQUIDs used in the 350 GHz Video Imager. This periodic response means that the readout system is not measuring the absolute current passing through the detectors, but rather changes in the current from some offset value, an offset value which is not known and can be different for each detector. When processing a set of detector outputs into a video, these detector offsets must be accounted for. The algorithm used to do this is described in Section 7.8.

To reduce the number of wires running into the cryostat, the 350 GHz Video Imager uses a time-division multiplexed (TDM) readout system [9, 73, 74]. Figure 4.16 shows a schematic of this readout system. The detectors are divided into a columns, each column containing 32 rows. Each detector output is coupled into the input coil of its own "1st-stage" SQUID(SQ1). Row address lines bias the 32 rows sequentially, so that at any given time only one detector per column is being read out by the system. This sequential addressing means that the current noise power spectral density of the SQUIDs is increased by a factor of 32 due to aliasing, but the current noise in the 350 GHz Video Imager's SQUIDs is low enough that SQUID noise is not a significant contribution to the total noise of the detectors. See, e.g., Figure 6.1 and Figure 6.15 for a demonstration that SQUID noise ($\sim 1 \times 10^{-10}\,\mathrm{A}/\sqrt{\mathrm{Hz}}$) is below the typical noise level of a detector biased into its standard operation conditions ($\sim 1 \times 10^{-9}\,\mathrm{A}/\sqrt{\mathrm{Hz}}$). To linearize the SQUID amplifier chain, feedback in the form of magnetic flux is applied to the SQ1 SQUIDs.

A set of electronics is required to control the multiplexed readout system and provide data to a computer for further analysis. The 350 GHz Video Imager uses the Multi-Channel Electronics (MCE) as the electronics control system [75–77]. The MCE was developed in order to allow simple, remote operation of TDM readout systems for submillimeter and millimeter astronomy. It comes equipped with a software suite for controlling the electronics itself. The entire electronics system for reading out 1024 detectors is contained within a single 15 in $\times$ 14 in $\times$ 14 in crate drawing 175 W. All communication with the controlling data acquisition computer is via a pair of fiber optic cables. See Figure 4.17 for a photo of the MCE.

The MCE supports extensive configuration options ranging from SQUID bias current values to multiplexing speed, to the order in which rows should be reported to client software [77]. This dissertation does not describe the process of choosing most of these parameters. The exceptions are the feedback control parameters, discussed in the next section, and the parameters that control the readout rate of the system, listed in Table 4.7. The table also gives the value of these parameters used by the 350 GHz Video Imager when taking videos. The rate at which data is reported to the data acquisition computer

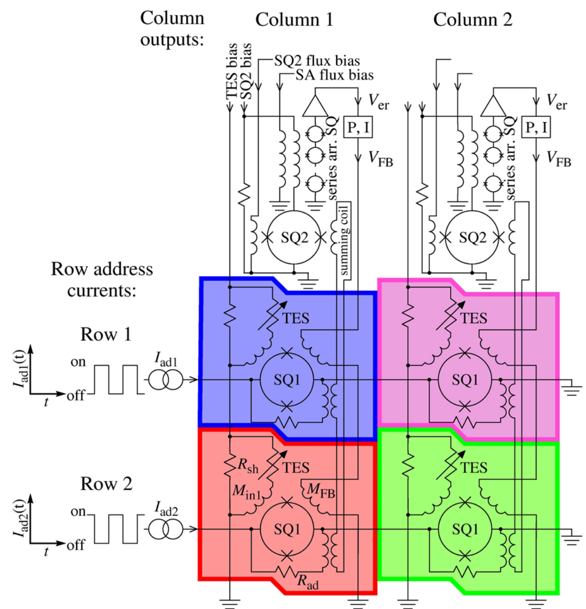

Figure 4.16: Schematic of the Time-Division Multiplexing (TDM) readout system used by the 350 GHz Video Imager. The detectors are divided into rows and columns (2 each shown here). Each detector is coupled to its own 1st-stage SQUID(SQ1). At any given time, only one row of SQUIDs is biased, indicated via the "Row address currents" on the left.

Figure 4.17: Photograph of the MCE unit used to readout the 350 GHz Video Imager's detectors. The MCE is 15 in wide.

Table 4.7: A few important configuration parameters for the MCE.

Parameter	Typical Value	Explanation
row_len	100	Number of 50 MHz clock cycles spent on each row.
num_rows	32	Number of rows to cycle over.
data_rate	5	The MCE only reports every data_rate-th sample to the data acquisition computer.

is given by

$$f_{ro} = \frac{50\,\text{MHz}}{\texttt{row\_len} \times \texttt{num\_rows} \times \texttt{data\_rate}} \tag{4.18}$$

Using the values in Table 4.7 the readout rate is 3125 Hz.

Using any value for data_rate other than 1 will lead to aliasing of noise. As discussed in Section 6.10, this raises the total amount of noise in the 350 GHz Video Imager's detectors by 16 % on average. This noise aliasing penalty can be reduced by configuring the MCE to internally apply a digital 4-pole lowpass filter prior to reporting data to the data acquisition computer [78].

4.8 MCE Servo Gain Parameters

The feedback applied to an SQ1 during frame $n+1$ is defined as [79]

$$FB_{n+1} = \frac{1}{2^{12}} \left[P_{FB} q_n + I_{FB} \sum_{i=1}^{n} e_i + D_{FB}(e_n - e_{n-1}) \right]. \tag{4.19}$$

Here e_n is the error observed during frame n, $q_n \equiv e_n + bq_n$ (where b is some number small than 1), and P_{FB}, I_{FB}, and D_{FB} are the proportional, integral, and derivative terms of the PID loop, respectively. The FB values are expressed in terms of DAC counter units applied to the SQ1 feedback, and the errors e are in terms of ADC values for the output of the readout chain. The 350 GHz Video Imager is operated with $P_{FB} = D_{FB} = 0$, so that the feedback simplifies to

$$FB_{n+1} = \frac{I_{FB}}{2^{12}} \sum_{i=1}^{n} e_i. \tag{4.20}$$

Using only I_{FB}, the MCE servo loop acts like a 1-pole filter. Higher values of I_{FB} increase the bandwidth of this filter until a "critical gain" is reached, at which point the feedback loop becomes unstable and begins to oscillate. I_{FB} should be chosen so that the

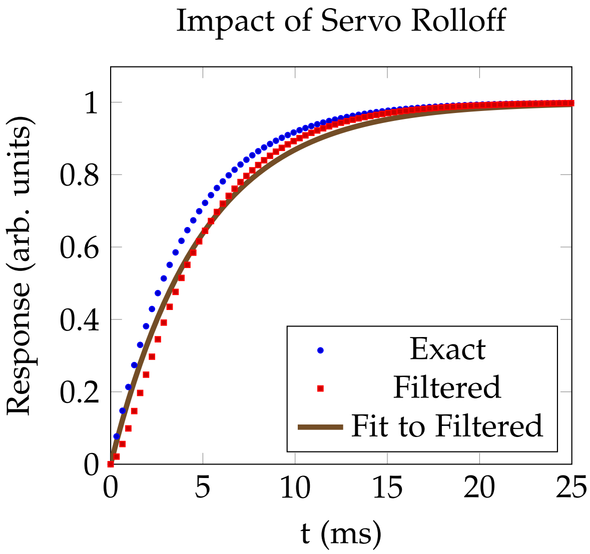

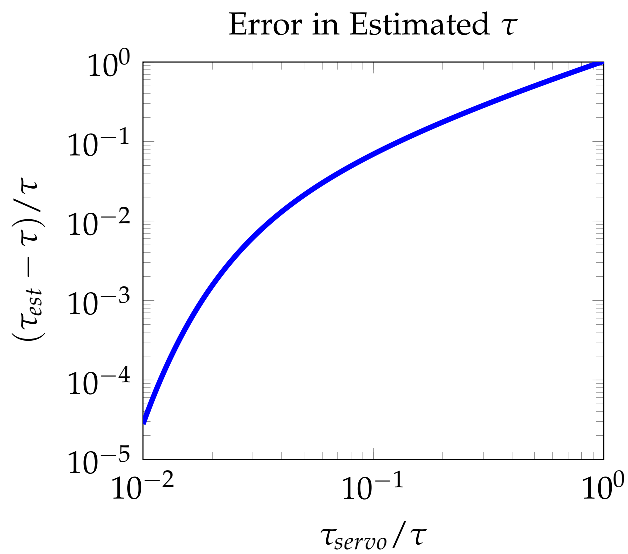

Figure 4.18: Plots summarizing requirements on τ_{servo} for accurate measurements of detector time constants. **Left** Plot showing exact response to step function of a detector with $\tau = 4$ ms, the response as filtered by a servo with $\tau_{servo} = 1$ ms, and the best fit to the filtered response. The estimated τ is 23 % too high. **Right** Plot showing fractional overestimate of τ vs. relative size of τ_{servo}. For less than 2 % error, $\tau_{servo}/\tau < 0.05$ is required.

bandwidth of this filter is greater than that of the detectors themselves, but I_{FB} should not approach the critical gain too closely.

The servo I_{FB} parameter was chosen to minimize SQUID noise and allow sufficient bandwidth to read out the full bandwidth of the detectors. The target servo bandwidth depends on the measurement being made. When operating the array in normal conditions, the data readout rate is either 3125 Hz or 3030.3 Hz, depending on whether the dark SQUID is read out. The time constant for the associated Nyquist frequencies are ~0.1 ms, so there is no need to use I_{FB} values with more bandwidth than this[11]. Electrical detector time constants are ~4 ms in the superconducting state, and ~0.14 ms in the normal state. While biased into the transition, τ_{eff} is in the range 1 ms – 4 ms.

Figure 4.18 shows the impact of the servo roll-off on estimation of time constants from single-pole response functions. To reduce the error in the estimated time constant below 2 %, the servo time constant should be below 5 % of the time constant to be measured. This criteria corresponds to 2×10^{-4} s for the superconducting state and as fast as 5×10^{-5} s for detectors operating in the transition.

[11]Doing so is counter-productive, because it will alias SQUID noise into the detector band

Measuring the bandwidth of the servo loop is challenging because roll-offs due to the L/R filter of the detector circuit itself make it difficult to identify the servo roll-off from power spectra. However, if the bath temperature is raised above T_c for the Al wire bonds connecting the TES circuit to the input coils of the 1st stage SQUIDs, the total resistance of the TES circuit is raised from 150 μΩ to 20 mΩ – 50 mΩ. This high resistance drives the Johnson noise of the load resistor below the SQUID noise, and pushes the L/R roll-off of the Johnson noise to 3×10^{-5} s or faster (3 dB frequency of 5 kHz or higher), making a measurement of the servo bandwidth much easier.

To choose I_{FB} values, I acquired data at the fastest multiplexing rate possible for 33 rows[12], 15,151.5 Hz while the system was at a temperature of 1.3 K. For every row and column that has a detector that responds in the superconducting state, I fit the resulting noise power spectrum to an equation of the form

$$\frac{N_{SQ}}{1 + (2\pi\tau_{servo})^2} \tag{4.21}$$

Where N_{SQ} is the white noise level and τ_{servo} gives the bandwidth of the servo loop.

Figure 4.19 shows the resulting white noise levels and τ_{servo} values for a range of servo gain values I_{FB}. The SQUID white noise level is higher when operating with negative I_{FB} values, so we have chosen to use positive I_{FB} values. When measuring time constants $I = 50$ has been used for all columns, to maximize the number of detectors below $\tau_{servo} = 2 \times 10^{-4}$ s. This places most detectors in a region where SQUID noise will be aliased into the measurement band, but because I always average over many measurements, the accuracy of these types of measurements is not affected by this noise aliasing.

For taking video images, the servo does not need to be run as aggressively. As shown in Figure 6.11, most detectors have τ_{eff} close to 1.25 ms, with only a few slower than this. A servo gain I_{FB} of 20 puts τ_{servo} below 0.6 ms for all detectors, so there is no need to operate at a higher I_{FB} when taking video images. Even operating with I_{FB} of 10 puts 95 % of the τ_{servo} below 1 ms, so operating at I_{FB} of 10 is also acceptable.

[12] This rate is achieved by only reporting one of the eight columns to the readout computer. The limiting factor in how fast the entire array can be multiplexed is packaging and sending the data to the readout computer.

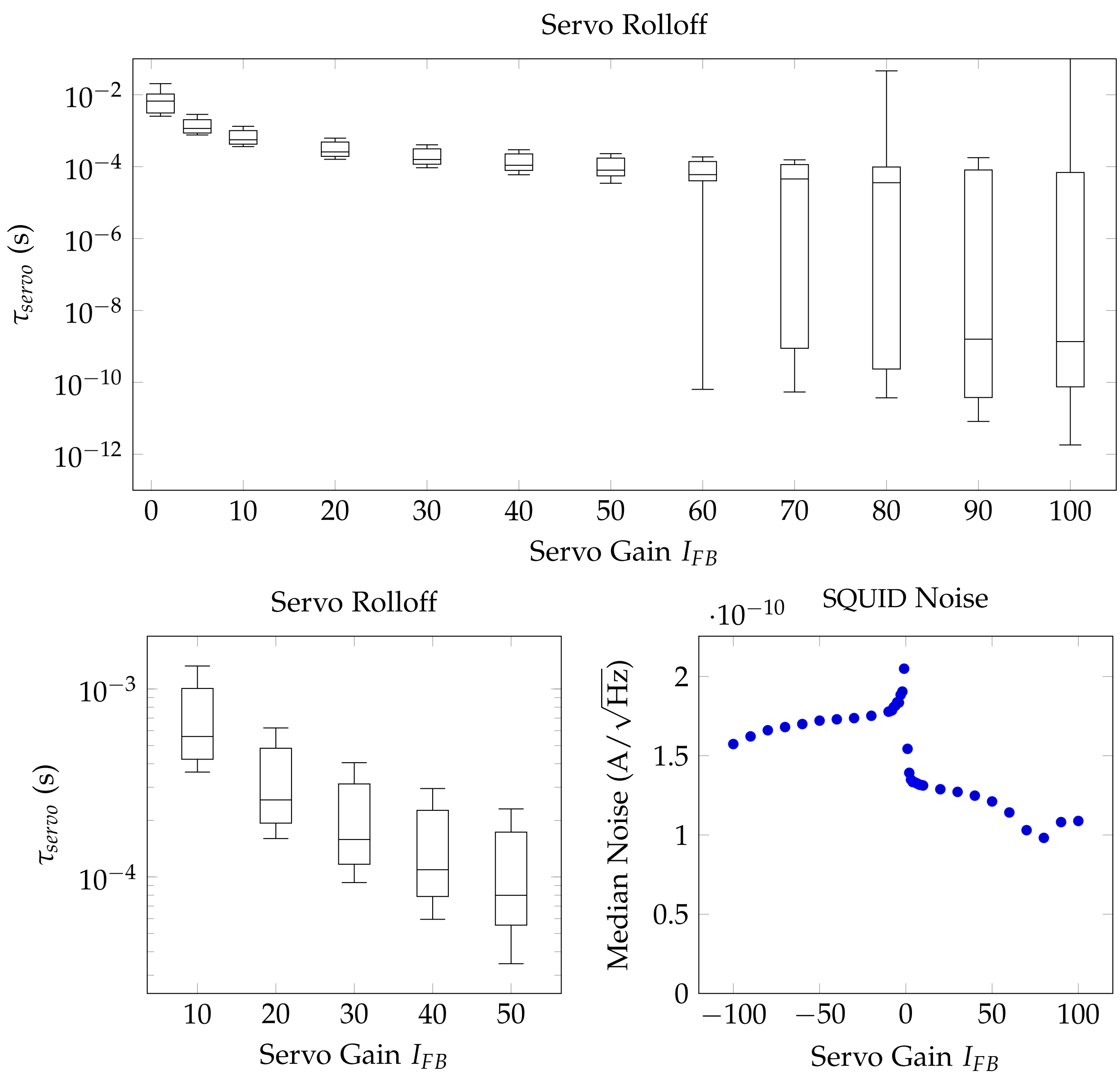

Figure 4.19: Plots summarizing behavior using different servo gains I_{FB}. In the two box plots, the boxes represent the 5 % – 95 % quantiles, the middle line represents the median, and the upper/lower whiskers represent the maximum/minimum values. All detectors that respond in the superconducting state are included. **Upper** Plot of SQUID τ_{servo} vs servo gain I_{FB}. Servo bandwidth increases with I_{FB}. At $I_{FB} \geq 60$, very small τ_{servo} begin to appear. This indicates either a roll-off above the bandwidth of the measurement, or an unstable servo loop. The few high τ_{servo} values at gains of 80 and 100 are a result of the fitting routine failing due to an unstable servo loop. **Lower Left** Close-up view of upper plot for gains from 10 to 50. **Lower Right** Plot of median SQUID white noise level vs. servo gain I_{FB}. Positive gains consistently give lower SQUID noise levels.

4.9 Acknowledgments

Bob Schwall of NIST designed the cryostat, assembled the He4-sorption fridge, and provided useful advice and help in the lab during commissioning of the cryostat. Bob Schwall and William Duncan of NIST designed the cryostat/mirror mount and the He4 sorption refrigerator. The refrigerator was filled with He4 by Simon Dicker at the University of Pennsylvania. Bob Schwall, Cale Gentry, and Ilya Smirnov wrote the LabVIEW program used to control the cryogenic system. William Duncan designed, procured, and assembled the optical system. The optical filters were designed by Peter Ade's group at Cardiff University in collaboration with William Duncan, and manufactured and measured at Cardiff. The MCE was provided by Mark Halpern's group at the University of British Columbia. Mandana Amiri and Matthew Hasselfield provided extensive, timely and invaluable support for the MCE hardware and software. Cale Gentry provided much help in the lab while taking initial still images with prototype detectors.

Chapter 5

Detector and Focal Plane Design

This chapter describes the design of the 350 GHz Video Imager's detectors and focal plane. Prior to fabrication of the 251-detector sub-array that is discussed in this dissertation, prototype detectors were fabricated and characterized. Because the measured properties of the prototype detectors are relevant to some of the parameter choices made for the sub-array detectors, this chapter begins with a short summary of the measured properties of those detectors. I then discuss the choice of parameters G, C, T_c and T_b for the sub-array detectors, the choice of shunt resistor value R_{sh} and Nyquist inductor L, followed by details of the detector design used to achieve these parameters. I then briefly describe the design of the focal plane, and end with the predicted detector noise and NETD for the system.

5.1 Prototype Detectors

The basic design and layout of the prototype detectors was the same as described in Section 5.3 for the sub-array detectors. Four prototype detectors were tested both in the dark and while open optically, and also used to take still images. The techniques used to characterize the prototype detectors were the same as those use to characterize the sub-array detectors, as described in Chapter 6. Table 5.1 lists parameters of these detectors, and Figure 5.1 contains plots showing $\mathcal{L}_I$, β_I, τ_{eff} and L_{crit} for these detectors, measured at a range of bias points.

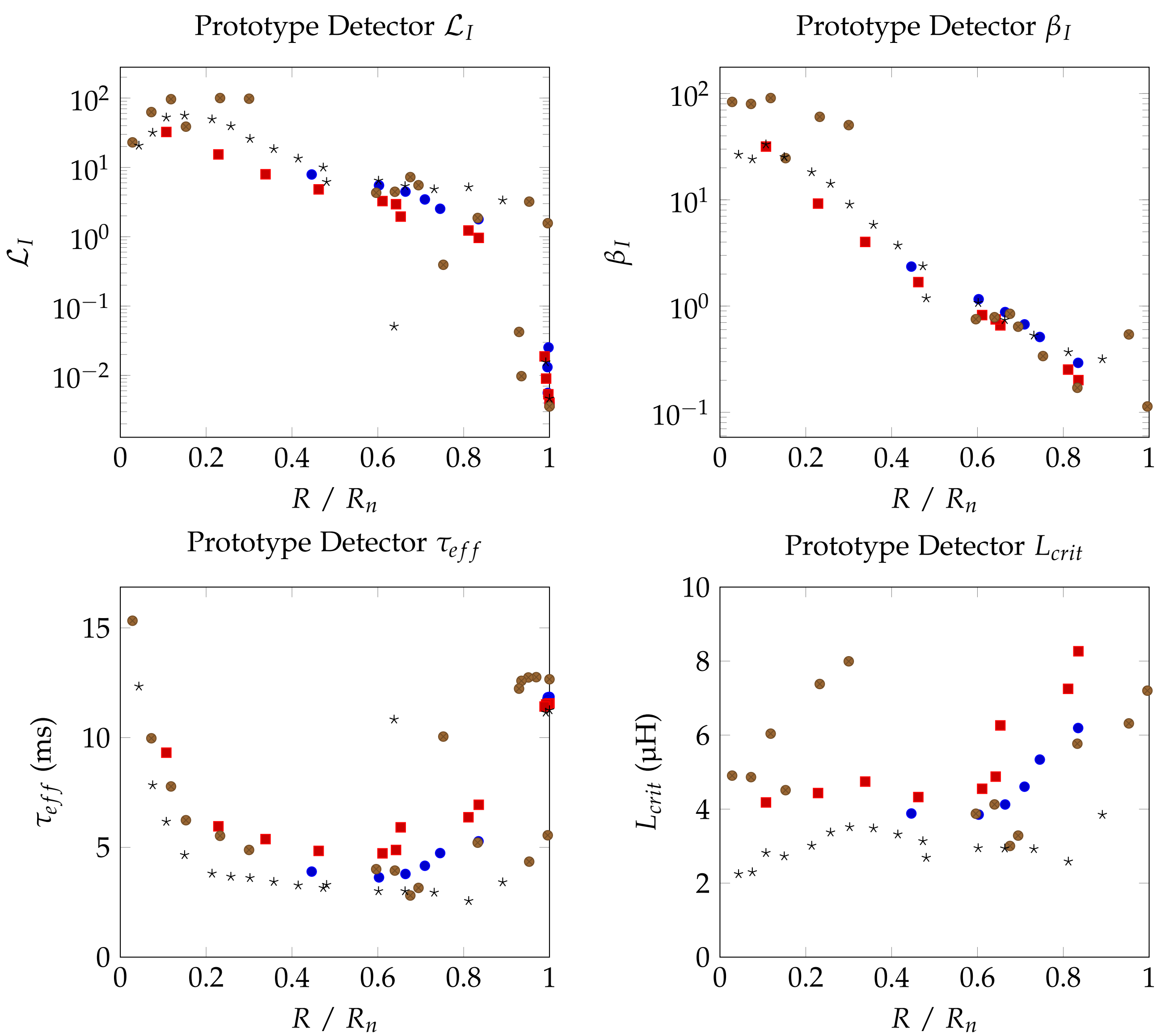

Figure 5.1: Plots showing $\mathcal{L}_I$, β_I, τ_{eff} and L_{crit} vs bias point for four prototype detectors. $\mathcal{L}_I$, β_I, and τ_{eff} were measured using the same techniques described in Chapter 6. The values of L_{crit} were calculated using Equation 3.29.

Table 5.1: Measured Properties of Prototype Detectors. The methods and procedures used to measure these properties were the same as described for the sub-array in Chapter 6.

Detector Property	Value
T_c	1.2 K
R_n	3.4 mΩ
n	3.9
G	5 nW K^{-1}
τ	12 ms
τ_{eff} (typical)	4 ms
$C = G\tau$	60 pJ K^{-1}
P_{opt}	150 pW K^{-1}
η_{tot}	0.25
$P_{sat}\|_{970\,\mathrm{mK}}$	920 pW

5.2 Bolometer Design Parameters

The primary parameters to be chosen when designing a TES bolometer are the superconducting critical temperature T_c, the thermal conductance G, and the TES island heat capacity C. These parameters are interrelated, and so cannot be chosen independently of each other. Some of the factors to consider are:

- Detector noise scales with $\sqrt{T_c^2 G}$, so that lower values of G and T_c improve noise.
- As discussed in Section 3.5, the saturation power of the TES detector scales roughly like GT_c, so that if G and T_c are too small, the optical power falling on the detector will raise the temperature of the membrane above T_c, saturating the device and rendering it inoperable.
- T_c must be chosen to be higher than the achievable bath temperature, and the bath temperature also affects the saturation power through Equation 3.2.
- The detector time constant τ_{eff} is proportional to the detector natural time constant $\tau = C/G$.

The following subsections outline the choice of T_b, T_c, G and C for the detectors in the first 251-detector sub-array.

Choice of T_b and T_c

The relationship between detector noise and saturation power can be examined in more detail. From Equation 3.28 we have

$$P_{sat} = \frac{GT_c}{n}\left(1 - \left(\frac{T_b}{T_c}\right)^n\right). \tag{5.1}$$

This can be solved for G and substituted into the expression for TES thermal fluctuation noise in Table 3.2, leading to

$$S_{TFN}^2 = \frac{nF(T_c, T_b)}{\frac{T_b}{T_c}\left(1 - (T_b/T_c)^n\right)} 4\,k_B T_b P_{sat}. \tag{5.2}$$

The TES temperature T_c appears only in the pre-factor, which depends only on the power-flow index n, the ratio T_b/T_c, and the form of F. This means that for fixed P_{sat} and T_b, the ratio T_c/T_b that gives the lowest detector noise depends only on n and the form of F. For values of n in the range 3–4, this optimal ratio is $T_c \approx 1.8T_b$, while the pre-factor itself is ~3.7.

As discussed in Section 4.6, the predicted loading on the 350 GHz Video Imager's detectors is 180 pW and the photon noise from this load is 0.85 fW/$\sqrt{\text{Hz}}$. Choosing a safety factor of 3 so that $P_{sat} = 3 \times 180\,\text{pW}$, and targeting detector noise equal to 50 % of the photon noise (so that total noise is a factor of $\sqrt{1.5} = 1.22$ higher than photon noise), we find the requirement on T_b to be

$$T_b < \frac{1}{3.7}\frac{NEP_{ph}^2}{4k_B P_{sat}} = \frac{1}{3.7}\frac{0.5 \times (0.85 \times 10^{-15})^2}{4 \times 1.38 \times 10^{-23}\,\text{J}\,\text{K}^{-1} \times 3 \times 180\,\text{pW}} = 3.6\,\text{K} \tag{5.3}$$

A 3.6 K bath temperature can be reached through the use of solely a mechanical cryocooler, which would simplify the design of the cryostat. However, this leaves little margin for error in the design and implementation of the system, so for the 350 GHz Video Imager we chose to use a He4-sorption fridge to allow setting the bath temperature well below 3.6 K.

The initial hopes for performance of the He4-sorption fridge were that its base temperature would be ~650 mK, implying an ideal T_c of ~1.2 K. This is a convenient T_c because it is the critical temperature of elemental Al [80], so Al was chosen as the TES material.

In practice, it was discovered during testing of the prototype detectors that the base temperature of the system was 950 mK under optical load, not 650 mK. With a bath temperature of 950 mK, the optimal choice of T_c would be $\sim$1.7 K; this higher T_c would allow a lower G to be used so that thermal fluctuation noise of the detectors would decrease. However, in order to change as little as possible between the prototype detectors and the first sub-array, I decided to continue using Al as the TES material.

Choice of G

Table 5.1 lists the measured properties and parameters of the prototype detectors. These detectors had P_{sat} at $T_b = 970$ mK, 5.1 times higher than the predicted optical load and 6.1 times the measured optical load. A safety factor of 5–6 is overly conservative, so for the sub-array I decided to target a G value of 3.8 nW K^{-1}, for a safety factor of 3.9 – 4.7.

Choice of C

The detector's heat capacity C is chosen to target a specific detector time constant τ_{eff} once G is chosen. G and C do not set τ_{eff} directly, rather they set the natural time constant τ, to which τ_{eff} is proportional via Equation 3.9. τ_{eff} must be fast enough to avoid blurring of video-rate images, but should be much larger than τ_{el} to avoid detector instability; see Section 3.6.

We can estimate the required value of τ_{eff} by considering the speed with which detectors move on the far-field focal plane and the size of the far-field beam. If v is the speed with which the detector far-field beam moves, and b_{fwhm} is the FWHM far-field beam width, then scanning over a point source will result in a timestream with a Gaussian "bump" with FWHM $q_{raw} \equiv b_{fwhm}/v$. The TES acts like a lowpass filter on this timestream with time constant τ_{eff}. The timestream after filtering is given by the convolution[1]

$$d_{filt}(t) = \int_{-\infty}^{t} \exp\left[-\frac{(2\sqrt{2\ln 2})^2}{2}\frac{t'^2}{(b_{fwhm}/v)^2}\right] \exp\left[-(t-t')/\tau_{eff}\right] dt'. \tag{5.4}$$

The FWHM of the bump after filtering will be q_{filt}. We can quantify the amount of blurring with a fractional blurring factor $(q_{filt} - q_{raw})/q_{raw}$.

As shown in Section 5.7, when scanned circularly the detectors trace out a circle of radius 18.7 cm. If FPS is the video frame rate, then v will be given by $(2\pi)(18.7\,\text{cm})FPS$. From Section 4.4, the predicted beam FWHM is 1.4 cm. Figure 5.2 shows what value of

[1]The factor $2\sqrt{2\ln 2}$ converts the FWHM of the timestream bump to the "standard deviation" term for the Gaussian.

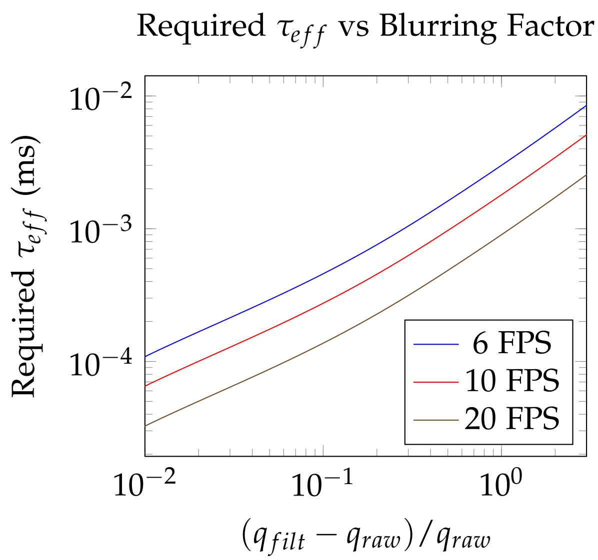

Figure 5.2: Plot of maximum allowed τ_{eff} as a function of fractional blurring factor, defined in the text, for three different video frame rates.

τ_{eff} is required in order to achieve a given blurring factor, for three different frame rates (6, 10, and 20 frames per second).

If we take 10 % as the maximum desired fractional blurring factor, then τ_{eff} must be 0.14 ms or faster to avoid blurring at 20 frames per second. From Table 5.1 this is ~30 times faster than the measured values for the prototype detectors. At 6 frames per second the requirement on τ_{eff} is 0.5 ms, ~8 times faster than the prototype detectors.

Either of these target values for τ_{eff} could be reached by reducing the thickness of the Au ring. However, such a large decrease in the detector time constant risks detector instability, and I did not want to risk losing an entire wafer of detectors due to instability. For that reason I decided to reduce C by a factor of only 2, by cutting the thickness of the Au ring in half. Given the design $G = 3.8\,\mathrm{nW\,K^{-1}}$, and the prototype value of $C = 60\,\mathrm{pW\,K^{-1}}$, this should give $\tau = 7.9\,\mathrm{ms}$, assuming the same properties for Au in the prototype detectors and the sub-arrays. As long as $\mathcal{L}_I$ and β_I at the operating bias point did not change from the prototype detectors, this would reduce τ_{eff} to $4\,\mathrm{ms} \times \frac{7.9}{12} = 2.6\,\mathrm{ms}$. C for subsequent sub-array fabrications can be adjusted lower based on the measurements of the first fabricated sub-array.

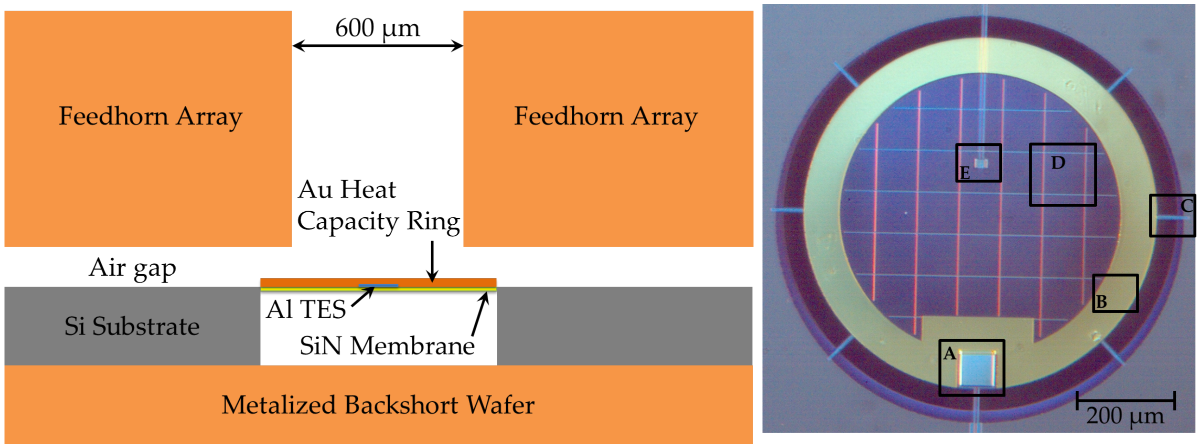

Figure 5.3: **Left** Cross-sectional schematic of a 350 GHz Video Imager detector. Other than the thickness of the TES, SiN membrane and Au Heat Capacity Ring, the schematic is to scale. **Right** Photograph of a prototype detector. The detectors fabricated for the sub-array are identical except for the length of the legs and the thickness of some of the layers; see Table 5.2. The labeled parts of the detector are **A:** Al TES **B:** Au heat capacity ring **C:** SiN leg connecting detector to substrate **D:** PdAu absorbing mesh **E:** PdAu heater resistor.

5.3 Detector Geometry

The 350 GHz Video Imager's detectors are fabricated using standard lithographic clean-room techniques on Si wafers. In order to achieve the targeted G and C values, the detectors are located on a suspended SiN membrane which is connected to the rest of the Si wafer by a set of thin SiN "legs". Figure 5.3 shows a cross-sectional schematic of the detectors, showing that they are suspended with no Si beneath them, as well as a labeled photograph of a prototype detector. The sub-array detectors are identical except for the length of the legs and the thickness of some of the layers; see Table 5.2.

The detectors are fabricated on 275 μm thick double-side-polished degenerate (Boron P-type) Si wafers. A layer of SiO2 is grown on top of the Si, followed by a layer of SiN, prior to the main fabrication steps. During fabrication the Nb wiring leads, Al TES, PdAu absorber, and Au heat-capacity ring are deposited, as well as an additional layer of insulator to allow wiring layers to cross over each other. The SiN and SiO2 is removed from the areas between the legs, and then a Deep Reactive Ion Etch process is used to remove all silicon from behind the detector membrane. This etch process does not remove SiN or SiO2, so that the legs, which still have SiN, are left in place. The result is a suspended membrane connected to the rest of the wafer by a set of "legs" which

Table 5.2: Dimensions of prototype and sub-array detectors. For the sub-array, only values differing from the prototypes are shown.

Detector Dimension	Prototype	Sub-Array
TES Size (l × w)	64 µm × 70 µm	
TES Thickness	250 nm	180 nm
SiN Thickness	500 nm	
SiO2 Base Thickness	120 nm	250 nm
SiO2 Cover Thickness	120 nm	200 nm
Number of Legs	8	
Leg Length	40 µm	67 µm
Leg Width	11 µm	
Au Ring Area	$(393\,\mu\mathrm{m})^2$	
Au Ring Thickness	2000 nm	1000 nm
Nb Lead Width	6 µm	
Nb Lead Thickness	200 nm	
PdAu Thickness	20 nm	

provide the thermal conductance G.

Table 5.2 lists dimensions for both the prototype and sub-array detectors.

The leg geometry of the prototype detectors was chosen based on a set of measurements taken at NIST on SiN membranes at temperatures near 1 K. The leg geometry for the sub-array detectors was based on simple scaling of the prototype detectors to the target G of $3.8\,\mathrm{nW\,K^{-1}}$. This scaling was slightly complicated by the change in thickness of the SiO2 layers, which was made in order to add additional protection to the wiring layers and better balance stress on the relieved membranes. Assuming that G scales linearly with the A/L of the legs, the sub-array G should be

$$G_{sub} = G_{proto}\frac{A_{sub}}{A_{proto}}\frac{l_{proto}}{l_{sub}} \tag{5.5}$$

$$= 5.0\,\mathrm{nW\,K^{-1}}\frac{(500+250+200)(11)}{(500+120+120)(11)}\frac{40}{67} \tag{5.6}$$

$$= 3.8\,\mathrm{nW\,K^{-1}} \tag{5.7}$$

Table 5.3 shows contributions to the heat capacity from all components of the bolometer. The membrane and Al TES alone have insufficient heat capacity, so an Au ring was added to provide the targeted heat capacity. The total heat capacity is dominated by the Au ring.

Table 5.3: Predicted contributions to total heat capacity of sub-array detectors. Note that the Debye T^3 contribution for Au is still significant at 1.2 K, so must not be ignored. All values listed are at 1.2 K.

Component	Volume (10^{-9} cm^3)	C_V (μJ/K/cm^3)	C_{tot} (μJ K^{-1})	Source
SiN	203.6	1.0	0.2	[81]
SiO2	183.2	3.1	0.6	[82, 83]
Al	0.8	196.8	0.2	[34]
Au	154.4	161.3	24.9	[84]
Total			25.8	

5.4 Shunts and Nyquist Inductors

The 350 GHz Video Imager uses spare shunt resistors and Nyquist inductors originally made for the Atacama B-Mode Search (ABS) project [85]. The design value for the shunt resistors was 180 μΩ and for the inductors 609 nH. These chips were already fabricated and available, and the values of R_{sh} and L are appropriate for the 350 GHz Video Imager's detectors.

The measured normal-state resistance of the prototype detectors was 3.4 mΩ, but the thickness of TES material was reduced for the sub-array by ~30 %, for a target sub-array normal-state resistance of 3.9 mΩ. This allows R_{sh} to be more than five times smaller than R_0 at bias points as low as $R_0 = 0.25R_n$, allowing a robust voltage bias.

As shown in the lower right plot of Figure 5.1, the smallest value of L_{crit} for any of the four prototype detectors across all bias points was 2000 nH. This value drops to 1300 nH given the faster design value of τ for the sub-array detectors. Therefore, $L = 609$ nH is low enough to ensure that the sub-array detectors are stable, with a large safety margin in case the values of $\mathcal{L}_I$ β_I, or τ changed between the prototype and sub-array. Lower values of L_{crit} would work as well, and may be considered if faster detector response times are targeted in a future iteration of this system.

5.5 Detector Wafer Layout

Figure 5.4 shows a photograph of the entire sub-array; the figure caption contains a detailed description of the features present on the sub-array. In addition to the detectors, the wafer includes Au pads for attaching Au heat-sinking wire bonds and holes used for gluing the detector wafer to an Au-covered backshort wafer (see Section 5.6). Note that all detectors have heater resistors on their membranes, but only a subset have the resistors connected to traces that lead to bond pads due to space limitations on the wafer.

The detectors are laid out on a square grid, chosen over a hexagonal close-packed layout because of the simpler wiring layout. The choice of a square grid does slightly compromise the system NETD by $\sim 5\,\%$, due to lower packing efficiency compared to a hexagonal array. Higher packing efficiency allows larger feedhorns, which for the 350 GHz Video Imager leads to higher spillover efficiency; see Figure 4.10.

Five locations in the 16×16 grid are missing detectors. The detector in the upper rightmost corner of Figure 5.4 was removed to allow placement of a central post in the focal plane, to which the feedhorn array is bolted. This provides an additional thermal link at the center of the feedhorn array for better heat sinking. Four detectors in the lower left were removed to allow placement of alignment features on the detector wafer. In practice these alignment features were not used, so some or all of these detectors could be recovered in a future design iteration.

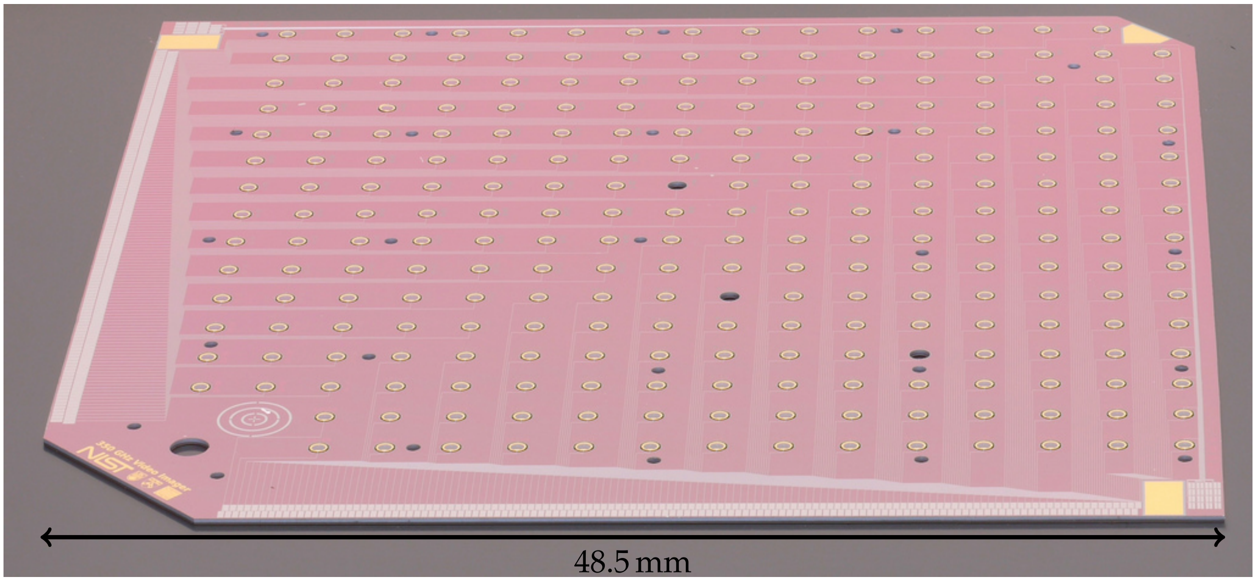

Figure 5.4: Photograph of the 251-detector sub-array. Bond pads for connecting to the detectors run along the left and bottom sides. In the upper left, lower right, and upper right corners are Au pads for connecting Au wire bonds to allow the wafer to be heat-sunk to the rest of the 1 K stage. The upper left and lower right corners also contain small bond pads for connecting to detector heaters. While all detectors have heater resistors on their membrane, only the detectors along the upper and right edges have these resistors wired to bond pads. The 26 small holes spaced throughout the wafer are used to glue the detector wafer to a backshort wafer (see text). The three larger holes in the middle of the wafer are detector sites where the membrane was broken during fabrication. The large hole in the lower left, as well as the "bulls-eye" feature to its immediate upper right, are alignment features, although they were not actually used. Photograph credit Dan Schmidt; full-resolution version available at `http://www.flickr.com/photos/quantumsensors/8592792487`.

5.6 Focal Plane Design

The 350 GHz Video Imager's detector arrays are mounted on an Al platter that is thermally sunk to the cold head of the He4-sorption fridge via a set of braided CU cables. Mechanically the focal plane is attached to an Al frame via four Ti-6Al-4V "spiders". The frame itself is bolted to the 6 K cold plate. See Figure 5.5 and Figure 5.6.

Figure 5.7 shows a cross-sectional view of the focal plane. Each sub-array is glued to a 275 μm thick Si "backshort" wafer that has been micro-machined to have the same outline as the sub-array and then covered with Au. The glue used was Stycast 2850 with

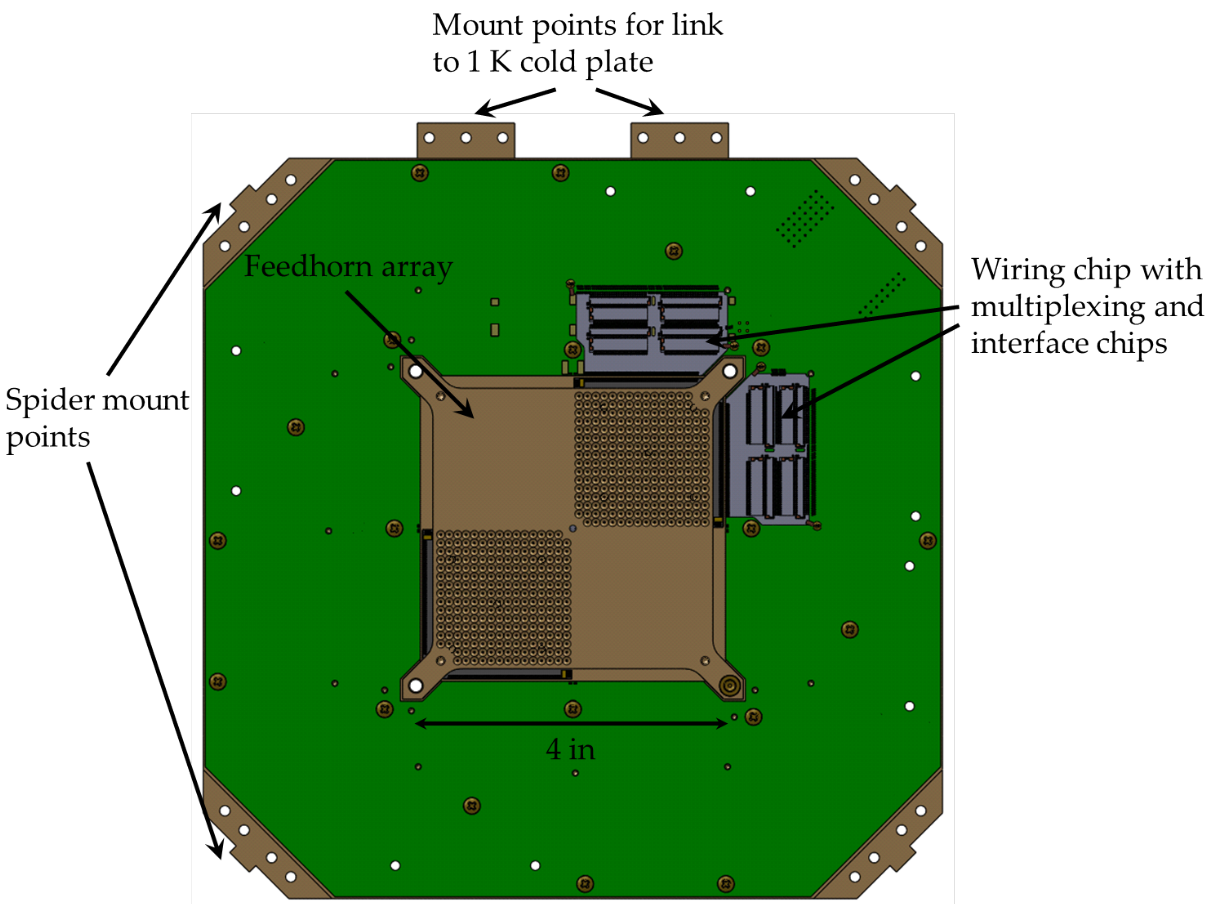

Figure 5.5: Schematic top view of the focal plane.

the LV 23 catalyst[2]. The glue was applied to the set of 26 holes in the detector wafer shown in Figure 5.4. This wafer stack is then attached to a 0.125 in thick Invar plate. Invar was chosen because its thermal contraction upon cooling is well-matched to Si [65]. The wafer stack is attached to the Invar plate with a thin layer of Apiezon-N thermal grease. Upon cooling to cryogenic temperatures Apiezon N grease solidifies, so that the detector wafer will not slip along the Invar. Even at room temperature the grease is very viscous, so that if the back of the wafer stack is entirely covered with a layer of grease the wafer will not slip under the influence of gravity if, e.g., it is stored facing horizontally in the cryostat while at room temperature.

The Invar plates must be attached to the Al platter in a way that accounts for the differential thermal contraction between Al and Invar, while ensuring that the detectors

[2]Henkel Emerson & Cuming, Billerica, MA

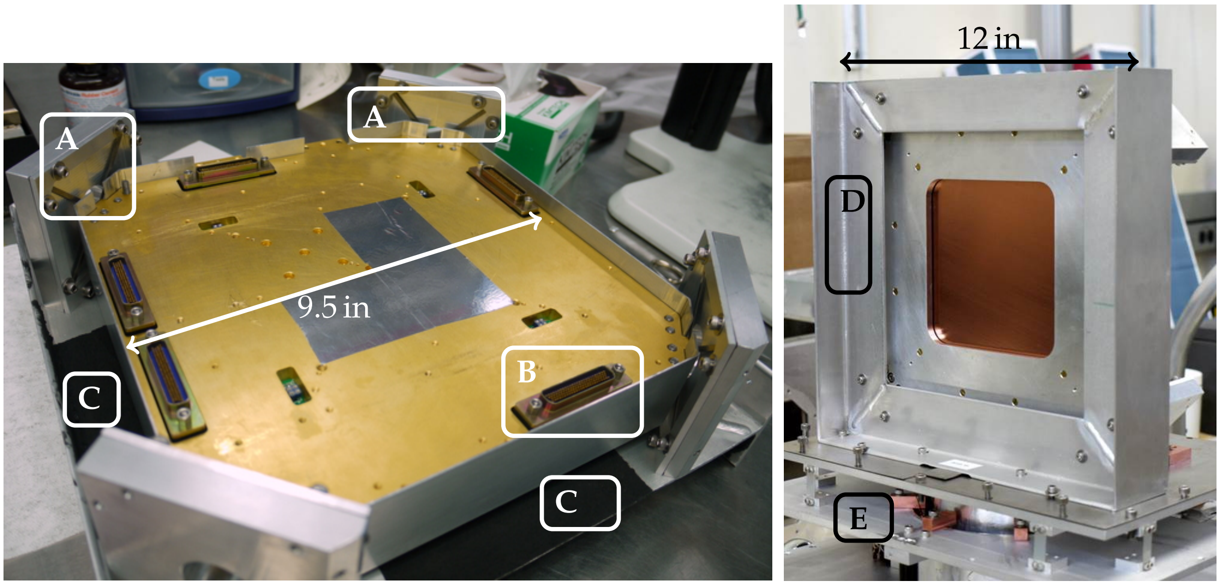

Figure 5.6: Photographs showing how the focal plane is attached to the 6 K Cold Plate. **Left** Back view of the focal plane. **A:** Ti-6Al-4V "spiders" which provide the thermal and mechanical link between the focal plane and the 6 K Cold Plate. A spider is located at each corner of the focal plane, where it is clamped into an Al block. The Al blocks are then bolted to an Al frame. **B:** One of the 100-pin MDM connectors that the wires from the MCE plug into. **C:** It is better for stray infrared light to be absorbed on the 6 K cold stage rather than the focal plane, so the Al frame has Berkeley Bock Black [86] applied to it for IR light absorption. **Right** Photograph of the Al frame and focal plane bolted onto the 6 K Cold Plate. The copper-colored area is the W1275 bandpass filter. **D:** Al frame. This photograph was taken prior to the application of the Berkeley Bock Black. **E:** The 80 K plate. Visible to the right of the **E** rectangle are the end-points of the Cu ropes that connect the PTC 2nd-stage cold head to the 80 K plate.

are correctly aligned to the feedhorns. This is done by aligning the Invar, feedhorns, and Al platter to each other using stainless steel dowel pins. Two pins align the feedhorns to the Al platter. The dowel pins are inserted into the Al platter, with one matching hole and one matching slot in the feedhorn array; a slot is used for one of the holes to avoid over-constraining the mechanical system. Two additional pins align each Invar plate to the Al platter. Again a matching hole and slot are present in the Invar, but in this case the slot is necessary not only to avoid over-constraining the system but also to account for the differential thermal contraction between Invar and Al.

The detector wafer is placed in the proper location on the Invar platter using an alignment jig, and while the Invar and grease have been warmed to ~ 30 °C, a temperature at which the thermal grease becomes less viscous, making it easier to adjust the position

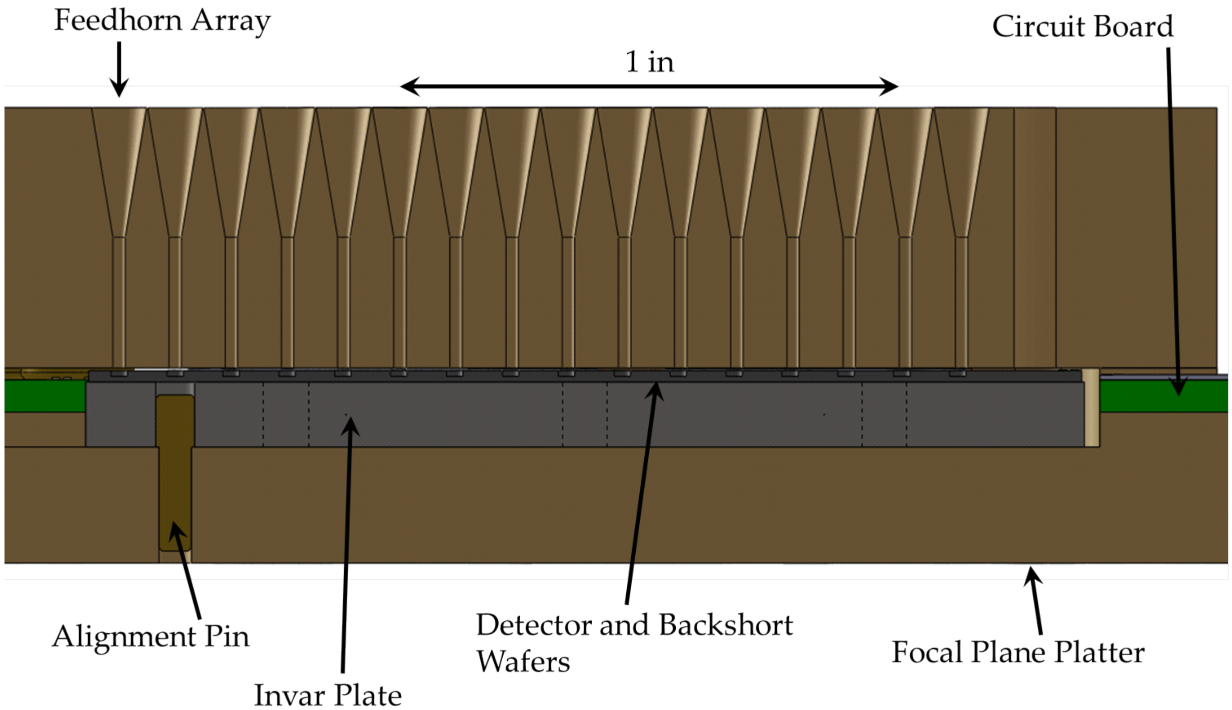

Figure 5.7: Schematic cross-section of the focal planes. The detector and backshort wafers are glued to each other and then attached to the Invar plate using thermal grease. The Invar plate and feedhorn array are aligned to the focal plane platter — and therefore each other — using brass dowel pins. The feedhorns and detectors are misaligned in this view because it depicts the positions of these components at room temperature. When cooled to 1 K, the Al feedhorn array and focal plane platter contract relative to the Invar plate and detector wafers, resulting in alignment between the feedhorns and detectors.

of the wafer. See Figure 5.8. This approach to mounting Si detector wafers on Invar and aligning to a feedhorn has been used by other instruments in the past, e.g. [58].

Four 100-wire woven Phosphor Bronze wire harnesses run from 300 K to the focal plane, heat sunk along the way at the 80 K and 6 K stages. These wires carry the readout signals to and from the MCE. Once they reach the focal plane a circuit board routes the wires to each sub-array. One 100-wire harness carried the row-address wires and the circuit board routes the wires to all multiplexing chips in series (32 chips for the full array). The other four 100-wire harnesses each carry SQUID bias and feedback wires for a single sub-array.

To aid in routing of the wires, each sub-array has two "wiring chips" associated with it, visible in Figure 5.10, and shown in schematic form in Figure 5.9. These chips aid

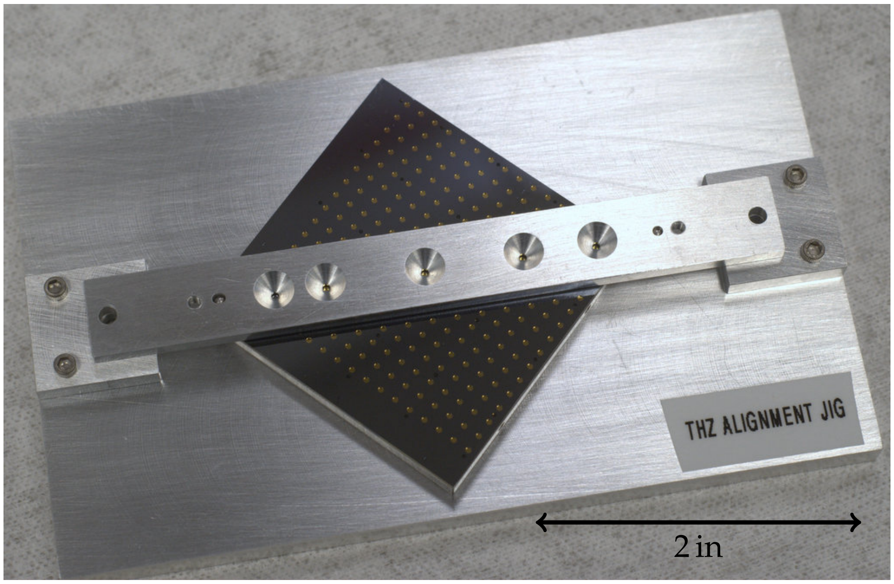

Figure 5.8: Photograph of the alignment jig used to align the 350 GHz Video Imager's sub-array to the Invar plate. The Invar plate and the metal bar are aligned to each other with dowel pins. The metal bar has conical cut-outs placed so that when detectors are aligned with them, the wafer is aligned properly to the Invar. In order to make it easy to move the detector wafer stack to the proper location, the entire assembly is warmed to 30 °C; at this temperature the thermal grease thins.

in routing row-address and detector bias wires. On top of each wiring chip are four multiplexing chips as well as four "interface" chips which contain Nyquist inductors and shunt resistors for the detectors.

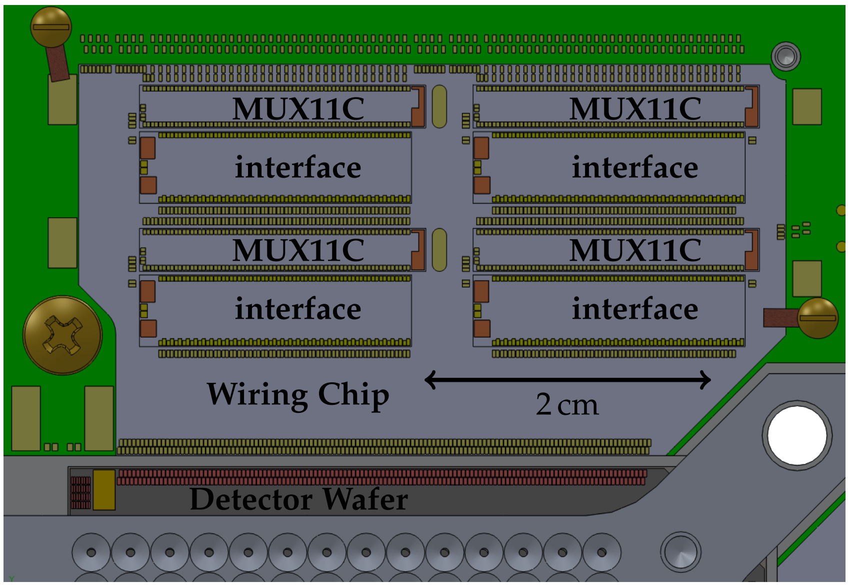

Figure 5.9: Schematic showing close-up view of the wiring chips with multiplexing and interface chips on top.

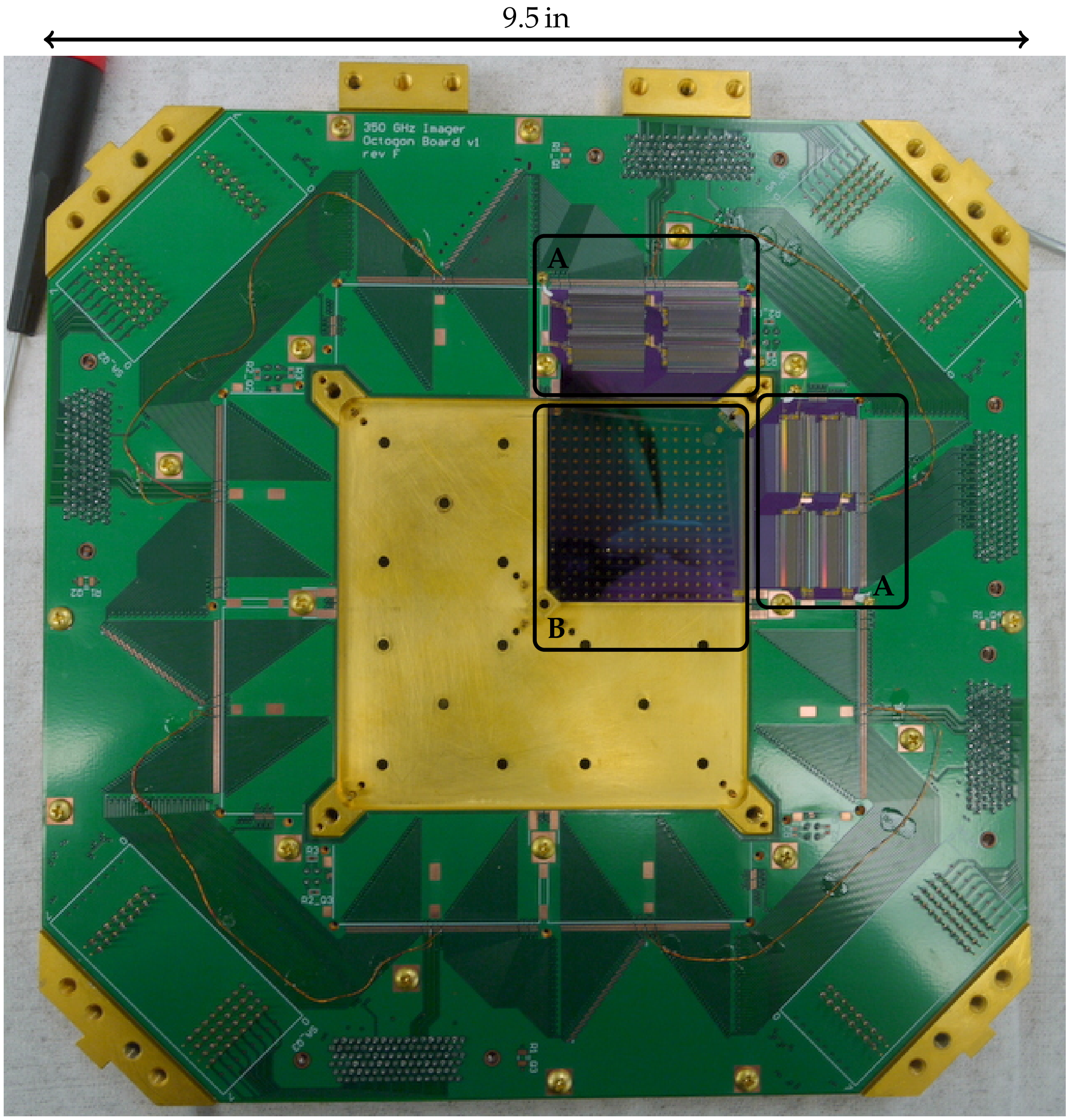

Figure 5.10: Photograph of the focal plane platter while being assembled. The platter was machined out of Al 6061 and then Au-plated. The green circuit board routes the 500 PhBr wires running from room temperature to the multiplexing and interface chips. The wiring chips (with multiplexing and interface chips on top) are labeled **A**, while the 251-detector sub-array is labeled **B**.

5.7 System Field of View

We have now have enough information to calculate the total field of view of the 350 GHz Video Imager. As discussed in Section 7.3, although the system is configured to focus at 16 m, the actual focal distance is 17 m, so I used values for that distance from Table 4.4. A 1 mm movement of the actuator produces a rotation of the secondary mirror of 0.276°; a 1.0° rotation of the secondary mirror displaces the beam of an on-axis detector by 19.33 cm at the far-field focal plane.

To convert actuator displacements into locations in the far-field, three additional factors should be considered. First, the Cassegrain optical system inverts images that it views, so that a beam from a detector in the lower left of the focal plane (as viewed from behind the detector focal plane) is pointed to the upper right on the far-field image (again as viewed from the system). Second, tilting the mirror displaces the beams in the same direction as the mirror is tilted; this is easily seen by thinking of the system in transmission, and imagining the way a ray of light is reflected off of a rotated mirror. Third, the actuators are oriented so that their rotation axes are rotated from horizontal/vertical by 45°. This all means that — as viewed from the cryostat — positive displacements of the DISP1 actuator shift beams up and to the right, while positive displacements of the DISP2 actuator shift beams up and to the left. If we consider an x-y coordinate system in the far-field, this means that the x and y displacement of the beams due to mirror movements are calculated as

$$\Delta x = \frac{\sqrt{2}}{2}\left(d_{\mathrm{DISP1}} - d_{\mathrm{DISP2}}\right) \times \frac{0.276^\circ}{1\,\mathrm{mm}} \times \frac{19.33\,\mathrm{cm}}{1^\circ} \tag{5.8}$$

$$\Delta y = \frac{\sqrt{2}}{2}\left(d_{\mathrm{DISP1}} + d_{\mathrm{DISP2}}\right) \times \frac{0.276^\circ}{1\,\mathrm{mm}} \times \frac{19.33\,\mathrm{cm}}{1^\circ} \tag{5.9}$$

Here d_{DISP1} and d_{DISP2} are the displacements of the two actuators in mm.

The maximum displacement of the LM-1 actuators is 3.5 mm. Assuming a circular scan, the maximum far-field displacement of the on-axis point will be $3.5\,\mathrm{mm} \times 0.276\,^\circ/\mathrm{mm} \times 19.33\,\mathrm{cm}/^\circ = 18.7\,\mathrm{cm}$. When fully populated with 1004 detectors, the four sub-arrays cover an area 86 mm × 86 mm, so the far-field radius of the circle covered by the detectors will be $\sqrt{2} \times (86\,\mathrm{mm}/2) \times 6.638\,\mathrm{mm\,mm}^{-1} + 18.7\,\mathrm{cm} = 55.8\,\mathrm{cm}$, for a total area covered of $0.98\,\mathrm{m}^2$. With a single 251-detector sub-array populated, the field of view will drop to $0.42\,\mathrm{m}^2$. If the scan is elliptical the areal field of view will be smaller still, though the elliptical shape may be more useful for some imaging scenarios.

5.8 Predicted Noise

Using the targeted value of G we can predict the total noise on the detectors as well as the expected NETD in video images. As discussed in Section 3.7, intrinsic detector noise should be dominated by thermal fluctuation noise, given by

$$S_{TFN}^2 = 4k_B T_0^2 G F(T_0, T_b). \tag{5.10}$$

Using $G = 3.8\,\mathrm{nW\,K^{-1}}$, $T_0 = 1.2\,\mathrm{K}$, and $F = 0.83$ leads to $S_{TFN} = 0.5\,\mathrm{fW}/\sqrt{\mathrm{Hz}}$. This is 60 % of Section 4.6's predicted photon noise of $0.85\,\mathrm{fW}/\sqrt{\mathrm{Hz}}$. Summing the two noise sources in quadrature gives for the total noise (referred to power absorbed in the detector) $S_{tot} = 1.0\,\mathrm{fW}/\sqrt{\mathrm{Hz}}$.

To estimate the NETD achieved by the 350 GHz Video Imagerwe use Equation 1.13:

$$NETD = \frac{NEP}{\eta_{tot} M k_B \Delta\nu} \frac{1}{s} \sqrt{\frac{A\,FPS}{2N}}. \tag{5.11}$$

With a fully-populated system of 1004 detectors sensitive to $M = 2$ polarization modes, 20 frames per second, $A = 1\,\mathrm{m}^2$ from Section 5.7, and $s = 1\,\mathrm{cm}$ resolution this leads to NETD = 38 mK. With a single sub-array populated NETD would increase to 50 mK, with the smaller number of detectors increasing NETD but the smaller field of view improving it.

5.9 Acknowledgments

Hsiao-Mei (Sherry) Cho fabricated the detectors and wiring chips, as well as providing much useful advice during the design and layout of both. The interface chips were designed — and spares kindly donated — by the ABS team. Jeff Van Lanen fabricated the backshort wafers and the Quantum Sensors Project SQUID fabrication team made the multiplexing chips. Colin Fitzgerald performed all wire bonding. Lisa Ferreira did the soldering of the 100-pin MDM connectors to the circuit board, as well as a variety of other detail-oriented soldering tasks. The idea to connect the focal plane the 6 K Cold Plate using the Ti-4Al-4V spiders was William Duncan's. Ilya Smirnov carried out a series of simulations to investigate advantages of square vs hexagonal detector grids, as well as required detector time constants to avoid blurring. Although these simulations are not discussed in this dissertation, they supported the conclusions of Section 5.2.

Chapter 6

Sub-array Characterization

In order to produce calibrated images, various properties of the sub-array detectors must be measured. In particular, to establish the image temperature calibration, we must know the detector power-to-current responsivity $S_I(0)$, which allows us to turn detector current into optical power, and the total optical efficiency, which allows us to turn the optical power into the temperature of an emitting object. Other measurements will also help us to improve the detectors for future generations of the system.

This chapter presents a series of detector measurements culminating in predictions of $S_I(0)$ for all working detectors, while Chapter 7 presents measurements of optical efficiency and establishes the temperature scale. This chapter also describes measurements of detector noise, showing that the noise is higher than the design value of Chapter 5 by a factor or ~ 2.5. A section discussing measurements of detector G, which is relevant to predictions of detector noise, is also included, as are sections discussing common mode noise, microphonic pickup and noise aliasing. Table 6.1 summarizes all of the measurements described in this chapter.

Several measurements are taken at "standard operating conditions" (SOC), which are the conditions under which the array is operated while acquiring video images. These conditions are bath temperature $T_b = 1100\,\mathrm{mK}$ and detector bias value DAC = 27,000[1], corresponding to $I_{bias} \approx 8\,\mathrm{mA}$. No heater bias is applied to any detectors under SOC. When referring to individual detectors, I use the notation RnCm. This notation refers to the detector read out on row n of column m, where the indices are zero-based.

[1] The detector bias lines are controlled by digital-to-analog converter (DAC) units as described in Section 4.7. Bias values in this chapter are in terms of DAC units, where DAC $= 2^{15} = 32768$ is the maximum bias that can be applied, and corresponds to $I_{bias} \approx 10\,\mathrm{mA}$

Table 6.1: Summary of measurements made on first 251-detector sub-array

Measurement	Section	Detectors Subset
R_{sh} and L_{ny}	6.2	All working detectors
Heater Resistors	6.3	Seven detectors with working heaters on column 0 and 1
τ	6.4	Four detectors with working heaters on column 0
G, T_c, n, P_{sat}	6.5	Seven detectors with working heaters on column 0 and 1
τ_{eff} and DC responsivity	6.6	Seven detectors with working heaters on column 0 and 1
$\mathcal{L}_I$, β_I, R at a range of bias values	6.7	Seven detectors with working heaters on column 0 and 1
$\mathcal{L}_I$, β_I, R at SOC	6.7	All working detectors
Detector noise at a range of bias values	6.11	Four detectors with working heaters on column 0 and 1

6.1 A path to DC responsivity

The DC detector responsivity under the desired operating condition of strong electrothermal feedback is given by Equation 3.7:

$$S_I(0) = \frac{1}{V_0(1 - R_{sh}/R_0)}, \tag{6.1}$$

where V_0 is the voltage across the TES at the bias value, R_0 is the resistance of the TES at the bias value, R_{sh} is the bias circuit shunt resistance, and the assumption of zero parasitic resistance has been made.

R_{sh} can be measured directly or, as described in this chapter, through Johnson noise. If full IV curves for the detectors are available — including enough of the normal branch to allow calibrating the normal-state resistance — then V_0 and R_0 are also known, and Equation 6.1 can be used to predict $S_I(0)$.

Unfortunately, this simple approach to $S_I(0)$ is not available for the 350 GHz Video Imager's detectors. The reason is that, as described in Section 6.5, the saturation power of the detectors is ~2 times higher than expected, which means that only some detectors can be driven into the normal state using bias current alone — even under optical load — and then only at bath temperatures very close to T_c. In particular, none of the detectors can be driven normal at the operating bath temperature of 1100 mK. This means that we do not have IV curves for any detectors under SOC, and thus no simple measurement of V_0 and R_0.

Instead, the approach taken here is to measure the response of the detectors to a step function in the applied detector bias current, referred to throughout this chapter as "bias step" measurements. Through Equation 3.16 this allows a measurement of R_0, $\mathcal{L}_I$, and β_I. Once R_0 is known, V_0 can be calculated from the known parameters of the bias circuit, and Equation 6.1 can be used to calculate $s_I(0)$.

However, because this approach yields values for $\mathcal{L}_I$and β_I, we are not limited to calculating $s_I(0)$ under the assumption of strong electrothermal feedback. Instead this chapter uses the full expression for the DC responsivity,

$$s_I(0) = \frac{1}{V0} \frac{\mathcal{L}_I}{1 + \beta_I + R_{sh}/R_0 + \mathcal{L}_I(1 - R_{sh}/R_0)}, \tag{6.2}$$

A small subset of the detectors used in taking images have working heaters. Once calibrated, these heaters allow a direct measurement of detector responsivity, which can be used as a check that the above procedure yields accurate predictions for $s_I(0)$.

6.2 Shunt Resistance Measurements

Measurements of the shunt resistors are required in order to calculate the current passing through the TES when taking IV curves. Knowledge of the shunt resistances also help us to verify that the detectors are operating under a robust voltage bias. Measurements of the Nyquist inductors allow us to calculate the detector electrical time constant τ_{el}, which aids in determination of detector stability as well as measurements of R_0, $\mathcal{L}_I$, and β_I through "bias step" measurements.

Our shunt resistors are located on interface chips that contain both shunt resistors and Nyquist inductors. The design resistance of the shunts was 180 μΩ, and the design inductance was 609 nH. Each chips contains 32 shunt resistors and 32 inductors.

To measure R_{sh} and L for these chips I took noise measurements using zero detector bias current at two different bath temperatures: 980 mK and 1160 mK. At these bath temperatures and at zero detector bias the detectors are superconducting, so that measured noise is due to the shunt resistor, any parasitic resistance, and SQUID noise in the multiplexed readout system itself. Data was collected at 3030.3 Hz, and 20 data acquisitions lasting 33 seconds were taken at each bath temperature.

A power spectrum was estimated for each detector for each data acquisition using MATLAB's `pwelch` function, using a FFT size of 2^{12}. Each resulting power spectrum was fit to a function of the form

$$\frac{4k_B T_b}{R_{sh}} \frac{1}{1 + (2\pi f (L/R_{sh}))^2} + SQ, \tag{6.3}$$

where k_B is Boltzmann's constant, T_b is the bath temperature for the measurement, and f is the frequency. The shunt resistance R_{sh}, inductance L, and readout chain white noise level SQ are the fit parameters.

Figure 6.1 shows histogram plots of the resulting R_{sh} and L values for 210 shunts and inductors. R_{sh} has a mean of 149 μΩ with standard deviation 6 μΩ. This uncertainty is equal to the measurement noise, although there are three shunts with values more than three standard deviations from the mean, suggesting that they may have a statistically significant different value than 149 μΩ. The values for R_{sh} include any parasitic resistance in the circuit, but no evidence for significant parasitic resistance has ever been seen, so this parasitic resistance is assumed to be zero throughout this dissertation.

The value for L includes the Nyquist inductance on the interface chip, the input inductance of the first-stage SQUID of the multiplexed readout system, as well as any parasitic inductance in the circuit. Using this approach it is not possible to extract the inductance of the Nyquist inductor itself, but this is not a problem because the total inductance is the relevant quantity for understanding the behavior of the detector and its circuit.

L has a mean of 568 nH with a standard deviation of 86 nH. However, this mean includes two sets of clear outliers: all values for multiplexing row 4 are clustered around 200 nH, and all values for multiplexing row 25 are clustered around 440 nH. The outlier L values are more clearly visible in the lower left plot in Figure 6.1. The reason for these low inductances is not understood, but the correlation with rows suggests that a problem with the fabrication mask is a possible explanation. Excluding rows 4 and 25, L has a mean of 587 nH with a standard deviation of 44 nH. This uncertainty is three times larger than the typical measurement uncertainty, so much of the remaining scatter indicates real variations in the inductance.

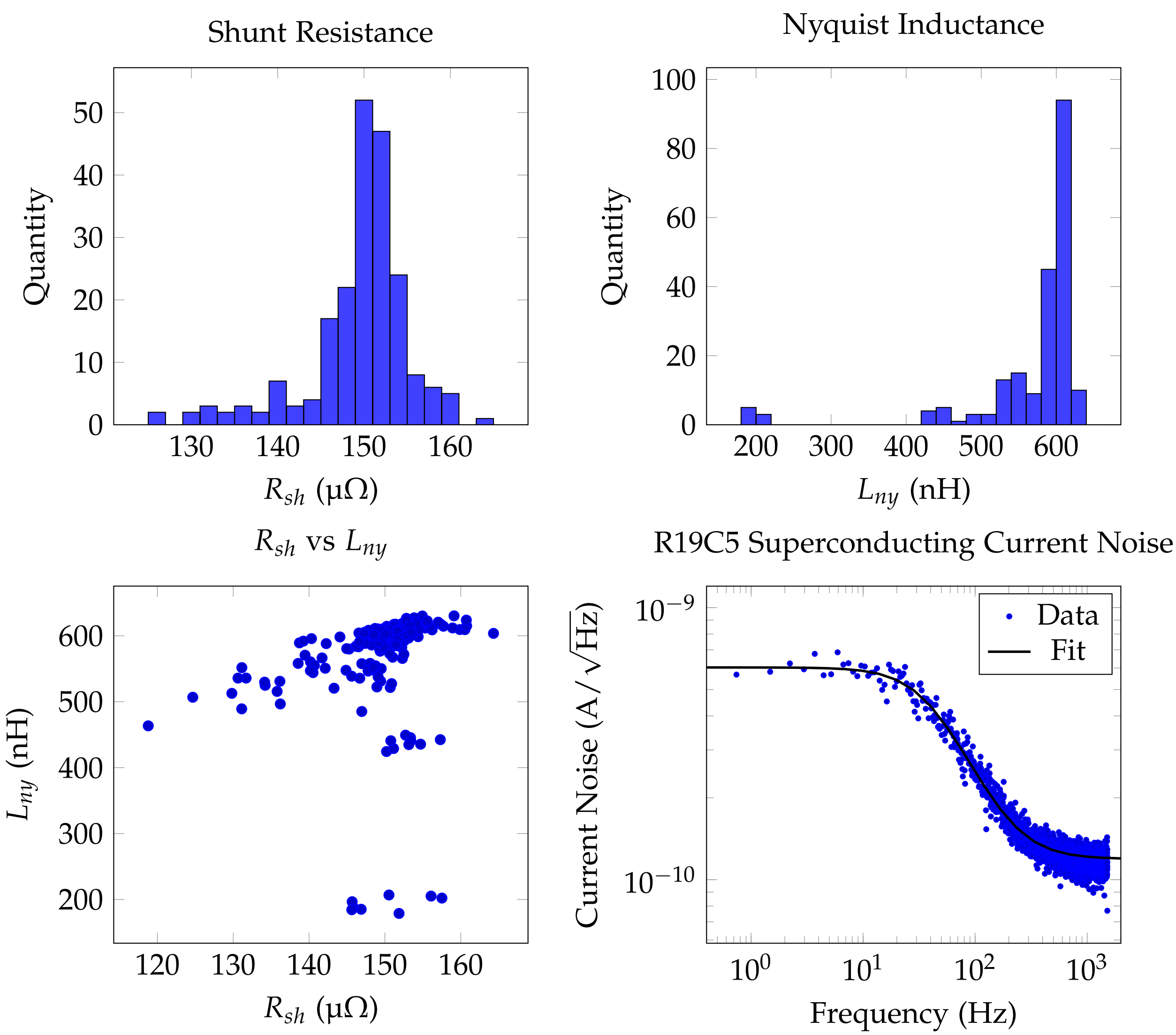

Figure 6.1: Plots summarizing results of measurements of shunts and Nyquist inductors. **Upper Left** Histogram of shunt resistance R_{sh}. **Upper Right** Histogram of total inductance in circuit, which includes the interface chip Nyquist inductor, the inductance of the SQ1 input coil, and any parasitic inductance. **Lower Left** Scatter plot showing all R_{sh} and L values. A correlation is apparent, the reason for which is not understood. **Lower Right** Plot showing current noise power spectrum for a single data acquisition for R19C5, along with predicted power spectrum based on best fit to Equation 6.3 across all data acquisitions. The best fit values are $R_{sh} = 155\,\mu\Omega$, $L = 616\,\text{nH}$, and SQUID white noise level of $1.2 \times 10^{-10}\,\text{A}/\sqrt{\text{Hz}}$.

6.3 Calibration of Heater Resistors

Calibrating the heater resistors is important because the heaters allow direct measurements of the detector responsivity $S_I(0)$. They also allow us to take full IV curves at all bath temperatures, which allows measurements of detector thermal conductance G and superconducting critical temperature T_c, which in turn can aid understanding of measurements of detector noise.

Thirty-one detectors have heater resistors. Twenty-three of these have the heater wire bonded to the heater bias line. Of these 23, there are nine detectors which show no response to applied heater power. This leaves 14 working detectors that show a response to applied heater power.

However, a short between one of the TES bias lines and the heater bias line means that ramping the current bias for columns 6 and 7 also ramps the heater bias for all detectors. This means that for the seven working heaters on columns 6 and 7, interpreting IV curves is difficult because a different amount of heater power is applied at each detector bias value. This means that for these seven detectors it is not possible to measure G or to calibrate the power being applied by the resistors.

This leaves seven detectors on columns 0 and 1 with heaters for which good IV curves can be taken, and G measured. The heaters on these seven detectors can be used to directly measure the detector responsivity, noise referred to input optical power, time constants and thermal conductance G. But these measurements require knowing the heater resistance.

Following the procedure outlined in Section 3.4, I took IV curves at $T_b = 1100\,\text{mK}$ using a range of heater biases. Figure 6.2 shows the results for R28C0. The upper left plot shows the TES IV curves. The upper right plot shows the same data, but transformed into TES Joule power and TES resistance. As applied heater current decreases, the Joule power at the start of the transition decreases. In the lower left, the Joule power at $0.99R_n$ is plotted vs applied heater current. A fit to Equation 3.24 is also plotted. Finally, the lower right plot shows the R vs P_J plots after the heater power has been added to each curve. This plot shows that the powers are equalized very high in the transition, where Joule power depends only on TES resistance. It also shows that this assumption breaks down deeper in the transition.

Table 6.2 lists all measured heater resistors. The seven heaters for columns 0 and 1 have a mean of $23.1\,\Omega$ with a standard deviation of $1.2\,\Omega$.

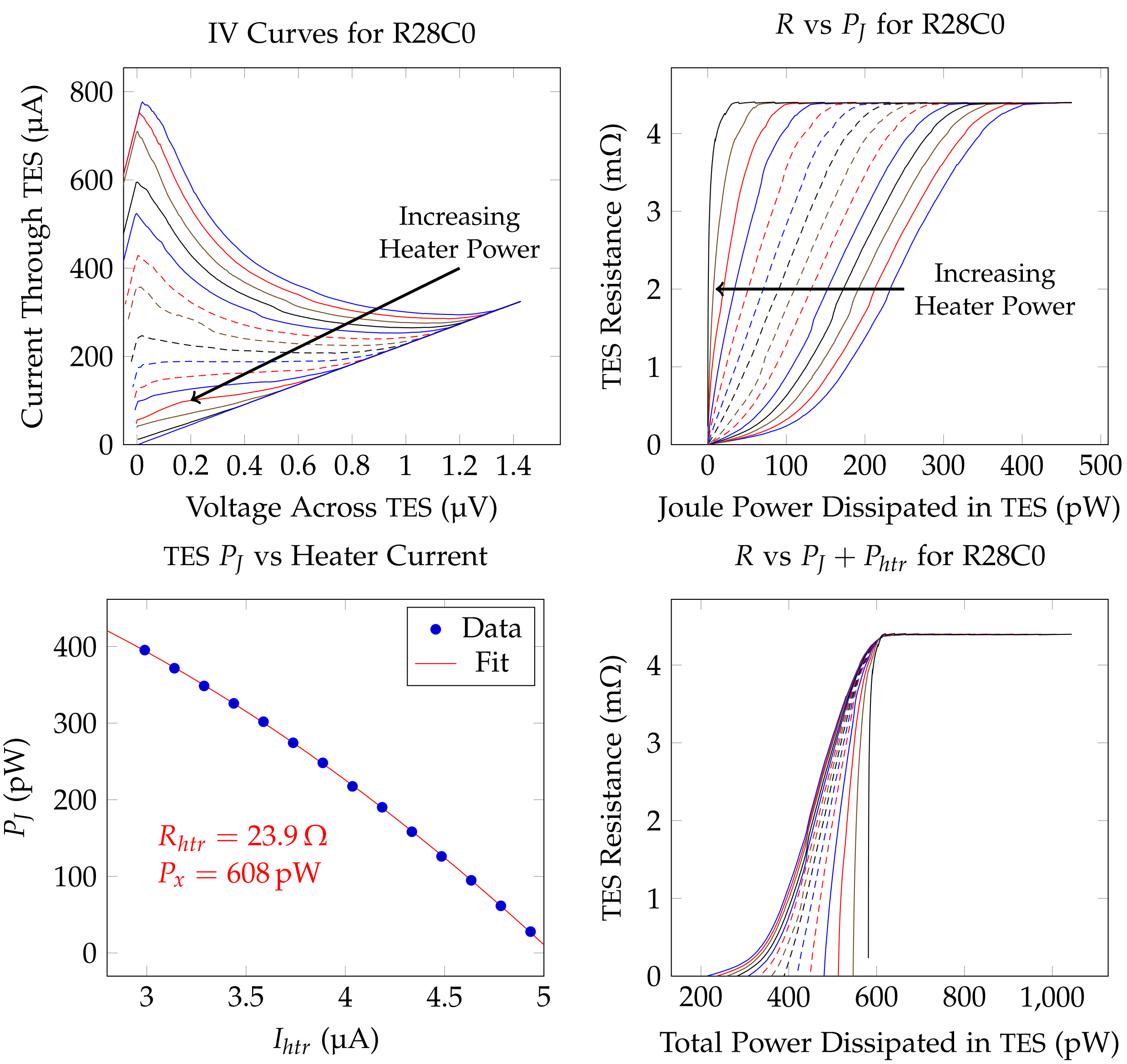

Figure 6.2: Plots related to heater measurements, for the case of R28C0. **Upper Left** IV curves. The IV curves should turn vertical when the detector becomes fully superconducting at zero voltage, but these curves shown a non-infinite slope. The reason for this is that the readout system as configured for these IV curves was unable keep up with the rapid change of current in the superconducting branch. **Upper Right** Same data as in upper left plot, but represented in terms of TES Joule power and resistance. As the bias current for the heaters is increased, the curves shift to the left. **Lower Left** Measured P_J vs heater current at $0.99R_n$, as well as the fit to Equation 3.24. **Lower Right** Same plot as upper right, but the heater power based on $R_{htr} = 23.6\,\Omega$ has been added to each curve.

Table 6.2: Measured detector properties. $P_{opt} = 150\,\text{pW}$ is assumed everywhere. Uncertainties are 95 % confidence intervals after marginalizing over other fit parameters, and do not include systematic uncertainties due to the unknown value of P_{opt}, uncertainty in the value of the shunt resistors, or possible errors in the calibration of the focal plane thermometer. The value of C is calculated using $C = \tau G$.

Detector	R_{htr} (Ω)	G ($\text{nW}\,\text{K}^{-1}$)	n	T_c (mK)	τ (ms)	R_n ($\text{m}\Omega$)	C ($\text{pJ}\,\text{K}^{-1}$)
R28C0	23.9	7.78 ± 0.08	3.55 ± 0.10	1209.0 ± 0.6	8.94 ± 0.1	4.39	70 ± 1.1
R29C0	23.5	7.73 ± 0.07	3.57 ± 0.09	1213.8 ± 0.6	8.82 ± 0.2	4.35	68 ± 1.4
R30C0	23.4	7.56 ± 0.10	3.67 ± 0.13	1215.4 ± 0.8	9.45 ± 0.1	4.32	71 ± 1.1
R31C0	23.0	6.89 ± 0.36	3.35 ± 0.50	1212.4 ± 3.2	10.22 ± 0.1	4.28	70 ± 3.7
R28C1	23.8	7.71 ± 0.08	3.58 ± 0.10	1213.6 ± 0.7	9.01 ± 0.1	4.36	69 ± 1.1
R30C1	20.4	6.35 ± 0.16	3.41 ± 0.24	1214.5 ± 1.6	9.51 ± 0.1	3.78	60 ± 1.6
R31C1	23.5	7.41 ± 0.25	3.70 ± 0.32	1215.8 ± 2.1	10.98 ± 0.1	4.38	81 ± 2.7
Mean	23.1	7.35	3.55	1213.5	9.56	4.27	70

6.4 Measurement of Natural Time Constant τ

Measurements of the detector natural time constant are useful because they directly effect the effective detector time constant τ_{eff}, which impacts the amount of blurring in video images. Knowledge of τ is also necessary in order to extract the parameters R_0, $\mathcal{L}_I$, and β_I from the "bias step" measurements which are then used to predict the DC detector responsivity $S_I(0)$.

The approach described in Section 3.3 was used to measure the natural time constant τ. The response to a step-function change in applied heater power was measured at bias values near the top of the transition at $T_b = 1100\,\text{mK}$. The response to multiple steps was averaged together prior to making a fit. For each bias value the time constant τ_{meas} and change in TES current δI was obtained from curve fits to Equation 3.12. A fit was then performed to Equation 3.20:

$$\tau_{meas} = \tau - \tau\mathcal{K}(I_{bias}\delta I). \tag{6.4}$$

In this fit, τ_{meas} is considered the dependent variable, the product $(I_{bias}\delta I)$ is the independent variable, and the variables that are fit for are τ and $\mathcal{K}$.

Figure 6.3 shows an example of fitting to Equation 6.4, and the measured values of τ are listed in Table 6.2. The average value of 9.6 ms is ~20 % slower than the design value of 7.9 ms. However, as shown in Section 6.7, the predicted values of τ_{eff} across

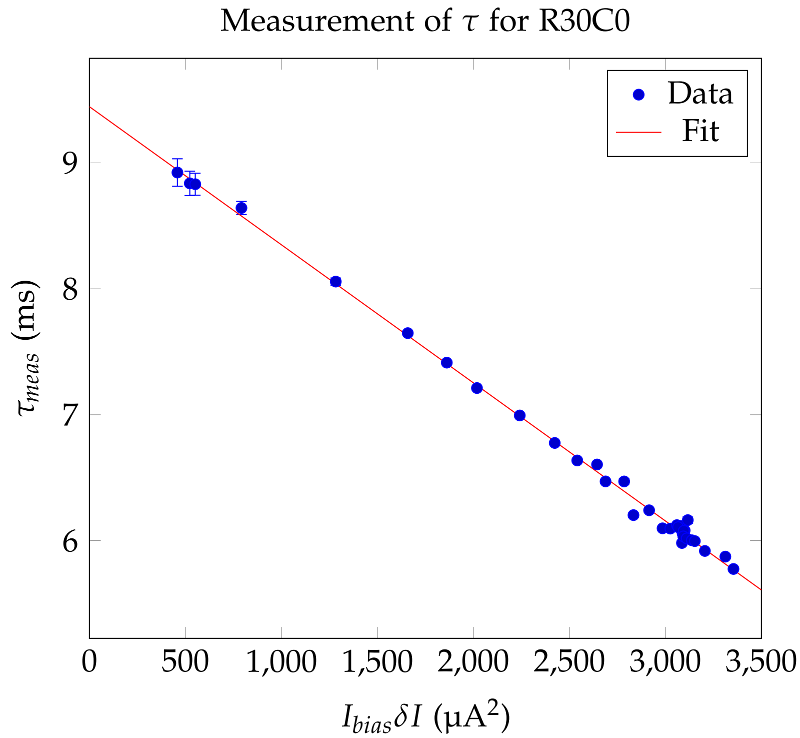

Figure 6.3: Plot showing measurement of natural time constant τ for R30C0. The fit is to Equation 6.4. The y-intercept at $I_{bias}\delta I = 0$ gives $\tau = 9.45$ ms.

all detectors are somewhat faster than the design value, so that the slower natural time constant does not pose any problems for operation of the array.

6.5 Measurement of TES G

With knowledge of the heater resistances, IV curves can be taken over a wide range of bath temperatures, which enables a measurement of the TES thermal conductance G, critical temperature T_C and power-flow index n. I took IV curves at bath temperatures ranging from 995 mK – 1160 mK, while adjusting the applied heater power so that each IV curve had a clear normal branch. Fits were performed against Equation 3.25:

$$P_{htr} + P_J + P_{opt} = \frac{GT_c}{n}\left(1 - \left(\frac{T_b}{T_c}\right)^n\right). \tag{6.5}$$

The parameters to be fit to are G, T_c, and n.

A problem arises because the data described in this section were taken when the cryostat was open, so that P_{opt} was non-zero, with an unknown value. Because P_{opt} is a simple additive constant, it is not possible to fit for this value unless another constraint is known, such as the value of T_c. Unfortunately, the TES circuit bias loop contains Al wire bonds, which have a T_c close to that of the detectors themselves, making a direct measurement of the detector T_c difficult[2].

However, the value of P_{opt} can be estimated in two different ways. First, the predicted optical load of 180 pW from Section 4.2 can be used. Second, optical load on the prototype detectors was estimated to be in the range 135 pW – 165 pW using IVcurve measurements. In this analysis I assume $P_{opt} = 150\,\text{pW}$, while also showing how different assumptions change the values of G, T_c, and n.

Table 6.2 lists the resulting values for G, T_c and n. Figure 6.4 contains a plot of the data and fit for R30C1, as well as scatter plots showing measurements of G, T_c and n. Figure 6.5 shows the effect of different assumptions for P_{opt} on measurements of G and T_c. The uncertainty of G due to varying P_{opt} is about the same size as the statistical uncertainty due to the fit, while the uncertainty of T_c is much larger than the statistical uncertainty. The uncertainty of n shows no apparent trend with P_{opt}. Specifically, a change in P_{opt} from 100 pW to 300 pW increases G by 5.7 %, increases T_c by 2.2 %, and leaves n unchanged.

As discussed in Section 5.2, the target G value for these detectors was 3.7 nW/K. The mean value for the seven measured detectors is $7.35\,\text{nW}\,\text{K}^{-1}$, ~2 times larger than the target. The reason for this discrepancy is not known.

[2]Because the Al wire bond material contains approximately 1 % Si, their T_c is expected to be higher than that the of the elemental Al TES itself. I nevertheless find that the resistance in the TES loop rises to 20 mΩ – 50 mΩ at temperatures above 1175 mK, which is much larger than the normal-state resistance of the TES itself. I interpret this as indicating the Al wire bonds go normal at lower temperatures than the TES.

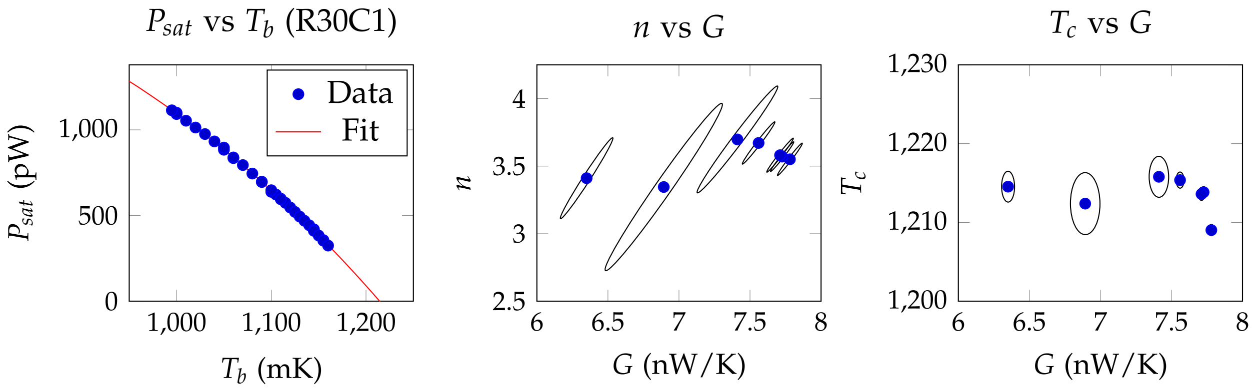

Figure 6.4: Plots summarizing results of G, T_c and n measurements for seven detectors with working heaters. All error bars and ellipses are 95 % confidence intervals for statistical error; any systematic error is not included. **Left** Plot showing P_{sat} vs T_b for R30C1, assuming $P_{opt} = 150\,\text{pW}$. The red line shows the best fit to Equation 6.5. The data covers 25 temperatures from 995 mK – 1160 mK, and 11 different heater biases. **Center** Scatter plot showing correlation between G and n, as well as error ellipses showing covariance between the estimated G and n vales. **Right** Scatter plot showing correlation between G and T_c, as well as error ellipses showing covariance between the estimated G and T_c vales.

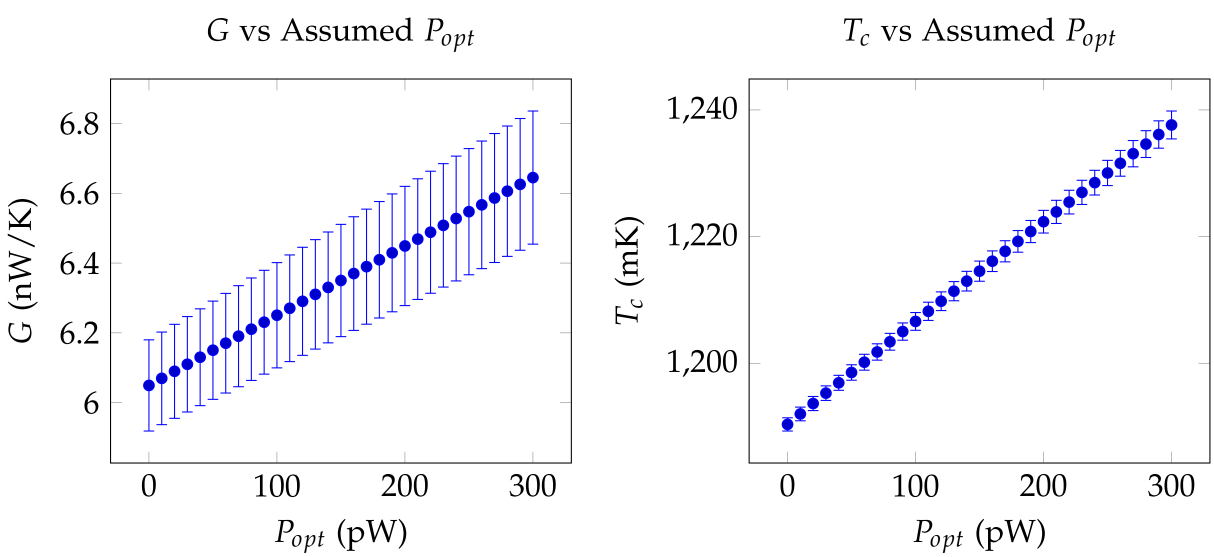

Figure 6.5: Plots showing effect of P_{opt} assumptions on G and T_c measurements. **Left** Plot showing variation of G for R30C1 vs assumed value of P_{opt}. The statistical uncertainty in G for this detector is approximately the same as the systematic uncertainty that results from the estimation of P_{opt}. **Right** Plot showing variation of T_c for R30C1 vs assumed value of P_{opt}. In this case the systematic uncertainty is larger than the statistical uncertainty, although the change is only 2.2 % as P_{opt} increases from 100 pW to 300 pW. The value of n shows no trend with P_{opt}.

6.6 Direct Measurement of Detector Responsivity and τ_{eff}

As discussed in the introduction to this chapter, the detector responsivity $s_I(0)$ is required in order to turn a set of detector timestreams (which area measured in terms of current) into a video image (which is presented in terms of the temperature of the observation target). Knowing the value of the effective detector time constant τ_{eff} can aid in understanding whether or not blurring is a problem in video images, as well as understanding any problems related to instability of a detector.

This section gives direct measurements of $s_I(0)$ and τ_{eff} for the seven detectors with working heaters. In addition to their intrinsic interest, these measurements are used in Section 6.7 as a check on the procedure used to estimate $s_I(0)$ and τ_{eff} for detectors without heaters.

Knowledge of R_{htr} allows a direct measurement of the DC responsivity and τ_{eff} for the seven detectors with heaters. Steps in heater bias current were applied to these detectors under SOC. The step size was made small so as to keep the detector response linear, and the response to many steps was averaged together to reduce noise. The result was fit to Equation 3.12:

$$\delta I(t) = -\delta P_{htr} s_I(0)(1 - e^{-t/\tau_{eff}}). \tag{6.6}$$

Figure 6.6 shows a sample fit to Equation 6.6. Table 6.3 lists the best-fit values of $s_I(0)$ and τ_{eff}.

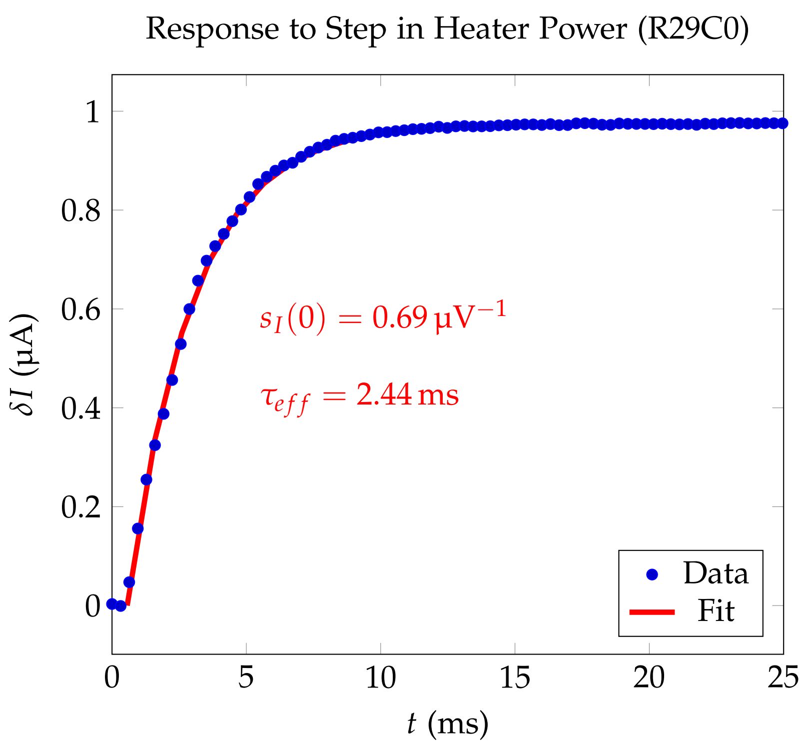

Figure 6.6: Plot showing response of detector R29C0 to step in applied heater power of 1.41 pW. Plots are for R29C0 biased into SOC. The data averaged over 32 steps (16 up and 16 down), along with best fit to Equation 6.6, are plotted. The step in applied power begins at $t \approx 0.6\,\mathrm{ms}$, not $t = 0\,\mathrm{ms}$.

Table 6.3: Detector properties while biased into transition. $P_{opt} = 150\,\mathrm{pW}$ is assumed everywhere. Values are for detectors under SOC. "N/A" indicates a property that has not been measured for that detector.

Detector	$s_I(0)$ (μV^{-1})	τ_{eff} (ms)	R (mΩ)	R/R_n	$\mathcal{L}_I$	α	β_I
R28C0	0.612	3.17	3.51	0.80	2.6	59	0.32
R29C0	0.691	2.44	3.34	0.76	4.0	90	0.45
R30C0	0.605	3.25	3.25	0.71	2.9	66	0.44
R31C0	0.687	2.81	2.72	0.62	8.9	155	1.98
R28C1	0.663	2.83	N/A	N/A	N/A	N/A	N/A
R30C1	0.731	2.44	N/A	N/A	N/A	N/A	N/A
R31C1	0.681	3.24	N/A	N/A	N/A	N/A	N/A

6.7 Measurements of Loop Gain and TES Current Sensitivity

As described in Section 3.2, steps in the applied bias current ("bias step" measurements) can be used to measure the detector parameters loop gain $\mathcal{L}_I$, current sensitivity β_I and bias value resistance R_0 for a detector. These parameters are then used to predict $s_I(0)$ and τ_{eff}. In order to make this measurement, the data acquisition rate must be fast enough to track the fast electrical response of the TES. In addition, the servo roll-off must be either fast enough not to affect the electrical response, or the effect of the servo roll-off must be included in the fit.

I took measurements at 15,625 Hz, which is fast enough to track the electrical response. I found that the servo roll-off was too slow to be ignored for many detectors, so the function to be fit to is Equation 3.16 after being passed through a single pole lowpass filter and including τ_{servo} as an additional fit parameter. The data was taken at eight bias DAC values.

Figure 6.7 and Figure 6.8 show the results of these measurements for the four detectors on column 0 with working heaters. The response to many steps is averaged together. The fits are generally good, but at some bias values a damped oscillatory response is present on top of the expected Equation 3.16 response. The source of this is not understood; two possible explanations are the presence of an additional "dangling" heat capacity in the electrothermal circuit of Figure 3.1 [87–89], or non-smooth structure in the detector's $R(T, I)$ curve.

Once values for $\mathcal{L}_I$, β_I and R are known, the DC responsivity $s_I(0)$ and τ_{eff} can be calculated from Equation 3.7 and Equation 3.9 respectively. To check the accuracy of these calculations, I also measured the response of the detectors to steps in applied heater power at the same bias values for four of the seven detectors. The results of these measurements, as well as the ratio of the calculated to measured values, are shown in Figure 6.9. The agreement between the calculated and measured values is good, indicating that response to detector "bias step" measurements can be used to predict $s_I(0)$ and τ_{eff} with good accuracy. This is important because only a few detectors have working heaters, making direct measurements of $s_I(0)$ and τ_{eff} impossible for most detectors.

"Bias step" measurements were also taken for all working detectors at SOC. Figure 6.10 summarizes these measurements of $\mathcal{L}_I$, β_I, and R, both in terms of histograms for each parameter as well as scatter plots showing covariance between them. Figure 6.11 shows

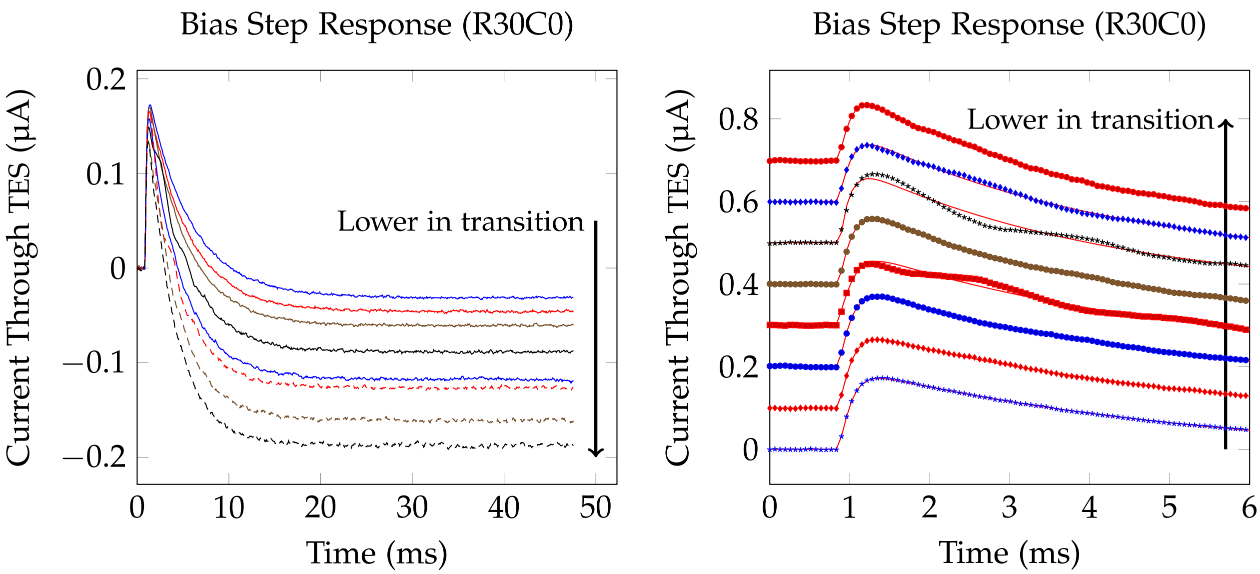

Figure 6.7: Plots showing response of a detector to a step function in applied bias current. **Left** Response of R30C0 as a function of time to step function in applied bias current, at a range of bias values. In all cases there is a rapid increase in the TES current followed by a slow decay to the final current, which for these bias values is always less than the initial current. This drop in current is a result of electrothermal feedback. As the detector is biased deeper into the transition the decrease in current becomes larger, as a consequence of increasing loop gain and decreasing bias voltage; see Equation 3.7. **Upper Right** Close-up view of initial stage of detector response. Both the data and the best-fit curve to Equation 3.16 are shown, and the responses are offset vertically for clarity. At some bias values a damped oscillatory response is present on top of the Equation 3.16 response; the source of this is not understood.

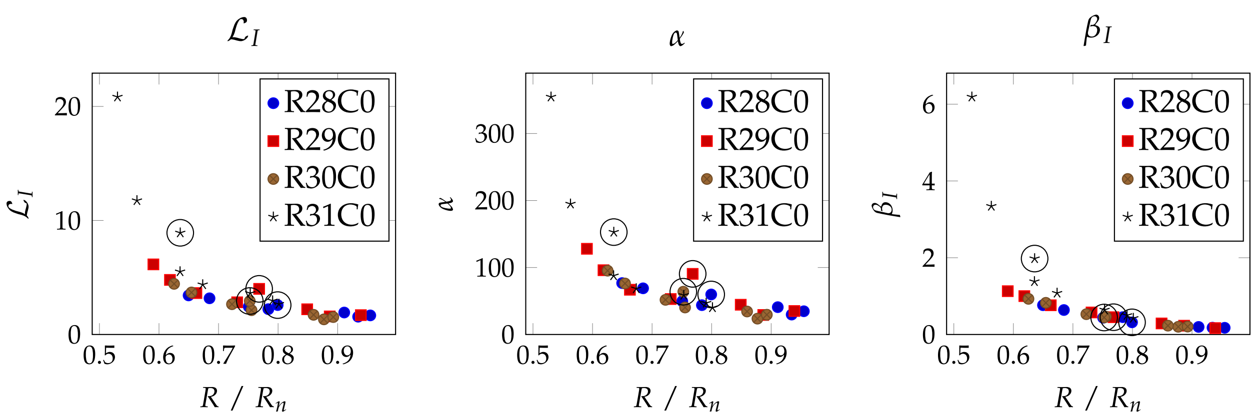

Figure 6.8: Plots showing results of fits for the four detectors tested at various bias values in this section. The circled points are for SOC.

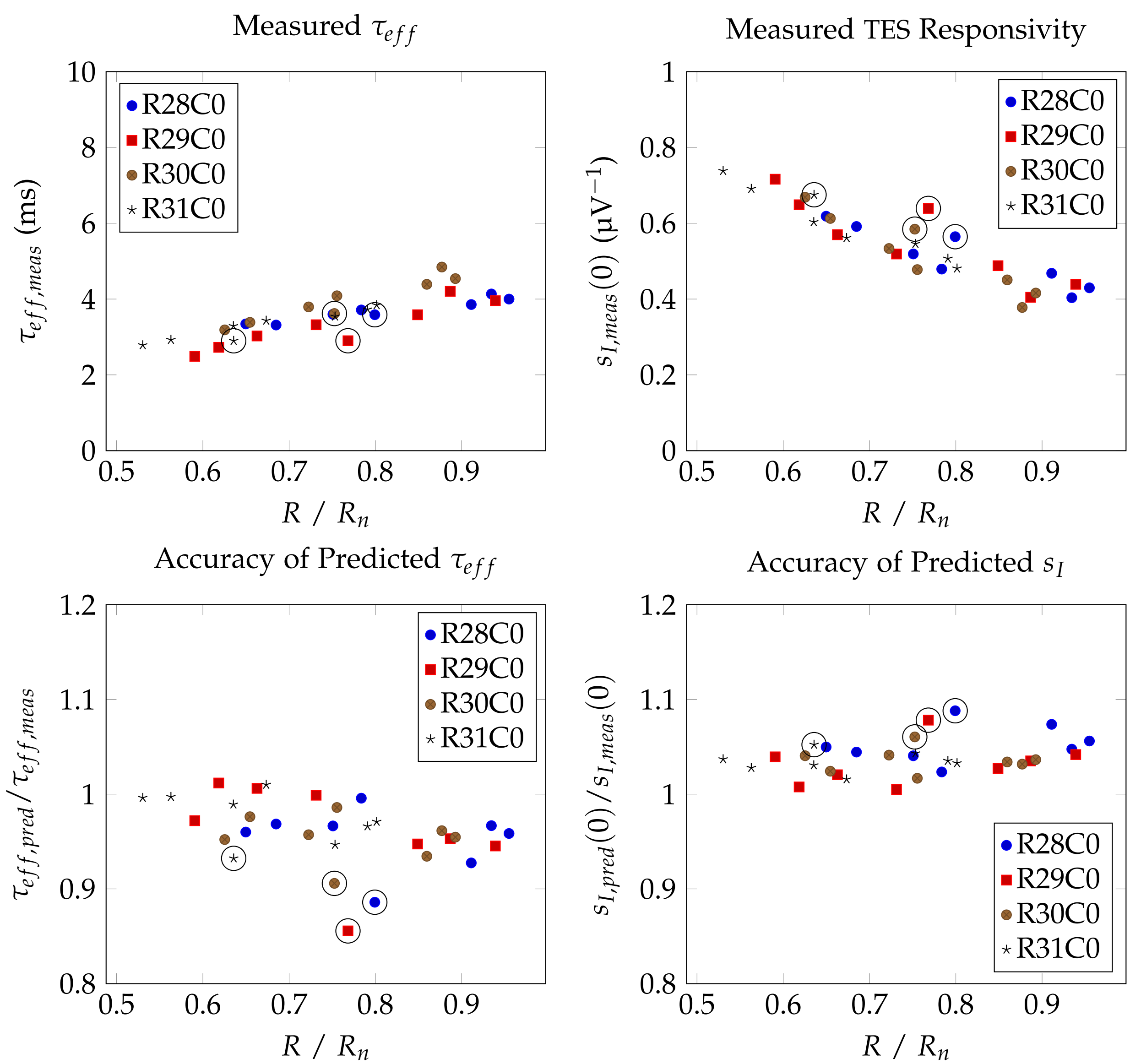

Figure 6.9: Plots showing measurements of detector response times τ_{eff} and responsivity $s_I(0)$ for the four detectors of column 0 with working heaters. The circled points are for the SOC. **Upper Left** Measurements of τ_{eff} for a range of bias value. **Upper Right** Measurements of $s_I(0)$ for a range of bias values. **Lower Left** Comparison of predicted and measured τ_{eff} for the same detectors. **Lower Right** Comparison of predicted and measured $s_I(0)$ for the same detectors.

histograms of the resulting predictions for τ_{eff} and $s_I(0)$. The predicted values of $s_I(0)$ are used in Section 7.7 to establish a temperature scale for imaging. 78 % of the working detectors have $\tau_{eff} < 2\,\text{ms}$. The detectors are, on average, somewhat faster than the 2.6 ms design value — due to somewhat higher than anticipated values of $\mathcal{L}_I$ at SOC — but not fast enough to eliminate blurring as a concern. The measurements of this chapter will allow more aggressive τ_{eff} design decisions for future detector fabrications, reducing the problems of blurring.

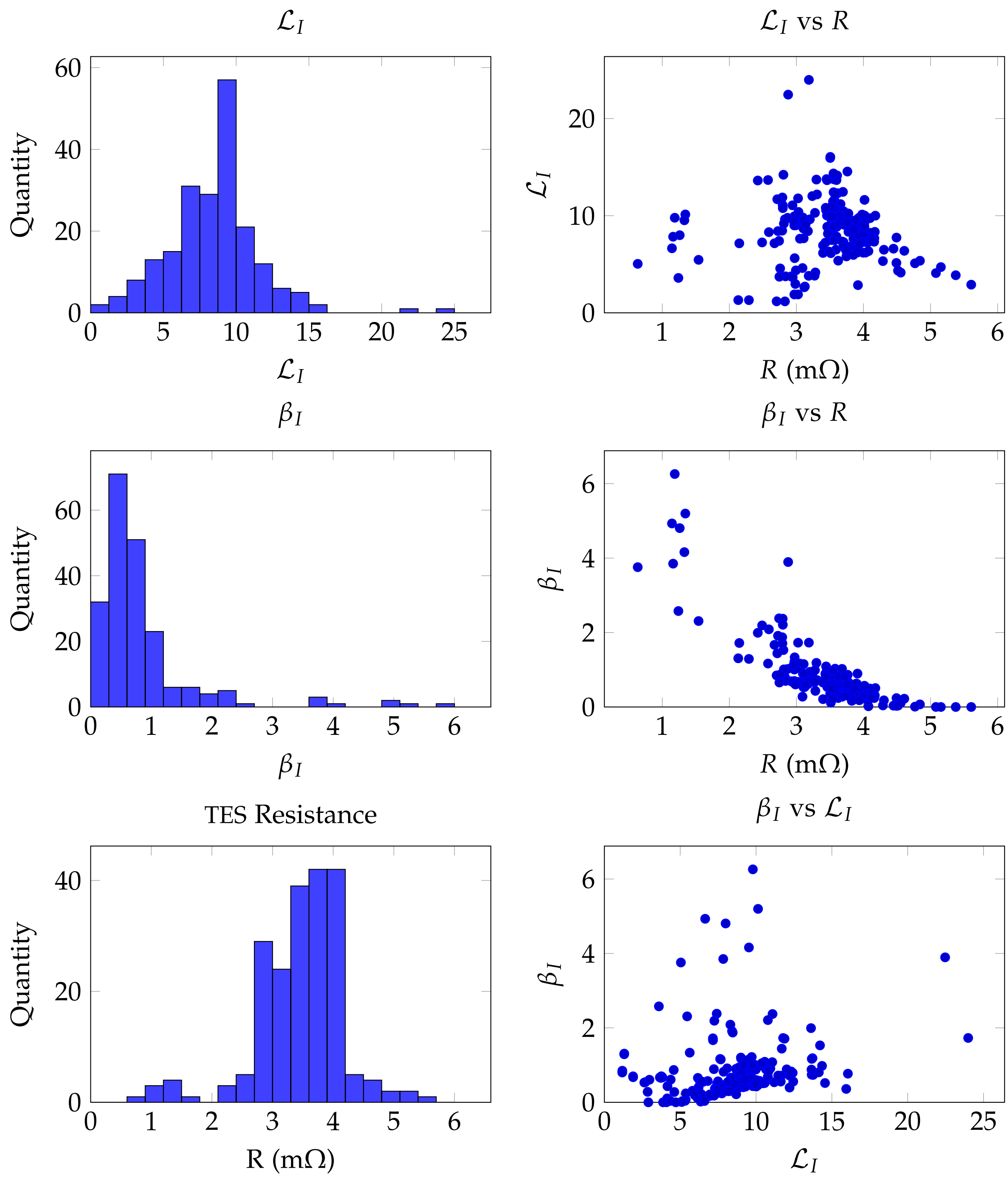

Figure 6.10: Plots summarizing results of "bias step" measurements for all working detectors. All data taken at SOC. **Left Plots** Histograms showing measured values of $\mathcal{L}_I$, β_I and R. **Right Plots** Scatter plots showing how the three parameters $\mathcal{L}_I$, β_I and R correlate with each other. Note that R is plotted, not R/R_n. This is because R_n is known only for those detectors on columns 0 and 1 with working heaters (see Section 6.3).

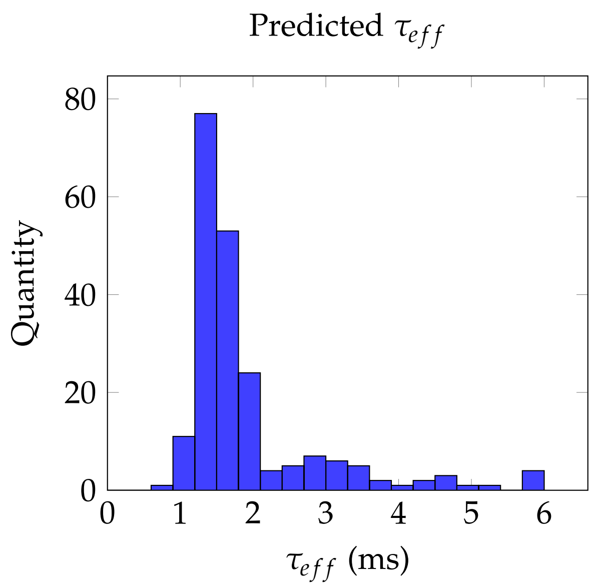

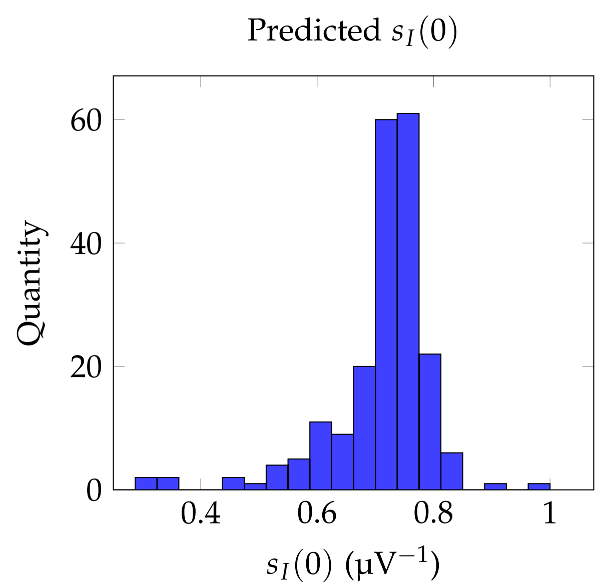

Figure 6.11: Plots showing distribution of predicted τ_{eff} and $s_I(0)$. The predictions use Equation 3.9 and Equation 3.7, with the values for R, $\mathcal{L}_I$and β_I shown in Figure 6.10, and R_{sh} values from Section 6.2. R_p is assumed to be zero in all cases.

6.8 Common Mode Signal and $1/f$ noise

Our detectors have significant $1/f$ noise, with a 3 dB knee of ~0.7 Hz. Most of this noise is due to bath temperature fluctuations which are uncontrolled by the Cryocon PID loop. Figure 6.12 contains plots summarizing this common-mode signal and $1/f$ noise. The upper left plot shows raw 10 minute detector timestreams for 15 detectors. The common mode signal is evident in these plots, and is much stronger than the white noise at frequencies of 1 Hz and slower. The upper right plot shows the same detector timestreams after removal of the mean of all "good" timestreams for columns 0 and 1 (the only columns which were biased for this test). The large reduction of $1/f$ noise is evident in this plot. The lower left plot shows direct evidence for this via the current noise power spectral density both before and after subtracting the common mode. Also plotted is the power spectral density after subtracting first the common mode and then the best-fit 4th order polynomial from the raw detector timestream. Subtracting the 4th order polynomial does reduce noise at very low frequencies, but the effect is small.

The power spectral density plot has two important features. First, a strong noise peak is located at 1.411 Hz. This is caused by the ~1.4 Hz cycle of the PTC; the physical mechanism could either be microphonic pickup of the vibrations caused by the PTC cycle, or variation in bath temperature induced by the cycle. This signal can be removed either through a common-mode subtraction scheme or a notch filter. Second, the detector noise signal is unaffected by the common mode signal at frequencies faster than 2 Hz. Because the frame rate of the video system is 6 FPS or faster, this indicates that the only impact of the strong common-mode noise signal on videos is the need to account for a time-varying detector offset. Our approach to dealing with this offset is covered in Section 7.8.

The lower right plot in Figure 6.12 shows the detector timestream for R28C0, translated into variation in bath temperature. We can define a differential thermal conductance relative to changes in bath temperature G_b via

$$G_b \equiv \frac{dP_b}{dT_b} = G\left(\frac{T_b}{T}\right)^{n-1}. \tag{6.7}$$

Then the equivalent bath temperature change for a given TES current change will be given by

$$\Delta T_b = \frac{\delta I}{s_I(0)G_b}. \tag{6.8}$$

For this test the bath temperature was set to 1100 mK, so the implied temperature variations over several-minute timescales are a few parts in 10^4.

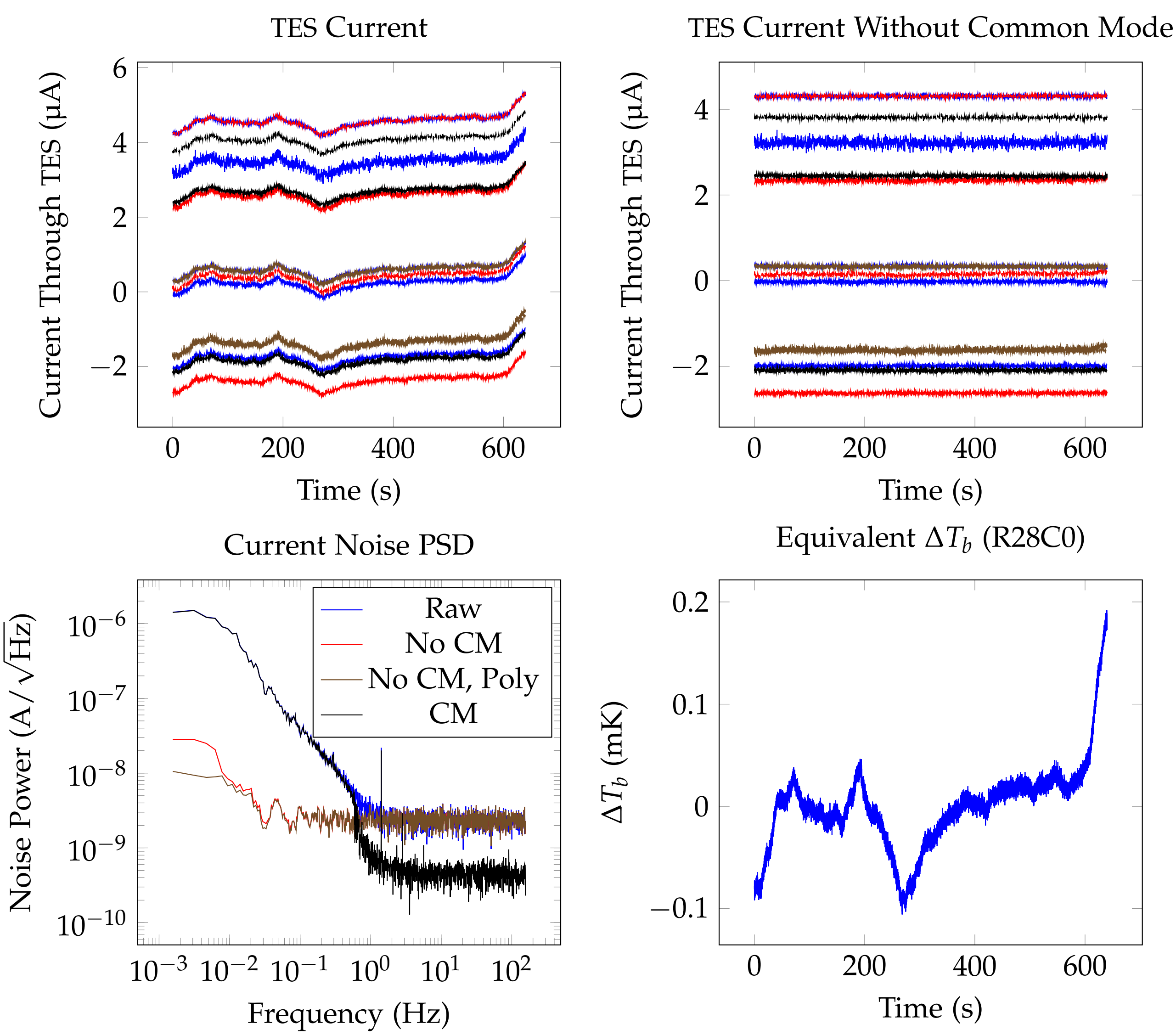

Figure 6.12: Plots summarizing common mode signal and $1/f$ noise. **Upper Left** Plot showing raw detector output for 15 detectors over a 10-minute data acquisition. The data was acquired at 312.5 Hz, but only every 100th data point is plotted. **Upper Right** The same data after removal of the common mode signal (as defined in the text). **Lower Left** Current noise power spectral density for the raw data, the raw data minus the common mode ("No CM"), the raw data minus the common mode and the best-fit 4th-order polynomial ("No CM, Poly"), and the common mode itself ("CM"). The strong noise peak at 1.411 Hz is due to the PTC, as explained in the text. **Lower Right** Raw timestream for R28C0, after conversion to an equivalent bath temperature variation, as described in the text.

6.9 Microphonic Pickup

TES detectors can be prone to microphonic pickup. The earliest version of the cryostat used for this project used a Gifford-McMahon (GM) cryocooler, which vibrates the cryostat significantly more than a PTC does. The prototype detectors had significantly higher noise levels with the GM cooler running than when it was off; in addition, the detector noise could be directly increased by striking the side of the cryostat with a soft mallet while the GM cooler was turned off. I interpreted this behavior as evidence for microphonic pickup, and as a result replaced the GM cooler with a PTC.

To check whether microphonic pickup was present for the production detectors and the PTC, I took noise data both with the PTC running and turned off. In both cases the bath temperature was held steady at 1100 mK using the Cryocon temperature controller. Common mode noise was removed and power spectra for each detector were calculated. Then the excess noise for each detector was calculated as

$$\sqrt{\frac{\sum_{f\geq 6} S^2_{I,\text{PTC}}(f)}{\sum_{f\geq 6} S^2_{I,\text{No PTC}}(f)}} \tag{6.9}$$

where $S^2_{I,\text{PTC}}$ and $S^2_{I,\text{No PTC}}$ are the measured current noise power spectral densities with the PTC turned on and off, expressed in units of A^2 /Hz.

Figure 6.13 shows a histogram of this excess noise. Most detectors have higher noise with the PTC on, but the mean excess noise is only 1 %. The figure also contains a plot of the power spectral density for R28C0 with the PTC on and off.

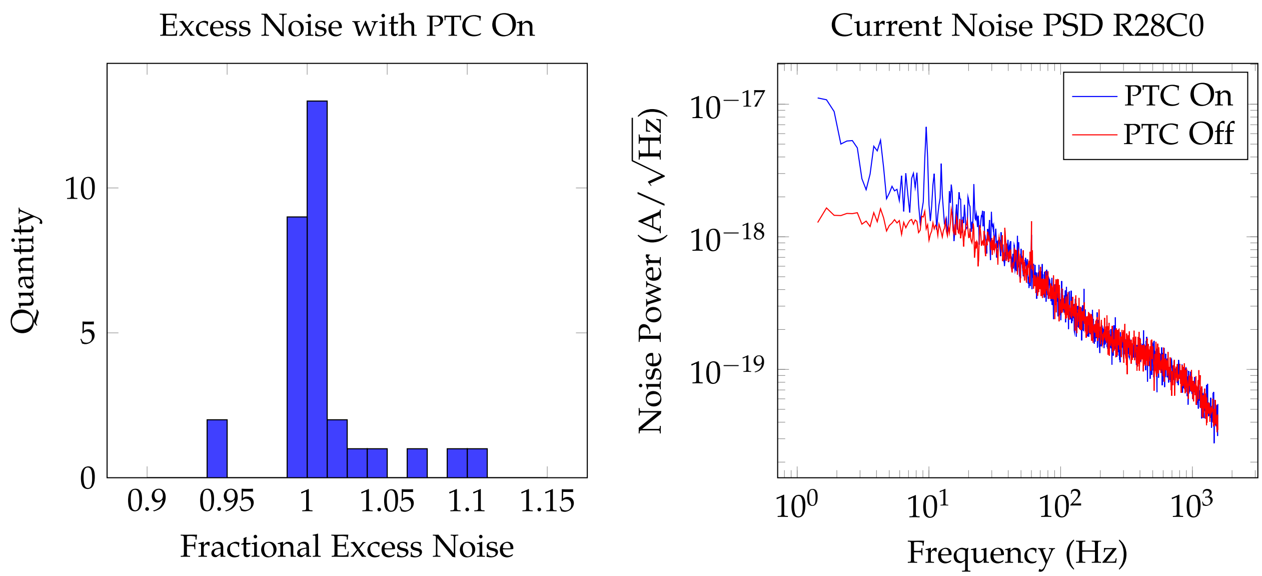

Figure 6.13: Plots showing impact of PTC on noise. **Left** Histogram showing excess noise due to the PTC, defined as ratio of total noise above 6 Hz (see text for precise definition). More detectors have higher noise with the PTC on than off, but the mean excess noise is only 1 %. **Right** Current noise for R28C0 with PTC on and off, after subtracting common mode noise. The noise below 30 Hz is 1.5–2.5 times higher with the PTC on, but the total noise at the relevant frequencies of $f >= 6$ Hz is only 2.9 %.

6.10 Noise Aliasing

As explained in Section 4.7, the MCE takes data at 15,625 Hz, but is only capable of sending data for the 251-detector sub-array to the readout computer at 3125 Hz. To reduce noise aliasing, the MCE can be configured to apply a 4-pole digital lowpass filter to the 15,625 Hz data stream prior to sampling at `data_rate` [78]. I have not yet implemented this filter, but plan to do so for future operation of the system.

To investigate how much noise is aliased from the 3125 Hz – 15,625 Hz band to below 3125 Hz in the absence of the MCE's digital lowpass filter, I acquired data under SOC for column 0 at the normal rate of 3125 Hz as well as at 15,625 Hz. Five data files were acquired for each case. For each row in column 0 and for each data file a power spectrum was taken after subtracting the common mode signal, and the excess noise was calculated as

$$\sqrt{\frac{\sum\limits_{6\leq f\leq 1562.5} S^2_{I,3125}(f)\Delta f}{\sum\limits_{6\leq f\leq 1562.5} S^2_{I,15625}(f)\Delta f}} \tag{6.10}$$

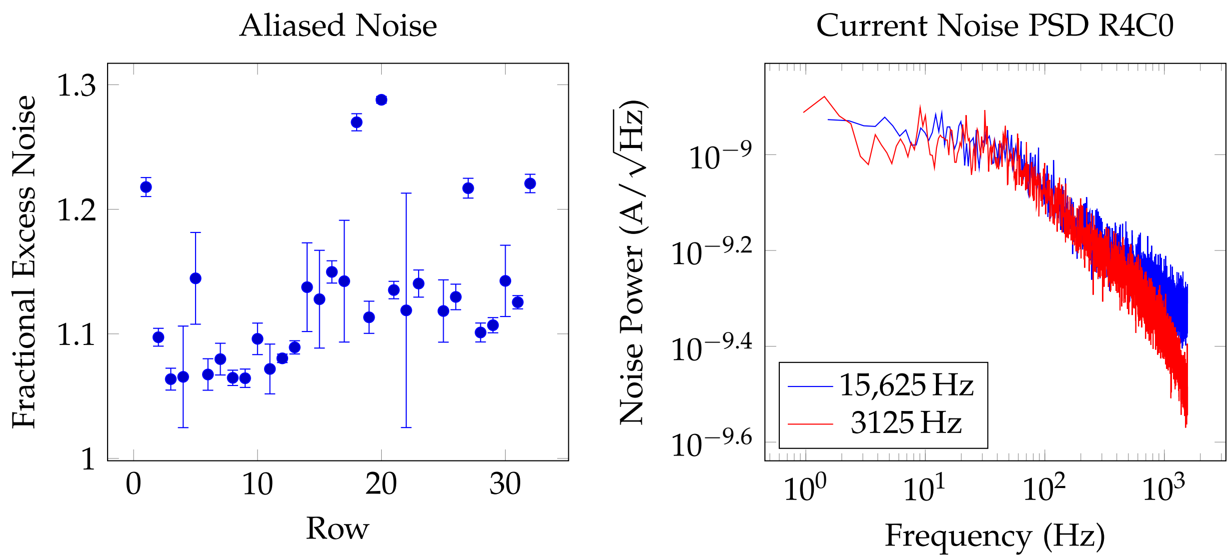

Figure 6.14: Plots showing impact of noise aliasing. **Left** Plot showing fractional excess noise (see text for definition) due to noise aliasing for all rows of column 0. The error bars are for 95 % confidence intervals, and the median excess noise is 12 %. **Right** Sample power spectra at 3125 Hz and 15,625 Hz for R4C0. For this detector the excess noise is 17 %.

where $S^2_{I,3125}$ and $S^2_{I,15625}$ are the measured current noise power spectral densities at the two different multiplexing rates, averaged over all 5 data files, expressed in units of A^2 /Hz. The sums are performed only over those frequency components in the range 6 Hz – 1562.5 Hz, and note that Δf is different for the two sampling rates.

Figure 6.14 summarizes the results. The average excess noise due to aliasing is 16 %, but some detectors have statistically significant higher levels of aliased noise; for example, R19C0 has 29 % excess noise.

The servo feedback parameter for these acquisitions was $I_{FB} = 50$, but when taking video images I_{FB} is typically set to 10 or 20. Because the slower servo feedback will roll off noise above 3125 , the level of aliased noise will be lower under these configurations.

6.11 Detector Noise

While taking the $\mathcal{L}_I$and β_I measurements described in Section 6.7, I also took noise data for the four detectors with working heaters on column 0. For each data acquisition the common mode signal was subtracted and the power spectra calculated using MATLAB's `pwelch` function. Figure 6.15 shows the resulting power spectra, both in terms of the directly measured current noise S_I^2, as well as in terms of noise referred to power absorbed in the bolometer, S_P^2. S_P^2 is calculated via

$$S_P^2 = S_I^2 / s_I(0), \tag{6.11}$$

where here the DC detector responsivity $s_I(0)$ is calculated using the measurements described in Section 6.7.

Also plotted is the predicted detector noise level for each detector at each bias value, using a "basic" noise model. This basic noise model uses the values of τ_{eff} and s_I calculated in Section 6.7, and the values of G and T_c measured in Section 6.5, assuming 150 pW of optical power. All three sources of detector noise from Section 3.7 are included. The predicted photon noise level of 0.85 fW/$\sqrt{\text{Hz}}$ from Section 5.8 is also included.

Several features are visible in these plots. First, R29C0 shows several noise lines, the origin of which is not understood. Second, for all four detectors the spread of noise levels in the range 1 Hz – 20 Hz is much smaller when referred to power absorbed on the bolometer than in terms of current noise. This is the expected behavior for a noise source that adds power directly to the bolometer. When expressed in terms of power absorbed in the bolometer, such noise will be the same at all bias values. But because detector responsivity changes with bias value, the noise level will be different when expressed in terms of current. Third, the shape of the noise curves are roughly as expected, with noise roll-offs happening at approximately the correct frequencies. Fourth, the measured noise levels are much higher than the predicted noise levels. R28C0 is 1.9 times higher, R29C0 is 5.8 times higher (dominated by the noise spikes), R30C0 is 1.7 times higher and R31C0 is 1.6 times higher.

The reason for this high level of noise is not known. One possible culprit is a higher than expected level of photon noise. Figure 6.16 plots the measured noise spectrum for R30C0 at SOC, along with the basic noise model and a noise model that includes enough additional photon noise to match the measured white noise level at low frequencies (photon noise level that is 1.9 times higher than predicted). A problem with explaining the noise spectra this way is that the measured spectrum shows a shelf at 100 Hz – 1000 Hz which is not present in any of the models.

Excess photon noise could be due to IR power leaking onto the detectors. Even a small amount of IR power can increase noise levels through the ν factor in Equation 3.33. It is also possible that a much higher level in-band optical power is falling on the detector than predicted. This would both increase the photon noise directly, and increase the predicted thermal fluctuation noise because of the link between assumed optical power and my measurements of G and T_c as discussed in Section 6.5.

Another possible explanation is a poor calibration of the readout system, so that the "real" current noise is ~ 2 times lower than measured. However, this would reduce the measured values of R_{sh} and L_{ny} by a factor of $2^2 = 4$. This is unlikely, because the measured values are close to the design values, and these design values have been confirmed by measurements of other interface chips of the same design[3].

I therefore conclude that the high level of detector noise is real, but I do not yet have a full explanation for the high values. Section 8.1 describes steps that can be taken to understand the source of this excess noise.

[3]John Appel, personal communication

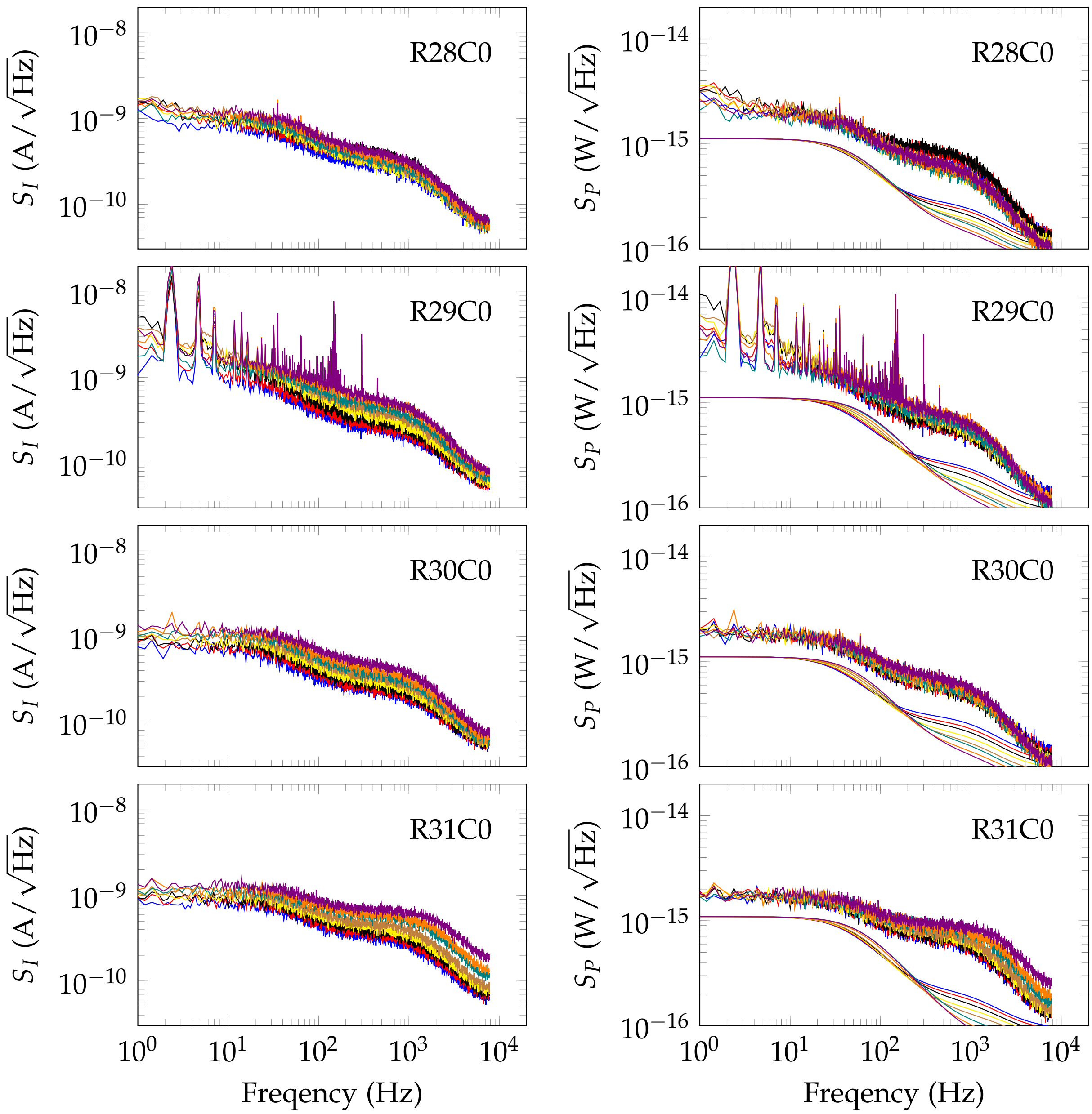

Figure 6.15: Plots showing detector noise for the four detectors with working heaters on column 0. The left column plots the directly measured current noise, after removing a common mode signal, at eight bias values from 25k to 32k. The right column shows the same noise spectra, but referred to power absorbed in the bolometer. For all four detectors, there is less spread in the low-frequency power noise than in the current noise, suggesting that the dominant source of noise at these frequencies deposits power on the bolometers. This behavior is expected of either thermal fluctuation noise or photon noise. Also plotted in the right column is the predicted noise spectrum, using parameters taken from Section 6.7, including $0.85\,\text{fW}/\sqrt{\text{Hz}}$ of photon noise. For all four detectors, the measured noise is higher than predicted by the noise model.

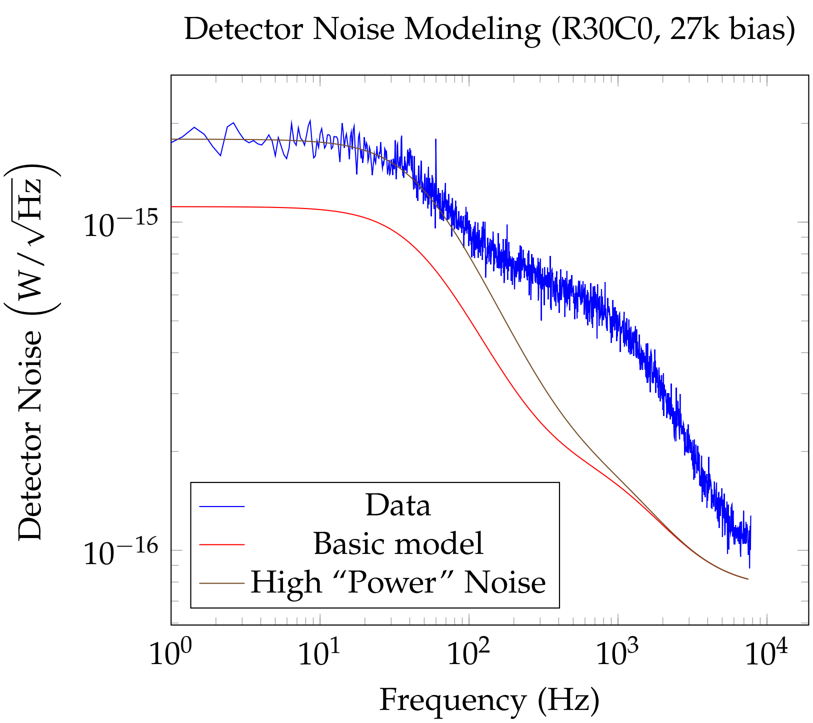

Figure 6.16: Plot showing measured noise for R30C0, referred to power absorbed in bolometer, along with two noise models. The red line is the basic detector noise model using measured values for all detector parameters as described in this chapter, including predicted $0.85\,\mathrm{fW}/\sqrt{\mathrm{Hz}}$ of photon noise. The black line is for a noise model that include enough excess photon noise to match the measured white noise level at low frequencies (1.9 times higher than predicted).

Chapter 7

Imaging

This chapter describes the process of producing videos from detector timestreams, as well as measurements required to support that process. I start with a brief description of which detectors are not used due to problems with their performance (Section 7.1). I then describe how we read out the position of the secondary mirror (Section 7.2), which controls where detectors are pointed at a given time, followed by a description of how we determine the focal distance, determine where each beam is pointing in the far-field, and the distance scale (Section 7.3–Section 7.5). I also present measurements of the optical efficiency of the system (Section 7.6) and a temperature scale calibration (Section 7.7). The algorithm used to produce video (and still) images is described in Section 7.8, and a discussion of the NETD in the images is in Section 7.9.

7.1 Detector Cuts

Approximately 16 % of the detectors in the first sub-array can not be used to generate images. For some detectors, the membranes are broken. Others appear intact upon visual inspection, but show no response to applied current even in the superconducting state. Others work as expected while superconducting, but can not be biased so as to show a response to changes in optical power. And some are extremely noisy or consistently show other problems in the data stream. Figure 7.3 and Figure 7.4 contain plots summarizing this information graphically, organized by detector position on the wafer and by readout row/column respectively.

To determine which detectors show no response in the superconducting state, the temperature of the focal plane was set to 975 mK, well below the T_c of the detectors. The

TES bias current was ramped, and data was acquired while running the readout system open-loop. As an example, Figure 7.1 shows the resulting data for rows 0 – 4 of all columns. Most row/column combinations show a response that maps out the V-Φ curve for the SQUID amplifier chain. The row/column combinations that show no response indicate either a broken detector line, a broken SQUID on a multiplexing chip, broken wire bonds, or some other problem in the readout system.

Another group of detectors remain superconducting at the chosen bias point and operating temperature of 1100 mK. This could be caused by an abnormally high G and/or T_c value, or by a short between the TES leads after the shunt resistor. Figure 7.2 shows the result of ramping the TES bias current over a small range while running the readout system open-loop, and while the detectors are biased at SOC.

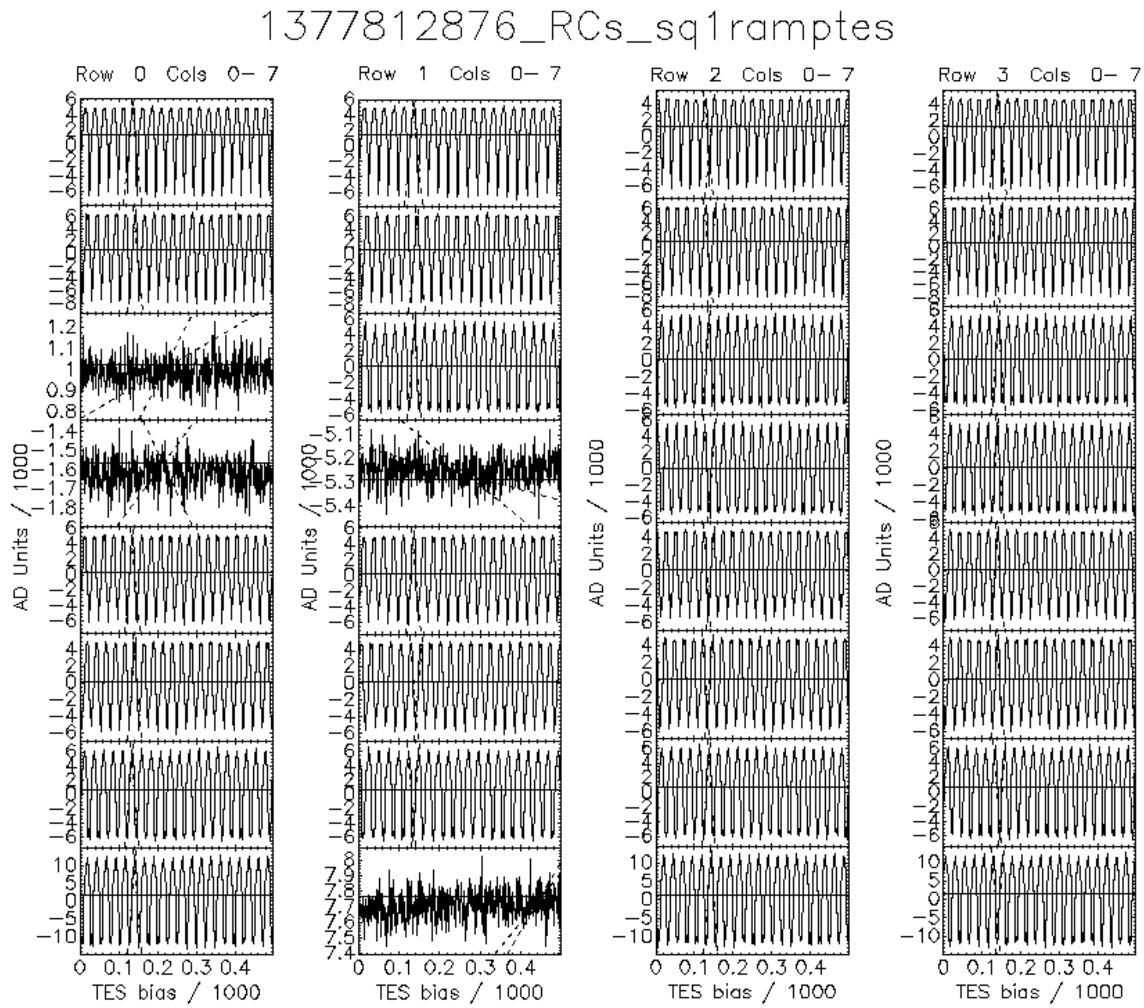

Figure 7.1: Plot showing response of SQUID amplifier chain to a ramp in the TES bias current, while TES is superconducting. Data is shown for rows 0–4 for all eight columns. R0C2, R0C3, R1C3, R1C7 all show no response, only noise (note the change in vertical scale for these rows/columns). The vertical axis is in Analog-to-Digital-Converter units for the output of the SQUID amplifier chain. The horizontal axis is the applied TES bias current in DAC units.

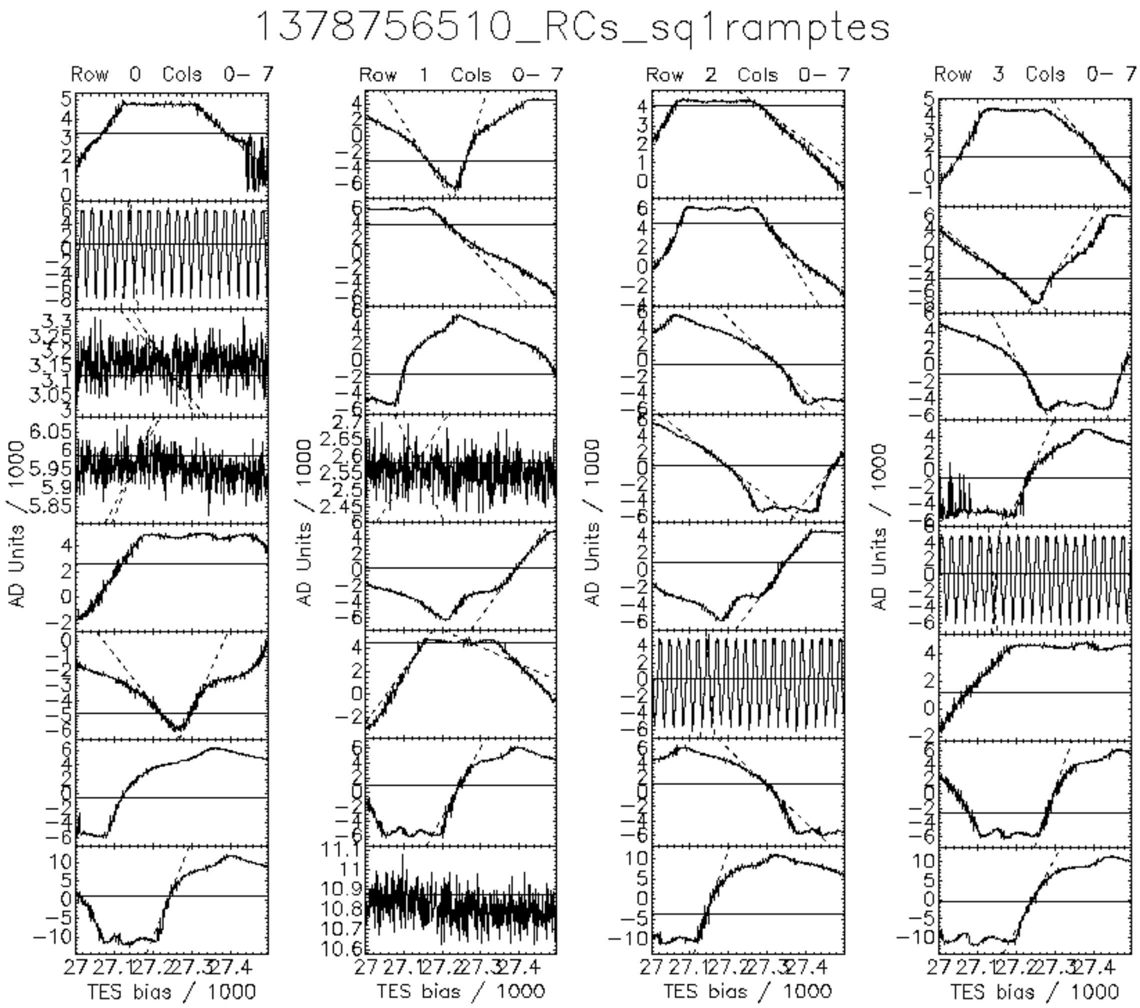

Figure 7.2: Plot showing response of SQUID amplifier chain to ramp in TES bias current, while TES is biased into transition. The total change in applied bias current is the same as in Figure 7.1. Data is shown for rows 0–4 for all eight columns. R0C2, R0C3, R1C3, R1C7 all show no response, only noise (note the change in vertical scale for these rows/columns). R0C1, R2C5 and R3C4 all respond as if they were still superconducting (see Figure 7.1). For the other detectors, the much slower mapping of the V-ϕ curve indicates a much higher resistance in the TES circuit loop, due to the TES sitting in the transition to the normal state. The axis units are the same as in Figure 7.1.

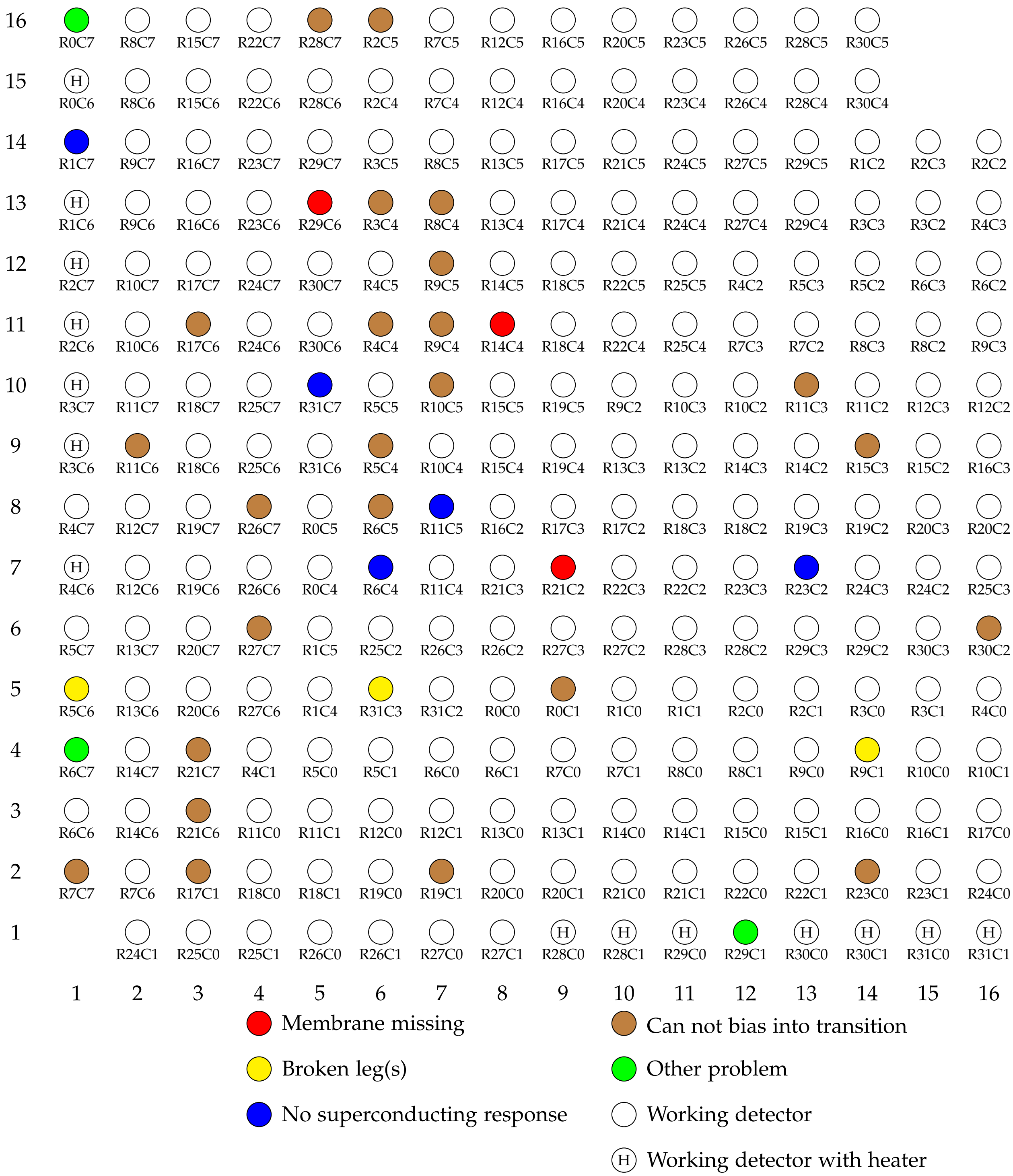

Figure 7.3: Figure showing detector layout on the wafer, highlighting which detectors have problems and which are working. Each detector is labeled (below) with its row/column. The x and y position indices of the detectors on the wafer are also shown.

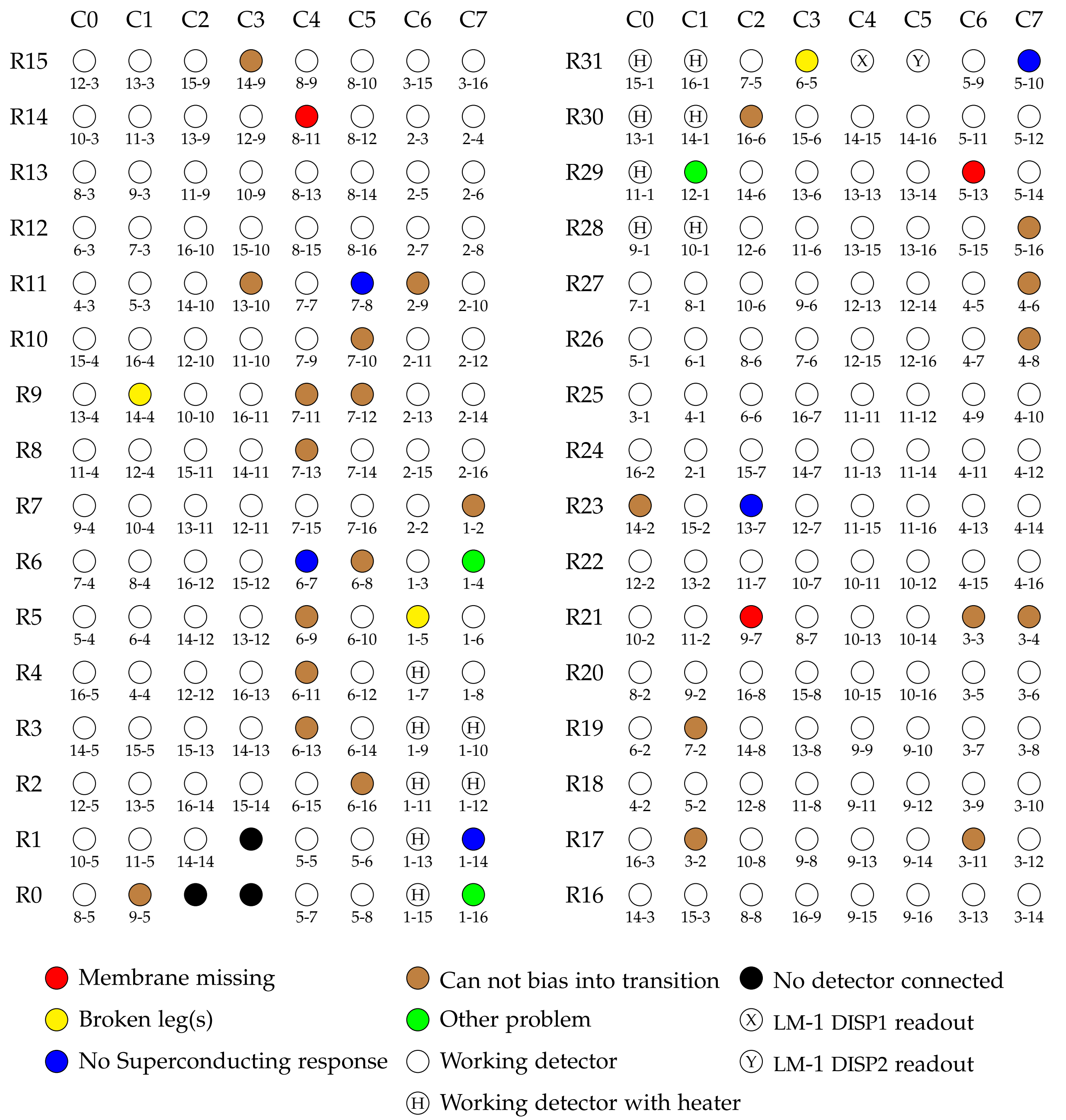

Figure 7.4: Figure showing same information as Figure 7.3, but organized in term of readout rows/columns. Each detector is labeled (below) with its position on the detector wafer. The row/column numbers are labeled on the left and top. Unused rows/columns as well as the rows/columns used to read out the position of the secondary mirror are also indicated.

7.2 Readout of Mirror Position

The 350 GHz Video Imager produces a time-ordered data stream ("timestream") containing the output of each detector as a function of time. In order to turn this timestream into a video, we must know where the optical system is pointing at all times. This section describes how this pointing information is recorded in the timestream data by the 350 GHz Video Imager. It is also necessary to know where each detector is pointed relative to the optical boresight position; this relative detector pointing information is extracted from beam maps, as discussed in Section 7.4.

The pointing of the optical system is determined by the positions of the two LM-1 actuators — DISP1 and DISP2 — that move the secondary mirror[1]. The actuator control hardware provides two voltage signals which are proportional to the positions of the actuators. This voltage signal is sent into the 350 GHz Video Imager cryostat by a pair coaxial cables. Inside the cryostat two 1 m long Phosphor Bronze AWG36 twisted pair wires carry the signal to the focal plane, where the signal is fed into the input coil of a 1st stage SQUID. Series resistors at room temperature (4.23 MΩ for DISP1, 4.36 MΩ for DISP2) are used to reduce the maximum current flowing through the wires to ~2 μA, which is a value appropriate for the 1st stage SQUID input.

This approach synchronizes the actuator position readout with the detector response, and allows both types of information to be read out by the same warm and cold electronics.

To convert the mirror output current to actuator displacement I configured the LM-1 actuators to move in sine-wave patterns with a frequency of 0.1 Hz. I fit the amplitude of the mirror output current to a sine wave; the ratio of the command displacement amplitude to the mirror output current amplitude gives the desired conversion factor. This procedure was carried out for eight different actuator displacement amplitudes ranging from 0.25 mm – 3.5 mm. The results are conversion factors of 2.93 mm μA^{-1} for DISP1 and 3.02 mm μA^{-1} for DISP2, with results for the different command amplitudes in excellent agreement.

To convert actuator displacement to displacements in the far-field of the system, we use Equation 5.8 and Equation 5.9, substituting $d = I \times$ conversion factor:

$$\Delta x = F_d \frac{\sqrt{2}}{2} \left(I_{\mathrm{DISP1}} \times \frac{2.93\,\mathrm{mm}}{1\,\mu\mathrm{A}} - I_{\mathrm{DISP2}} \times \frac{3.02\,\mathrm{mm}}{1\,\mu\mathrm{A}} \right) \times \frac{0.276^\circ}{1\,\mathrm{mm}} \times \frac{19.33\,\mathrm{cm}}{1^\circ} \qquad (7.1)$$

[1]See Section 4.2

$$\Delta y = F_d \frac{\sqrt{2}}{2} \left(I_{\mathrm{DISP1}} \times \frac{2.93\,\mathrm{mm}}{1\,\mu\mathrm{A}} + I_{\mathrm{DISP2}} \times \frac{3.03\,\mathrm{mm}}{1\,\mu\mathrm{A}} \right) \times \frac{0.276^\circ}{1\,\mathrm{mm}} \times \frac{19.33\,\mathrm{cm}}{1^\circ} \tag{7.2}$$

Here I have also introduced a fit parameter F_d, which allows us to account for any error in manufacturing of the optics, errors in the ZEMAX model, or errors in the actual vs command displacement of the LM-1 actuator. The direct measurements of distances in the far-field described in Section 7.5 show that $F_d = 1.098$, and this value is used in all analysis for the remainder of this chapter.

I also tested whether cross-talk appears between the actuator readout and the detectors. To test this both actuators were moved in a 6 Hz sine-wave pattern over their maximum displacement range of ± 3.5 mm, while the detectors were biased at SOC. Both actuators were moved at the same time, roughly 135° out of phase. The level of cross-talk present can be quantified by performing a least-squares fit of each detector timestream $\vec{d}_{rc}$ to the model

$$\vec{d}_{rc} = A_1 \vec{d}_{\mathrm{DISP1}} + A_2 \vec{d}_{\mathrm{DISP2}}. \tag{7.3}$$

Here $\vec{d}_{\mathrm{DISP1}}$ and $\vec{d}_{\mathrm{DISP2}}$ are the measured outputs for each actuator.

The fit values for A_1 and A_2 were clustered near zero, and were small compared to the noise in the detector timestream. As a more stringent test, I calculated the cross-talk amplitudes A_1 and A_2 for each detector twice: once for the first half of the data acquisition and once for the second half. If cross-talk is present to a statistically significant level, a scatter plot of the cross-talk amplitudes for the two halves of the data acquisition should show signs of correlation. As can be seen in Figure 7.5, the points are clustered about the origin and no correlation is apparent.

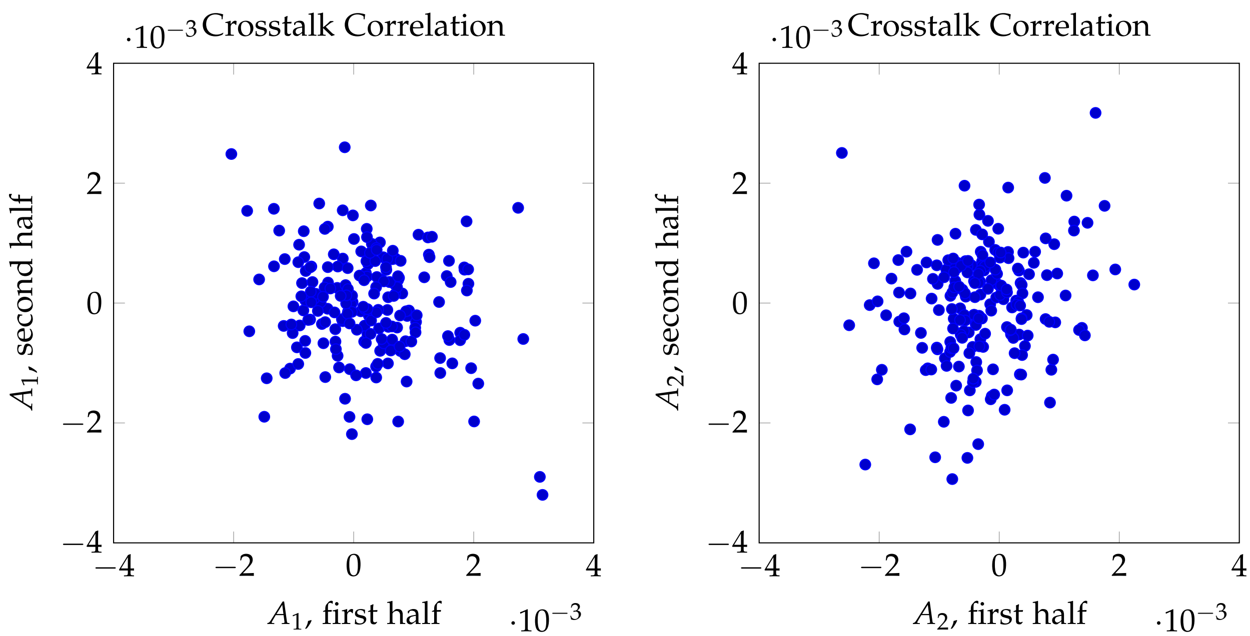

Figure 7.5: Plot showing cross-talk amplitudes. The left plot is for DISP1, the right for DISP2. Each actuator was moved +/- 3.5 mm at 6 Hz while the detectors were biased at SOC. The best-fit cross-talk amplitude for each actuator and detector were calculated for both the first half and the second half of the data acquisition, and these amplitudes are plotted against each other in these plots. The lack of correlation in the scatter plots, as well as the clustering around the origin, indicate that any cross-talk present cannot be distinguished from noise in the detectors.

7.3 Focus Distance

As described in Section 4.2, the 350 GHz Video Imager is designed to focus at distances of 16 m – 28 m. All results described in this chapter were with the 350 GHz Video Imager configured to focus at 16 m. To check the actual distance to the target focal plane, beam maps as described in Section 7.4 were performed with the black-body source located at different distances from the cryostat. The focus distance was found to be 17 m in front of the vertex of the primary mirror. Figure 7.6 shows beam maps for the same detector taken at 17 m and at 15.8 m. At 17 m the black-body aperture is well defined and much warmer than its surroundings. At 15.8 m, the black-body aperture is visible, but poorly defined with significant side-lobes. The temperature of the aperture is much closer to the background than in the 17 m case.

The reasons for the difference between the measured focus position and the focus position predicted using ZEMAX are not understood. It is possible that the cryostat is

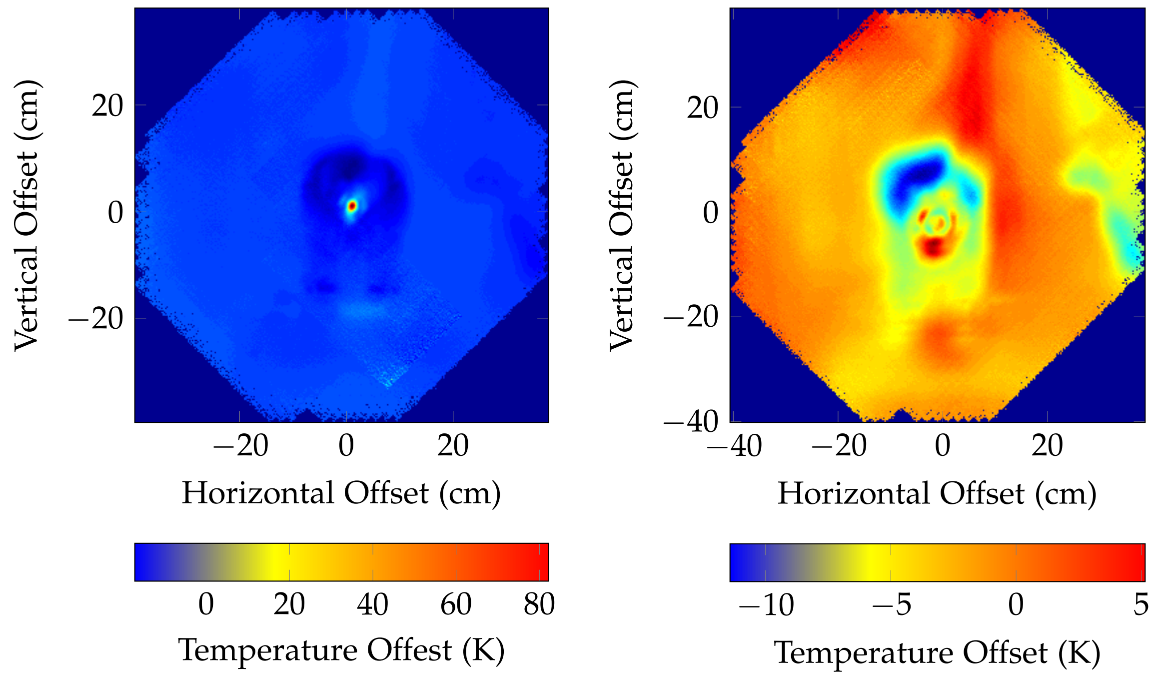

Figure 7.6: Plots showing impact of observing objects not located at the far-field focal plane. In both cases the 1030 °C black-body source with aperture diameter set to 0.4 in (1.0 cm) was observed. The acquisitions were taken 2.5 minutes apart, with the only change being the distance between the black-body and the primary mirror. **Left** Still image taken with the black-body located 17 m from the primary mirror. The aperture is clearly defined and 80 K warmer than its surroundings. **Right** Still image taken with the black-body located 15.8 m from the primary mirror. The black-body aperture is poorly defined with prominent side-lobe features, and a temperature no more than 5 K – 10 K warmer than the surroundings.

located incorrectly relative to the mirrors, or that there were errors in the manufacturing or assembly of the optical components.

7.4 Beam Maps

As discussed in Section 4.4, the 350 GHz Video Imager feedhorns are predicted to have beams that are circularly symmetric and well-approximated by Gaussians with FWHM of 1.2 cm at the target. To verify these predictions beam maps were performed by raster scanning the beams over a stationary 1030 °C black-body source.

The source used was an IR Labs IR-563/301[2] black-body. This source reaches a

[2]IRLabs, Inc. Tucson, AZ. USA

maximum of 1030 °C and has apertures ranging in size from 0.0125 in – 0.6 in. Best results were achieved by covering an area around the black-body source with Al foil; this eliminated hot spots in the image due to the warmth of the housing of the black-body source itself. The aperture diameter was set to 0.2 in (0.51 cm), which is smaller than the predicted beam and will have a minimal effect on the measured beam width.

The 350 GHz Video Imager beams were raster scanned over the black-body source by moving one actuator at 6 Hz while the other actuator moved much more slowly at 0.1 Hz. Scans were taken with the black-body in two different locations to ensure coverage of the entire sub-array. At each black-body position two scans were taken with DISP1 as the fast actuator and two with DISP2 as the fast actuator, for a total of eight scans.

For each scan, the data stream for each detector was "binned" as described in Section 7.8 to produce a beam map for each detector. No common mode or polynomial was removed from the timestreams. Actuator displacements were converted to distances in the far-field using the conversion factors discussed in Section 7.2. The following 2-D elliptical Gaussian profile was then fit to each beam map:

$$P(x,y) = O + A\exp\left[-\frac{1}{2}\left(\frac{(x-x_0)\cos\theta + (y-y_0)\sin\theta}{\sigma_1}\right)^2 - \frac{1}{2}\left(\frac{-(x-x_0)\sin\theta + (y-y_0)\cos\theta}{\sigma_2}\right)^2\right]. \quad (7.4)$$

Here x and y represent the position in the beam map, while x_0, y_0, σ_1, σ_2, θ, A, and O are the parameters to be fit. O represents an overall DC offset in the map level. Only the points within 3 cm of the map peak were included in the fit. Beam maps at the edge of the scan were discarded, as were beam maps where the fitting routine performed poorly. The θ, σ_1, and σ_2 parameters were all defined such that $\sigma_1 > \sigma_2$ and $0 < \theta < 180°$. The beam parameters across the eight scans were then averaged together to produce final beam maps. Figure 7.7 summarizes the final fit parameters for all the beams. As can be seen from the width of the fit parameter histograms, the beam ellipticity and angle offset from the x-axis are statistically significant.

Figure 7.8 shows the final beam maps. The beams are elliptical, with a mean $\sigma_1/\sigma_2 = 1.6$. The mean beam angle is 70° counter-clockwise from the x-axis. The beam size FWHM is 1.4 cm, and is calculated from

$$2\sqrt{2\ln 2}\sqrt{\sigma_1\sigma_2} \quad (7.5)$$

where the prefactor $2\sqrt{2\ln 2}$ converts from the Gaussian parameters $\sigma_{1,2}$ to the FWHM of the Gaussian.

In Section 4.4, it was shown that the expected FWHM beam width from this measurement is 1.2 cm, only about 15 % smaller than observed. The close match between the measured and predicted FWHM beam widths is encouraging, but the beams should be circular rather than strongly elliptical as observed. Another discrepancy between the measured and predicted beams is the distance between the beams. The best-fit grid spacing between detector beams in the far field is 2.0 cm. Using the plate scale extracted from ZEMAX in Section 4.2, this is equivalent to a 3.0 mm detector spacing on the focal plane array, which is 8.6 % larger than the design spacing of 2.73 mm.

The reasons for these discrepancies are not known. Possible explanations for the error in plate scale are misalignment of the feedhorns with the primary and secondary mirrors, and errors in fabrication of the mirrors or feedhorns. Either of these problems could also lead to elliptical beams, as could diffraction off the aperture stop located in the 50 K radiation shield. Another possible explanation for the elliptical beams could be misalignment between the detectors and the feedhorns. As described in Section 4.4, such misalignment leads to differential coupling between the two polarizations, and because the polarized beams from smooth-walled conical feedhorns are elliptical, misalignment could lead to elliptical measured beams.

To show the instantaneous field of view of the array compared to the area of the scanned image, Figure 7.12 shows the locations at which the beams are pointing when the LM-1 actuators are set to their zero positions.

Although the ellipticity of the beams is puzzling, the resolution is close to target, and the ellipticity is not a barrier to using the system to take video images.

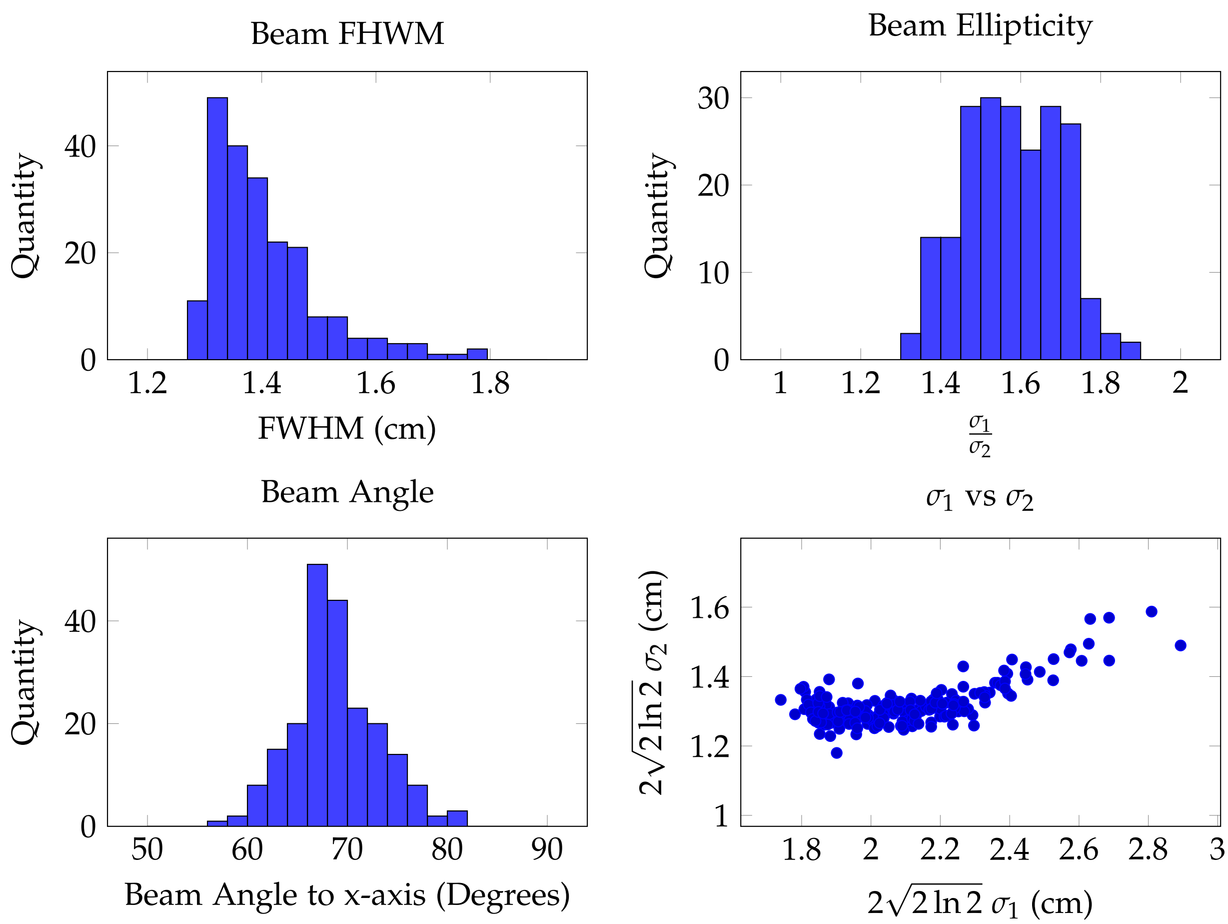

Figure 7.7: Plots summarizing final fit parameters for all beams. The histogram in the lower right shows that there is ~ 3 times more scatter in σ_1 than in σ_2.

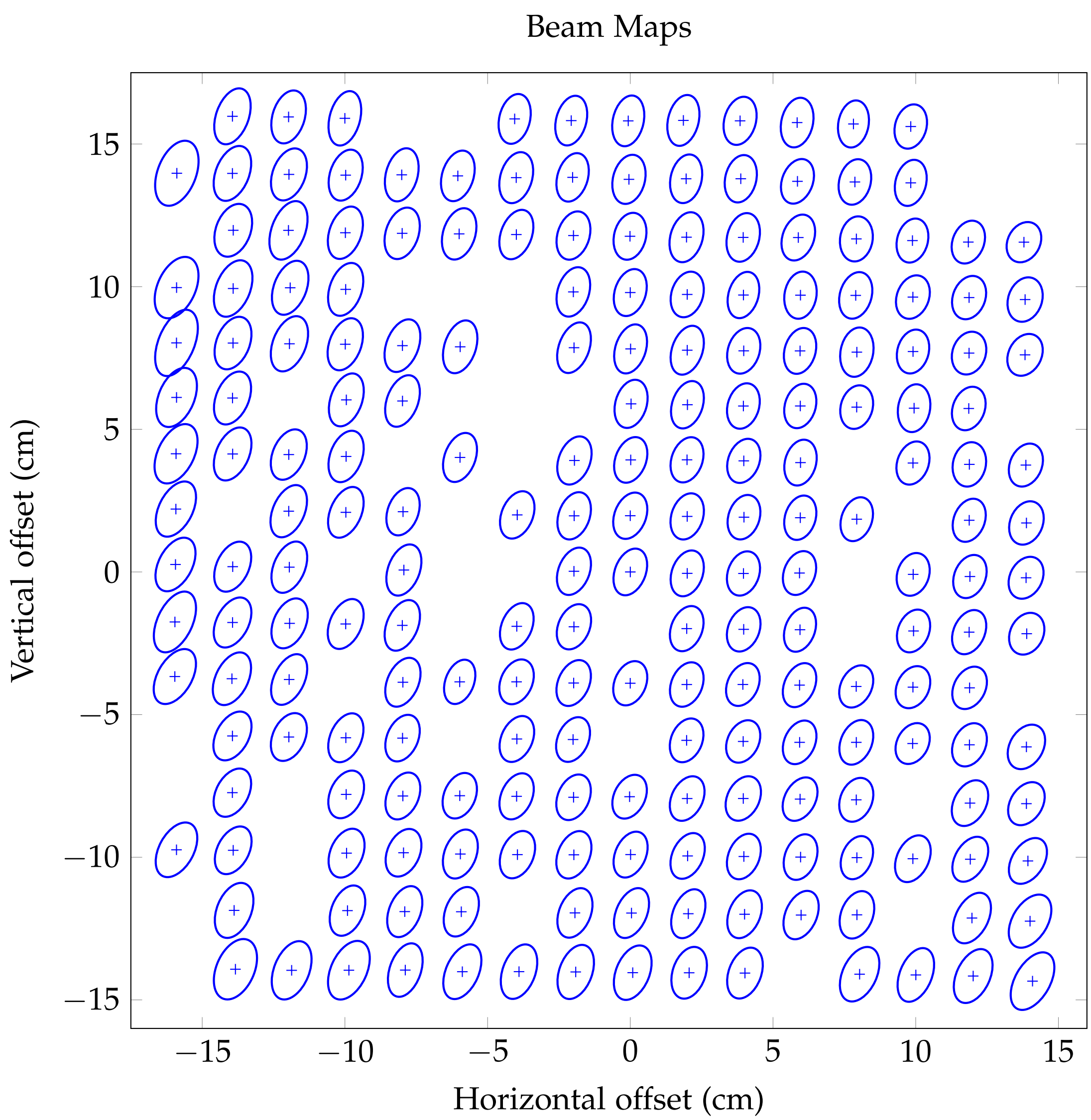

Figure 7.8: Plot showing final beam maps. The ellipses represent the full-width-half-maximum (FWHM) of the best-fit 2-D Gaussian for each beam. The beams are elliptical, with a mean σ_1/σ_2 of 1.6, mean beam angle to the x-axis of 70°, and beam FWHM of 1.4 cm. The four grid locations in the extreme upper right corner, as well as the extreme lower left grid point, have no detectors and therefore no beams. All other missing beams are for cut detectors, as discussed in Section 7.1. The offset is relative to detector R17C3.

7.5 Direct Measurement of Distance Scale and Image Resolution

To measure the factor F_d described in Section 7.2, I placed a Styrofoam cooler filled with liquid Nitrogen (LN2) in the far-field of the system and scanned it with the system, using the data acquired to create still images. A sheet of Eccosorb AN72[3] was placed in the cooler to serve as a cold black surface for the system to observe. Images were acquired of the cooler itself, as well as the cooler with Al foil strips taped to the outside. Each strip was ~4 cm tall, and the strips were 14.5 cm, 29 cm, and 47.2 cm long. The interior of the cooler is 67.7 cm wide. For each image the FWHM width of the strip — or the cold space inside the cooler — was calculated by taking a cut through the still image centered on the strip or cooler (see Figure 7.9).

The result of these measurements is that $F_d = 1.098$.

Using the same cooler filled with LN2, a dime (diameter 17.91 mm) was taped to the outside of the cooler and a still image was taken. Figure 7.10 shows the resulting still image, as well as a close-up of the are with the dime. A 2-D Gaussian was fit to the

[3]Emerson & Cuming Microwave Products, Inc.

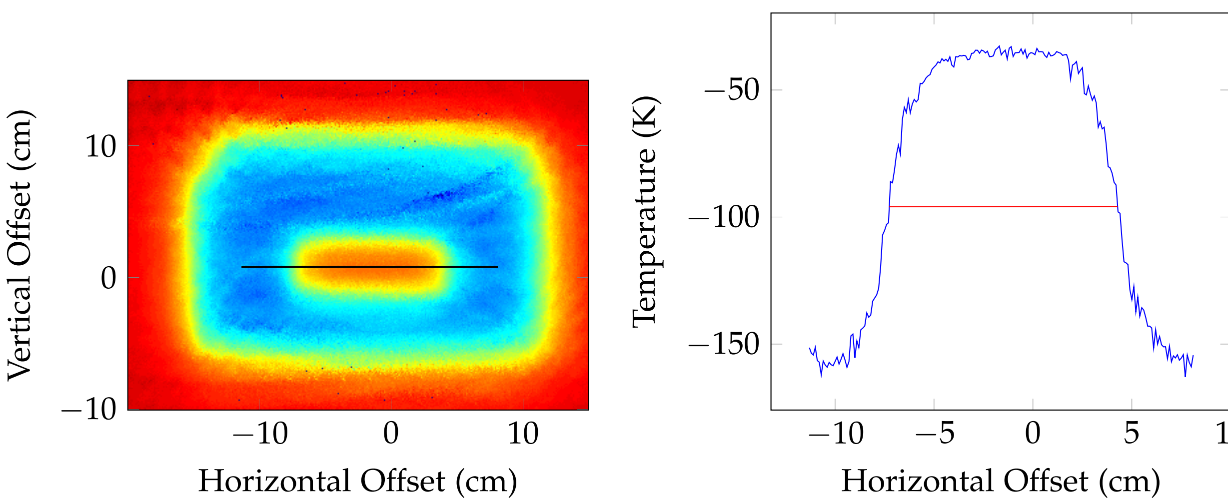

Figure 7.9: Plots explaining measurement of distance scale. The left plot shows a close-up of the Styrofoam cooler filled with LN2, with a 14.5 cm by 4 cm strip taped to the outside. A cut of this image through the middle of strip (identified by the thin black line) is shown on the right. The FWHM of this cut is shown as the red line. This measurement was repeated for two other Al foil strips, as well as the cooler without any Al foil strips, in order to establish the distance scale.

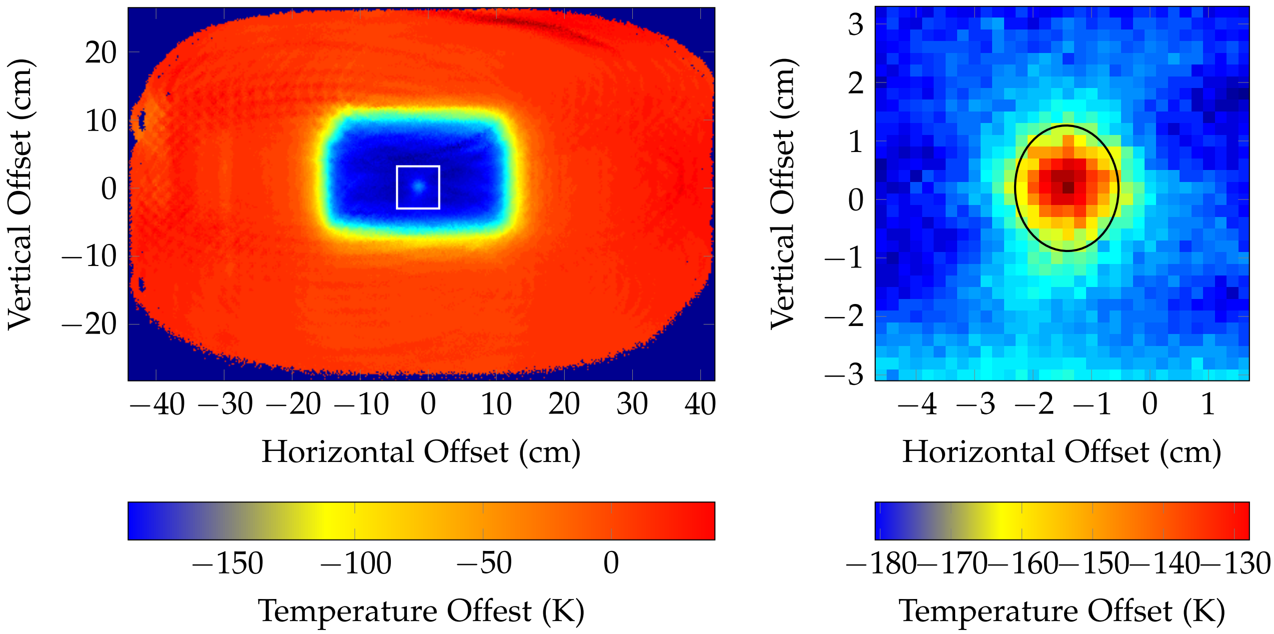

Figure 7.10: Plots showing still image of Styrofoam cooler filled with LN2, with a dime (diameter 1.791 cm) taped to the outside. Red is warm, blue cold; the temperature scales are different in the two plots. **Left** The full map of the cooler. The white rectangle shows the area of the detail on the right. **Right** Detail of area within white rectangle: the dime. The black ellipse shows the FWHM of the best-fit ellipse to the map. The ellipticity is 1.2, the FWHM of the principal axes are 1.8 cm and 2.2 cm, for an overall FWHM of $\sqrt{1.8 \times 2.2} = 2.0\,\text{cm}$.

resulting map. The best-fit Gaussian has ellipticity 1.2 — smaller than the individual beams — and the FWHM of the dime map is 1.95 cm — larger than the beams. Both differences are expected from convolution of the beam with the dime, which is not a point source. The FWHM of the dime map is 2.0 cm, which is 15 % larger than the expected value of 1.7 cm. This serves as a rough confirmation of the beam size and locations as determined in Section 7.4.

7.6 Optical Efficiency

To measure the total optical efficiency of the system, IV curves can be taken while a detector's beam is pointing at two known temperature loads. As discussed in Section 3.4, the difference in Joule power at $0.99R_n$ gives the difference in total power dissipated in the bolometer. In this case, the power difference will be caused by the different amount of power absorbed in the bolometer while observing the two temperatures. If the two temperatures are T_1 and T_2, then the total optical efficiency η_{tot} is given by

$$\eta_{tot} = \frac{P_{iv,1} - P_{iv,2}}{P_{opt}(T_2) - P_{opt}(T_2)}, \tag{7.6}$$

where P_{IV} is the Joule power in the detector at $0.99R_n$ and $P_{opt}(T)$ is the optical power in both polarizations emitted by the source in a single spatial mode, given by Equation 4.11.

For a good measurement the load temperatures T_1 and T_2 should be as far apart as possible, and the detector's far-field beam should be filled by the load in each case. I used the same "Eccosorb AN72 submerged in LN2" setup as described in Section 7.5 for the cold temperature load. For the warm temperature load I used a sheet of Eccosorb AN72 backed by a thin sheet of Al. "Room Temperature" here is assumed to be 295 K (71.3 °F).

The boiling temperature of LN2 is 75.6 K in Boulder, CO, where these measurements were made[4], but this does not mean that the temperature seen by the beams when pointed at the cooler is exactly 75.6 K.

- The beams are looking through the 1.625 in thick Styrofoam walls of the cooler, which may have some emission themselves.
- Although the Eccosorb AN72 sunk in LN2 is opaque at 350 GHz, it may reflect some amount of light from the surrounding room.
- It is possible that a small amount of water vapor could condense on the outside of the cooler, leading to further emission.

For the purposes of this measurement I assumed that the cold Eccosorb AN72 was black and that no water vapor was condensed on the cooler, which is consistent with a visual examination. However, I do allow for a non-unity transmittance τ for the Styrofoam in the analysis below.

For each of eight detectors, four IV curves were taken under three conditions: pointing at the room-temperature Eccosorb AN72 ("ecco"), pointing at the cold Eccosorb AN72 in the cooler ("LN2"), and looking at the Eccosorb AN72 with the cooler's lid placed directly in front of the cooler ("lid"). The lid is 2 in thick and the cooler's side is 1.625 in thick. I assume that the transmittance takes the form $e^{-d\kappa}$, where d is the thickness of the material and κ is some constant which characterizes the attenuation length of 350 GHz

[4]Assuming typical atmospheric pressure of 82.2 kPa (Noah Newman, Colorado Climate Center, personal communication) and using standard values for LN2 vapor pressure [90]

light in Styrofoam. Given this assumption, if the transmittance through the cooler's wall is τ, then the transmittance through the lid is given by $\tau^{2/1.625} = \tau^{1.23}$.

The optical powers viewed under these three conditions is then given by (with $T_h = 295\,\mathrm{K}$ and $T_c = 76\,\mathrm{K}$)

$$P_{opt,ecco} = P_{opt}(T_h) \tag{7.7}$$

$$\begin{aligned} P_{opt,LN2} &= \tau P_{opt}(T_c) + (1-\tau)P_{opt}(T_h) \\ &= P_{opt}(T_h) - \tau(P_{opt}(T_h) - P_{opt}(T_c)), \end{aligned} \tag{7.8}$$

$$\begin{aligned} P_{opt,lid} &= \tau^{1.23} P_{opt,LN2} + (1-\tau^{1.23})P_{opt}(T_h) \\ &= P_{opt}(T_h) - \tau^{2.23}(P_{opt}(T_h) - P_{opt}(T_c)). \end{aligned} \tag{7.9}$$

Here these optical powers include both polarizations and are referred to power emitted at the target. The differences in optical power absorbed in the bolometer will then be

$$\Delta P_{b,ecco-LN2} = \eta_{tot}\tau(P_{opt}(T_h) - P_{opt}(T_c)) \tag{7.10}$$

$$\Delta P_{b,lid-LN2} = \eta_{tot}\tau(1-\tau^{1.23})(P_{opt}(T_h) - P_{opt}(T_c)). \tag{7.11}$$

These last two equations can be solved for η_{tot} and τ. The results are

$$\tau = \sqrt[1.23]{1 - \frac{\Delta P_{b,lid-LN2}}{\Delta P_{b,ecco-LN2}}}, \tag{7.12}$$

$$\eta_{tot} = \frac{\Delta P_{b,ecco-LN2}}{\tau(P_{opt}(T_h) - P_{opt}(T_c))}. \tag{7.13}$$

The full set of three IV curves was repeated three times over the course of several hours. The transmittance τ of the cooler wall was found to be $\sim 90\,\%$ and the optical efficiency η_{tot} was 13.5 %. Table 7.1 gives the results of these measurements averaged over all detectors and all repetitions.

This optical efficiency is roughly half of the value predicted in Section 4.6. It is not clear where the optical power is being lost. Chapter 8 describes future measurements that could help troubleshoot this problem.

Table 7.1: Results of optical efficiency measurements. The values are medians and the uncertainties give the 25 % – 75 % range of measured values.

Quantity	Value
η_{tot}	13.5 ± 0.9 %
τ	90.6 ± 4.8 %
$P_{b,ecco-LN2}$	25.6 ± 0.5 pW
$P_{b,lid-LN2}$	2.0 ± 1.0 pW

7.7 Temperature Scale Calibration

The output of the readout system gives changes in current passing through the detectors. In order to convert this current change to a temperature change we must first convert the current changes to changes in power absorbed in the bolometer by dividing by the power-to-current responsivity s_I. To convert this to temperature changes in the far-field of the system, we must use the total optical efficiency η_{tot}, as well as the Rayleigh-Jeans limit of the optical power per spatial mode from a blackbody with a uniform temperature (see Section 4.6). The result is that the conversion from current to temperature is given by

$$\Delta T = \frac{\Delta I}{s_I(0) 2 k_B \eta_{tot} \Delta \nu}. \tag{7.14}$$

Ideally this temperature scale would be measured directly by allowing the detectors to observe two known temperature loads and measuring the resulting change in current. However, several difficulties arise in practice. As the amount of optical power absorbed in a detector changes, the point occupied by the detector on its $R(T, I)$ surface changes, so that $\mathcal{L}_I$ β_I, and the bias voltage V_0 all change. This leads to a changing responsivity with optical load through Equation 3.7, resulting in a non-linear detector response. For small changes in load (such as we expect in images taken with the system) the changes will be small and can be ignored. But in order to obtain an accurate measurement of the temperature scale, it is desirable to use a large change in temperature, such as the difference between room temperature and LN2. For these larger temperature changes the change in responsivity may be significant.

To check for detector non-linearity with varying optical load, I measured the detector responsivity directly using heaters both when the system was observing Eccosorb AN72 and when the cryostat window was covered with Al foil. Covering the window with foil reduces the optical power reaching the detectors from outside the cryostat by ~ 38 pW. For two of the detectors this led to an increase in responsivity of ~ 1 %, while for the other two the increase was ~6.5 %. This makes it difficult to calibrate the temperature scale of the detector response more accurately than 10 % when using a LN2 load.

Stable, uniform temperature distributions using stirred liquid water are available [91] and should be used if a more accurate temperature scale is desired in the future.

For this dissertation, however, I have not made these measurements. Instead I have assumed that all detectors have the same optical efficiency as was measured for eight detectors in Section 7.6, $\eta_{tot} = 0.136$. For $s_I(0)$ I have used the predicted values at SOC of Section 6.7, with the exception of three detectors (R24C3, R25C1, R25C3) for which the predicted $s_I(0)$ was clearly incorrect, as judged from inspecting detector timestreams and still images. For these three detectors I have assumed a responsivity equal to the mean of all other predicted responsivities.

As a check on the accuracy of this temperature scale, the still image on the left of Figure 7.10 has ~180 K of contrast between the coldest section at the middle of the cooler and the warm area to the left of the cooler. Using the estimate for transmittance τ of the cooler walls of 0.9, the expected temperature differential is $0.9(295 - 76) = 197$ K. Given the fact that responsivity will increase with optical loading, which leads to underestimates of temperature difference via Equation 7.14, these numbers are in reasonable agreement, indicating that the temperature scale is accurate to within ~20 %.

7.8 Image Processing Algorithm

This section describes the algorithm used to turn raw detector timestreams into video images. The algorithm currently used is simple, processing each video frame independently.

The algorithm's steps are as follows:

1. The MCE channels containing the actuator displacement (R31C4 for DISP1 and R31C5 for DISP2) are converted to displacements in the far-field as described in Section 7.2.

2. Determine full range of far-field displacements, accounting for all detectors. Define a 1 cm grid that covers this range in both x and y directions.

3. Each detector's output is multiplied by its "current-to-temperature" calibration factor (see Section 7.7). At this point the units for all detector timestreams should be the same, but each detector timestream will have some unknown offset.

4. Divide detector timestreams into sections for each video frame based on MCE readout rate and frequency at which the secondary mirror is rotating. If the mirror frequency is f_m and the readout frequency is f_{ro}, then each video frame will cover $\lceil f_{ro}/f_m \rceil$ samples. **Example:** If the readout frequency is 3125 Hz and the mirror frequency is 6 Hz, then each video frame will cover $\lceil \frac{3125}{6} \rceil = \lceil 520.83 \rceil = 521$ samples.

5. For each video frame

   a) Perform the following processing for each detector that is not on the cut list described in Section 7.1:

      i. If the detector's timestream shows evidence of glitches, do not include that detector's timestream for this video frame. The algorithm used to identify glitches is the following:

         A. Calculate the differences $\Delta f_j = f_{j+1} - f_j$ between each consecutive value in the timestream.

         B. Calculate the standard deviation of the differences Δf_j.

         C. If the absolute value of any Δf_j is greater than five times the standard deviation, identify this detector as having a glitch, so that it will be ignored for this video frame. On average this affects 3.2 detectors per frame.

      ii. Subtract the median value of this detector's timestream for this video frame. The advantages and disadvantages of this approach to removing detector offsets is discussed below.

      iii. If the detector does not have a glitch, determine which image pixel the detector is pointing to at each point in time, using both the pointing position from the actuator readout described in Section 7.2 and the beam pointing information from Section 7.4.

      iv. Add the detector's value to that pixel for the frame.

      v. Keep track of the total number of samples that have been added to each pixel.

   b) After each detector has been processed for the frame, divide the total value for each pixel by the number of samples across all detectors that have been used for that pixel.

6. To improve contrast, clip the temperature scale to the range $-3\,\mathrm{K}$ to $-3\,\mathrm{K}$. Any pixels in the image with no data were assigned a temperature of $-3\,\mathrm{K}$.

7. After all video frames have been processed, convert the resulting 3-dimensional array to a video using MATLAB's `VideoWriter` object.

Discussion of Videos Taken With the 350 GHz Video Imager

Figure 7.11 shows four still images from a video that was processed according to this algorithm. This video can be viewed online at `http://www.youtube.com/watch?v=ul_fd-KWH38`. They show the author with a ceramic knife hidden beneath a button-down cotton shirt. The ceramic knife is visible as a dark area on the left of the shirt. A darker line running down the center of the shirt is due to the extra layer of cotton backing the buttons; this additional cloth produces more attenuation of the warm light from the body, and so appears cooler.

The total temperature contrast in the images of Figure 7.11 is 6 K, but as described above higher and low values of temperature have been clipped to improve contrast. In the raw images, the mean total contrast across all frames with the person present is 8.2 K.

To estimate the expected contrast we can take the following into account:

- Human skin temperature is typically in the range 33 °C – 35 °C = 306.2 K – 308.2 K [92].
- The emissivity of human skin has been reported as 0.65 at 100 GHz and 0.93 at 500 GHz [16]. Interpolating between these values leads to an emissivity of 0.825 at 350 GHz.
- The temperature the room in which theses images were taken was ~295 K.

If the coldest temperature in the images is given by the room temperature, then the total contrast in the image is predicted as

$$0.825 \times 307\,\mathrm{K} + (1 - 0.825) \times 295\,\mathrm{K} - 295\,\mathrm{K} = 9.9\,\mathrm{K}. \tag{7.15}$$

This is 1.7 K larger than observed. Given uncertainties in the actual skin temperature of the person in the image, the true emissivity of human skin at 350 GHz, the true background temperature and the true temperature of the illuminating light, the near agreement between the predicted and observed values gives confidence that the temperature scale is roughly correct.

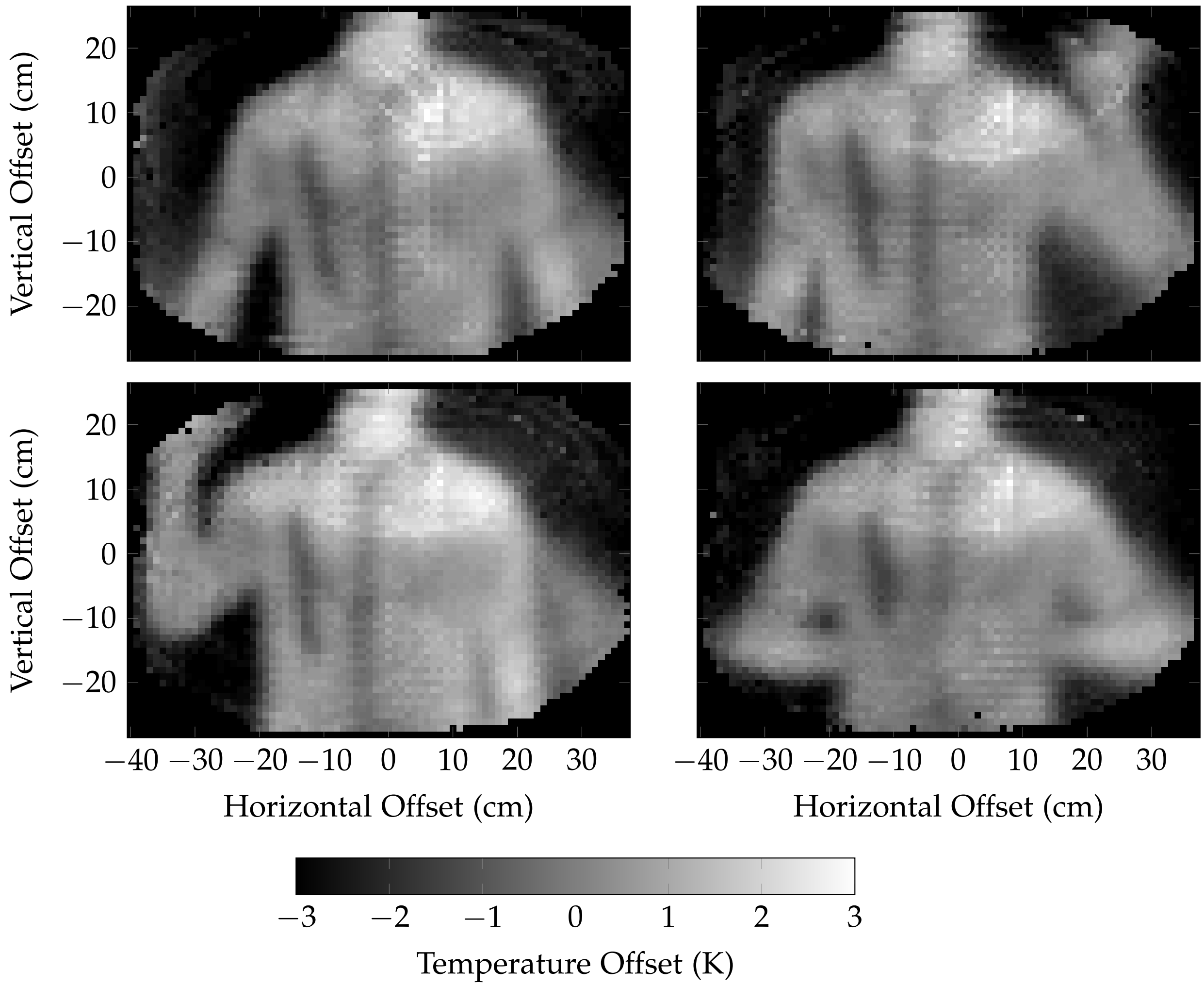

Figure 7.11: Sample still images from a video taken with the 350 GHz Video Imager. Time proceeds left-to-right and top-to-bottom. The stills are 20 frames (3.33 s) apart. The person in the images is the author. A ceramic knife hidden beneath a button-down cotton shirt is visible on the left of each image. The darker line running down the center of the shirt is due to the extra layer of cotton backing the buttons; this additional cloth produces more attenuation of the warm light from the body. As discussed in the text, the temperature range in these images was clipped to ± 3 K for better contrast. The total contrast in the raw images is 8.2 K, about 1.7 K lower than expected. See text for discussion.

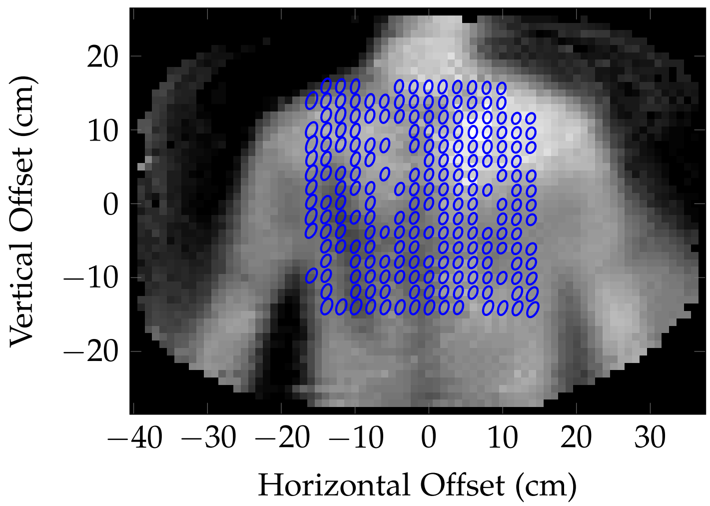

Figure 7.12: Plot showing where beams are pointed in far-field. The background image is frame 25 from the video discussed in Section 7.8. The beam FWHM ellipses are in blue.

Discussion of Median-Subtraction

As discussed in Section 4.7, the output of the readout system does not give the absolute current passing through each detector. Instead it gives the change in current relative to some offset, which is not a-priori known. My approach for dealing with this offset is, for each video frame, to subtract from each detector's timestream the median of that detector's timestream during that video frame. Although crude, this approach does a good job of accounting for the offsets in the detector timestreams, as well as accounting for the common-mode drift described in Section 6.8. However, elliptical scanning artifacts are still visible in the images of Figure 7.11. These artifacts arise in part because the median-subtraction scheme will work "perfectly" only in the case where the median temperature viewed by each detector during the frame is the same. If this is not true for a particular detector, the ellipse traced out by that detector in the image will appear warmer or cooler than its surroundings (depending on whether the distribution that it viewed was cooler or warmer than its surroundings), leading to elliptical scanning artifacts.

An additional consequence of this approach is that the median color in each video frame will be the same; i.e., a particular color in frame 1 may not represent the same temperature in frame 10. This effect can be see in the early frames of the video available online. In that video the early frames of the image are looking at the background of the lab, and only later does a person move into the frame. As the person moves into the frame, some areas of the background become darker, not because they are changing to a lower temperature, but because they are now lower relative to the median temperature in the frame. Although surprising when first seen, this effect does not prevent the system from being effective in detecting concealed weapons.

Other image processing algorithms could be used to deal better with the detector offsets. One method would be to take a "flat" image of a uniform temperature distribution prior to taking videos, and use this image to normalize all detector offsets relative to each other. However, an approach would still be needed to deal with common-mode drift, as well as other sources of low-frequency $1/f$ noise which could cause detector offsets to drift independently of each other.

Another method is to use the fact that the ellipse mapped out by each detector during a video frame overlaps with the ellipses of many other detectors. It should be possible to take advantage of this to set the offsets for each detector correctly on a frame-by-frame basis. It is possible that an approach like this could also be used to normalize the responsivity of all the detectors relative to each other.

An iterative approach is also possible, based on the fact that median-subtraction evidently comes close to properly removing detector offsets. An algorithm could be developed which checks whether the points mapped out by each detector's ellipse are different than the neighboring points. If the difference crosses some threshold, the offset could be adjusted and the frame processed with a new set of offsets. This process could be repeated until a self-consistent image is created.

Other algorithmic approaches are certainly possible as well, and should be a focus of future work.

7.9 Image Noise Model

The temperature scale established in Section 7.7 allows us to convert the measured detector white-noise level of $\sim 2.4 \times 10^{-15}\,\mathrm{W}/\sqrt{\mathrm{Hz}}$ to a temperature noise via

$$S_T = \frac{S_P(0)}{2k_B \eta_{tot} \Delta\nu}. \tag{7.16}$$

This results in a temperature noise level of $\sim 15 \times 10^{-3}\,\mathrm{K}/\sqrt{\mathrm{Hz}}$, referred to the temperature viewed in the far-field of the system.

To use this noise level to make a prediction for the NETD in the image we can use the radiometer equation [93]:

$$\mathrm{NETD} = \frac{S_T}{\sqrt{2t_{dwell}}}, \tag{7.17}$$

where t_{dwell} is the total integration time including all detectors for each pixel in the image[5].

All images in this chapter contain ~ 4030 pixels, each $1\,\mathrm{cm}^2$ in area[6]. Each video frame lasts $\frac{1}{6}$ s, and there are ~ 210 good detectors contributing. t_{dwell} is thus given by

$$t_{dwell} = \frac{210 \times \frac{1}{6}\,\mathrm{s}}{4030} = 8.7\,\mathrm{ms}. \tag{7.18}$$

Plugging this into Equation 7.17 gives an NETD of ~ 115 mK.

Verifying this noise level in a video image is difficult because we do not know a-priori whether there are any regions in the image which have a flat temperature distribution. However, if we place a sheet of Eccosorb AN72 directly in front of the cryostat window, where all detector beams are large and covering similar areas, then all detectors should be viewing close to the same temperature distribution. If data is acquired in this state, while the secondary mirror is moving, and the resulting timestreams are run through the same software used to create "real" videos, then the standard deviation of the temperature in each frame should give a good estimate of the NETD.

I carried out this procedure, creating a "flat" video with 19 frames. The mean NETD across the 19 frames is 101 mK. Figure 7.13 shows a histogram of the NETD distribution from all 19 frames, a histogram showing the temperature offset distribution for the second frame (which has $NETD = 100\,\mathrm{mK}$), the second frame itself, and one of the still images from Figure 7.11. Both still images use the same temperature-difference-to-gray-scale mapping.

Comparing the two frames visually, it is clear that NETD in the true video frame is dominated not by detector noise, but by artifacts of the scan, visible as elliptical arcs in the image. These artifacts are likely caused by the median-subtraction scheme of Section 7.8 not properly accounting for the detector offsets. Nevertheless, in areas of the video still where there appear to be few scan artifacts (such as the arm on the lower right), the level of noise in the video still appears comparable to the flat still, indicating that 100 mK is a reasonable estimate of the NETD in the image caused by detector noise.

The agreement between the predicted NETD of 115 mK and the observed flat image NETD of 100 mK is an encouraging sign that we understand the behavior of the system.

[5] In this equation the factor of 2 accounts for the fact that the noise power spectral density is defined so that the total variance in the signal is given by the integral of the power spectral density up to the one-half of the sampling frequency, i.e. up to the Nyquist frequency.

[6] Although the images shown are all rectangular, due to the elliptical scanning pattern the actual area of the images that contains data is smaller than the rectangle.

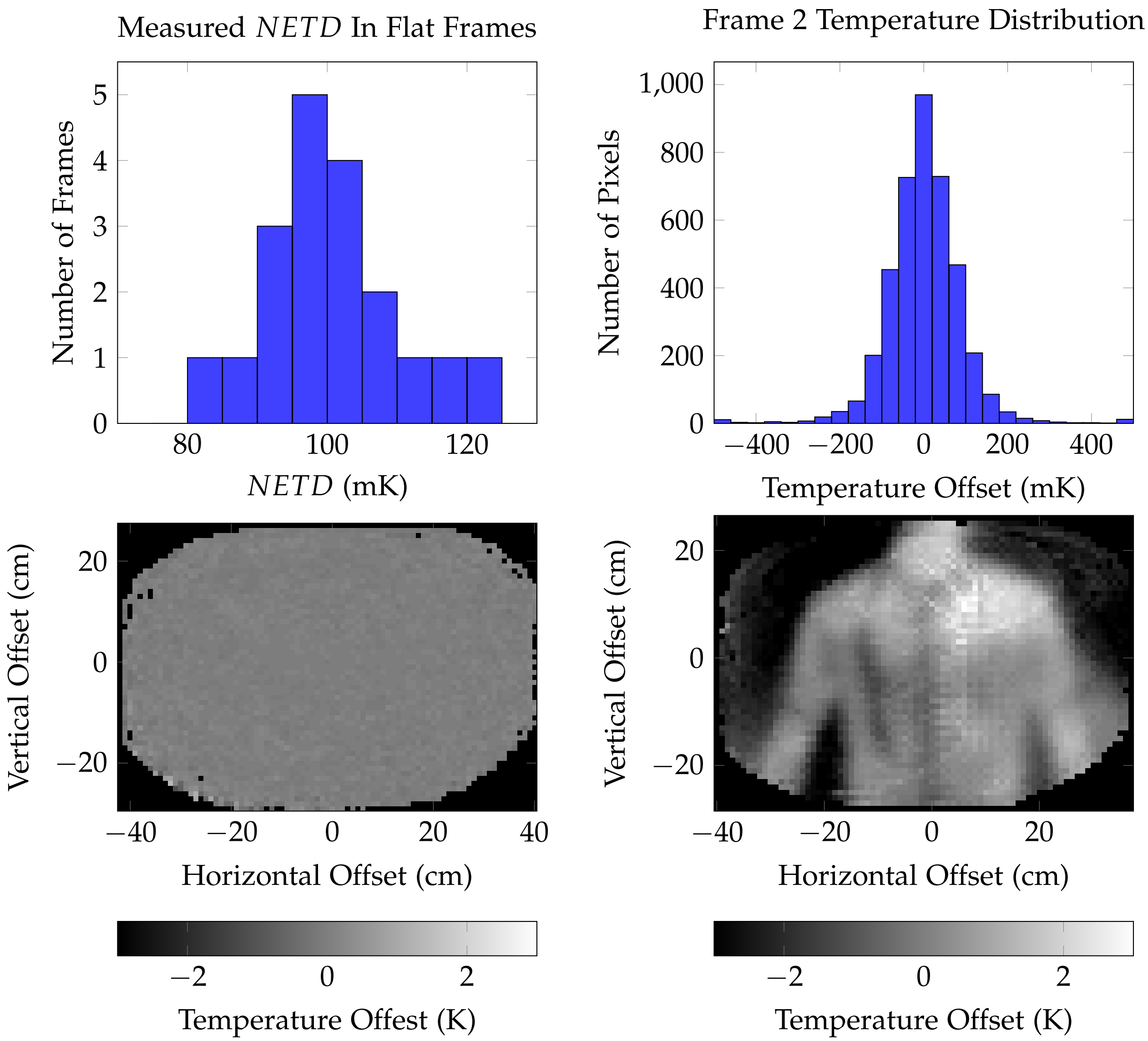

Figure 7.13: Plots relating to measurement of NETD in flat frame images. **Upper Left** Histogram of NETD for each of 19 frames taken from a "flat" video image. This NETD is defined as the standard deviation of the temperatures across all pixels which were visited by at least one detector. **Upper Right** Histogram showing distribution of temperature offsets within the second video frame, which has an NETD of 100 mK. The far left and far right bins include outliers that extend all the way to −1 K on the left and 1.5 K on the right. Removing these outliers results in NETD values that are roughly 15 % smaller. **Lower Left** The second frame of the flat video. **Lower Right** Frame 25 of the video discussed is Section 7.8. These two frames use the same temperature-offset-to-color mapping to aid in visual comparison.

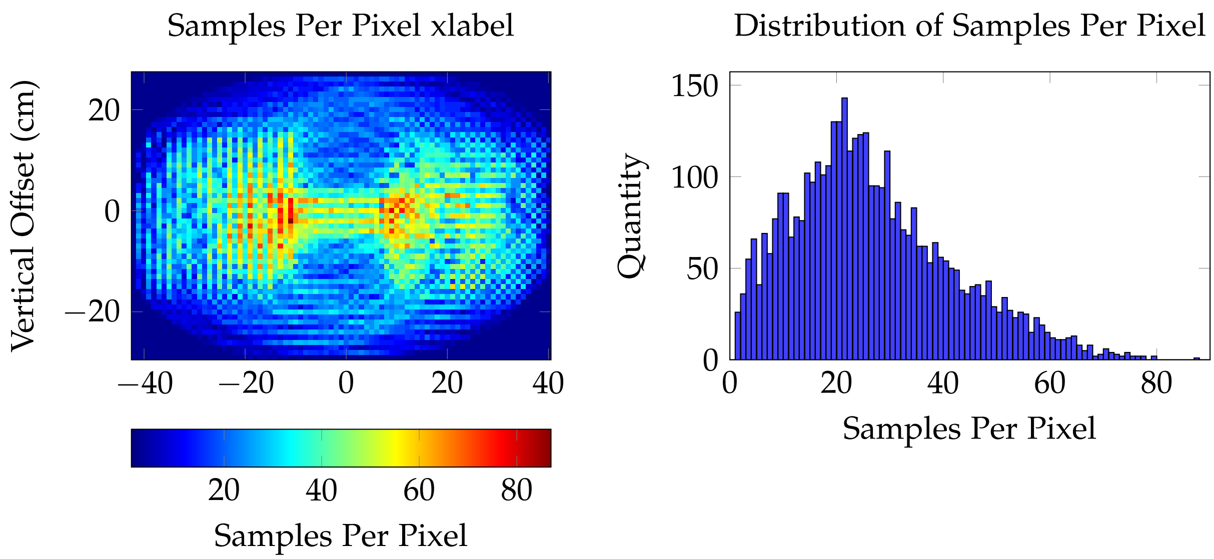

Figure 7.14: Distribution of samples per pixel for flat field image shown in Figure 7.13. Different video frames have slightly different distributions, but the overall features are all similar to what is shown here. The bins in the histogram on the right are one sample wide, so that it can be seen that a handful of pixels around the outer edge receive only one sample.

However, there are several ways in which the noise modeling used in this section simplifies matters:

- The white noise level for each detector is different.
- The total integration time per pixel is not uniform. Some pixels end up receiving more detector samples than others, as shown in Figure 7.14.
- The detector noise is not white. Equation 7.17 is strictly only true for a noise spectrum that is white, while the detector noise spectrums have roll-offs due to the detector time constant τ_{eff}, SQUID noise, a roll-off due to the SQUID servo loop, and other features. Because the noise roll-offs reduce the variance of the detector timestream, this should tend to reduce noise in the map. However, the roll-offs also mean that consecutive samples in a detector timestream are correlated, so that averaging them will not reduce noise by the full "square-root of the number of samples" factor that is appropriate for uncorrelated noise.

A more careful analysis of these factors would be useful, but has not yet been performed.

Chapter 8

Summary and Future Work

This dissertation has described the motivation for, the design of, and the operation of a 350 GHz video imaging system intended for concealed weapons detection. The system uses superconducting Transition Edge Sensor (TES) bolometers to detect the 350 GHz light, and the first of four planned 251-detector sub-arrays has been installed into the system. The spatial resolution is 1.4 cm FWHM at the system focus distance of 17 m, and the system has sufficient sensitivity to take video images that reveal the presence of a knife concealed under a cotton shirt. At 6 frames per second, observing a 0.78 m $\times$ 0.55 m field of view with 1 cm pixels, the Noise Equivalent Temperature Difference (NETD) of video frames observing a uniform temperature distribution is 100 mK. This meets the requirements on NETD outlined in Section 1.2 for challenging passive imaging scenarios. Video images of realistic scenes have higher NETD due to artifacts of the scanning process, but algorithmic approaches to eliminating these artifacts have been outlined.

8.1 Future Work on This System

Future work on this system should focus on improving image processing algorithms, solving the existing technical problems and using the system to perform studies of passive imaging phenomenology. Image processing was addressed in Section 7.8.

There are three technical problems with the system that should be addressed: the elliptical beams, the low optical efficiency, and the high detector noise. It is not known whether the beam ellipticity is caused by a problem inside the cryostat (such as poor alignment between detectors and feedhorns) or outside the cryostat (such as poor alignment of the cryostat and beams with the primary and secondary mirrors). One approach for distinguishing between these two possibilities is to measure the beam shapes immediately outside the cryostat window. Manufacturing errors in one or more of the optical components are also a possibility.

Solving the optical efficiency problem requires understanding where in the optical chain the efficiency loss occurs. A first step towards understanding this would be to measure the optical efficiency at the cryostat window by chopping between warm and cold loads. If this efficiency is higher that the efficiency at the far-field focal plane, this would be a sign that the lost efficiency is due to optical spillover. If the efficiency is that same, this would indicate that the optical power is lost inside the cryostat. Measurement of the far-field optical efficiency of all working detectors might reveal a trend across the focal plane, which could point to a fabrication problem with either the detectors or the feedhorn array.

Determining the source of the excess detector noise could be more challenging. If the noise drops significantly when the cryostat is closed optically, that will be an indication that the problem is caused by excess photon noise. Because the optical efficiency is poor, this photon noise would likely be caused by stray light reaching the detectors, so the 1 K focal plane should be checked carefully for this. If high noise persists when the cryostat is optically closed, that could be a sign that the noise originates in the detectors, possibly due to dangling heat capacity.

A second 251-detector sub-array was fabricated simultaneously with the sub-array that is currently installed in the 350 GHz Video Imager. This sub-array was designed to have a G value 16 % lower than the sub-array that is currently installed, but should be otherwise identical. If the detector noise, optical load, or optical efficiency are significantly different between these two sub-arrays, this could indicate a problem in fabrication.

Installation of the second sub-array will also improve system performance. The additional detectors could be used to reduce image NETD, increase the field of view, or increase the video frame rate.

Studies of phenomenology will focus on different sizes, shapes, and types of concealed objects, combined with different types of clothing. Because the 350 GHz Video Imager has been built by a team with little prior experience in the area of passive security imaging, we should identify partners among potential users of standoff passive imaging systems. This will help us to ensure that the tests that we carry out will lead to results that are applicable to realistic operational scenarios, and can be compared to results using other imaging techniques.

8.2 Polarization and Multi-band Imaging

Following phenomenology studies using the existing system, there will be an opportunity to use it to test polarization-sensitive detectors as well as detectors that are sensitive to more than one optical band (i.e., multiple colors). Polarization-sensitive and multi-color TES detector technology already exists and could quickly be deployed into the existing system for testing.

Development of polarization-sensitive TES bolometers has been driven by the desire to measure the polarization of the Cosmic Microwave Background radiation. Polarization-sensitive focal planes have been installed in a number of telescopes and are currently taking data [54–57, 85]. Figure 8.1 shows a photograph of a polarization-sensitive detector developed by a collaboration of which I am a member [94]. Ring-loaded feedhorns direct light onto a pair of orthogonal “fins” which couple light onto microstrip transmission lines. The light is then split into two frequency bands defined by quarter wave stub filters. Each polarization in each frequency band is detected by a separate TES bolometer. This allows a single feedhorn on the focal plane to detect not only two polarizations, but also two colors.

It is not clear whether polarization-sensitive detectors, or multi-color detectors, will provide advantages for passive security imaging. Reflected light will be polarized to some extent, but since the concealed objects are illuminated from all directions, one would expect the net polarization to be low. Nevertheless, there may be scenarios where uneven illumination is expected, and in such cases polarization may provide additional information. Models addressing the usefulness of polarization for security imaging do exist, and should be used when deciding whether or not to build a polarization-sensitive system [95].

The primary advantage of multi-color detectors is that they allow higher optical bandwidth while avoiding atmospheric absorption lines. It may be that implementing band-stop filters could achieve the same benefit at lower cost. An intriguing idea would be to attempt to use color information to identify different materials. For example, many explosive materials have absorption features in the 0.6 THz – 3 THz region [2, 3]. Unfortunately most of these features are above 1 THz, where clothing and the atmosphere are much less transparent than at 350 GHz.

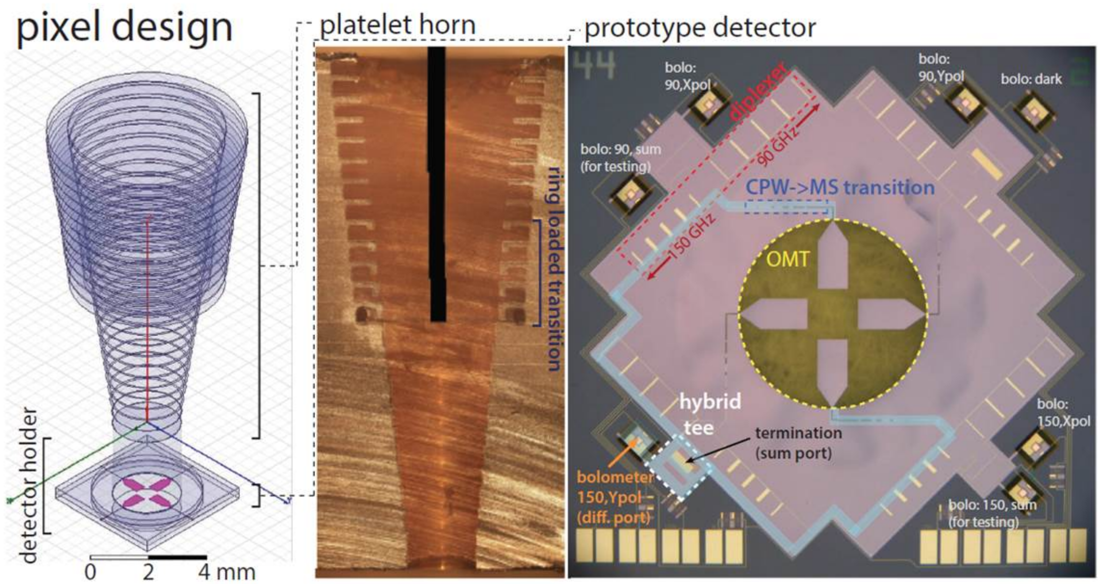

Figure 8.1: A multi-color, polarization-sensitive detector. This detector is sensitive to both polarizations in bands centered at 90 GHz and 150 GHz. Light is coupled onto the detector by a ring-loaded feedhorn. On the left is a schematic of the feedhorns, in the middle is a cross-sectional photograph of a prototype feedhorn. The feedhorns are assembled from micro-machined silicon wafers that are then Au-plated. On the right is a prototype pixel. Two pairs of fins ("OMT") couple each polarization onto microstrip. A diplexer separates the 90 GHz and 150 GHz signals. The "hybrid tee" rejects unwanted waveguide modes. This figure is taken from [94], which contains more details on these detectors.

8.3 Directions for Future Systems

Following resolution of the remaining technical issues, and investigation of imaging phenomenology, we will be ready to design a second-generation system. Such a system would be designed with a specific operational scenario in mind, which would set requirements for standoff distance, resolution and image NETD. But regardless of the details of the specifications, areas to focus on for such a system are likely to include size/portability and cost.

The overall system size is set by the standoff distance and desired spatial resolution, which directly determine the size of the optical aperture via Equation 1.1. Moving to higher frequencies can reduce the size of the required optical aperture, but at the cost of lower image contrast due to decreased transmission through clothing and the atmosphere.

Nevertheless, this trade-off may be worthwhile for some applications. There are no technical reasons why TES bolometers could not work well at frequencies of 1 THz.

If the target application requires the aperture size to remain at 1.3 m, or even become larger, it may be desirable to use a different focusing element than that used in this system. Possibilities include segmented mirrors (which have proven successful for larger apertures [96]), aluminized plastic mirrors, or a large-diameter Fresnel lens [97].

Reducing the size of the optical aperture or moving to a Fresnel lens will likely reduce the cost of the system. Three other ways to potentially reduce cost are to eliminate the need for scanning, operate at a higher bath temperature, or migrate to a detector technology that is easier to fabricate.

Eliminating the need for scanning will reduce cost by simplifying the design of the optical components and removing the need for motors to move those components. But in order to maintain the same field of view, as well as ensure a Nyquist-sampled focal plane, many more detectors are required. The cost and number of required detectors will depend on the desired field of view, optical design, and target wavelength. Work on multiplexing techniques capable of reading out 10,000 or more TES detectors has begun [98], but this technology is not as mature as the TDM readout system used for the 350 GHz Video Imager. A careful cost analysis of all of these factors will need to be performed.

Operating at higher bath temperatures can reduce cost if the new bath temperature can be achieved without the use of a secondary cooling system such as the He4-sorption refrigerator used for the 350 GHz Video Imager. As described in Section 5.2, it should be possible to make photon-noise-limited TES bolometers operating at a bath temperature of 3.6 K. This bath temperature can be reached through the use of a cryocooler only, with no other refrigeration stages needed. The ideal T_c for this bath temperature would be ~ 6.5 K. However, to-date little work has been done on making voltage-biased TES bolometers work at such (relatively) high temperatures, so it is not clear what problems might appear that would need to be solved. Again, a careful cost analysis is required.

Finally, voltage-biased TES bolometers are not the only low-temperature detectors that can be fabricated in large quantities, read out with a reasonable number of wires, and achieve photon-noise-limited performance. One promising detector technology is the Microwave Kinetic Inductance Detector (MKID). As mentioned in Section 2.3, one group is already working on a passive imaging system that will use these detectors.

Like TES detectors, MKIDs use superconducting materials at low temperatures, but the principle of operation is different. The superconducting material is chosen so that its gap energy $2\Delta = 3.5 k_b T_c$ is below the energy $h\nu$ of the photons to be detected. Light is focused directly onto the superconducting film, so that it breaks Cooper pairs, which induces a change in the inductance of the superconductor. By making the superconductor a part of a resonant circuit, this change in inductance can be detected as a change in the resonant frequency. The detector operating temperature is at or below $T_c/5$ to suppress thermal generation of quasiparticles. This approach to detection of light offers a natural way to multiplex many detectors on a single readout line, because the resonant frequency can be placed at GHz frequencies where large amounts of readout bandwidth are available.

The -10 dB lower band edge for the 350 GHz Video Imager is 318 GHz, so the maximum T_c for an MKID detector is 4.3 K, a value that can be achieved using TiN or Ti-TiN-Ti films [99, 100]. The operating temperature would be $4.3\,\mathrm{K}/5 = 0.86\,\mathrm{K}$, which should be achievable with an improved 1 K cryogenic design.

MKID detectors reduce fabrication cost because fewer material layers and fabrication steps are required. They also reduce wiring cost because a single coaxial cable can bias and read out many detectors. But they also require more complicated room-temperature electronics to perform the readout, as well as low-noise amplifiers inside the cryostat. The technology is also not yet as mature as TES detectors with multiplexed SQUID readout. Once again, a careful evaluation of the costs and benefits of MKID detectors will need to be performed.

In summary, several promising approaches for reducing system portability, cost, and complexity are available. The 350 GHz Video Imager described in this dissertation demonstrates that 100 mK NETD video images at 17 m standoff distances are achievable using large-format arrays of cryogenic detectors. Following resolution of the remaining technical issues and investigation of imaging phenomenology, we will be ready to design a second-generation system. The second-generation system will start to bring the advantages of practical, cost-effective, high-sensitivity passive imaging to the security community.

Bibliography

[1] Paul W. Kruse. “Why The Military Interest In Near-Millimeter Wave Imaging?” In: *Proceedings of the SPIE*. Millimeter Optics. Vol. 0259. 1981, pp. 94–99. DOI: 10.1117/12.959648.

[2] John F. Federici, Brian Schulkin, Feng Huang, Dale Gary, Robert Barat, Filipe Oliveira, and David Zimdars. “THz imaging and sensing for security applications—explosives, weapons and drugs”. In: *Semiconductor Science and Technology* 20.7 (July 1, 2005), S266. ISSN: 0268-1242. DOI: 10.1088/0268-1242/20/7/018.

[3] A. Giles Davies, Andrew D. Burnett, Wenhui Fan, Edmund H. Linfield, and John E. Cunningham. “Terahertz spectroscopy of explosives and drugs”. In: *Materials Today* 11.3 (Mar. 2008), pp. 18–26. ISSN: 1369-7021. DOI: 10.1016/S1369-7021(08)70016-6.

[4] Z. Popovic and E.N. Grossman. “THz Metrology and Instrumentation”. In: *IEEE Transactions on Terahertz Science and Technology* 1.1 (Sept. 2011), pp. 133–144. ISSN: 2156-342X. DOI: 10.1109/TTHZ.2011.2159553.

[5] A. Rogalski and F. Sizov. “Terahertz detectors and focal plane arrays”. In: *Opto-Electronics Review* 19.3 (Sept. 1, 2011), pp. 346–404. ISSN: 1230-3402, 1896-3757. DOI: 10.2478/s11772-011-0033-3.

[6] George Rieke. *Detection of Light: From the Ultraviolet to the Submillimeter*. 2nd Edition. Cambridge University Press, 2003. 380 pp. ISBN: 9780521017107.

[7] P. L. Richards. “Bolometers for infrared and millimeter waves”. In: *Journal of Applied Physics* 76.1 (July 1, 1994), pp. 1–24. ISSN: 0021-8979, 1089-7550. DOI: 10.1063/1.357128.

[8] K. D. Irwin. “An application of electrothermal feedback for high resolution cryogenic particle detection”. In: *Applied Physics Letters* 66.15 (Apr. 10, 1995), pp. 1998–2000. ISSN: 0003-6951, 1077-3118. DOI: 10.1063/1.113674.

[9] J. A. Chervenak, K. D. Irwin, E. N. Grossman, John M. Martinis, C. D. Reintsema, and M. E. Huber. “Superconducting multiplexer for arrays of transition edge sensors”. In: *Applied Physics Letters* 74.26 (June 28, 1999), pp. 4043–4045. ISSN: 0003-6951, 1077-3118. DOI: 10.1063/1.123255.

[10] Jongsoo Yoon, John Clarke, J. M. Gildemeister, Adrian T. Lee, M. J. Myers, P. L. Richards, and J. T. Skidmore. "Single superconducting quantum interference device multiplexer for arrays of low-temperature sensors". In: *Applied Physics Letters* 78.3 (2001), pp. 371–373. ISSN: 0003-6951, 1077-3118. DOI: 10.1063/1.1338963.

[11] W. S. Holland, D. Bintley, E. L. Chapin, A. Chrysostomou, G. R. Davis, J. T. Dempsey, W. D. Duncan, M. Fich, P. Friberg, M. Halpern, K. D. Irwin, T. Jenness, B. D. Kelly, M. J. MacIntosh, E. I. Robson, D. Scott, P. a. R. Ade, E. Atad-Ettedgui, D. S. Berry, S. C. Craig, X. Gao, A. G. Gibb, G. C. Hilton, M. I. Hollister, J. B. Kycia, D. W. Lunney, H. McGregor, D. Montgomery, W. Parkes, R. P. J. Tilanus, J. N. Ullom, C. A. Walther, A. J. Walton, A. L. Woodcraft, M. Amiri, D. Atkinson, B. Burger, T. Chuter, I. M. Coulson, W. B. Doriese, C. Dunare, F. Economou, M. D. Niemack, H. a. L. Parsons, C. D. Reintsema, B. Sibthorpe, I. Smail, R. Sudiwala, and H. S. Thomas. "SCUBA-2: the 10 000 pixel bolometer camera on the James Clerk Maxwell Telescope". In: *Monthly Notices of the Royal Astronomical Society* 430.4 (Apr. 21, 2013), pp. 2513–2533. ISSN: 0035-8711, 1365-2966. DOI: 10.1093/mnras/sts612.

[12] J. E. Bjarnason, T. L. J. Chan, A. W. M. Lee, M. A. Celis, and E. R. Brown. "Millimeter-wave, terahertz, and mid-infrared transmissionthrough common clothing". In: *Applied Physics Letters* 85.4 (July 23, 2004), pp. 519–521. ISSN: 0003-6951, 1077-3118. DOI: 10.1063/1.1771814.

[13] David M. Sheen, Douglas L. McMakin, and Thomas E. Hall. "Cylindrical millimeter-wave imaging technique for concealed weapon detection". In: *Proceedings of the SPIE*. Vol. 3240. 1998, pp. 242–250. DOI: 10.1117/12.300061.

[14] Douglas L. McMakin, Paul E. Keller, David M. Sheen, and Thomas E. Hall. "Dual-surface dielectric depth detector for holographic millimeter-wave security scanners". In: *Proceedings of the SPIE*. Vol. 7309. 2009, pages. DOI: 10.1117/12.817882.

[15] Brendan N. Lyons, Emil Entchev, and Michael K. Crowley. "Reflect-array based mm-wave people screening system". In: vol. 8900. 2013, pages. DOI: 10.1117/12.2028108.

[16] R. Appleby and H.B. Wallace. "Standoff Detection of Weapons and Contraband in the 100 GHz to 1 THz Region". In: *IEEE Transactions on Antennas and Propagation* 55.11 (2007), pp. 2944–2956. ISSN: 0018-926X. DOI: 10.1109/TAP.2007.908543.

[17] Max Born and Emil Wolf. *Principles of Optics: Electromagnetic Theory of Propagation, Interference and Diffraction of Light*. Cambridge University Press, Oct. 13, 1999. 1007 pp. ISBN: 9780521642224.

[18] R. Appleby. "Passive millimetre–wave imaging and how it differs from terahertz imaging". In: *Philosophical Transactions of the Royal Society of London. Series A: Mathematical, Physical and Engineering Sciences* 362.1815 (Feb. 15, 2004). PMID: 15306527, pp. 379–393. ISSN: 1364-503X, 1471-2962. DOI: 10.1098/rsta.2003.1323.

[19] Douglas T. Petkie, Corey Casto, Frank C. De Lucia, Steven R. Murrill, Brian Redman, Richard L. Espinola, Charmaine C. Franck, Eddie L. Jacobs, Steven T. Griffin, Carl E. Halford, Joe Reynolds, Sean O'Brien, and David Tofsted. "Active and passive imaging in the THz spectral region: phenomenology, dynamic range, modes, and illumination". In: *Journal of the Optical Society of America B* 25.9 (Sept. 1, 2008), pp. 1523–1531. DOI: `10.1364/JOSAB.25.001523`.

[20] J. W. Goodman. "Some fundamental properties of speckle". In: *Journal of the Optical Society of America* 66.11 (Nov. 1, 1976), pp. 1145–1150. DOI: `10.1364/JOSA.66.001145`.

[21] Douglas T. Petkie, Jennifer A. Holt, Mark A. Patrick, and Frank C. De Lucia. "Multimode illumination in the terahertz for elimination of target orientation requirements and minimization of coherent effects in active imaging systems". In: *Optical Engineering* 51.9 (2012), pp. 091604–1. ISSN: 0091-3286. DOI: `10.1117/1.OE.51.9.091604`.

[22] Mark A. Patrick, Jennifer A. Holt, Colin D. Joye, and Frank C. De Lucia. "Elimination of speckle and target orientation requirements in millimeter-wave active imaging by modulated multimode mixing illumination". In: *Journal of the Optical Society of America A* 29.12 (Dec. 1, 2012), pp. 2643–2656. DOI: `10.1364/JOSAA.29.002643`.

[23] K.B. Cooper, R.J. Dengler, N. Llombart, B. Thomas, G. Chattopadhyay, and P.H. Siegel. "THz Imaging Radar for Standoff Personnel Screening". In: *IEEE Transactions on Terahertz Science and Technology* 1.1 (Sept. 2011), pp. 169–182. ISSN: 2156-342X. DOI: `10.1109/TTHZ.2011.2159556`.

[24] Neil A. Salmon. "Scene simulation for passive and active millimetre- and submillimetre-wave imaging for security scanning and medical applications". In: *Proceedings of the SPIE*. Passive Millimetre-Wave and Terahertz Imaging and Technology. Vol. 5619. 2004, pp. 129–135. DOI: `10.1117/12.581401`.

[25] Steven W. Smith. *The Scientist & Engineer's Guide to Digital Signal Processing*. California Technical Pub, 1997. 626 pp. ISBN: 978-0966017632.

[26] Joseph Nemarich. *Microbolometer Detectors for Passive Millimeter-Wave Imaging*. ARL-TR-3460. Army Research Laboratory, Mar. 2005.

[27] James H. Schaffner, Jonathan J. Lynch, Keith V. Guinn, Joel N. Schulman, Harris P. Moyer, Ross Bowen, and Marcel Musni. "A wideband radiometer module for an unamplified direct detection scalable W-band imaging array". In: *Proceedings of the SPIE*. Vol. 6948. May 1, 2008, p. 5. ISBN: 0277-786X. DOI: `10.1117/12.776893`.

[28] David Wikner and Erich Grossman. "Demonstration of a passive, low-noise, millimeter-wave detector array for imaging". In: *Proceedings of the SPIE*. Vol. 7309. 2009, pages. DOI: `10.1117/12.821197`.

[29] Chris Mann. "First demonstration of a vehicle mounted 250GHz real time passive imager". In: *Proceedings of the SPIE*. Vol. 7311. 2009, pages. DOI: `10.1117/12.821775`.

[30] Digital Barriers. *Extra sensory perception: see the threat more clearly with TeraHertz. A technical comparison of the ThurVision solution*. V1.01 4-2013 TP-THV.

[31] Michael Tinkham. *Introduction to Superconductivity*. 2nd Edition. Mineola, NY: Dover Publications, Inc., 1996. 482 pp. isbn: 9780486134727.

[32] D. H. Andrews, W. F. Brucksch Jr, W. T. Ziegler, and E. R. Blanchard. “Attenuated Superconductors I. For Measuring Infra-Red Radiation”. In: *Review of Scientific Instruments* 13.7 (July 1942), pp. 281–292. issn: 0034-6748, 1089-7623. doi: 10.1063/1.1770037.

[33] J. Clarke, G. I. Hoffer, P. L. Richards, and N.-H. Yeh. “Superconductive bolometers for submillimeter wavelengths”. In: *Journal of Applied Physics* 48.12 (Dec. 1977), pp. 4865–4879. issn: 0021-8979, 1089-7550. doi: 10.1063/1.323612.

[34] K. D. Irwin and G. C. Hilton. “Transition-Edge Sensors”. In: *Cryogenic Particle Detection*. Ed. by C. Enss. Topics in Applied Physics 99. Springer-Verlag Berlin Heidelberg, 2005, pp. 63–149. isbn: 3-540-20113-0.

[35] Erik Heinz, Marco Schubert, Michael Starkloff, Torsten May, Detlef Born, Gabriel Zieger, Günter Thorwirth, Solveig Anders, Vyacheslav Zakosarenko, Torsten Krause, André Krüger, Marco Schulz, and Hans-Georg Meyer. “Toward high-sensitivity and high-resolution submillimeter-wave video imaging”. In: *Optical Engineering* 50.11 (2011), pages. issn: 0091-3286. doi: 10.1117/1.3654089.

[36] Erik Heinz, Torsten May, Detlef Born, Gabriel Zieger, Katja Peiselt, Anika Brömel, Solveig Anders, Vyacheslav Zakosarenko, Torsten Krause, André Krüger, Marco Schulz, and Hans-Georg Meyer. “Development of passive submillimeter-wave video imaging systems”. In: *Proceedings of the SPIE*. Vol. 8715. 2013, pages. doi: 10.1117/12.2018848.

[37] Torsten May. “Next Generation of the Sub-millimetre Wave Security Camera “THZ-Videocam””. KRYO 2013 Workshop. Oct. 8, 2013.

[38] Erich Grossman, Charles Dietlein, Juha Ala-Laurinaho, Mikko Leivo, Leif Gronberg, Markus Gronholm, Petteri Lappalainen, Anssi Rautiainen, Aleksi Tamminen, and Arttu Luukanen. “Passive terahertz camera for standoff security screening”. In: *Applied Optics* 49.19 (July 1, 2010), E106–E120. doi: 10.1364/AO.49.00E106.

[39] A. Luukanen, M. M. Leivo, A. Rautiainen, M. Grönholm, H. Toivanen, L. Grönberg, P. Helistö, A. Mäyrä, M. Aikio, and E. N. Grossman. “Applications of superconducting bolometers in security imaging”. In: *Journal of Physics: Conference Series* 400.5 (Dec. 17, 2012), p. 052018. issn: 1742-6596. doi: 10.1088/1742-6596/400/5/052018.

[40] Jari S. Penttilä, Hannu Sipola, Panu Helistö, and Heikki Seppä. “Low-noise readout of superconducting bolometers based on electrothermal feedback”. In: *Superconductor Science and Technology* 19.4 (Apr. 1, 2006), p. 319. issn: 0953-2048. doi: 10.1088/0953-2048/19/4/013.

[41] Peter K. Day, Henry G. LeDuc, Benjamin A. Mazin, Anastasios Vayonakis, and Jonas Zmuidzinas. "A broadband superconducting detector suitable for use in large arrays". In: *Nature* 425.6960 (Oct. 23, 2003), pp. 817–821. ISSN: 0028-0836. DOI: 10.1038/nature02037.

[42] K. Wood, S. Doyle, E. Pascale, S. Rowe, P. Hargrave, C. Dunscombe, W. Grainger, A. Papageorgiou, L. Spencer, and P. Mauskopf. "KIDCAM — A passive THz imager". In: *2011 36th International Conference on Infrared, Millimeter and Terahertz Waves (IRMMW-THz)*. 2011 36th International Conference on Infrared, Millimeter and Terahertz Waves (IRMMW-THz). Oct. 2011, pp. 1–2. DOI: 10.1109/irmmw-THz.2011.6105184.

[43] John C. Mather. "Bolometer noise: nonequilibrium theory". In: *Applied Optics* 21.6 (Mar. 15, 1982), pp. 1125–1129. DOI: 10.1364/AO.21.001125.

[44] Douglas A. Bennett, Daniel S. Swetz, Daniel R. Schmidt, and Joel N. Ullom. "Resistance in transition-edge sensors: A comparison of the resistively shunted junction and two-fluid models". In: *Physical Review B* 87.2 (2013), p. 020508. DOI: 10.1103/PhysRevB.87.020508.

[45] W. S. Boyle and K. F. Rodgers Jr. "Performance Characteristics of a New Low-Temperature Bolometer". In: *Journal of the Optical Society of America* 49.1 (1959), pp. 66–69. DOI: 10.1364/JOSA.49.000066.

[46] Jonas Zmuidzinas. "Thermal Noise and Correlations in Photon Detection". In: *Applied Optics* 42.25 (Sept. 1, 2003), pp. 4989–5008. DOI: 10.1364/AO.42.004989.

[47] M.J Devlin, S.R Dicker, J Klein, and M.P Supanich. "A high capacity completely closed-cycle 250 mK He-3 refrigeration system based on a pulse tube cooler". In: *Cryogenics* 44.9 (Sept. 2004), pp. 611–616. ISSN: 0011-2275. DOI: 10.1016/j.cryogenics.2004.03.001.

[48] Lake Shore Cryogenics, Inc. *Cryogenic Reference Tables*. URL: http://www.lakeshore.com/Documents/LSTC_appendixI_l.pdf (visited on 02/24/2014).

[49] Carole E. Tucker and Peter A. R. Ade. "Thermal filtering for large aperture cryogenic detector arrays". In: *Proceedings of the SPIE*. Millimeter and Submillimeter Detectors and Instrumentation for Astronomy III. Vol. 6275. 2006, 62750T. DOI: 10.1117/12.673159.

[50] James W. Lamb. "Miscellaneous data on materials for millimetre and submillimetre optics". In: *International Journal of Infrared and Millimeter Waves* 17.12 (Dec. 1, 1996), pp. 1997–2034. ISSN: 0195-9271, 1572-9559. DOI: 10.1007/BF02069487.

[51] Sophocles J. Ordanidis. *Electromagnetic Waves and Antennas*. Feb. 26, 2014. URL: http://eceweb1.rutgers.edu/~orfanidi/ewa/.

[52] Peter A. R. Ade, Giampaolo Pisano, Carole Tucker, and Samuel Weaver. "A review of metal mesh filters". In: *Proceedings of the SPIE*. Millimeter and Submillimeter Detectors and Instrumentation for Astronomy III. Vol. 6275. 2006, 62750U. DOI: 10.1117/12.673162.

[53] D. S. Swetz, P. a. R. Ade, M. Amiri, J. W. Appel, E. S. Battistelli, B. Burger, J. Chervenak, M. J. Devlin, S. R. Dicker, W. B. Doriese, R. Dünner, T. Essinger-Hileman, R. P. Fisher, J. W. Fowler, M. Halpern, M. Hasselfield, G. C. Hilton, A. D. Hincks, K. D. Irwin, N. Jarosik, M. Kaul, J. Klein, J. M. Lau, M. Limon, T. A. Marriage, D. Marsden, K. Martocci, P. Mauskopf, H. Moseley, C. B. Netterfield, M. D. Niemack, M. R. Nolta, L. A. Page, L. Parker, S. T. Staggs, O. Stryzak, E. R. Switzer, R. Thornton, C. Tucker, E. Wollack, and Y. Zhao. "Overview of the Atacama Cosmology Telescope: Receiver, Instrumentation, and Telescope Systems". In: *The Astrophysical Journal Supplement Series* 194.2 (June 1, 2011), p. 41. issn: 0067-0049. doi: 10.1088/0067-0049/194/2/41.

[54] B. Keating, S. Moyerman, D. Boettger, J. Edwards, G. Fuller, F. Matsuda, N. Miller, H. Paar, G. Rebeiz, I. Schanning, M. Shimon, N. Stebor, K. Arnold, D. Flanigan, W. Holzapfel, J. Howard, Z. Kermish, A. Lee, M. Lungu, M. Myers, H. Nishino, R. O'Brient, E. Quealy, C. Reichardt, P. Richards, C. Shimmin, B. Steinbach, A. Suzuki, O. Zahn, J. Borrill, C. Cantalupo, E. Kisner, E. Linder, M. Sholl, H. Spieler, A. Anthony, N. Halverson, J. Errard, G. Fabbian, M. Le Jeune, R. Stompor, A. Jaffe, D. O'Dea, Y. Chinone, M. Hasegawa, M. Hazumi, T. Matsumura, H. Morii, A. Shimizu, T. Tomaru, P. Hyland, M. Dobbs, P. Ade, W. Grainger, and C. Tucker. "Ultra High Energy Cosmology with POLARBEAR". In: *arXiv:1110.2101 [astro-ph]* (Oct. 10, 2011).

[55] R. O'Brient, P. A. R. Ade, Z. Ahmed, R. W. Aikin, M. Amiri, S. Benton, C. Bischoff, J. J. Bock, J. A. Bonetti, J. A. Brevik, B. Burger, G. Davis, P. Day, C. D. Dowell, L. Duband, J. P. Filippini, S. Fliescher, S. R. Golwala, J. Grayson, M. Halpern, M. Hasselfield, G. Hilton, V. V. Hristov, H. Hui, K. Irwin, S. Kernasovskiy, J. M. Kovac, C. L. Kuo, E. Leitch, M. Lueker, K. Megerian, L. Moncelsi, C. B. Netterfield, H. T. Nguyen, R. W. Ogburn, C. L. Pryke, C. Reintsema, J. E. Ruhl, M. C. Runyan, R. Schwarz, C. D. Sheehy, Z. Staniszewski, R. Sudiwala, G. Teply, J. E. Tolan, A. D. Turner, R. S. Tucker, A. Vieregg, D. V. Wiebe, P. Wilson, C. L. Wong, W. L. K. Wu, and K. W. Yoon. "Antenna-coupled TES bolometers for the Keck array, Spider, and Polar-1". In: *Proceedings of the SPIE*. Vol. 8452. 2012, pages. doi: 10.1117/12.927214.

[56] J. E. Austermann, K. A. Aird, J. A. Beall, D. Becker, A. Bender, B. A. Benson, L. E. Bleem, J. Britton, J. E. Carlstrom, C. L. Chang, H. C. Chiang, H. M. Cho, T. M. Crawford, A. T. Crites, A. Datesman, T. de Haan, M. A. Dobbs, E. M. George, N. W. Halverson, N. Harrington, J. W. Henning, G. C. Hilton, G. P. Holder, W. L. Holzapfel, S. Hoover, N. Huang, J. Hubmayr, K. D. Irwin, R. Keisler, J. Kennedy, L. Knox, A. T. Lee, E. Leitch, D. Li, M. Lueker, D. P. Marrone, J. J. McMahon, J. Mehl, S. S. Meyer, T. E. Montroy, T. Natoli, J. P. Nibarger, M. D. Niemack, V. Novosad, S. Padin, C. Pryke, C. L. Reichardt, J. E. Ruhl, B. R. Saliwanchik, J. T. Sayre, K. K. Schaffer, E. Shirokoff, A. A. Stark, K. Story, K. Vanderlinde, J. D. Vieira, G. Wang, R. Williamson, V. Yefremenko, K. W. Yoon, and O. Zahn. "SPTpol: an instrument for CMB polarization measurements with the South Pole Telescope". In: *Proceedings of the SPIE*. Vol. 8452. 2012, pages. doi: 10.1117/12.927286.

[57] M. D. Niemack, P. A. R. Ade, J. Aguirre, F. Barrientos, J. A. Beall, J. R. Bond, J. Britton, H. M. Cho, S. Das, M. J. Devlin, S. Dicker, J. Dunkley, R. Dünner, J. W. Fowler, A. Hajian, M. Halpern, M. Hasselfield, G. C. Hilton, M. Hilton, J. Hubmayr, J. P. Hughes, L. Infante, K. D. Irwin, N. Jarosik, J. Klein, A. Kosowsky, T. A. Marriage, J. McMahon, F. Menanteau, K. Moodley, J. P. Nibarger, M. R. Nolta, L. A. Page, B. Partridge, E. D. Reese, J. Sievers, D. N. Spergel, S. T. Staggs, R. Thornton, C. Tucker, E. Wollack, and K. W. Yoon. "ACTPol: a polarization-sensitive receiver for the Atacama Cosmology Telescope". In: *Proceedings of the SPIE*. Vol. 7741. 2010, pages. DOI: 10.1117/12.857464.

[58] D. Schwan, P. a. R. Ade, K. Basu, A. N. Bender, F. Bertoldi, H.-M. Cho, G. Chon, John Clarke, M. Dobbs, D. Ferrusca, R. Güsten, N. W. Halverson, W. L. Holzapfel, C. Horellou, D. Johansson, B. R. Johnson, J. Kennedy, Z. Kermish, R. Kneissl, T. Lanting, A. T. Lee, M. Lueker, J. Mehl, K. M. Menten, D. Muders, F. Pacaud, T. Plagge, C. L. Reichardt, P. L. Richards, R. Schaaf, P. Schilke, M. W. Sommer, H. Spieler, C. Tucker, A. Weiss, B. Westbrook, and O. Zahn. "Invited Article: Millimeter-wave bolometer array receiver for the Atacama pathfinder experiment Sunyaev-Zel'dovich (APEX-SZ) instrument". In: *Review of Scientific Instruments* 82.9 (Sept. 29, 2011), p. 091301. ISSN: 0034-6748, 1089-7623. DOI: 10.1063/1.3637460.

[59] J. E. Carlstrom, P. A. R. Ade, K. A. Aird, B. A. Benson, L. E. Bleem, S. Busetti, C. L. Chang, E. Chauvin, H.-M. Cho, T. M. Crawford, A. T. Crites, M. A. Dobbs, N. W. Halverson, S. Heimsath, W. L. Holzapfel, J. D. Hrubes, M. Joy, R. Keisler, T. M. Lanting, A. T. Lee, E. M. Leitch, J. Leong, W. Lu, M. Lueker, D. Luong-Van, J. J. McMahon, J. Mehl, S. S. Meyer, J. J. Mohr, T. E. Montroy, S. Padin, T. Plagge, C. Pryke, J. E. Ruhl, K. K. Schaffer, D. Schwan, E. Shirokoff, H. G. Spieler, Z. Staniszewski, A. A. Stark, C. Tucker, K. Vanderlinde, J. D. Vieira, and R. Williamson. "The 10 Meter South Pole Telescope". In: *Publications of the Astronomical Society of the Pacific* 123.903 (May 1, 2011), pp. 568–581. DOI: 10.1086/659879.

[60] P. J. B. Clarricoats. *Corrugated Horns for Microwave Antennas*. In collab. with A. D. Olver. Vol. 18. IEE Electromagnetic waves series. London, UK: Peter Peregrinus Ltd., 1984. 231 pp. ISBN: 0863410030.

[61] Constantine A Balanis. *Antenna Theory: Analysis and Design*. Hoboken, NJ: Wiley Interscience, 2005. ISBN: 047166782X 9780471667827.

[62] Paul F Goldsmith. *Quasioptical systems: Gaussian beam quasioptical propagation and applications*. Piscataway, NJ: IEEE Press, 1998. ISBN: 0780334396 9780780334397 0412839407 9780412839405.

[63] H. E. Green. "The Radiation Pattern of a Conical Horn". In: *Journal of Electromagnetic Waves and Applications* 20.9 (2006), pp. 1149–1160. ISSN: 0920-5071. DOI: 10.1163/156939306777442999.

[64] M.S. Narasimhan and B.V. Rao. "Modes in a conical horn: new approach". In: *Proceedings of the Institution of Electrical Engineers* 118.2 (1971), p. 287. ISSN: 00203270. DOI: 10.1049/piee.1971.0050.

[65] J. W Ekin. *Experimental techniques for low-temperature measurements: cryostat design, material properties, and superconductor critical-current testing*. Oxford; New York: Oxford University Press, 2006. ISBN: 0198570546 9780198570547 9780191524691 0191524697.

[66] Thomas A. Milligan. *Modern Antenna Design*. 2nd. John Wiley & Sons, Inc., 2005. 614 pp.

[67] Roger F Harrington. *Time-harmonic electromagnetic fields*. New York: John Wiley & sons, 2001. ISBN: 9780471208068 047120806X.

[68] R. Ulrich. "Far-infrared properties of metallic mesh and its complementary structure". In: *Infrared Physics* 7.1 (Mar. 1967), pp. 37–55. ISSN: 0020-0891. DOI: 10.1016/0020-0891(67)90028-0.

[69] Lewis B. Whitbourn and Richard C. Compton. "Equivalent-circuit formulas for metal grid reflectors at a dielectric boundary". In: *Applied Optics* 24.2 (1985), pp. 217–220. DOI: 10.1364/AO.24.000217.

[70] A. Datesman, J. McMahon, L. Bleem, R. Weikle, V. Yefremenko, Gensheng Wang, V. Novosad, C. Chang, A. Crites, J. Mehl, S. Meyer, and J. Carlstrom. "Analytical solutions for the design and evaluation of absorber-coupled waveguide bolometer detectors". In: *Microwave Symposium Digest (MTT), 2011 IEEE MTT-S International*. Microwave Symposium Digest (MTT), 2011 IEEE MTT-S International. June 2011, pp. 1–4. DOI: 10.1109/MWSYM.2011.5972882.

[71] P. W. Chapman, O. N. Tufte, J. David Zook, and Donald Long. "Electrical Properties of Heavily Doped Silicon". In: *Journal of Applied Physics* 34.11 (1963), pp. 3291–3295. ISSN: 0021-8979, 1089-7550. DOI: 10.1063/1.1729180.

[72] John Clarke and Alex I Braginski, eds. *The SQUID Handbook: Fundamentals and Technology of SQUIDs and SQUID Systems*. Weinheim; Cambridge: Wiley-VCH, 2002. ISBN: 3527402292 9783527402298.

[73] Piet A. J. de Korte, Joern Beyer, Steve Deiker, Gene C. Hilton, Kent D. Irwin, Mike MacIntosh, Sae Woo Nam, Carl D. Reintsema, Leila R. Vale, and Martin E. Huber. "Time-division superconducting quantum interference device multiplexer for transition-edge sensors". In: *Review of Scientific Instruments* 74.8 (July 23, 2003), pp. 3807–3815. ISSN: 0034-6748, 1089-7623. DOI: 10.1063/1.1593809.

[74] Carl D. Reintsema, Jörn Beyer, Sae Woo Nam, Steve Deiker, Gene C. Hilton, Kent Irwin, John Martinis, Joel Ullom, Leila R. Vale, and Mike MacIntosh. "Prototype system for superconducting quantum interference device multiplexing of large-format transition-edge sensor arrays". In: *Review of Scientific Instruments* 74.10 (Sept. 25, 2003), pp. 4500–4508. ISSN: 0034-6748, 1089-7623. DOI: 10.1063/1.1605259.

[75] E. S. Battistelli, M. Amiri, B. Burger, M. Halpern, S. Knotek, M. Ellis, X. Gao, D. Kelly, M. MacIntosh, K. Irwin, and C. Reintsema. "Functional Description of Read-out Electronics for Time-Domain Multiplexed Bolometers for Millimeter and Sub-millimeter Astronomy". In: *Journal of Low Temperature Physics* 151.3 (May 1, 2008), pp. 908–914. ISSN: 0022-2291, 1573-7357. DOI: 10.1007/s10909-008-9772-z.

[76] E. S. Battistelli, M. Amiri, B. Burger, M. J. Devlin, S. R. Dicker, W. B. Doriese, R. Dünner, R. P. Fisher, J. W. Fowler, M. Halpern, M. Hasselfield, G. C. Hilton, A. D. Hincks, K. D. Irwin, M. Kaul, J. Klein, S. Knotek, J. M. Lau, M. Limon, T. A. Marriage, M. D. Niemack, L. Page, C. D. Reintsema, S. T. Staggs, D. S. Swetz, E. R. Switzer, R. J. Thornton, and Y. Zhao. "Automated SQUID tuning procedure for kilo-pixel arrays of TES bolometers on the Atacama Cosmology Telescope". In: *Proceedings of the SPIE*. Vol. 7020. 2008, pages. DOI: 10.1117/12.789738.

[77] *MCEWiki*. 2014. URL: http://e-mode.phas.ubc.ca/mcewiki/index.php/Main_Page (visited on 2014).

[78] MCE Team. *Digital 4-pole Butterworth Low-pass filter - MCEWiki*. MCE Wiki. URL: http://e-mode.phas.ubc.ca/mcewiki/index.php/Digital_4-pole_Butterworth_Low-pass_filter (visited on 2014).

[79] MCE Team. *Data mode - MCEWiki*. MCE Wiki. 2013. URL: http://e-mode.phas.ubc.ca/mcewiki/index.php/Data_mode (visited on 12/23/2013).

[80] B. T. Matthias, T. H. Geballe, and V. B. Compton. "Superconductivity". In: *Reviews of Modern Physics* 35.1 (1963), pp. 1–22. DOI: 10.1103/RevModPhys.35.1.

[81] W. Holmes, J. M. Gildemeister, P. L. Richards, and V. Kotsubo. "Measurements of thermal transport in low stress silicon nitride films". In: *Applied Physics Letters* 72.18 (May 4, 1998), pp. 2250–2252. ISSN: 0003-6951, 1077-3118. DOI: 10.1063/1.121269.

[82] R. C. Zeller and R. O. Pohl. "Thermal Conductivity and Specific Heat of Non-crystalline Solids". In: *Physical Review B* 4.6 (Sept. 15, 1971), pp. 2029–2041. DOI: 10.1103/PhysRevB.4.2029.

[83] B. L. Zink and F. Hellman. "Specific heat and thermal conductivity of low-stress amorphous Si–N membranes". In: *Solid State Communications* 129.3 (2004), pp. 199–204. ISSN: 0038-1098. DOI: 10.1016/j.ssc.2003.08.048.

[84] William S. Corak, M. P. Garfunkel, C. B. Satterthwaite, and Aaron Wexler. "Atomic Heats of Copper, Silver, and Gold from 1 K to 5 K". In: *Physical Review* 98.6 (June 15, 1955), pp. 1699–1707. DOI: 10.1103/PhysRev.98.1699.

[85] A. Kusaka, T. Essinger-Hileman, J. W. Appel, P. Gallardo, K. D. Irwin, N. Jarosik, M. R. Nolta, L. A. Page, L. P. Parker, S. Raghunathan, J. L. Sievers, S. M. Simon, S. T. Staggs, and K. Visnjic. "Modulation of CMB polarization with a warm rapidly-rotating half-wave plate on the Atacama B-Mode Search (ABS) instrument". In: *arXiv:1310.3711 [astro-ph]* (Oct. 14, 2013).

[86] M. J. Persky. "Review of black surfaces for space-borne infrared systems". In: *Review of Scientific Instruments* 70.5 (May 1, 1999), pp. 2193–2217. ISSN: 0034-6748, 1089-7623. DOI: 10.1063/1.1149739.

[87] H. F. C. Hoevers, A. C. Bento, M. P. Bruijn, L. Gottardi, M. a. N. Korevaar, W. A. Mels, and P. A. J. de Korte. "Thermal fluctuation noise in a voltage biased superconducting transition edge thermometer". In: *Applied Physics Letters* 77.26 (Dec. 25, 2000), pp. 4422–4424. ISSN: 0003-6951, 1077-3118. DOI: 10.1063/1.1336550.

[88] B. L. Zink, J. N. Ullom, J. A. Beall, K. D. Irwin, W. B. Doriese, W. D. Duncan, L. Ferreira, G. C. Hilton, R. D. Horansky, C. D. Reintsema, and L. R. Vale. "Array-compatible transition-edge sensor microcalorimeter gamma-ray detector with 42eV energy resolution at 103keV". In: *Applied Physics Letters* 89.12 (Sept. 20, 2006), p. 124101. ISSN: 0003-6951, 1077-3118. DOI: 10.1063/1.2352712.

[89] I. J. Maasilta. "Complex impedance, responsivity and noise of transition-edge sensors: Analytical solutions for two- and three-block thermal models". In: *AIP Advances* 2.4 (Oct. 10, 2012), p. 042110. ISSN: 2158-3226. DOI: 10.1063/1.4759111.

[90] M. R. Moussa, R. Muijlwijk, and H. Van Dijk. "The vapour pressure of liquid nitrogen". In: *Physica* 32.5 (May 1966), pp. 900–912. ISSN: 0031-8914. DOI: 10.1016/0031-8914(66)90021-8.

[91] Charles Dietlein, Zoya Popovic, and Erich N. Grossman. "Aqueous blackbody calibration source for millimeter-wave/terahertz metrology". In: *Applied Optics* 47.30 (Oct. 20, 2008), pp. 5604–5615. DOI: 10.1364/AO.47.005604.

[92] N. L. Ramanathan. "A new weighting system for mean surface temperature of the human body". In: *Journal of Applied Physiology* 19.3 (May 1, 1964). PMID: 14173555, pp. 531–533. ISSN: 8750-7587, 1522-1601.

[93] John Daniel Kraus, Martti Tiuri, Antti V Räisänen, and Thomas D Carr. *Radio Astronomy*. Powell, Ohio (P.O. Box 85, Powell 43065): Cygnus-Quasar Books, 1986. ISBN: 1882484002 9781882484003.

[94] Rahul Datta, Johannes Hubmayr, Charles Munson, Jason Austermann, James Beall, Dan Becker, Hsiao-Mei Cho, Nils Halverson, Gene Hilton, Kent Irwin, Dale Li, Jeff McMahon, Laura Newburgh, John Nibarger, Michael Niemack, Benjamin Schmitt, Harrison Smith, Suzanne Staggs, Jeff Van Lanen, and Edward Wollack. "Horn Coupled Multichroic Polarimeters for the Atacama Cosmology Telescope Polarization Experiment". In: *arXiv:1401.8029 [astro-ph]* (2014).

[95] Neil A. Salmon. "Polarimetric scene simulation in millimeter-wave radiometric imaging". In: *Proceedings of the SPIE*. Radar Sensor Technology VIII and Passive Millimeter-Wave Imaging Technology VII. Vol. 5410. 2004, pp. 260–269. DOI: 10.1117/12.562206.

[96] J. W. Fowler, M. D. Niemack, S. R. Dicker, A. M. Aboobaker, P. A. R. Ade, E. S. Battistelli, M. J. Devlin, R. P. Fisher, M. Halpern, P. C. Hargrave, A. D. Hincks, M. Kaul, J. Klein, J. M. Lau, M. Limon, T. A. Marriage, P. D. Mauskopf, L. Page, S. T. Staggs, D. S. Swetz, E. R. Switzer, R. J. Thornton, and C. E. Tucker. "Optical design of the Atacama Cosmology Telescope and the Millimeter Bolometric Array Camera". In: *Applied Optics* 46.17 (June 10, 2007), pp. 3444–3454. DOI: 10.1364/AO.46.003444.

[97] D.N. Black and James C. Wiltse. "Millimeter-Wave Characteristics of Phase-Correcting Fresnel Zone Plates". In: *IEEE Transactions on Microwave Theory and Techniques* 35.12 (Dec. 1987), pp. 1122–1129. ISSN: 0018-9480. DOI: 10.1109/TMTT.1987.1133826.

[98] K. D. Irwin, H. M. Cho, W. B. Doriese, J. W. Fowler, G. C. Hilton, M. D. Niemack, C. D. Reintsema, D. R. Schmidt, J. N. Ullom, and L. R. Vale. "Advanced Code-Division Multiplexers for Superconducting Detector Arrays". In: *Journal of Low Temperature Physics* 167.5 (June 1, 2012), pp. 588–594. ISSN: 0022-2291, 1573-7357. DOI: 10.1007/s10909-012-0586-7.

[99] Henry G. Leduc, Bruce Bumble, Peter K. Day, Byeong Ho Eom, Jiansong Gao, Sunil Golwala, Benjamin A. Mazin, Sean McHugh, Andrew Merrill, David C. Moore, Omid Noroozian, Anthony D. Turner, and Jonas Zmuidzinas. "Titanium nitride films for ultrasensitive microresonator detectors". In: *Applied Physics Letters* 97.10 (Sept. 10, 2010), p. 102509. ISSN: 0003-6951, 1077-3118. DOI: 10.1063/1.3480420.

[100] Michael R. Vissers, Jiansong Gao, Martin Sandberg, Shannon M. Duff, David S. Wisbey, Kent D. Irwin, and David P. Pappas. "Proximity-coupled Ti/TiN multi-layers for use in kinetic inductance detectors". In: *Applied Physics Letters* 102.23 (June 14, 2013), p. 232603. ISSN: 0003-6951, 1077-3118. DOI: 10.1063/1.4804286.